In–Situ Synthesis of Ferrites Nano Particles using Sonochemical Route

P. P. Goswami[1], H.A. Choudhury[2], S. Chakma[1,*] and V. S. Moholkar[1]
[1]Department of Chemical Engineering, [2]Center for Energy
Indian Institute of Technology Guwahati
Guwahati – 781039, Assam, India
* E–mail: sankar@iitg.ernet.in

Abstract

This paper reports the additives free sonochemical synthesis of manganese ferrite and cobalt ferrite nano–particles using metal acetate as precursors. The synthesis of the ferrites occurs in three steps, viz. hydrolysis of acetates, oxidation of hydroxides and in–situ micro–calcination of metal oxides, and these are facilitated by physical and chemical effects of cavitation bubbles. The collisions between metal oxide particles induced by shock waves generated by transient cavitation are able to cross the activation energy barrier leading to formation of ferrites. The analysis of experimental result showed that $MnFe_2O_4$ and $CoFe_2O_4$ are found to be in nano scale, with uniform morphology and well crystalline nature. Thus, sonochemical route is one of the facile and environmental friendly techniques for synthesis of ferrite nano–particle.

Keywords: Manganese ferrite, Cobalt ferrite, Ultrasound, Cavitation.

1. Introduction

Metal ferrites or spinel ferrites nano–particles are one of the most interesting research areas due to their extra ordinary properties and their applications such as magnetic sensors, medical implants, watches, transformer circuits, generator, telecommunications, magnetic fluids and magnetic resonance imaging, microwave absorbers and similar other applications [1–3]. In the last few decades, numerous scientists have reported various conventional techniques for synthesis of metal nano–particles, such as: sol–gel method [4,5], micro–emulsions [6,7], reverse micelles [8], auto–combustion [9] and co–precipitation [10]. Recently few papers are published which dealt with sonochemical route for synthesis of ferrite nano–particles [11–14], in which the reaction mixture is exposed to ultrasound irradiation to provide a required activation energy to overcome the barrier to form ferrites. In sonochemical synthesis of ferrites, acetate metal salts are hydrolyzed followed by oxidation of ferrous hydroxide and the reaction of two metal oxides.

In this study, we have tried to emphasize the links between chemistry of ferrite synthesis and physics of ultrasound and cavitation bubbles by coupling the experimental results with numerical simulations of cavitation bubble dynamics. In sonochemical route, Fe_2O_3 is formed in two step reactions: (i) hydrolysis of iron acetate and (II) oxidation of ferrous hydroxide by H_2O_2 generated by transient collapse of cavitation bubbles. Another effect of ultrasound is the shockwaves which helps the particles of metal oxide to undergo in–situ calcinations in reaction mixture itself due to highly energetic collisions between them induced by it. During the transient collapse, the temperature and pressure inside the bubble reach extremely high, approximately 5000 K and 500 bar respectively. At these extreme conditions of the bubbles, these particles can also undergo in–situ micro–calcination in the thin liquid shell surrounding the bubble where the temperature reaches very high [15–17]. The general mechanism of ferrite synthesis using sonochemical method is as follows [Eqn. 1-6]:
Generation of oxidizing species through sonolysis of water:

$$H_2O \longrightarrow {}^\bullet OH + {}^\bullet H \tag{1}$$

$$2\,{}^\bullet OH \longrightarrow H_2O_2 \tag{2}$$

Hydrolysis of metal acetate to form their respective hydroxide and oxides:

$$Fe(CH_3COO)_2 + 2\,H_2O \longrightarrow Fe(OH)_2 + 2\,CH_3COOH \tag{3}$$

$$X(CH_3COO)_2 + 2\,H_2O \longrightarrow XO + 2\,CH_3COOH + 2\,H_2O \tag{4}$$
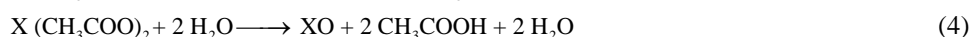
Where, X represents the metals either Mn or Co. Then the ferrous hydroxide again undergoes a reaction to form its oxide by reacting with H_2O_2 generated by transient collapse of the cavitation bubble. Consequently, the two metal oxides, XO and Fe_3O_4 can react to form XFe_2O_4 through the following reaction) to form.

$$3\,Fe(OH)_2 + H_2O_2 \longrightarrow Fe_3O_4 + 4\,H_2O \tag{5}$$

$$2\,Fe_3O_4 + 3\,XO \xrightarrow{[O]} 3\,XFe_2O_4 \qquad (6)$$

For this present study, XFe_2O_4 is the representative of $MnFe_2O_4$ and $CoFe_2O_4$.

2. Materials and methods

Materials: The following chemicals were used for synthesis of ferrites nanoparticles: iron (II) acetate (AR Grade, Sigma–Aldrich), manganese acetate (AR Grade, Sigma–Aldrich), cobalt acetate (AR Grade, Sigma–Aldrich), HCL (AR Grade, Merck), NaOH (pellets form, Merck). All the chemicals were used as received from the suppliers.

Methods: In 20 mL de–ionized water, a 0.2 M of manganese acetate or cobalt acetate was prepared with 0.4 M of iron (II) acetate. Then the reaction mixture was sonicated for 30 min in pulse mode (20 s on 5 s off) using an ultrasonic probe (13 mm OD, 20 kHz) driven by micro–processor controlled unit (Model: VCX500, 500 W). The probe was operated at 20% amplitude with theoretical power dissipation of 100 W. The temperature of the reaction mixture was maintained at $70^{\circ}C$ ($\pm4^{\circ}C$) during all the experiments. The pH of the solution was controlled by drop–wise addition of either 0.1N HCl or 0.1N NaOH solution. One should be noted that, there was no addition of external H_2O_2 to the reaction mixture during the synthesis of ferrite nano–particles, as required for the oxidation of ferrous hydroxide. Moreover, no external calcination was employed to the obtained solid products after the sonication.

Numerical modeling of cavitation bubble dynamics: The physical and chemical effects induced by ultrasound and cavitation bubbles in the system were estimated using the diffusion limited ordinary differential equation (ODE) model with boundary layer approximation proposed by Toegel et al. [18]. This model is basically derived from the comprehensive partial differential equation (PDE) model of Storey and Szeri [19], which demonstrated that vapor entrapment in the cavitation bubble, leading to formation of radicals is essentially a diffusion limited process. The main components of the model are set of 4 ODEs as follows: (1) Keller–Miksis equation for the radial motion of the bubble [20]. (2) Equation for the diffusive flux of water vapor and heat conduction through bubble wall. (3) Overall energy balance treating the cavitation bubble as an open system. For greater details readers may see our previous papers [21,22]. The set of 4 ODEs are also given below [Eqn. 7-18]:

1. Radial motion of the cavitation bubble: $\left(1-\dfrac{dR/dt}{c}\right)R\dfrac{d^2R}{dt^2}+\dfrac{3}{2}\left(1-\dfrac{dR/dt}{3c}\right)\left(\dfrac{dR}{dt}\right)^2 = \dfrac{1}{\rho_L}\left(1+\dfrac{dR/dt}{c}\right)(P_i-P_t)+\dfrac{R}{\rho_L c}\dfrac{dP_i}{dt}-4v\dfrac{dR/dt}{R}-\dfrac{2\sigma}{\rho_L R}$ (7)

Internal pressure in the bubble: $\quad P_i = \dfrac{N_{tot}(t)\,kT}{\left[4\pi\left(R^3(t)-h^3\right)/3\right]}$ (8)

Pressure in bulk liquid medium: $\quad P_t = P_0 - P_A\sin\left(2\pi ft\right)$ (9)

2. Diffusive flux of water molecules: $\dfrac{dN_W}{dt}=4\pi R^2 D_W\dfrac{\partial C_W}{\partial r}\bigg|_{r=R}\approx 4\pi R^2 D_W\left(\dfrac{C_{W,R}-C_W}{l_{diff}}\right)$ (10)

Instantaneous diffusive penetration depth: $l_{diff}=\min\left(\sqrt{\dfrac{RD_w}{|dR/dt|}},\dfrac{R}{\pi}\right)$ (11)

3. Heat conduction across bubble wall: $\dfrac{dQ}{dt}=4\pi R^2\lambda\dfrac{\partial T}{\partial r}\bigg|_{r=R}\approx 4\pi R^2\lambda\left(\dfrac{T_0-T}{l_{th}}\right)$ (12)

Thermal diffusion length: $l_{th}=\min\left(\sqrt{\dfrac{R\kappa}{|dR/dt|}},\dfrac{R}{\pi}\right)$ (13)

4. Overall energy balance: $C_{V,mix}dT/dt=dQ/dt-P_idV/dt+\left(h_W-U_W\right)dN_W/dt$ (14)

Mixture heat capacity: $C_{V,mix}=\sum C_{V,i}N_i$ (where, $i = N_2/O_2/H_2O$) (15)

Molecular properties of water: Enthalpy: $h_w = 4kT_o$ (16)

Internal energy: $U_W=N_WkT\left(3+\displaystyle\sum_{i=1}^{3}\dfrac{\theta_i/T}{\exp(\theta_i/T)-1}\right)$ (17)

Heat capacity of various species ($i = N_2/O_2/H_2O$): $C_{V,i}=N_ik\left(f_i/2+\sum\left((\theta_i/T)^2\exp(\theta_i/T)\big/\left(\exp(\theta_i/T)-1\right)^2\right)\right)$ (18)

The initial conditions of the ODEs are as follows: at $t = 0$, $R = R_o$, $dR/dt = 0$, $N_w = 0$, $Q = 0$, $T = T_0$. Thermodynamic data for various species is given in Table 1. The thermal conductivity and diffusion coefficient (transport parameters for the heat and mass transfer) are determined using Chapman–Enskog theory using Lennard–Jones 12–6 potential at the

bulk temperature of the liquid medium [23–26]. As the time scale for the diffusion of gases is much higher than the time scale of bubble dynamics, this model ignores the diffusion of gas across bubble interface. The ODEs in the bubble dynamics model are solved simultaneously using Runge–Kutta adaptive step size method [27]. Various parameters used in the simulation of bubble dynamics equation (air bubble) and their numerical values are as follows: ultrasound frequency (f) = 40 kHz; ultrasound pressure amplitude (P_A) = 150 kPa; bubble radius (R_o) = 5 µm and 10 µm; water vapor pressure = 2500 Pa (calculated using Antoine type correlation). Various physical properties of water are as follows: density (ρ_L) = 1000 kg/m^3, kinematic viscosity (ν) = 10^{-6} Pa–s, surface tension (σ) = 0.072 N/m and velocity of sound (c) = 1481 m/s.

Physical effect of ultrasound: Ultrasound propagates through the medium in the form of longitudinal wave with series of compression and rarefaction, and causes rapid oscillatory motion of fluid elements called as microstreaming. This motion gives rise to intense micro–mixing in the medium. The magnitude of the microstreaming velocity is given by: $u = P_A/\rho c$. Substituting values of P_A as 1.5×10^5 Pa, ρ = 1000 kg/m^3, and c = 1481 m/s, gives u = 0.101 m/s.

Sonochemical effect of cavitation bubbles: The numerical solution of bubble dynamics model predicts the temperature, pressure and the number of gas & solvent molecules in the bubble at transient collapse. At transient collapse, temperature and pressure reach in extreme conditions, which result dissociation of molecules to form various chemical species. To calculate the composition of the bubble at the time of collapse, we assume that thermodynamic equilibrium is attained [28]. The equilibrium mole fraction of different chemical species in the bubble at the peak conditions reached at transient collapse is estimated using Gibbs free–energy minimization technique [29]. The radial motion of cavitation bubbles generates intense convection in the medium through two phenomena [Eqn. 19-20]:

(i)   Micro–convection [30]: $V_{turb}(r,t) = \dfrac{R^2}{r^2}\left(\dfrac{dR}{dt}\right)$ (19)

(ii)   Shock waves (or Acoustic waves) [31,32]: $P_{AW}(r,t) = \dfrac{\rho_L}{4\pi r}\dfrac{d^2 V_b}{dt^2} = \rho_L\dfrac{R}{r}\left[2\left(\dfrac{dR}{dt}\right)^2 + R\dfrac{d^2 R}{dt^2}\right]$ (20)

Where, V_b is the volume of the bubble. A representative value of r is taken as 1 mm. In bubble dynamic model, direct estimation of initial bubble radius is very difficult. Several phenomena such as rectified diffusion, fragmentation of the bubble etc. cause continuous change in this parameter. In a multi–bubble system, a large variation in this parameter may be expected. In order to investigate the influence of this parameter, two numerical values for this parameter, viz. 5 and 10 µm, are selected for this present study. The equilibrium composition of the bubble contents was determined using the FactSage software [33], which is based on the free–energy minimization algorithm proposed by Eriksson [29].

Table 1. Thermodynamic data for various species (data taken from ref. [23–25])

Species	Degrees of freedom (translational + rotational) (f_i)	Lennard–Jones force constants		Characteristic vibrational temperatures θ (K)
		σ (10^{-10} m)	ε/k (K)	
N$_2$	5	3.68	92	3350
O$_2$	5	3.43	113	2273
H$_2$O	6	2.65	380	2295, 5255, 5400

3. Results and Discussion

We would like to mention that no external calcination was applied to the solid particle after the sonication. The product was characterized using Xray powder diffractometer (Bruker, Advanced D8) with monochromatic Cu–K$_\alpha$ (λ=1.5406 Å) radiation operated in the range from 20 to 70°. The mean crystallite particle size (D_{xrd}) of the product was calculated from the most intense peak (311) using Debye–Scherrer equation [34,35]: $D_{xrd} = 0.9\lambda/(\beta \cos\theta)$, where, λ is the X–ray wavelength, β is the half width of the relevant diffraction peak; θ is the Bragg's angle. The morphology of the nano–particles was determined using field emission scanning electron microscope (FE–SEM, Model: SIGMA VP, Make: Carl Zeiss Microscopy GmbH, Germany). The experimental results are presented in Figs. 1 and 2. The FE–SEM micrograph of the as–synthesized ferrite particles are shown in Fig. 1a and 1b. It could be seen that the ferrite particles are more or less spherical in shape and with narrow size distribution.
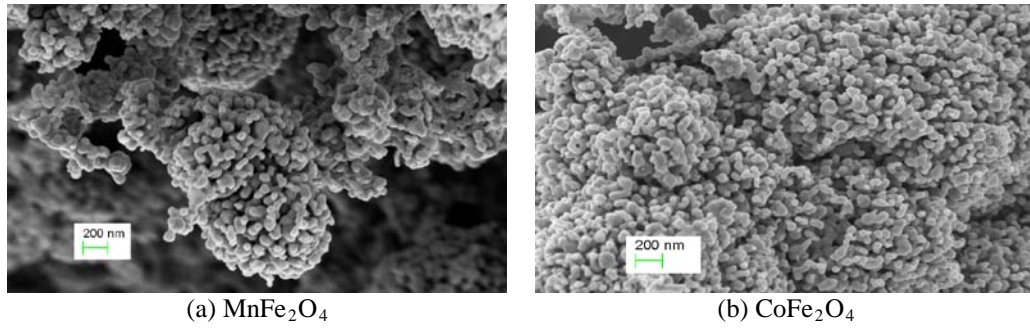
(a) MnFe$_2$O$_4$ (b) CoFe$_2$O$_4$

Fig. 1. Field emission scanning electron microscopic (FE–SEM) images of manganese ferrite and cobalt ferrite

The X–ray diffractogram of the solid product obtained after sonication is given in Fig. 2. Fig. 2 shows the diffraction peaks corresponding to the characteristics crystallographic planes of the spinel structure of ferrites [(112), (220), (311), (400), (422), (440)]. These miller indices indicate the single phase ferrites with face–centered cubic (FCC) crystal [36]. The average crystal size of the particles was calculated using Debye–Scherrer equation and it has been found to be 39 nm and 24 nm for MnFe$_2$O$_4$ and CoFe$_2$O$_4$, respectively. It should be noted that the ferrite nano–particles are formed during sonication itself, without any external calcination of the material. This essentially indicates the hypothesis of in–situ micro–calcination of the oxide precursors induced due to the energetic collisions between the particles, as they get drifted in high pressure amplitude shock wave generated by the cavitation bubble during transient collapse.
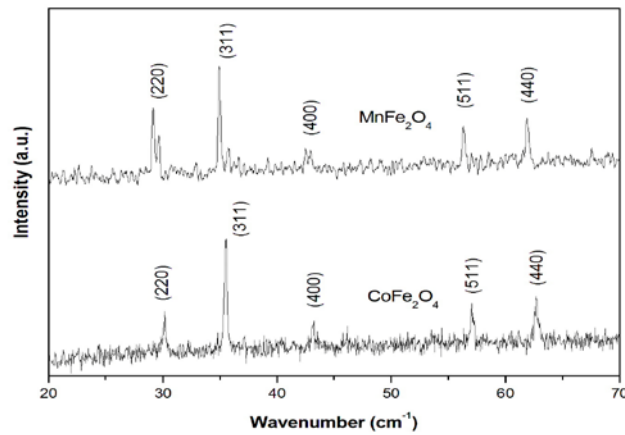
Fig. 2. XRD results of manganese ferrite and cobalt ferrite (without any external calcination)
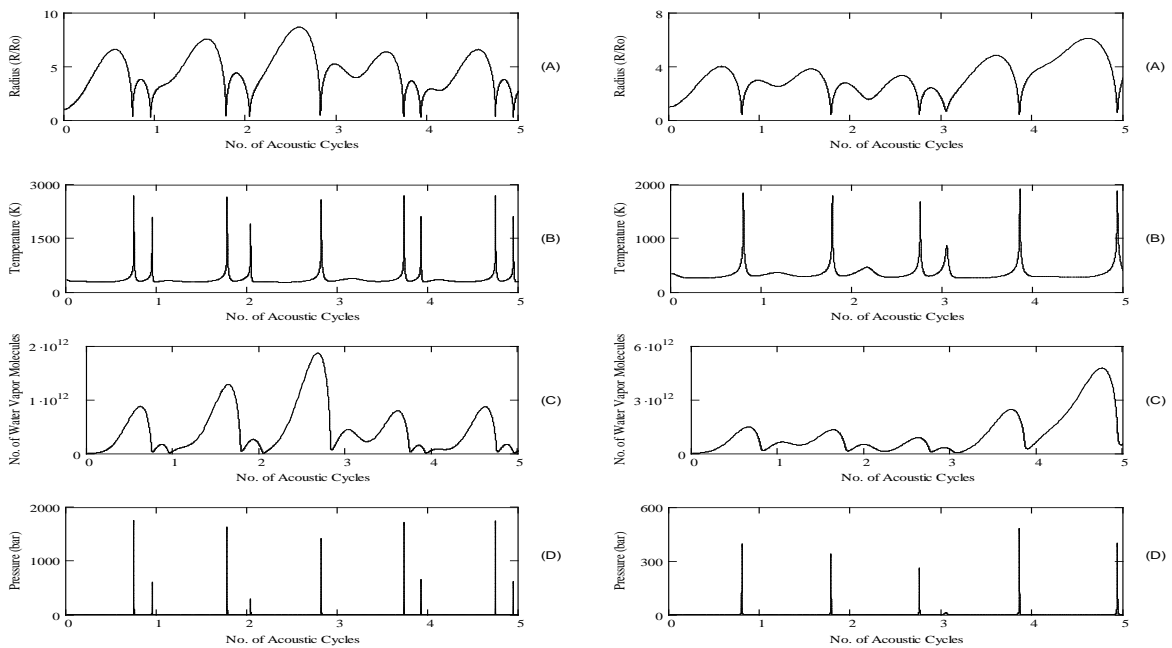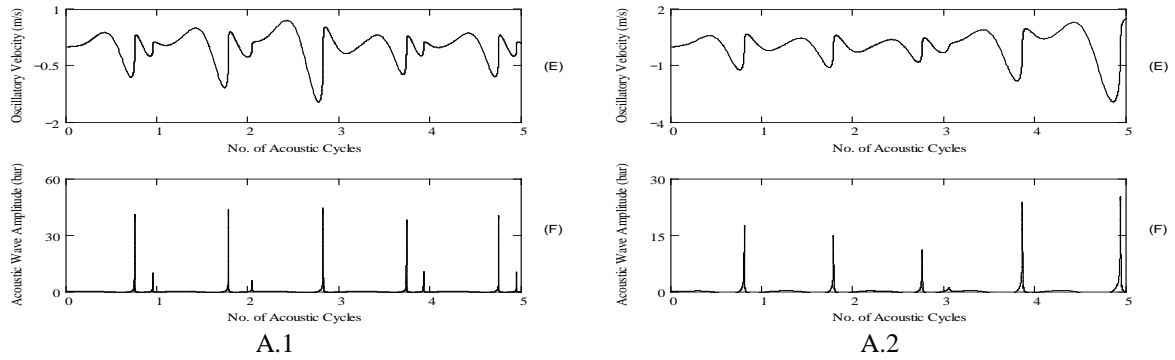
Fig. 3. Simulations of radial motion of 5 micron air bubble in water (A.1) and 10 micron air bubble in water (A.2). $f = 20$ kHz; $P_A = 150$ kPa; $P_o = 101.3$ kPa (atmospheric). Time history of (A) radius of the bubble; (B) temperature inside the bubble; (C) water vapor evaporation in the bubble; (D) pressure inside the bubble; (E) microturbulence generated by the bubble; (F) acoustic waves emitted by the bubble.

The simulation results of the bubble dynamic model are presented in Fig. 3, while the equilibrium composition of bubble contents is given in Table 2. The results of the bubble dynamic model shown in Table 2 also give an estimation of the temperature and pressure during the first collapse of the bubble. It could be seen from Table 2 that the number of water molecules in the bubble at the first collapse are 4–15 times higher than the number of gas molecules; and this is because, at the bubble interface the evaporation and diffusion of water vapor in the bubble is proportional to the vapor pressure of water, as a result a large amount of water vapor enters into bubble during expansion and gets entrapped in the consequent collapse phase. Also at the extreme conditions of the bubble, the temperatures reached at 2683 and 1844 K for 5 and 10 µm bubbles, respectively. These temperatures are quite high, which causes in–situ micro–calcination of the metal oxides. That is why no external calcination is needed for formation of ferrite nano–particles. The temperature peaks for 5 µm bubble are higher than that of for 10 µm bubble. This can be attributed to the higher expansion of 5 µm bubble during the rarefaction cycle of ultrasound, as a result of which it undergoes more intense collapse during cavitation. Table 2 also gives the magnitude of the shock waves and the velocity of the micro–turbulence generated by the bubble. The micro–convection velocity for 10 µm is two folds higher than the micro–convection velocity for 5 µm.

Table 2. Summary of simulation results at the first collapse of bubbles (air bubble)

Conditions at the first collapse of the bubble	
5 µm air bubble	10 µm air bubble
$T_{max} = 2683$ K	$T_{max} = 1844$ K
$P_{max} = 175.3$ MPa	$P_{max} = 39.72$ MPa
$V_{turb} = 1.083$ m/s	$V_{turb} = 2.204$ m/s
$P_{AW} = 4.097$ MPa	$P_{AW} = 1.751$ MPa
$N_{N2} = 1.13$ E+10	$N_{N2} = 8.07$ E+10
$N_{O2} = 3.02$ E+09	$N_{O2} = 2.15$ E+10
$N_W = 8.17$ E+10	$N_W = 3.41$ E+11

Table 3. Summary of equilibrium composition of species in the bubble at the first collapse

	Equilibrium composition of species in the bubble at collapse	
Species	5 µm air bubble	10 µm air bubble
N_2	1.16×10^{-1}	1.81×10^{-1}
O_2	2.83×10^{-2}	4.73×10^{-2}
H_2O	2.80×10^{-2}	7.69×10^{-1}
O	5.69×10^{-5}	1.99×10^{-6}
H	2.57×10^{-6}	–
O_3	2.28×10^{-7}	–
H_2	2.29×10^{-5}	1.42×10^{-5}
OH	8.08×10^{-4}	3.92×10^{-4}
HO_2	4.22×10^{-5}	1.16×10^{-5}
H_2O_2	4.60×10^{-6}	3.56×10^{-6}
NO	4.57×10^{-3}	1.17×10^{-3}
NO_2	1.11×10^{-4}	2.37×10^{-5}
N_2O	8.69×10^{-6}	–
HNO	9.69×10^{-7}	–

HNO_2	1.76×10^{-5}	5.29×10^{-6}

4. Conclusion

In this study, we have presented the additives free sonochemical route for synthesis of ferrite nano–particles. Under the ultrasound irradiation, the metal acetates as precursors are hydrolyzed and oxidized to form metal oxides. High energy collisions between the particles due to the shock waves generated by transient collapse of cavitation bubble causes synthesis of ferrites through in–situ micro–calcination of the oxide particles. Most notably, no external calcination is needed for formation of ferrites. Experimental results showed that spinel crystalline structure ferrite nano–paticles can be synthesized using only sonochemical method. We believe that results of this preliminary study could form useful guidelines for further research in the area of sonochemical synthesis of nano–sized ferrites.

5. References

[1] E.C. Snelling, Soft Ferrites: Properties and Applications, 2nd ed., *Butterworth Publishing*, London, 1989.

[2] D.C. Jiles, Introduction to Magnetism and Magnetic Materials, 2nd ed., *Chapman and Hall*, London, 1991.

[3] M.A. Willard, L.K. Kurihara, E.E. Carpenter, S. Calvin, and V.G. Harris, "Chemically prepared magnetic nanoparticles", *Int. Mater. Rev. Vol.*, Vol. 49, pp. 125–170, 2004.

[4] B.G. Toksha, S.E. Shirsath, S.M. Patange, and K.M. Jadhav, "Structural investigations and magnetic properties of cobalt ferrite nanoparticles prepared by sol–gel auto combustion method", *Solid State Commun.*, Vol. 147, pp. 479–483, 2008.

[5] K. Winiarska, I. Szczygieł, and R. Klimkiewicz, "Manganese–zinc ferrite synthesis by the sol−gel autocombustion method. Effect of the precursor on the ferrite's catalytic properties", *Ind. Eng. Chem. Res.*, Vol. 52, pp. 353−361, 2013.

[6] Y. Ahn, E.J. Choi, S. Kim, and H.N. Ok, "Magnetization and Mossbauer study of cobalt ferrite particles from nanophase cobalt iron carbonate", *Mater. Lett.*, Vol. 50, pp. 47–52, 2001.

[7] D.O. Yener and H. Giesche, "Synthesis of pure and manganese–, nickel–, and zinc doped ferrite particles in water–in–oil microemulsions", *J. Am. Ceram. Soc.*, Vol. 84, pp.1987–1995, 2001.

[8] Y. Lee, J. Lee, C.J. Bae, J. Park, H. Noh, J. Park, and T. Hyeon, "Large–scale synthesis of uniform and crystalline magnetite nanoparticles using reverse micelles as nanoreactors under reflux conditions", *Adv. Funct. Mater.*, Vol. 15, pp. 503–509, 2005.

[9] S.H. Xiao, W.F. Jiang, L.Y. Li, and X.J. Li, "Low–temperature auto–combustion synthesis and magnetic properties of cobalt ferrite nano–powder", *Mater. Chem. Phys.*, Vol. 106, pp. 82–87, 2007.

[10] I. Elahi, R. Zahira, K. Mehmood, A. Jamil, and N. Amin, "Co–precipitation synthesis, physical and magnetic properties of manganese ferrite powder", *Afr. J. Pure Appl. Chem.*, Vol. 6, pp. 1–5, 2012.

[11] M. Sivakumar, A. Gedanken, W. Zhang, Y.W. Du, D. Bhattacharya, Y. Yeshurun, and I. Felner, "Nanophase formation of strontium hexaferrite fine powder by the sonochemical method using $Fe(CO)_5$", *J. Magn. Magn. Mater.*, Vol. 268, pp. 95–104, 2004.

[12] B.R. Reddy, T. Sivasankar, M. Sivakumar, and V.S. Moholkar, "Physical facets of ultrasonic cavitational synthesis of zinc ferrite particles", *Ultrason. Sonochem.*, Vol. 17, pp. 416–426, 2010.

[13] K.D. Bhatte, D.N. Sawant, D.V. Pinjari, A.B. Pandit, and B.M. Bhanage, "One pot green synthesis of nano sized zinc oxide by sonochemical method", *Mater. Lett.*, Vol. 77, pp. 93–95, 2012.

[14] H.A. Choudhury, A. Choudhary, M. Sivakumar, and V.S. Moholkar, "Mechanistic investigation of the sonochemical synthesis of zinc ferrite", *Ultrason. Sonochem.*, Vol. 20, pp. 294–302, 2013.

[15] T.J. Mason and J.P. Lorimer, "Applied sonochemistry – the uses of power ultrasound in chemistry and processing", *J. Chem. Technol. Biotechnol.*, Vol. 79, pp. 207–208, 2004.

[16] K.S. Suslick, Ultrasound: Its chemical, physical and biological Effects, *VCH*, New York, 1998.

[17] C. Gong and D.P. Hart, "Ultrasound Induced Cavitation and Sonochemical Yields", *J. Acoust. Soc. Am.*, Vol. 104, pp. 2675–2682, 1998.

[18] R. Toegel, B. Gompf, R. Pecha, and D. Lohse, "Does water vapor prevent upscaling sonoluminescence?", *Phys. Rev. Lett.*, Vol. 85, pp. 3165–3168, 2000.

[19] B.D. Storey and A.J. Szeri, "Water vapor, sonoluminescence and sonochemistry", *Proc. R. Soc. Lond. Ser. A*, Vol. 456, pp. 1685–1709, 2000.

[20] J.B. Keller and M.J. Miksis, "Bubble oscillations of large amplitude", *J. Acoust. Soc. Am.*, Vol. 68, pp. 628–633, 1980.

[21] S. Chakma and V.S. Moholkar, "Mechanistic features of ultrasonic desorption of aromatic pollutants", Chem. Eng. J., Vol. 175, pp. 356–367, 2011.

[22] S. Chakma and V.S. moholkar, "Physical mechanism of sono–Fenton process", *AIChE J.*, doi:10.1002/aic.14150, 2013.

[23] J.O. Hirschfelder, C.F. Curtiss, and R.B. Bird, Molecular Theory of Gases and Liquids, *Wiley*, New York, 1954.

[24] E.U. Condon and H. Odishaw, Handbook of physics, *McGraw Hill*, New York, 1958.

[25] R.C. Reid, J.M. Prausnitz, and B.E. Poling, Properties of gases and liquids, *McGraw Hill*, New York, 1987.

[26] R.B. Bird, W.E. Stewart, and E.N. Lightfoot, Transport phenomena, 2nd ed., *Wiley*, New York, 2001.

[27] W.H. Press, S.A. Teukolsky, B.P. Flannery, and W.T. Vetterling, Numerical Recipes, 2nd ed., *Cambridge University Press*, New York, 1992.

[28] J.S. Krishnan, P. Dwivedi, V.S. Moholkar, "Numerical investigation into the chemistry induced by hydrodynamic cavitation", *Ind. Eng. Chem. Res.*, Vol. 45, pp. 1493–1504, 2006.

[29] G. Eriksson, "Thermodynamic studies of high temperature equilibria—XII: SOLGAMIX, a computer program for calculation of equilibrium composition in multiphase systems", *Chem. Scr.*, Vol. 8, pp. 100–103, 1975.

[30] Y.T. Shah, A.B. Pandit, and V.S. Moholkar, Cavitation reaction engineering, *Plenum Press*, New York, 1999.

[31] S. Grossmann, S. Hilgenfeldt, M. Zomack, and D. Lohse, "Sound radiation of 3 MHz driven gas bubbles", *J. Acoust. Soc. Am.*, Vol. 102, pp. 1223–1227, 1997.

[32] V.S. Moholkar and M.M.C.G. Warmoeskerken, "An integrated approach to optimization of an ultrasonic processor", *AIChE J.*, Vol. 49, pp. 2918–2932, 2003.

[33] FactSage software, http://www.factsage.com/, access on June– 2013.

[34] V. Drits, J. Srodon, and D.D. Eberl, "XRD measurement of mean crystallite thickness of illite an illite/smectite: reappraisal of the kubler index and the scherrer equation", *Clay. Clay Miner.*, Vol. 45, pp. 461–475, 1997.

[35] Y. Koseoglu, F. Alan, M. Tan, R. Yilgin, and M. Ozturk, "Low temperature hydrothermal synthesis and characterization of Mn doped cobalt ferrite nanoparticles", *Ceramic. Int.*, Vol. 38, pp. 3625–3634, 2012.

[36] M.G. Naseri, E.B. Saion, H.A. Ahangar, A.H. Shaari, and M. Hashim, "Simple synthesis and characterization of cobalt ferrite nanoparticles by a thermal treatment method", *J. Nanomater.*, ID 907686, pp. 1–8, 2010.

Paper ID: MS-02

Influence of Porosity on Flexural Strength and Flexural Modulus of an Eco-ceramic Membrane

Sujoy Bose and Chandan Das[1]
[1]Department of Chemical Engineering
Indian Institute of Technology Guwahati
Guwahati, Assam, India
Tel.: +91 361 2582268; Fax: +91-361-2582291
Email: cdas@iitg.ac.in

Abstract

This paper deals with the relationship between porosity and flexural strength along with flexural modulus of an eco-ceramic membrane. The eco-ceramic membrane is made of kaolin, feldspar and sawdust (pore former) along with two binders i.e. sodium metasilicate and boric acid. The membrane is prepared using uniaxial dry compaction process by applying two different pressures (7.84 and 11.76 MPa) followed by sintering in a muffle furnace at 850°C. Volumetric porosity is determined by gravimetric analysis of water. The evaluation of modulus of rupture (MOR) test (flexural strength and flexural modulus) has been done using three-point bend test (ASTM D790) at room temperature. Based on these results, it has been observed that with decrease in porosity from 28% to 11%, flexural strength increases from 4.46 to 13.29 MPa along with an increase in flexural modulus from 0.62 to 1.89 GPa.

Keywords: Eco-ceramic, porosity, flexural strength, flexural modulus

1. Introduction

Membrane technology advances significantly in various areas of chemical and biochemical processing, especially ceramic membranes for their high thermal stability and handling of corrosive feedstock. Present and ongoing research in membrane technology aims to use low-cost raw materials to minimize the cost of ceramic membranes [1,2].

Nowadays fundamental research regarding fabrication of ceramic membranes is focused towards different type of precursors like sawdust and their impact on porous texture and mechanical strength of the inorganic matrix [3]. In addition to this, the feature of such research is to find such a raw material which not only can provide thermally and mechanically stable membrane but also can offer low manufacturing cost.
The environmentally conscious ceramics i.e., eco-ceramics have some benefits over traditional ceramics like low energy consumption during the entire manufacturing process of composites, availability of wide variety of microstructures. The use of sawdust provides a low-cost starting material that has the capabilities of presenting agreeable porous structures that are normally produced by traditional ceramic processing techniques.
Porosity, an important characteristics of ceramic membranes, act as crack initiation sites and has an influence on mechanical strength. Ceramic membranes can be porous or dense, depends on the particle size of raw materials, as well as drying and sintering.Ceramic products undergo thermal and mechanical stress during sintering. Both flexural strength and flexural modulus are the key physical parameters of ceramic material as they are brittle in nature.
The flexural strength is the material's ability to resist deformation under load and depends on crack initiators or flaws present initially inside the ceramics and the amount of raw materials present in the specimen.But these crack initiators are not identical in nature and can provide rupture of membranes at different loading forces [4]. A relationshipbetween themechanical strengthand Young's modulus of

ceramic specimens is also well known [5].On the other hand, flexural modulus is an intensive property which does not depend on the size or the amount of material in the specimen and the presence of cracks. Hypothetically, linearity between the flexural strength and flexural modulus is valid when flexural modulus is measured separately, not simultaneously with mechanicalstrength.

The objective of this paper is to verify the effect of porosity on the flexural strength and flexural modulus for the fabricated eco-ceramic membrane and a linear relationship between flexural strength and flexural modulus.

2.   Materials and methods

The chemicals used in this study are kaolin (LobaChemiePvt. Ltd., Mumbai, India, >99.5%), sawdust (taken from local sawmill), and feldspar (National Chemicals, Gujarat, India) for the fabrication of eco-ceramic membrane support served for different functional aspects. Kaolin is used to provide low plasticity and high refractory properties to the membrane support. Sawdust is used as a pore former and releases CO_2 gas when heated. The released carbon dioxide gas emits via some uneven paths which makes the membrane porous and contributes to the membrane porosity. Feldspar employs to offer a glassy matrix in the early stage of the firing process, bonded the other raw materials of the system together. Sodium metasilicate (M/s Lobachemie, India) and boric acid (M/s Merck Specialities Pvt. Ltd., India) have been used as binder.Sodium metasilicate enhance the mechanical strength by making silicate bonds among all the raw materials. Boric acid acts as a colloidal agent and forms metallic metaborates during sintering process, also maintains homogeneity in the membrane structure by increasing dispersion properties of the inorganic precursors.

The tubular support membrane is prepared by thorough mixing and grinding of dry inorganic raw materials (kaolin, saw dust, feldspar and binders) of two different compositions using mixer machine and ceramic mortar. Four membranes have been prepared by applying two different forming pressures (7.84 and 11.76 MPa) namely M1 to M4, listed in Table 1. All the mixtures placed separately into a cylindrical mould (50 mm diameter, 50mm height and thickness of 10 mm) made by mild steel. The raw materials are pressed into the mould using hydraulic press (Velan Engineering, Tamilnadu, India) by uniaxial dry compaction. Then the mixture is kept under distributed pressure for 1 min to prevent the propagation deformation and kept homogeneity in the raw material mixture. The irregular shape and sizes of sawdust particles is separated using Gyratory shaker. The fabricated membrane is removed cautiously from the mould and subjected to two heat treatment steps. Firstly, the membrane is dried at room temperature for 24 h. After that, it is dried at 100°C for 12 h in a muffle furnace followed by heating at 250°C for 24 h. Secondly, the membrane is heated from 250°C to the desired temperature at a heating rate of 2°C/min. Then the membrane is kept into the furnace for 5 h for sintering at 850°C. Then the membrane is cooled by an atmospheric cooling process implemented by switching off the muffle furnace which is earlier maintained at a desired sintering temperature. The membranes achieved a hard, rigid and porous texture after sintering.

Characterization techniques include volumetric porosity determination technique and three-point bend test (ASTM D790) to determine the porosity and the modulus of rupture (flexural strength and flexural modulus).The volumetric porosity of all the membranes is calculated by gravimetric analysis of water, based on the entrapment of water in the pores of the membrane walls. Initially, the dry sintered membranes are measured, then the membranes are dipped into deionized water for 24 hours. The soaked membranes then dried by tissue paper and weighed.The volumetric porosity is calculated using equation number 1, given below.

$$\varepsilon_v = \left(W_2 - W_1\right)\Big/\rho_{H_2O}.V \tag{1}$$

Where, W_2, W_1, ρ_{H_2O} and V are the weights of the wet and dry membrane samples, the density of the deionized water and the volume of the fabricated membrane, respectively.

Table 1. Properties of the fabricated eco-ceramic tubular membrane

Combinations	Applied pressure in MPa	Kaolin in %	Sawdust in %	Feldspar in %	SM in %	BA in %
M1	7.84	50	10	30	5	5
M2	7.84	50	10	25	10	10
M3	11.76	50	10	30	5	5
M4	11.76	50	10	20	10	10

A measurement of flexural strength and flexural modulus has been done on ASTM standard equation. This test can affect the structure of the tested material and create microcracks in ceramic materials as ceramics are brittle in nature. For that reason, a flexion of the sample is often used for ceramic materials, called three-point-bending testis performed to measure the strength of the prepared specimen using a Universal Tensile Test Machine (Deepak polyplastPvt. Ltd., India) maintaining 60 mm support span at room temperature at a stroke rate of 0.5 mm/min. Rectangular bar-shaped specimens are prepared by maintaining thickness/length ratio 1:16 for determining the flexural strength at room temperature. The flexural strength and flexural modulus for rectangular shape specimen is generated by the instrument automatically using equation number 2 and 3, mentioned earlier.

$$\sigma_{UF} = 3P_{max}.L\big/2bh^2 \tag{2}$$

$$E_F = mL^3\big/4bh^3 \tag{3}$$

Where, σ_{UF} and E_F is the flexural strength and flexural modulus of the ceramic material, P_{max} is the maximum load at failure, L is the specimen length between the two support points, b is the specimen width, h is the specimen thickness, m the initial slope of the load–deflection curve.

3. Results and discussions

3.1. Effect of pressure and binder on Porosity

The volumetric porosity of M1 to M4 sintered at 850°Cis listed in Fig.1. In this study, the porosity of the membranes isdependent on two major factors: (i) effect of forming pressure; and (ii) amount of binder.Fig.1 shows the influence of forming pressure and amount of binder on the porosity of M1, M2, M3 and M4 membranes. Porosityis reducing abruptly with increasing binder content as well as forming pressure, is due to more and more contact of particles with each other at higher temperature.But, the difference in porosity is not so much higher though the variation in forming pressure is high.
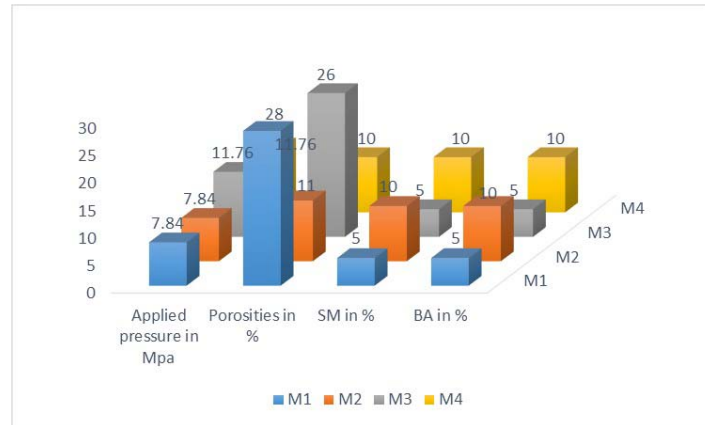
Fig. 1. Influence of forming pressure and binder content on porosity of the fabricated membrane

3.2. Effect of porosity on modulus of rupture (MOR)

	M1	M2	M3	M4
Flexural strength in Mpa	4.46	13.29	6.72	11.99
flexural modulus in Gpa	0.62	1.89	1.01	1.61
Porosities in %	28	11	26	10
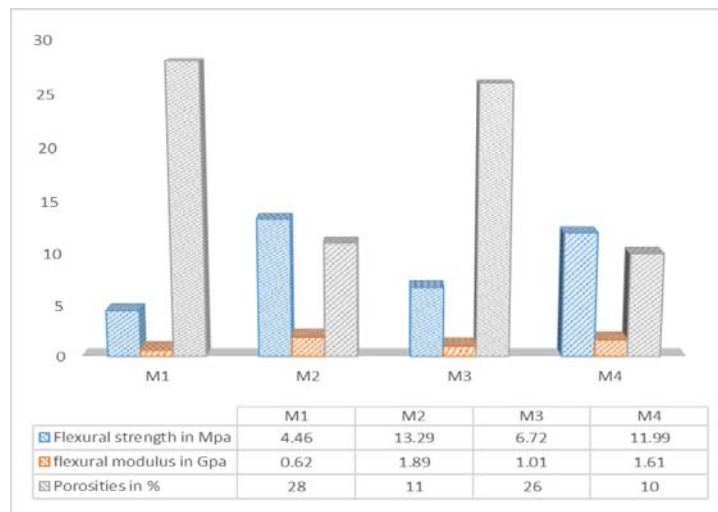
Fig. 2. Dependence of modulus of rupture (MOR) on the porosity of the fabricated membrane

Fig. 2 shows a linear relationship between flexural strength and flexural modulus versus porosity during three-point bend test at room temperature. During sintering, the particles starts to form necks with each other. With increasing sintering temperature, the initially formed necks become broader, the shrinkage becomes larger and causes an abrupt decrease in porosity.Less porous texture inhibits crack propagation, results a higher flexural strength and flexural modulus. In Fig. 2, the result of M2 and M4 strongly approves this theory and establishes that flexural strengthof a ceramic membrane is inversely proportional to the porosity of that particular ceramic.A typical relationship between the deflection and loading force of the fabricated eco-ceramic sample in the three-point-bending test is depicted in Table 2.It is observed from the table that percentage deflection is 5% for M2, M3 and M4 whereas it is only 2% for M1. This is due to the presence of less amount of binders present in M1. Though M3 contains same amount of binders as in M1, it is showing 5% deflection as it is fabricated at higher pressure.

Table 2. Dependence of deflection on loading forces

Combinations	Loading Force 1 in N	Deflection in mm	Loading Force 1 in N	Deflection in mm	Percentage of deflection
M1	5.5	0	7.73	0.02	2
M2	9.31	0	16.69	0.05	5
M3	6.11	0	10.06	0.05	5
M4	5.52	0	11.82	0.05	5

4. Conclusion

A verification of theoretical linearity between flexural strength and flexural modulus versus porosity is performed with fabricated eco-ceramic membrane made of cheap raw materials (kaolin, sawdust, feldspar, sodium silicate and boric acid) at 850°C.The conducted experiments clearly summarizes that
(a) with increase in forming pressure and high binder content, porosity decreases
(b) both flexural strength and flexural modulus increase linearly with decrease in porosity

5. References

[1] Y. Donga, S. Chena, X. Zhang, J. Yang, X. Liu, and G. Menga, "Fabrication and characterization of low cost tubular mineral-based ceramic membranes for micro-filtration from natural zeolite", *Journal of Membrane Science*, Vol.281, No.1-2, pp. 592-599, 2006.
[2] B.K. Nandi, R. Uppaluri, and M.K. Purkait, "Preparation and characterization of low cost ceramic membranes for micro-filtration applications", *Applied Clay Science*, Vol.42, No.1-2, pp. 102-110, 2008.
[3] F.T. Owoeye, O.S. Olokode, P.O. Aiyedun, H.O. Balogun, and B.U. Anyanwu, "Preparation and Characterization of Ceramic Microfiltration Membrane for Water Treatment", *The Pacific Journal of Science and Technology*, Vol.13, No.2, pp. 28-38, 2012.
[4] D. Bortzmeyer, G. Langguth, and G. Orange, "Fracture mechanics of green products", *Journal of the European Ceramic Society*, Vol.11, No.1, pp. 9-16, 1993.
[5] I. Štubňa, A. Trník, Peter Šín, R. Sokolář, and I. Medved, "Relationship between mechanical strength and young's modulus in traditional ceramics", *Materials and Technology*, Vol.45, No. 4, pp.375–378, 2011.

Studying the Effects of Deformation on Microstructure and Mechanical Behavior of Al-Cu Alloys

N. Nafsin and H. M. M. A. Rashed

Department of Materials and Metallurgical Engineering, Bangladesh University of Engineering and Technology, Dhaka-1000, Bangladesh
Email: nazia@mme.buet.ac.bd; hrashed@mme.buet.ac.bd

Abstract

Aluminum alloys with a wide range of properties are used in engineering structures. Selecting the right alloy for a given application entails considerations of its tensile strength, density, ductility, formability, workability, weldability, and corrosion resistance, to name a few. Aluminum alloys are used extensively in aircraft due to their high strength-to-weight ratio. On the other hand, pure aluminum metal is much too soft for such uses, and it does not have the high tensile strength that is needed for airplanes and helicopters. Thus various alloying elements are added to aluminum to enhance the mechanical properties of aluminum. Copper has been the most common alloying element almost since the beginning of the aluminum industry, and a variety of alloys in which copper is the major addition were developed. The current research emphasizes establishment of relationship between microstructure and cold deformation behavior of aluminum copper alloys. Aluminum copper alloys with varying Cu% were casted and their chemical compositions were determined using Optical Emission Spectroscopy (OES). These alloys undergone cold deformation and their microstructures were examined using optical microscope. Finally the effects of deformation were studied by measuring the hardness of those alloys.
.

Keywords: Aluminum copper alloy, microstructure, cold deformation, hardness, CALPHAD.

1. Introduction

Aluminum alloys are alloys in which aluminum (Al) is the predominant metal. The typical alloying elements are copper, magnesium, manganese, silicon and zinc. There are two principal classifications, namely casting alloys and wrought alloys, both of which are further subdivided into the categories heat-treatable and non-heat-treatable. About 85% of aluminum is used for wrought products, for example rolled plate, foils and extrusions. Cast aluminum alloys yield cost effective products due to the low melting point, although they generally have lower tensile strengths than wrought alloys. Aluminum alloys are widely used in engineering structures and components where light weight or corrosion resistance is required [1].

The most important cast aluminum alloy system is Al-Cu. The addition of copper as main alloying element (mostly range 3–6 wt. %, but can be much higher), with or without magnesium as alloying constituent (range 0–2 %), allows material strengthening by precipitation hardening, resulting in very strong alloys. Also the fatigue properties are very good for this series. In contrast, the presence of copper is detrimental for corrosion resistance [2]. Copper tends to precipitate at grain boundaries, making the metal very susceptible to pitting, intergranular corrosion and stress corrosion. These copper rich zones are more noble/cathodic than the surrounding aluminum matrix and act as preferred sites for corrosion through galvanic coupling. In addition, copper has unfavorable effect on anodizing of these alloys. Copper precipitates dissolve in the anodizing electrolytes (acid electrolytes for porous film formation) leaving holes in the oxide, and solute copper migrates under the high electric field towards the aluminum/oxide interface compromising the anodic film properties.

Up to 12 wt. % copper the strength of the alloy can increase through precipitation hardening, with or without the presence of magnesium; hardening is achieved through the precipitation of Al_2Cu or Al_2CuMg intermetallic phases during ageing process which leads to strengths second only to the highest strength 7xxx series alloys [2]. Above 12 wt. % Cu the alloy becomes brittle. Copper also improves fatigue properties, high-temperature

properties and machinability of the alloy. These alloys are used for high strength structural applications such as aircraft fittings and wheels, military vehicles and bridges, forgings for trucks, etc [2, 3].

Environmental legislation to reduce emission of greenhouse gases is forcing transportation industries to find out substitutes of steels–currently profoundly used in vehicle production. Aluminum, being lighter than steel, is considered as an exciting alternative material in such applications. Different aluminum alloys are being prototyped by varying composition and by developing suitable microstructure with different heat treatment schedules. The current study includes the microstructural effects on deformation of aluminum alloys. Aluminum alloys of specified composition were casted and homogenized at 400 ^{o}C for four hours. Afterwards microstructures of as cast and homogenized alloys were observed. Compression tests involving 10%, 20% and 50% deformations were performed on the homogenized samples. Finally the changes in microstructure and hardness due to deformation of aluminum alloys were studied.

2. Experimental Details

The investigated materials consists aluminum as a primary constituent and copper is the major addition varied with 2, 4, 6%.

2.1. Alloy Preparation

All experimental alloys were prepared by liquid metallurgy route using pure aluminum (99.8%) and electrolytic copper (99.9%). The metals were melted in an induction furnace at predetermined weight percentages. The molten metal was poured into a permanent metal mold made of cast iron with a dimension of 200 cm length, 50 cm width and 80 cm height. The die was preheated to 200 ^{o}C. The compositions of the alloys were determined using Optical Emission Spectrometer (Shimadzu PDA 700) as shown in Table 1. The samples were cut into small pieces for homogenization treatment at 400 ^{o}C for four hours in a BlueM Electric furnace. After holding for 4 hour samples were quenched in water to retain the precipitates. Then heat treated alloys were deformed by compression to 10%, 20% and 50% each.

Table 1: Chemical composition of as cast aluminum alloys

Alloy	Al	Fe	Si	Cu	Ni	Mg
Al-2%Cu	97.48	0.26	0.00	**1.97**	0.189	0.09
Al-4%Cu	96.06	0.07	0.08	**3.69**	0.00	0.06
Al-6%Cu	93.55	0.058	0.12	**6.16**	0.01	0.06

The experimental work was segmented into two phases. The first phase consists of specimen preparation such as melting, casting and heat treatment of samples with different compositions in the aluminum-copper system. The second phase includes mechanical characterization like compression and hardness and microstructural studies using optical microscope of as cast and heat-treated samples. For microstructural observation, specimens were cut into 25 mm^3 size, and ground and polished using conventional metallographic sample preparation route. The microstructures were observed in un-etched condition using Optica B-600 MET trinocular upright metallurgical microscope and images of same resolution and of same RGB numbers were acquired using OpticaTM Vision Pro software package. CALPHAD method was used to predict the phases developed in these alloys [4-9].

2.2 Mechanical Tests

The casted alloys were undergone deformation by compression test. Each alloy was deformed to 10%, 20% and 50% in a Universal Testing Machine (UTM). The test was carried out at ambient temperature in accordance with ASTM E9-89a standard. Hardness of the specimens was measured by using a standard Rockwell Hardness testing machine in HRF scale with a 60 kg load and using 1/16" diamond indenter. Five readings were taken for each specimen at different locations to circumvent the possible effect of any alloying element segregation and the average value was considered.

3. Results and Discussion

3.1 Effect of Heat treatment on Microstructure and Hardness

Fig. 1 shows hardness of as cast and homogenized aluminum alloys containing 2-6% Cu. It clearly reveals that hardness of aluminum alloys increases with Cu% in both as cast and homogenized condition due to the increase of Cu bearing phase Al$_2$Cu (obtained from CALPHAD analysis as shown in Fig. 2) in the microstructure. There is little decrease in hardness values after homogenization treatment. This may be due to the fact that some of these phases go into solution in the matrix as indicated by their microstructures (Fig. 3).
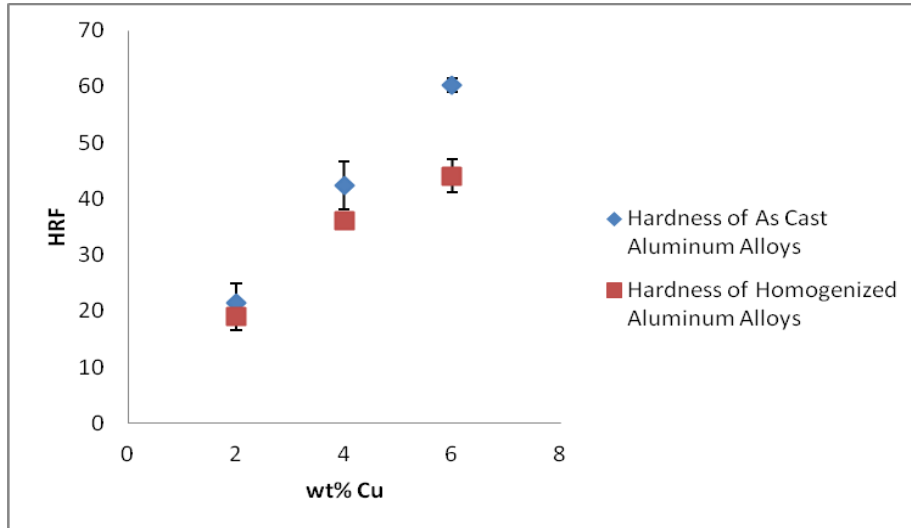
Fig. 1: Effect of Cu % and heat treatment on hardness of aluminum copper alloys
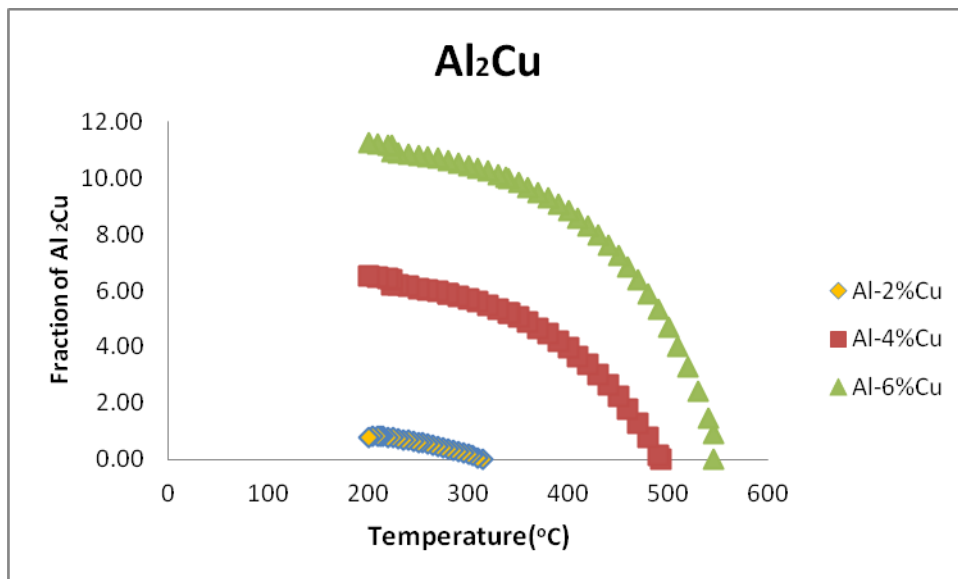
Fig. 2: Fraction of Al_2Cu in aluminum copper alloy with temperature
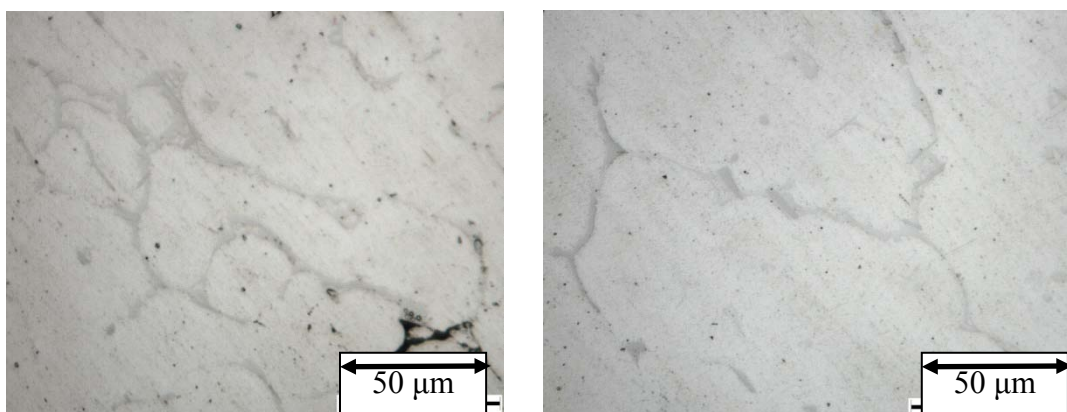
Fig. 3: Microstructure of Al-4% Cu alloys (a) As cast and (b) Homogenized

3.2 Effect of Deformation on Microstructure and Hardness

After deformation of the homogenized alloys to 10%, 20% and 50%, a large increase in hardness was evident. For each alloy, hardness was increased with increasing the amount of total deformation. Fig. 4 shows the effect of deformation on hardness. This increase in hardness is due to the presence of stored energy in the microstructure due to increase of dislocation density. Deformation increases the number of dislocations by interactions of dislocation during deformation and other defects, which cause an enhancement of hardness values [9-13]. Deformation also attributes a change in microstructure. It was observed that for each alloy the initial necklace like phases (Al_2Cu and Al_7Cu_2M) were destructed with the extent of deformation as shown in Fig. 5. As the amount of deformation increases, phases those provide an increase in hardness are no longer being in a continuous form, thereby have little significance in increasing hardness (Fig. 4).
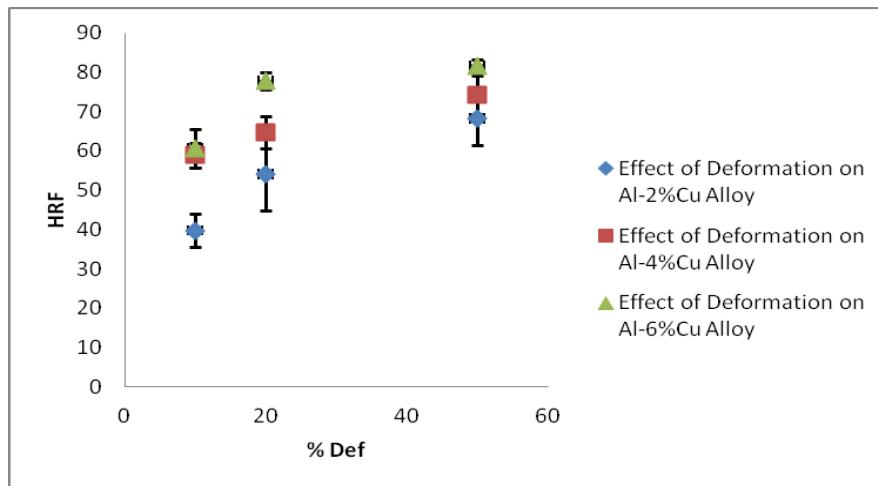
Fig. 4: Effect of deformation on hardness of aluminum copper alloys

(a)

(b)

(c)
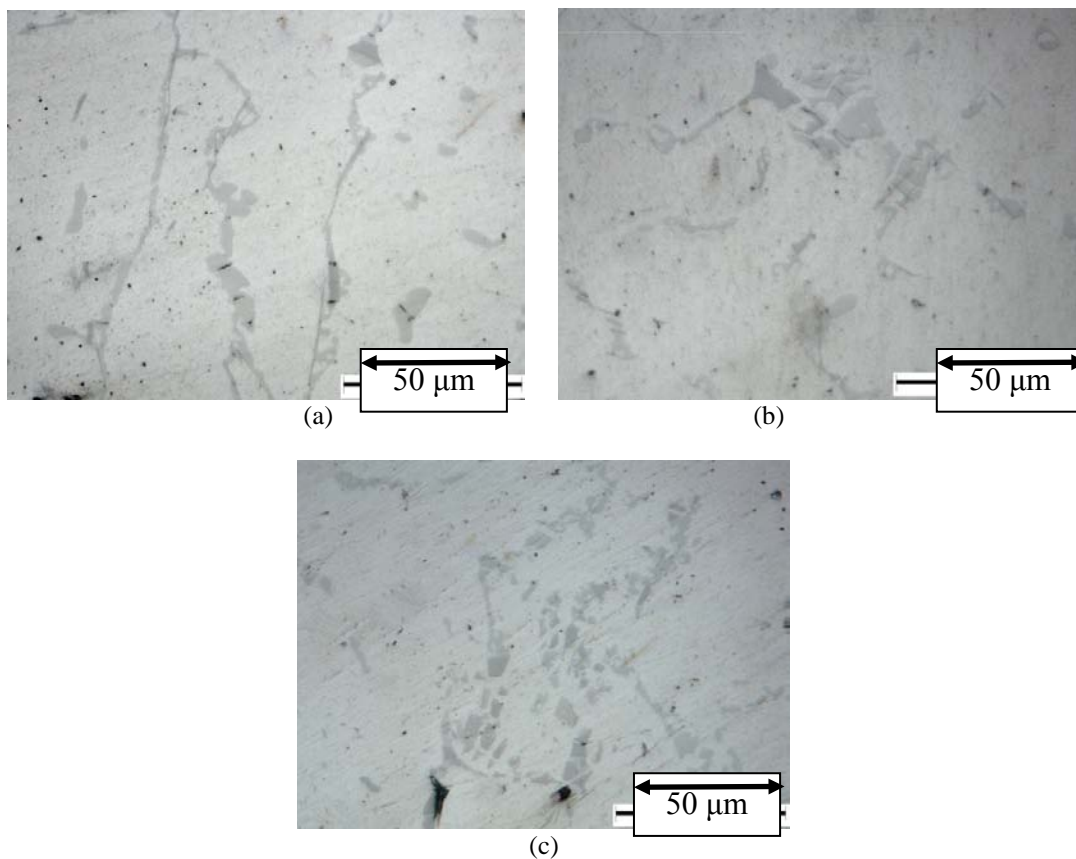
Fig. 5: Microstructure of Al-6% Cu (a) 10% (b) 20% and (c) 50% deformation

4. Conclusion

This study emphasizes the effect of deformation on microstructure and hardness of aluminum alloys with varying amount of copper. Results obtained from this study are summarized below:

(i) Deformation causes an increase in hardness than non-deformed homogenized alloy due to changes in dislocation density. Deformation increases the number of dislocations by interactions of dislocation during deformation and other defects, which cause an enhancement of hardness values. High dislocation density results in a large number of dislocation interactions which results in high strength and hardness.

(ii) With increasing amount of deformation, hardness continues to increase for different copper addition. Also, the higher the copper content, the greater the hardness.

(iii) Deformation also changes the microstructure by destroying the necklace like shape of Al-Cu phases. For this reason, with larger amount of deformation, the increment of hardness may not be very significant.

5. References

[1] Arnold, I. J. Polmear, *Light Alloys*, 1995

[2] H.N. Girisha, K.V. Sharma, Effect of magnesium on strength and microstructure of aluminum, copper, magnesium alloys, International Journal of Scientific Engineering and Research, Vol. 3, issue 2, 2012.

[3] A. Zhu, B. M. Gable, G. J. Shiflet, E. A. Jr. Starke, "Trace element effects on precipitation in Al–Cu–Mg–(Ag, Si) alloys: a computational analysis", Acta Materialia 52, pp. 3671–3679, 2004.

[4] S. Zhang,∗, Q. Han, Zi-Kui Liu, "Thermodynamic modeling of the Al–Mg–Na system", Journal of Alloys and Compounds 419, pp. 91–97, 2006.

[5] N. Saunders, "The Modelling of Stable and Metastable Phase Formation in Multi-Component Al-Alloys", 9th International Conference on Aluminium Alloys, Brisbane, Australia, 2-5 August, 2004.

[6] N. Saunders, Z. Guo, A.P. Miodownik and J.-Ph.Schillé, "Modelling the Material Properties and Behaviour of

Multicomponent Alloys", International Congress on FEM Technology with ANSYS CFX & ICEM CFD Conference, 22nd CAD-FEM Users' Meeting 2004.

[7] T.E. Quested, A.T. Dinsdale, A.L. Greer, "Thermodynamic modelling of growth-restriction effects in aluminium alloys", Acta Materialia 53, pp. 1323–1334, 2005.

[8] J. Lacaze and R. Valdes, CALPHAD-type Assessment of the Al–Mg–Si System", Monatshefte f€u ur Chemie 136, pp. 1899–1907, 2005.

[9] S. O. Adeosun, O. I. Sekunowo, S.A. Balogun, L.O. Osoba, "Effect of Deformation on the Mechanical and Electrical Properties of Aluminum-Magnesium Alloy", Journal of Minerals & Materials Characterization & Engineering, Vol. 10, No.6, pp.553-560, 2011 jmmce.org

[10] A. Abdulhaqq, P. Hamid, S. Ghosh,, O. Jain, and R. Subrata, "Processing, Microstructure and Mechanical Properties of Cast in-situ Al (Mg,Mn)-Al$_2$O$_3$(MnO2) Composites" Metallurgical and Materials Transactions A, Vol. 36A, pp 221, 2005.

[11] N. Roy, A. Samuel and F. Samuel, Metallurgical and Materials Transactions, Vol. 27A, pp. 415-429, 1996.

[12] D. Lassance, M. Schmitz, F. Delannay and T. Pardoen, "Linking Microstructure and High Temperature Ductility in Aluminum alloys AA6xxx." Seminar paper available online at: www.hallf.kth.se/forskning/ecf15/ECF-proceedings/Lassance, 2002.

[13] R. Valiev, N. Krashkov and K. Tsenev, "Plastic Deformation of Alloys with Submicron-grained Structure." Materials Science and Engineering A, Vol.153, Issue 3, pp.172-196, 1991.

Paper ID: MS-04

Performance of Recycled Coarse Aggregate in Concrete Mix

B. Ahmed[1*], M. A. A. Mahmood[2] and H. M. Rasel[3]
[1]Lecturer, Department of Civil Engineering, Rajshahi University of Engineering & Technology
Rajshahi-6204, Bangladesh (bulbulruet@gmail.com)
[2]Lecturer, Department of Glass and Ceramic Engineering, Rajshahi University of Engineering &
Technology, Rajshahi-6204, Bangladesh (abdullah2038@gmail.com)
[3]Assistant Professor, Department of Civil Engineering, Rajshahi University of Engineering &
Technology, Rajshahi-6204, Bangladesh (hmrruet@gmail.com)

Abstract

Extensive amount of concrete materials is used in building industries. The scarcity of natural coarse aggregate along with enhances demand, the recycling coarse aggregate has become a necessary and demand oriented work. The aim of this project work is to evaluate the performance of the recycled coarse aggregate by performing a comparative study of compressive and bond strength of both fresh and recycled concrete. Results indicate that compressive and bond strength of concrete prepared by using recycled coarse aggregate is 87.49% and 77.58% respectively of the average compressive and bond strength of concrete prepared by using fresh coarse aggregate. Therefore, concrete with recycled coarse aggregate may be suitably used for the construction work, such as light grade concrete, ordinary concrete, sub-base of foundation, bridge abutments etc.

Keywords: Recycling Materials, Construction Materials and Aggregates as construction Materials, Compressive Stress of Concrete, Bond Stress of Concrete.

1. Introduction

Concrete is an important versatile construction material used in wide variety of situations [1]. It is like an artificial stone manufactured from a mixture of binding material with water. Coarse aggregate and fine aggregate are used as inert materials. Concrete is being widely used in construction works. The need for inert materials is also increasing. Due to the growing demand of coarse aggregate as inert material now, it becomes important to recycle the used coarse aggregate. In the growing wake of scarcity of natural aggregate and geometric rise in its price structure the need to recycle coarse aggregate from demolished waste obtained from non-functional and obsolete buildings, debris obtained from earth quake or natural calamity such as flood and cyclone has become necessary and demand oriented work. The concrete yard of pre-fabricated units also contributes concrete waste. Since concrete accounts for about 75% by weight of all construction materials used in building industries, the demolished concrete is expected to constitute [3].

2. Objectives of the study:

  i. To compare the compressive strength of concrete between concrete prepared from fresh coarse aggregate and concrete prepared from recycled coarse aggregates.
  ii. To ascertain the extent of the use of recycled coarse aggregate in concrete from the above comparison study.

3. Research methodology

3.1 Recycled aggregate

Among the engineering materials the aggregate (sand & khoa) play an important role for construction purposes. When a construction work is completed with passage of long time it may collapse or damage by their ages or any hook or by crook. When building collapse or damage then many coarse & fine aggregate are rejected [2]. But by various ways, the aggregate may be recycled the important road material (C.A & F.A.) used in their construction can be recycled after use to produce materials to height quality possible in order to have a minimum effect on the supply of natural resources.

3.2 Importance of recycled coarse aggregate

Construction &demolition is two twin sisters. The building and urban areas where we live have had to change in harmony with the needs of the age in these circumstances it is natural to consider demolition work as being as important as construction work in the sound development of urban areas. In congested in particular the quality of the demolition technique becomes as essential element which determines the success of city. In addition to efficiency in demolition, strategies must be adopted to avoid noise, vibration and dust which affect the surrounding environment and there must be efficient disposal of the waste product. The effective reuse of these waste products can be of great importance socially as well as economically.

3.3 Beneficiary of recycling: The benefits of recycle aggregate are as follows;
- i. Save money for local governments and other purchasers.
- ii. Create additional business opportunities.
- iii.   Conserve diminishing aggregate resources.
- iv.   Save energy when recycling is done on site.
- v. Help local government meet their goal of reducing disposal by 50 percent.

3.4 Need utility of recycled coarse aggregate
- i. The distinct utility of the use of concrete with recycled coarse aggregate are as follows;
- ii. Reduced external transport of waste to relatively side i.e. Reduction of traffic density.
- iii. Reduce transportation cost of natural coarse aggregate at the demolished sites.
- iv. This lessens the environment pollution considerably.
- v. With lower replacement of N.C.A by R.C.A replacement no substantial decrease in compressive strength.
- vi. R.C.A can be used in pre-fabricated units such as concrete blocks, PVC fabricated roofing materials.

4. Specification of materials to be used for test specimen
The whole project was performed with Portland cement, sand, fine aggregate and coarse aggregate. The Specific gravity of cement is 3.15 and compressive strength of cement is 3500 psi [4]. Local sand was used. The finnes modulus and unit weight of sand was determined as 2.42 and 2.78 respectively. The fresh coarse aggregate was used and its finnes modulus is 5.57 and unit weight 80 pcf. The recycled coarse aggregate was used and its finnes modulus is 5.96 and unit weight 82pcf.

Figure 1: Particle Size Distribution Curve for Sand   Figure 2: Particle Size Distribution Curve for Fresh C.A

Figure 3: Particle Size Distribution Curve for Recycled C.A

4.1 Mix design

It will be worthwhile to recall that at this stage the relationship between aggregate and paste, which the two essential ingredient of concrete. Workability of the mass is provided by the lubricating effect of the paste and is influenced by the amount of dilution of paste [5]. The strength of concrete is limited by the strength of paste, since mineral aggregate with rate exception are for stronger than the paste compound. Essentially the permeability of concrete is governed by the quality and continuity of the paste, since little water flows through aggregate either under pressure or by capillary. Further the predominant contribution to drying, shrinkage of concrete is that of paste. Since the properties of concrete are governed to a considerable extent by the paste, it is helpful to consider more closely the structure of the paste. The fresh paste is a suspension, not a solution of cement in water. The more dilute the paste, the greater the spacing between cement particles and thus the weaker will be the ultimate paste structure. Since the quality of water required also depends upon almost of paste, it is important that as a little paste as possible should be used and hence the importance of grading.

4.1.1 Various methods of proportioning:

i. Arbitrary proportion, ii. Maximum density method, iii. Fineness modulus method, iv. Surface area method, v. A.C.I curve method and, vi. Grading curve method

4.1.1.1 Design of concrete mixes by ACI method

This method of proportioning was recommended by A.C.I. committee 212 [6], having gone into the details about the various methods of mix designing procedures. The A.C.I. committee mix methods assume certain basic facts, which have seen substantiated by field experiments on large work. They are;

a)   The method makes use of the established fats, that our a considerable range of practical proportions by fresh concrete of given slump are containing a reasonably well graded aggregate for given maximum size will have practically a constant total water content regardless of variations in water cement ratio and cement content which are necessarily interrelated.

b)   It makes use of relation that the optimum day rotted volume of coarse aggregate per unit volume of concrete depends on its maximum size and fineness modulus of the fine aggregate regardless of shape of pastilles.

c)   Irrespective of the compaction even after complete compactions done, a define percentage of air remain which is inversely proportional to the maximum size of the aggregate.

4.1.1.2 Required data

For mix design the data to be required are as follows;

i. Fineness modally of selected fine aggregate.

ii. Unit weight of dry coarse aggregate.
iii. Specific gravity of coarse and fine aggregate.
iv. Absorption characterizes of both coarse and fine aggregate.
v. Specific gravity of cement.

4.1.1.3 Design of concrete mixes for the project work by ACI method (FCA)
Specification:
Desired strength = 20.71N/mm^2. Max. Size of coarse aggregate =19.05 mm.
Slump desired =50.8 mm. Sp. Gravity of coarse aggregate = 1.89
Fineness modulus of fine aggregate =2.42 Sp. Gravity of fine aggregate = 2.78
Sp. Gravity of cement = 3.15   Bulk density of coarse aggregate = 79.8 pcf.
Solution:
Water requirement =300 lb per cubic yard of concrete
Water cement ratio = 0.55
So, Quantity of cement = 545.5 lb
Bulk volume of coarse aggregate = 0.665 per unit vol. of concrete
Hence the wt. of coarse aggregate per cubic yard of concrete = 0.665×79.8×27 = 1432.81 lb
The total absolute vol. of mix ingredient per cubic yard of concrete-
Cement = 545.5/(3.15×62.4) = 2.78 cft
Water = 300/62.4 = 4.81 cft
Coarse aggregate = 1432.81/(1.89×62.4) = 12.15 cft
Air entrapped = 27/100 = 0.27 cft
Total vol. = 2.78+4.81+12.15+0.27 = 20.01 cft
So the vol. of fine aggregate = 27-20.01 = 6.99 cft
Wt. of fine aggregate = 6.99×2.78×62.4 = 1212.57 lb
So, the wt. of material per cubic yard of concrete = 3490.88 lb
Hence the density of concrete = 3490.88/27 = 129.29 lb/cft
And the ratio of Cement: Sand: Khoa = 1:2.22:2:3

4.1.1.4 Design of concrete mixes for the project work by ACI method (RCA)
Desired strength = 20.71N/mm^2. Slump desired = 50.8 mm.
Max. Size of coarse aggregate = 19.05 mm. Sp. Gravity of coarse aggregate = 1.92
Fineness modulus of fine aggregate = 2.42. Sp. Gravity of fine aggregate = 2.78
Sp. Gravity of cement = 3.15. Bulk density of coarse aggregate = 81.6 pcf.
Solution:
Water requirement = 300 lb per cubic yard of concrete
Water cement ratio = 0.55
So, Quantity of cement = 545.5 lb
Bulk volume of coarse aggregate = 0.665 per unit vol. of concrete
Hence the wt. of coarse aggregate per cubic yard of concrete = 0.665×81.6×27 = 1465.13 lb
The total absolute vol. of mix ingredient per cubic yard of concrete-
Cement = 545.5/ (3.15×62.4) = 2.78 cft
Water = 300/62.4 = 4.81 cft
Coarse aggregate = 1432.81/(1.92×62.4) = 12.23 cft
Air entrapped = 27/100 = 0.27 cft
Total vol. = 2.78+4.81+12.23+0.27 = 20.09 cft
So the vol. of fine aggregate = 27-20.09 = 6.91 cft
Wt. of fine aggregate = 6.91×2.78×62.4 = 1198.69 lb
So, the wt. of material per cubic yard of concrete = 3509.32 lb
Hence the density of concrete = 3505.32/27 = 129.97 lb/cft
And the ratio of Cement: Sand: Khoa = 1:2.19:2:69

4.1.1.5 Preparation of specimens
i. At first sand and khoa were screened by the sieve according to their requirements.
ii. Concrete constructions (sand, cement, khoa) were measured to dry separately by weight according to required proportions.
iii. The khoa were soaked thoroughly 24 hours and then made them surface dry saturated before use.
iv. Sand and cement were mix to dry on a clean platform until the mix was uniform.

v. The coarse aggregate then added to mix of cement and sand admixture and the whole were mixed thoroughly.

vi. The moulds were oiled by lubricating oil, before placing concrete in the mould.

vii. The concrete was compacted by vibrator till   the water appeared on top and no khoa was then left uncover by mortar.

viii. The cast specimens were then left for 24 hour of moist curing.

4.1.1.6 Casting and curing of specimens

The specimens were stripped from moulds after 24 hours of casting as shown in Figure 4(a) for compressive strength test and Figure 4(b) for bond strength test. All the specimens were carefully cured by immersing in clean water on the water bath of the laboratory. Most concrete gains strength most rapidly during the first days and weeks. Structural design is generally based on the 28 days strength and 70% of which is reached at the end of first week after casting. The test specimens were cured 28 days.

(a)   (b)
Figure 4: Cylinder for (a) Compressive Strength& (b) Bond Strength.

5. Results and discussions

The compressive strength of which is obtained from this is given in the table 1 for F.C.A and for R.C.A. The result of bond strength which is recorded during test from the universal testing machine is listed in the table 2 for F.C.A and for the R.C.A. For fresh concrete cylinders, from test result the average compressive strength of those cylinders was obtained 0.0124 Mpa and bond strength is 4.34×10^{-3} Mpa. For recycled concrete cylinders, from the test result the average compressive strength and bond strength of that cylinder was obtained 0.0098 Mpa and 3.37×10^{-3} Mpa respectively, which was about 83.49 % and 77.58% of the average compressive and bond strength of the fresh concrete cylinders. If compressive strength of recycled concrete is compared well with the fresh concrete and the value of compressive strength for recycled concrete is very near the value of compressive strength for fresh concrete, then it can be said that the recycled concrete is performing well. Ten fresh concrete cylinders were casted with medium workability, for compressive and bond strength. From the test result the average compressive strength of the cylinders was obtained 0.0124 Mpa. Again ten recycled concrete cylinders were casted for compressive and bond strength. The compressive strength of the recycled concrete was 0.0098 Mpa, which is about 83.49 % of the compressive strength of the fresh concrete and the average bond strength is $3.37\times10^{-}$ Mpa which is 77.58% of the average bond of the fresh concrete. However, from the above discussion, it can be concluded that the recycled coarse aggregate can be suitably used as coarse aggregate for concrete.

Table 1: Compressive Strength of Concrete When Used Fresh Aggregate (FCA) and Recycled Aggregate (RCA)

Sam-ple No.	Curing Period (day)	Crushing Load (kN) For FCA	Compressive Strength (Mpa) For FCA	Ave. compressive Strength (N/mm²)	Crushing Load (kN) For RCA	Compressive Strength (Mpa) For RCA	Ave. compressive Strength (Mpa)
1	28	205	0.014		160	0.009	
2	28	230	0.013		195	0.011	
3	28	250	0.014	0.0124	200	0.011	0.0098
4	28	195	0.011		180	0.010	
5	28	180	0.010		150	0.008	

Table 2: Bond Strength of Concrete When Used Fresh Aggregate (FCA) and Recycled Aggregate (RCA)

Sample No.	Curing Period (day)	Crushing Load (kN) For FCA	Bond Strength (Mpa) For FCA	Ave. Bond Strength (N/mm^2)	Crushing Load (kN) For RCA	Bond Strength (Mpa) For RCA	Ave. Bond Strength (Mpa)
1	28	30	3.94×10^{-3}		22	2.89×10^{-3}	
2	28	36	4.74×10^{-3}		36	4.74×10^{-3}	
3	28	27	3.55×10^{-3}	4.34×10^{-3}	20	2.63×10^{-3}	3.37×10^{-3}
4	28	32	4.21×10^{-3}		27	3.55×10^{-3}	
5	28	40	5.26×10^{-3}		23	3.03×10^{-3}	

6. Conclusions

The following conclusion can be drawn from the investigation;

i. The compressive strength of concrete prepared by using fresh coarse aggregate is 0.0124 Mpa and that for recycled coarse aggregate is 3.37×10^{-3} Mpa.

ii. The compressive strength of concrete prepared by using recycled coarse aggregate is 83.49% of the average bond strength of concrete prepared by using fresh coarse aggregate.

iii. The recycled coarse aggregate can be successfully used in concrete as a replacement of fresh C.A in the construction work like bridge abutment, light grade concrete, ordinary concrete sub-base of foundation etc.

7. References

[1] Aziz, M.A.A Text book of Engineering Materials, Published by Kazi Mahfuzur Rahman, Revise edition, June, 1986.

[2] Graf, in 1973, Frondistan Yannas in 1977 and M. Musheron in 1984

[3] Project work of Md. Kamrul Hasan and M. Emdadul Hoque on "Performance Evaluation of the Recycled Coarse Aggregate in Concrete" August, 2003.

[4] Rangwala, Engineering Materials, Charotar Publishing House, Opposite Amul Dairy, Court Anand-3888001, India.

[5] Shetty, M.S Concrete Technology, S.Chand & company Ltd, Ram Nagar, New Delhi-110055.

[6] Sinha A.N." Demolition of waste & its reuse" 27th International Conference on "Our world in Concrete & Structure" vol.1.p. 541-544, 29-30 August 2002, Singapore.

Separation of Silica from Local Clay

Hosne Ara[1], Tasmia Zaman[2] and A.S.W. Kurny[1]

[1]Department of Materials and Metallurgical Engineering, Bangladesh University of Engineering & Technology (BUET), Dhaka-1000, Bangladesh.

[2]Department of Glass and Ceramic Engineering, Rajshahi University of Engineering & Technology (RUET), Rajshahi-6204, Bangladesh.

E-mail: zaman.tasmia@yahoo.com

Abstract

The work was done to separate silica from local clay by various separation methods such as washing and wet sieving. Two different types of local clay were used for this purpose. Washing method was done to separate the clay particles. During washing an electrolyte was added to keep the clay particles in suspension. After separation chemical analysis of the separated clay was done. It revealed the presence of 58% silica in clay. Separated silica was then characterized by scanning electron microscope (SEM). SEM showed the sharp edge and smooth surface of silica particles but silica and impurity particles could not be differentiated. In case of wet sieving, separated silica was characterized by Optical Microscopy (OM) and Polarized Light Microscopy (PLM). Optical and Polarized Light Microscopy helped to determine the mineralogy of silica. From OM mainly quartz particles were identified while Polarized Light Microscope helped to identify the other minerals like Muscovite, Biotite and Kyanite. From Optical Microscopy it was seen that oxides of iron formed a thin layer on the silica particles. So for purification of silica some sort of leaching will be necessary.

Keywords: Wet sieving,Polarized Light Microscopy,Mineralogy, Electrolyte, SEM.

1. Introduction

Silicon and oxygen are the earth's two most abundant elements and together they make silica, one of the earth's three most common rock forming minerals. The mass of the Earth's crust is 59 percent silica, the main constituent of more than 95 percent of the known rocks.

Silica occurs in three main crystalline forms. The principal occurrence is as the mineral quartz but it also occurs in other rarer mineral forms known as tridymite and cristobalite. It is a very durable mineral resistant to heat and chemical attack and it is these properties that have made it industrially interesting to man.

The first industrial uses of crystalline silica were probably related to metallurgical and glass making activities a few thousand years BC. It has continued to support human development throughout history, being a key raw material in the industrial revolution especially in the glass, foundry and ceramics industries. Silica contributes to today's information technology revolution being used in the plastics of computer mouse and providing the raw material for silicon chips.

For industrial use, pure deposits of silica sand capable of yielding products of at least 95 percent silica are required. Often much higher purity values are needed [1-2].

Washing is the most common separation process. Clay may contain quartz, feldspar, mica, colored minerals, sometimes soluble salts and occasionally organic matter. Washing process is so adjusted to separate clay and silica particles as far as possible. Washing process may, however, need some adjustment depending upon the individual characteristics of the clay under washing. The washing schedule has to be worked out taking into consideration the peculiarity of the clay to be washed and the impurities present [3].

Most sieve analyses are carried out dry. But there are some applications which can only be carried out by wet sieving. This is the case when the sample which has to be analyzed is e.g. a suspension which must not be dried; or when the sample is a very fine powder which tends to agglomerate (mostly < 45 µm) – in a dry sieving process this tendency would lead to a clogging of the sieve meshes and this would make a further sieving process impossible. A wet sieving process is set up like a dry process: the sieve stack is clamped onto the sieve shaker and the sample is placed on the top sieve. Above the top sieve a water-spray nozzle is placed which supports the sieving process additionally to the sieving motion. The rinsing is carried out until the liquid which is discharged through the receiver is clear [4].

2. Experimental procedure

Separation of silica by washing method

Around 4 grams of sample were mixed with 500 ml water. The mixture was stirred with the help of a stirring machine at a fixed speed (1000 rpm). After stirring, a settling time was given for the mixture. The settling time allowed the silica particles to settle down while the clay particles remained in the suspension. Then the silica and clay particles were separated. The silica particles were dried and after drying weight were measured. During the separation 0.3grams of an electrolyte [(0.1gram Na_2CO_3 + 0.2 gram $Na_2SiO_3.9H_2O$) +100 ml water] was added in the mixture. It aided the separation process.

Chemical analysis of clay

After separation chemical analysis of the separated clay was done. The determination of percentage of Silica (SiO_2), Ferrite (Fe_2O_3) and Alumina (Al_2O_3)of the separated clay was done according to the standard chemical analysis procedure.

SEM analysis

Finally, the separated silica particles were taken for SEM analysis. Silica samples were mounted on specimen stub and as silica is not electrically conductive, it was made electrically conductive by gold sputtering.
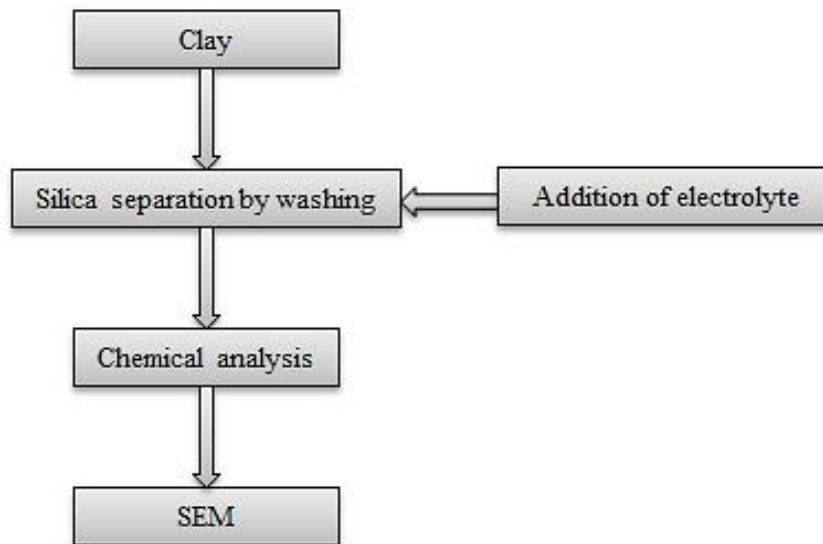
Fig. 1. Separation of silica from local clay by washing method

Separation of silica by wet sieving

At first sample was placed on a sieve having smallest opening, then distilled water was poured on it. Distilled water was used to avoid iron or some other impurities coming into the sample through water. The mixture was allowed to pass through sieve openings. Sand particles remained at the upper portion ofthe sieve. Washing continued until sand particle become free from clay. Obtained silica was then dried in the oven**.**

Microscopic analysis

After the separation of clay, silica samples were observed under optical and polarizing light microscope respectively**.**

Optical mineralogy

Finally Optical mineralogy was done on the basis of polarizing micrograph. Some mineral other than quartz was identified by this work.
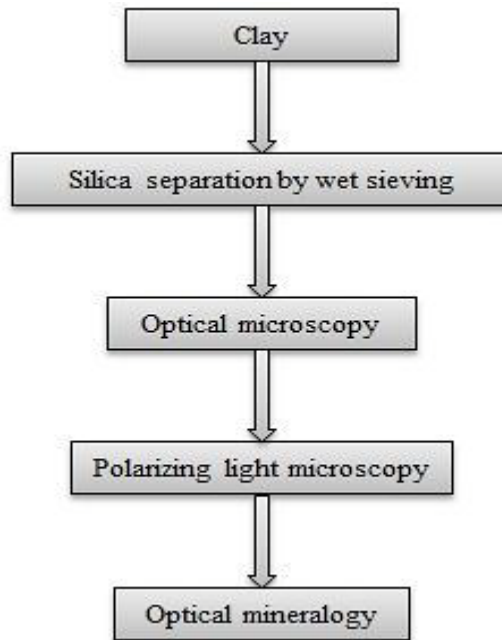
Fig. 2. Separation of silica from local clay by wet sieving method

3. Result and discussions

Effect of stirring and settling time
Table 1 and 2 shows the experimental data of obtained silica during washing method at different parameters. First, the stirring time was varied and the effect was observed.There was no significant change during this experiment (Fig. 3).

Table 1. Data of silica obtained with different stirring time

Sample (grams)	Water (ml)	Stirring time (seconds)	Stirring speed (rpm)	Silica obtained (grams)
4	500	10	1000	2.130
		15		2.195
		20		2.161
		25		2.093
		60		2.309
		600		2.066

Then, the settling time was varied to observe the change of silica content. The amount of silica was increased with increasing the settling time (Fig. 4).

Table 2. Data of silica obtained with different settling time

Sample (grams)	Water (ml)	Stirring time (seconds)	Stirring speed (rpm)	Settling time (seconds)	Silica obtained (grams)
4	500	300	1000	15	2.279
				30	2.251
				45	2.284
				60	2.235
				120	2.465
				180	2.484
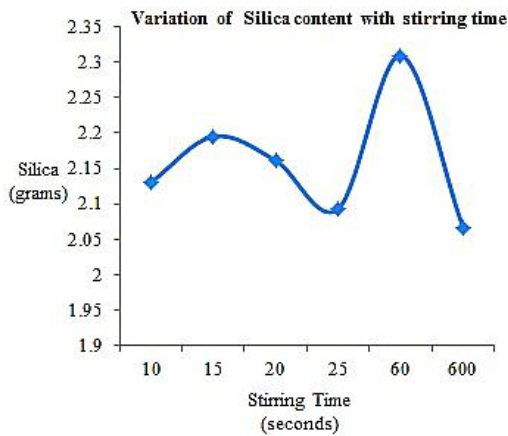
Fig. 3. Variation of silica obtained with stirring time   **Fig. 4.** Variation of silica obtained with settling time
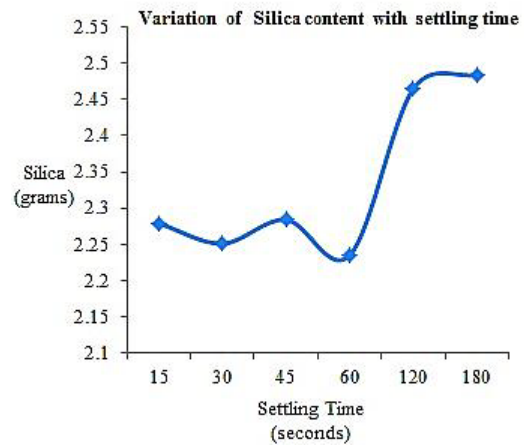
Effect of electrolyte addition

Table 3 shows the effect of electrolyte addition on separation process. The effect was significant. As the amount of electrolyte increased the amount of separated silica also increased. But settling time had higher effect than electrolyte in this work.

Table 3. Data of silica obtained during electrolyte addition

Electrolyte (ml)	Clay (grams)	Water (ml)	Stirring time (seconds)	Stirring speed (rpm)	Silica obtained (grams)
5					2.153
10					2.172
20					2.216
25	4	500	10	1000	2.218
100 (0.3 g)					2.462
100(0.6 g)					2.481

Chemical analysis

Chemical analysis of the separated clay was done to know the percentage of silica. Around 58 percent silica was present in the separated clay (Fig. 5). It was clear from the analysis that most of the silica particles retained with clay. Washing method could not separate all the silica particles.So wet sieving was carried out. It gave higher percentage of separated silica than washing method.
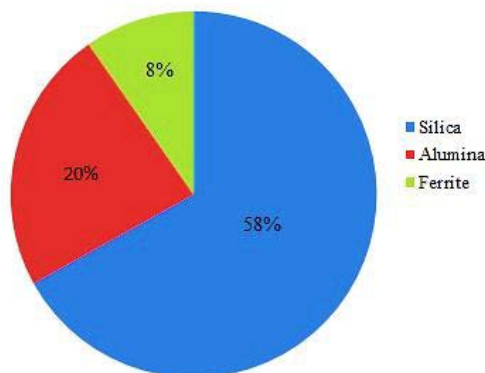
Fig. 5. Pie chart of chemical analysis report

SEM analysis

Fig. 6 shows the scanning electron micrographs of the separated silica particle has sharp edges and more or less smooth surface. By observing these micrographs silica particles could not be separated from impurity particles.
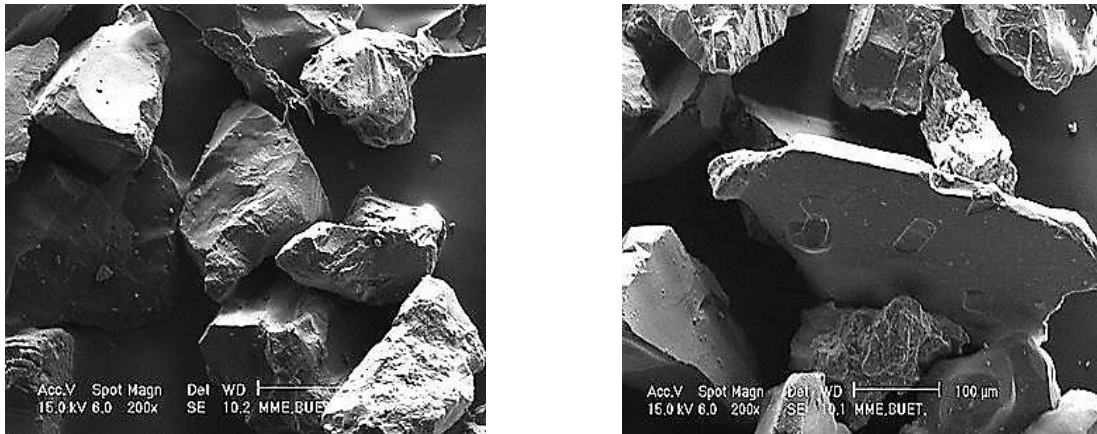
Fig. 6. SEM micrograph of silica obtained by washing method

Optical micrograph

Optical micrographscould differentiate the quartz particles from others. Fig. 7 shows the transparent particles of silica. The red colored particles were silica with thin layers of iron oxide. But OM could not identify the other impurities.

Fig. 7. OM micrograph of silica obtained by wet sieving

Polarized light microscopic analysis
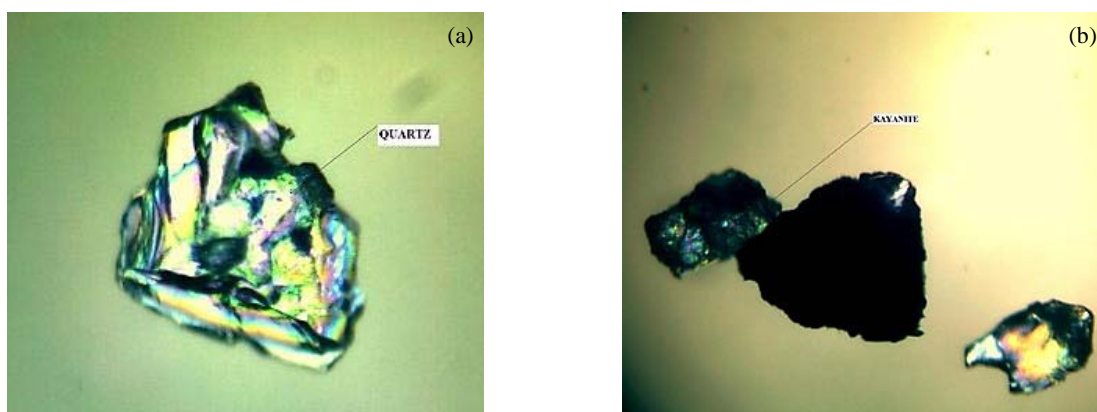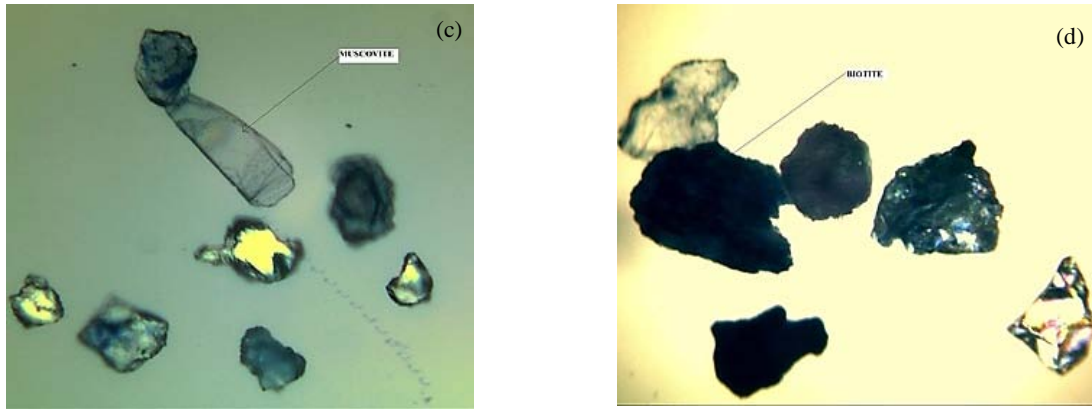
Fig. 8. Polarized light micrograph of (a) Quartz, (b) Kayanite, (c) Muscovite and (d) Biotite

Fig.8 shows the micrographs obtained from polarizing microscope where most of the minerals identified were quartz. Some muscovite, biotite and kayanite were also present. Minerals were identified by seeing their colors at cross polar and plane polar mode.

4. Conclusions

Washing method could not separate all silica particles. Most of the silica particles retained with clay. Moreover, large amount of impurities were present in the separated silica particles. On the other hand compared to washing method wet sieving method separated more silica particles. SEM didn't help to separate quartz minerals from others. It only showed the sharp edged particles with smooth surface. Optical and polarized light micrographs helped to identify the other minerals along with quartz. The micrographs showed the presence of thin layer of iron oxides on silica particles. So for purification of silica from iron oxide some sort of leaching will be necessary.

5. Acknowledgements

6. References

[1] M. Sundararajan,S. Ramaswamy and P. Raghavan, "Evaluation for the Beneficiability of White Silica Sands from the Overburden of Lignite Mine situated in Rajpardi district of Gujarat, India", *Journal of Minerals & Materials Characterization & Engineering,*Vol.8, No.9, pp. 701-713, 2009.

[2] W.E. Worrall, Clays and Ceramic Raw Materials, *Elsevier,* 2nd edition, pp. 14-24, 1986.

[3] A. Meunier, Clays, *Springer,* 1st edition, 2005.

[4] J.H.Harker, J.R.Backhurst and J.M. Coulson, J.F. Richardson, Chemical Engineering, *Elsevier Science,*5th edition 2002.

Effect of Clay and Moisture Content on the Properties of Molding Sand

Tasmia Zaman[1], M. A. A. Mahmood[1]and A. Hafiz Zaman[2]
[1]Department of Glass and Ceramic Engineering, Rajshahi University of Engineering & Technology (RUET), Rajshahi-6204, Bangladesh.
[2]Department of Mechanical Engineering, Rajshahi University of Engineering & Technology (RUET), Rajshahi-6204, Bangladesh.
E-mail: zaman.tasmia@yahoo.com

Abstract

The work was done to understand the effects of molding sand characteristics (percent clay and moisture content) on the properties of green sand molding mixture. Locally found sand was used for this experiment. Sieve analysis was done to calculate the American Foundry men's Society (AFS) grain fineness number and to know the particle size distribution. Percent clay content and percent moisture content of the as received sand was determined to make different types of sand mixtures. Initially two batches of sand were taken. The first one was using as received sand (B_1) and other one was using only two sieve fractions that retained the maximum amount of sand (B_2). Six different types of sand mixtures were prepared from each batch. For first three mixtures (B_{11}, B_{12} and B_{13}), moisture content was fixed (3.5%) but clay content varied to 8, 12 and 16% respectively. On the other hand, for the other three mixtures (B_{14}, B_{15} and B_{16}), clay content was fixed (8%) but moisture content was 2, 3.5 and 4% respectively. Same procedure was followed for making the second batch mixtures (B_{21}, B_{22}, B_{23}, B_{24}, B_{25} and B_{26}).Finally those samples were taken for permeability, hardness, green compressive strength testing. The experiment found that, mechanical properties like hardness and green compressive strength was higher for B_1 than B_2. Clay content had significant effect on permeability, hardness or GCS while moisture content had a little effect.

Keywords: Sieve analysis, AFS fineness number, Mesh, Hardness, Permeability.

1. Introduction

One of the best-known applications of clay is in the manufacture of such articles as pottery. Another major application of kaolinite is in the paper industry where it may be used either as filler or for coating paper. The metallurgical industry employs clay mixed with sand to form molds that are used for casting operation [2-3].

The major production of castings is in sand molds. Molding sands are mixtures of three basic ingredients. Green sand contains clay, water as well as the principal constituent, silica. These components provide the bulk and plasticity required of the molding sand. Other materials may be added to the sand mixture to enhance certain of the properties [1-2].

Molding sand may contain about 2 to 50% of clay. With suitable water content, it is the principal source of the strength and plasticity of the molding sand. Clay is thus the bond or binder of the molding sand which increases the strength of molding sand. But after the saturation point, further increase in clay content will not cause an increase of strength of the aggregate [3-5].

Water, present in amounts of about 1.5 to 8%, activates the clay in the sand, causing the aggregate to develop plasticity and strength. The water is adsorbed by the clay up to a limiting amount. Excess water can act as a lubricant, and makes the sand more plastic and more moldable though the strength may be lowered [1].

The size and distribution of sand grains is determined with the AFS sieve analysis test. A well distributed sand grain will have higher strength but lower permeability. For ferrous castings, the AFS number should be low so that the permeabilityof the molding sand will be high. On the other hand for non-ferrous castings, the number should be higher to lower the permeability [6-7].

2. Experimental procedure

Sieve analysis

Sieve analysis was done to make two different batches of sand. The test of determining the AFS grain fineness number was performed on a dried locally found sand sample (B_1). A set of standard testing sieve was used toscreen the sand. These sieves were stacked in sequence with the coarsest sieve at the top and placed in sieve shaker. About 200 grams of sand was placed at the top sieve and after 15 minutes of both horizontal and vertical vibration, the weight of the sand retained in each sieve was carefully weighted. The second batch of sand (B_2) was made using two sieve fractions that retained the maximum amount of sand.
AFS grain fineness number was calculated by the following equation:

$$\text{AFS grain fineness no.} = \frac{\text{Total product}}{\text{Total percentage of sand retained}} \quad (1)$$

Calculation of percent clay content

A portion of the sand samples of both batches were thoroughly dried at 220°C for about 4 hours. 50 grams of the dried sand was placed in a wash bottle and then 475 cc of distilled water and 25 cc of 3% caustic soda solution were added in it. The mixture was stirred for 5 minutes in a rapid sand washer. Sufficient water was added up to the level line marked on the bottle. The liquid was then siphoned off after 10 minutes. It was repeated twice. Then the sand was dried and its weight was taken. The difference between the initial and final weight gave the percent clay content.

Measurement of percent moisture content

50 grams of sand sample was placed in a pan. The timer for the blower of the moisture teller was set for approximately 5 minutes and air at 110°C was blown over and thorough the sand. The sand was weighted again. The difference between two weights gave the moisture content in it.

Permeability test

To determine the permeability of sand batches, samples of 2 inches diameter and 2 inches height was prepared by ramming the required quantity of sand in a tube with three blows of standard rammer. The specimen was placed in the mercury cup of the permeability meter. The air drum was raised to take 2000 cm^3 of air into the air drum. Then the whole air was allowed to escape through the specimen with a pressure of 10gm/ cm^3 and the time was recorded. The following equation gave the permeability number:

$$P = \frac{Vh}{Apt} \quad (2)$$

P= Permeability number
$\quad$ V= Volume of air=2000 cm^3
$\quad$ h=Height of specimen=5.08 cm
$\quad$ A=Cross sectional area of specimen=20.268 cm^2
$\quad$ p=Air pressure=10gm/ cm^3
$\quad$ t=Time in minutes

Hardness test

The hardness of the rammed samples was measured by using an indentation type mold hardness tester where a spring loaded 0.5 inch diameter steel ball was pressed into the samples. The hardness number was read directly from dial gage.

Green compressive strength test

Green compressive strength was measured by using Universal sand strength machine. This machine contains a pusher arm and a weight arm. The weight arm applies load on specimen. The specimens were loaded until break.

3. Result and discussions

Table 1 shows the data obtained during sieve analysis. From equation 1 AFS grain fineness number was calculated. It was found 65 which mean the average grain size of sand was 65 and it corresponds to the sieve number whose openings would just pass all the sand particles if all were of the same size. It can be also seen from the table that, Batch 2 (B_2) was 2-screen or mesh type. That means only two sieves had retained sand more than 10%. So, it was clear that, the distribution of particles of Batch 2 (B_2) was poor compared to Batch 1 (B_1) as B_2 contained only two sizes of particles. Distribution of particles played significant role in other properties like permeability, hardness, green compressive test etc.

Table 1. Experimental data of sieve analysis

US series equivalent sieve no.	Sand retarded (grams)	Percent retained (A)	Cumulative percentage	Multiplier (C)	Product (AxC)
6	0	0	0	3	0
12	0	0	0	5	0
40	11.86	5.93	5.93	30	177.9
70	131.92	65.96	71.81	50	3298
140	50.63	25.32	97.21	100	2531.5
200	4	2	99.21	140	280
270	0.57	0.29	99.49	200	57
Pan	0.62	0.31	99.80	300	93
Total		**99.80**			**6734.40**

The data can be used in two ways. First, a distribution curve showing the total percent retained on each sieve may be plotted as in Figure 1 or the cumulative percentage showing the total percent obtained which is coarser than any particular screen may be plotted. Second, the average grain fineness may be computed.
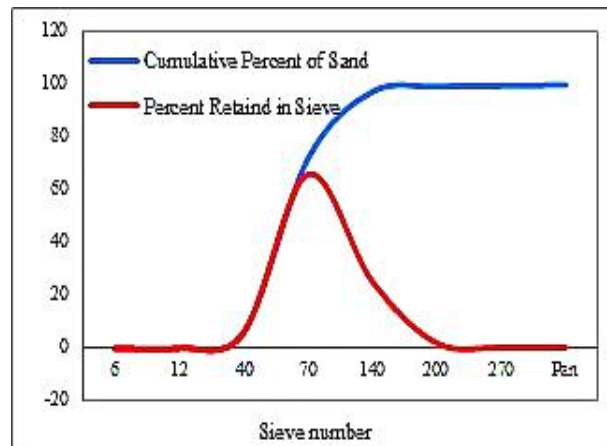
Fig. 1. Graphical representation of sieve analysis data

Effect on permeability

Figure2 and 3 shows the variation of permeability with clay and moisture content for both B_1 and B_2 batches.Permeability remained more or less unchanged when percent clay contentwas varied (Fig.2). On the other hand, when percent clay content was fixed (8%), permeability increased with increase in moisture content for both B_1 and B_2 batches (Fig. 3).
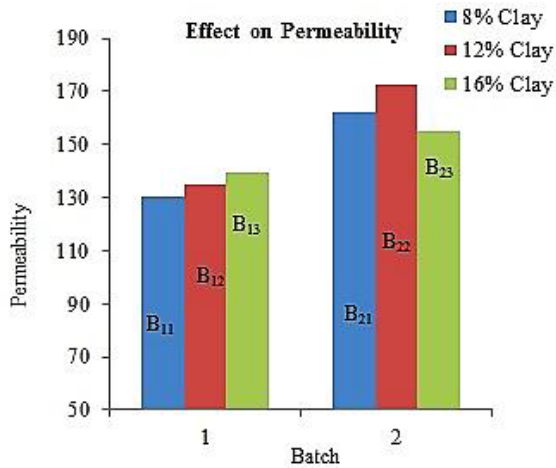
Fig. 2. Variation of permeability with %clay
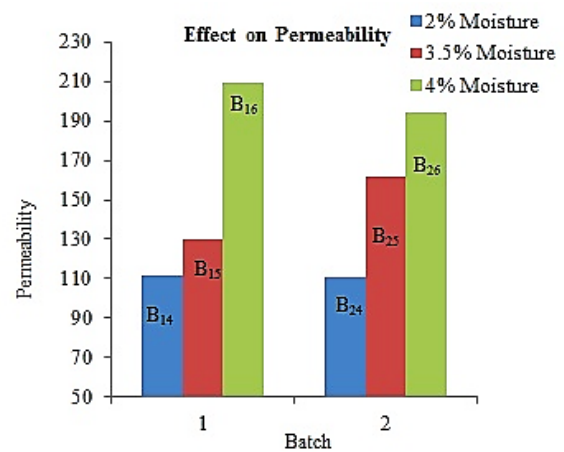
Fig. 3. Variation of permeability with % moisture

Effect on hardness

As the percent of clay content increased, the mold hardness increased for both batches (percent moisture content 3.5%). But B_1 showed higher hardness than B_2 (Fig. 4). Figure 5 shows the increase of mold hardness with moisture content. Again B_1 gave better result than B_2. Mold hardness was higher when percent clay content was varied.
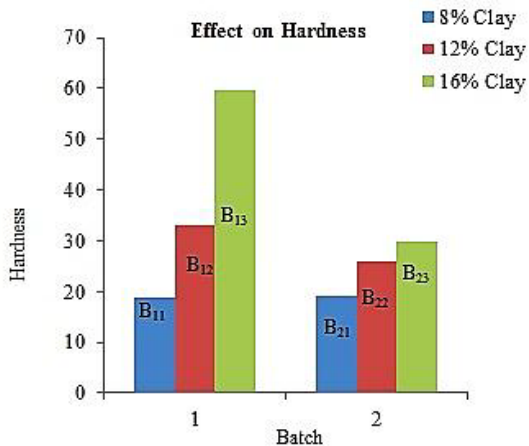
Fig. 4. Variation of hardness with %clay
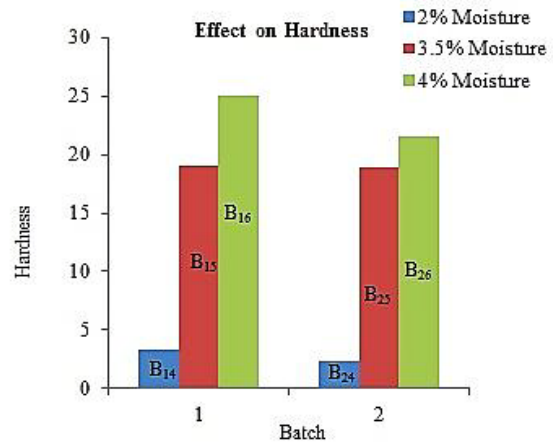
Fig. 5. Variation of hardness with %moisture

Effect on green compressive strength (GCS)

Figure6 and 7shows the variation of green compressive strength with percent clay and moisture content respectively. The clay and moisture content had significant effect on GCS. For fixed 3.5% moisture, B_1 showed higher GCS. While for B_2, GCS was lower and it decreased with increase in clay content (Fig. 6). Moisture content had a little effect on green compressive strength. So, changing the content of moisturegave almost same result for both B_1 and B_2 (Fig. 7).
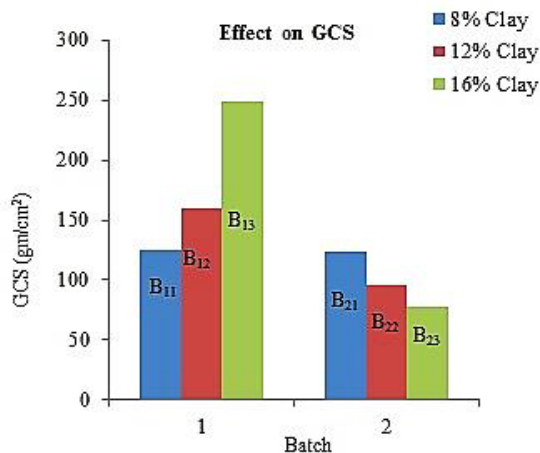
Fig. 6. Variation of GCS with % clay
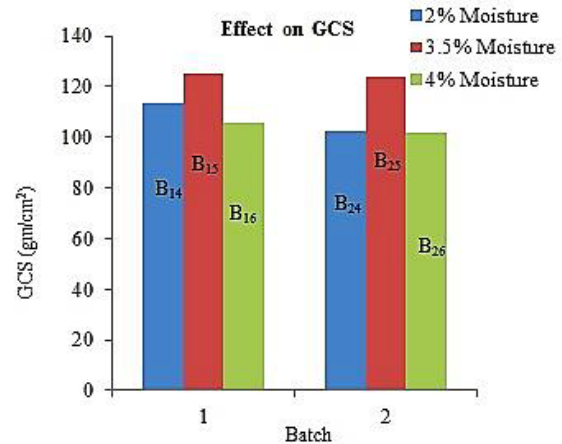
Fig. 7. Variation of GCS with % moisture

4. Conclusions

Clay particles are basically finer than sand particles. So, permeability should decrease by the addition of clay. But as B_2 had only two sizes of particles its distribution was poor and permeability was higher than B_1. So particle size and distribution was the major factor for the variation of permeability. Addition of clay particles had a little effect on permeability.

Clay acts as binder. Normally with increasing clay content mold hardness increases. This is because with increasing clay content bonding also increases. This was true for B_1 but again due to the poor distribution of particles B_2 didn't give any significant result. On the other hand, moisture played a vital role in increasing mold hardness.

In case of green compressive strength, 16% clay content gave around 250 gm/cm^2 GCS of molding sand for batch 1 sample. While when moisture content was varied the GCS value varied from 100-120 gm/cm^2. Variation of moisture had almost the same effect for Batch 1 and 2. Again poor distribution of particles caused lower green compressive strength for batch 2 samples when clay content was varied.

5. Acknowledgement

6. References

[1] R.W. Heine, C.R. Lopor (Jr.) and P.C. Rosenthal, Principles of Metal Casting, *McGraw-Hill,* 2nd edition, pp. 84-119, 1955.

[2] M.S. Abolarin, O.A. Olugboji and I.C. Ugwuoke, "Experimental investigation on local refractory materials for furnace construction", *Proc. 5th Ann. Eng. Conf.Federal University of Technology,Minna, Nigeria,* pp. 82-85, 2004.

[3] F.O. Akinbode, "An investigation on the properties of termite hill as refractory material for furnace lining", *Indian Foundry Journal,* Vol. 42, No. 9, pp. 3-10, 1996.

[4] W.E. Worrall, Clays and Ceramic Raw Materials, *Elsevier Applied Science*, 2nd edition, pp. 1-4, 1986.

[5] W.D. Kingery, H.K. Bowmen, and D.R. Uhlman, Introduction to Ceramics, *John Wiley & Sons,*2nd edition, pp. 16-17, 1975.

[6] A. Mousharraf, M.S. Hossain and M.F. Islam, "Potential of Locally Available Clay as Raw Material", *Journal of Chemical Engineering, IEB,* Vol. ChE. 26, No. 1, pp. 34-79, 2011.

[7] J.F. Shackelford, R.H. Doremus, Ceramic and Glass Materials Structure, Properties and Processing, *Springer,* 1st edition, pp. 111-132, 2008.

Effect of Cu in Al-Si Alloys with Phase Modelling

E. A. Ashrafi, A. Hasan and H. M. M. A. Rashed
Department of Materials and Metallurgical Engineering,
Bangladesh University of Engineering and Technology, Dhaka-1000, Bangladesh
E-mail: ashrafi.mme@gmail.com, hrashed@mme.buet.ac.bd

Abstract

A comparison study on copper content and effect of homogenisation treatment was performed between two Al-Si alloys containing varying amount of copper. Observation of microstructure revealed the formation of several intermetallic phases due to the presence of copper. Image analysis on the acquired images confirmed the relative changes in percent phase fractions due to larger amount of copper since the total amount of intermetallic phases was increased. Also, higher copper content showed a positive response on measured hardness values. Homogenisation at 300^oC caused increased hardness up to 2 hour for age-hardening, which was decreased significantly after 4 hour of heating due to over-ageing. Solidification calculations by thermodynamic modelling approach showed that Al_2Cu and Al_3Ni_2 phases were predicted to be most stable at the homogenisation temperature and these two phases were responsible for the increased in hardness due to copper addition.

***Keywords:** CALPHAD, Phase Modelling, Aluminium Alloys.*

1. Introduction

Aluminium is the most abundant metal in the earth's crust. It makes up about 8% by weight of the earth's solid surface [1]. Aluminium alloys with a wide range of properties are used in engineering structures. These properties can be largely modified by changing the alloy composition. Silicon, copper, zinc and magnesium are the most commonly used alloying elements in aluminium, which have sufficient solid solubility.

The effect of copper addition on the structural features and mechanical properties of Al-Si-Cu alloy have shown that copper addition increase the strength of these alloys [2-6]. Yield stress, hardness and micro-hardness increase with increase in copper content regardless of alloy composition [7]. Copper also improves machinabilitiy; however, castability, ductility and corrosion resistance are all decreased. The higher silicon alloys (e.g. Al–10Si–2Cu) are used for pressure die castings, whereas alloys with lower silicon and higher copper (e.g. Al–3Si–4Cu) are used for sand and permanent mould castings. In general, the Al–Si–Cu alloys are used for many of the applications of Al-Si alloys but where higher strength is needed. One example is the use of alloy 319 (Al–6Si–3.5Cu) for die cast (permanent mould) automotive engine blocks and cylinder heads in place of cast iron [8].

The as-cast microstructure of cast aluminium alloys normally displays significant segregation and super-saturation [8]. For this, homogenisation of aluminium alloys is often done to improve workability and mechanical properties by dissolving the non-equilibrium, brittle and inter-dendritic constituents, and by providing a more homogeneous structure.

Thermodynamic models have been developed for the calculation of various thermo-physical and physical properties with the aim of providing thermo-physical and physical properties for various types of multi-component alloys during solidification. Thermodynamic phase modelling approach is based on CALPHAD (CALculation of PHAse Diagrams) method [9], which is used for calculation of a wide range of materials properties for alloys and is particularly aimed at multi-component alloys. Using phase analysis modelling approach and microstructure analysis, it is possible to identify the phases present in the microstructure of an alloy, which has direct influences on the mechanical properties.

In this work, the effects of copper content and homogenisation treatment on microstructure and hardness values were studied using modelling, microstructural study and image analysis method.

2. Experimental

A master alloy was prepared by melting locally available aluminium pistons used for automobiles. Afterwards, copper wire was added at some predefined weight fractions into the master alloy to alter alloy composition. The raw materials were melt into a gas fired crucible pit furnace and were cast in a sand mould in the shape of a long rectangular bar. For changing the alloy composition, second casting was done in a permanent metal mould of circular cross-section (Length 170 mm, Diameter 17 mm). For both alloys, the melt was heated up to 850°C and poured at 800°C. Compositions of both alloys were measured by Optical Emission Spectrometer (Shimadzu PDA 700) and verified by wet chemical analysis methods. The average compositions found from OES analysis are shown in Table 1.

Table 1. Compositions of alloys used in experiment (in wt%)

Alloy	Al	Si	Cu	Mg	Fe	Ni	Mn
Master	86.09	7.99	**3.5**	0.76	0.70	0.51	0.34
Second	81.69	7.80	**8.46**	0.58	0.60	0.48	0.29

Homogenisation of the second alloy was done in a BlueM Electric furnace at 300°C for 1, 2 and 4 hours. After homogenisation, the samples were quenched in water to retain the microstructure.

The hardness of the alloys at several steps was measured by Universal Testing Machine (Brinell hardness) and Rockwell Hardness Tester (in F scale). Then these values were converted into Rockwell B scale.

Microstructures of all samples were studied in unetched condition. All images were taken in Optica B-600 MET trinocular upright metallurgical microscope, using OpticaTM Vision Pro software. Images were taken at 500X magnification under the same RGB values and pixel resolutions for comparing. Image of graticule scale (1 div = 0.01 mm) was also taken at the same magnification to quantify the dimensions of microstructure.

Image analysis was accomplished using ImageJ version 1.43u to find out the percentages of different phases. At least 10 images of microstructures for each alloy were taken and analysed to find out the average values of the amounts of phase areas/fractions. Modelling of the alloys was done using thermodynamic modelling approach to predict the relationships among composition, temperature, phases and properties.

3. Results and Discussion

Microstructure observation

Fig. 1 shows the microstructure of as-cast master alloy and second alloy. In both images, presence of silicon and several intermetallic compounds in aluminium matrix are identified. Some of these phases were present as particles in the microstructure. Phases were identified based on previous works for these alloys [10-12].

The microstructure of the second alloy is somewhat different from the master alloy due to presence of more copper (Fig. 1(b)). Inter-particle spacing of the phases were small in this higher intermetallics containing alloy.
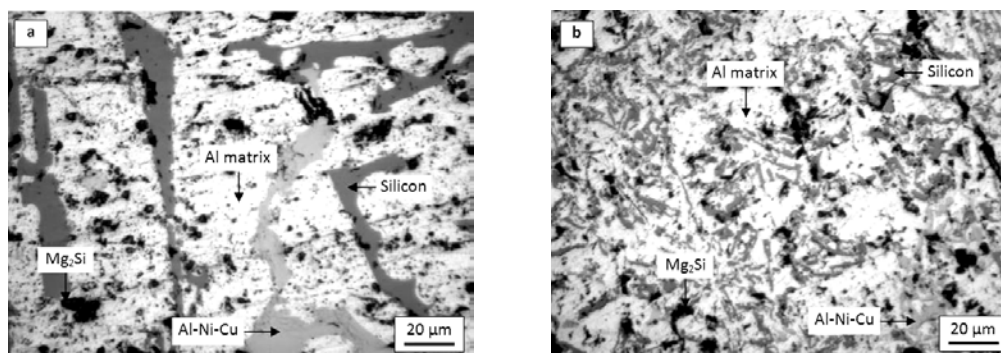
Fig 1. Microstructure of as-cast a) master alloy & b) second alloy

Fig. 2 shows the microstructure of the second alloy after homogenisation at 300°C. After homogenisation of 1 hour, the fine particles of silicon and intermetallics are distributed around the dendritic pure aluminium matrix. With increased homogenisation time, the dendrites start to disappear and the particles grow in size due to higher

atomic movement for longer time due to diffusion. After 4 hours of treatment, dendrites are removed completely, whereas the particles have grown all throughout the matrix.
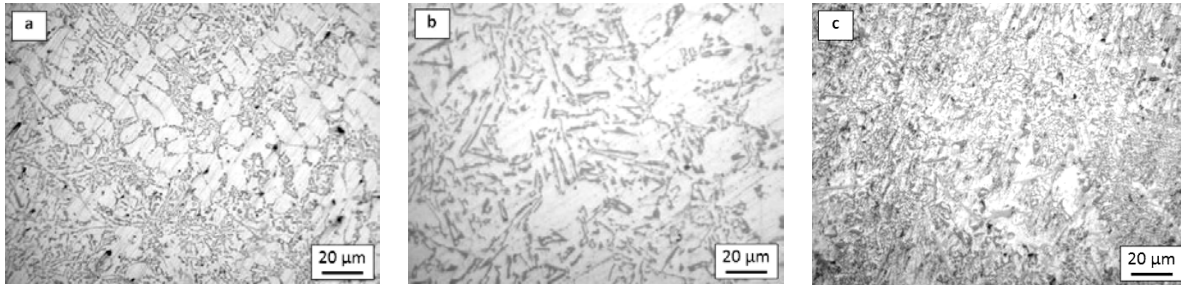
Fig 2. Microstructure of second alloy after heating at 300°C for a) 1 hour, b) 2 hour & c) 4 hour

Image analysis

Image analysis results are shown in Fig. 3. From the achieved data, it can be seen that the amount of intermetallic compounds have increased significantly in the second alloy attributed to copper addition. The fraction of silicon did not increase in an appreciable amount since silicon does not form any primary phase with copper.
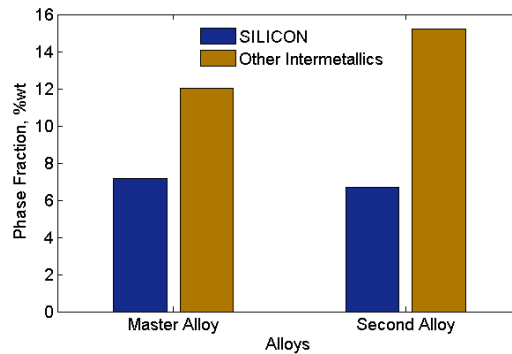
Fig. 3. ImageJ analysis result

Thermodynamic modeling

From the Step Temperature calculation predicted in thermodynamic modelling, the evolution and abolition of different phases in the master alloy are clearly observed in Fig. 4. It is evident that an Al-Ni phase (Al$_3$Ni$_2$) evolves at about 520°C, grows up to 2 wt% and then totally abolishes at 400°C. While this phase decreases in amount, another Al-Cu-Ni phase (Al$_7$Cu$_4$Ni) evolves at 490°C and grows up to 4.40 wt% and then remains stable with lowering temperature. Therefore, those aluminium and nickel content in Al-Ni phase are transferred to the new Al-Cu-Ni phase.

Also, the alpha solid solution increases to 3.80 wt% after nucleating at 620°C, and reduces to 2.50 wt% with lowering temperature. At the same period, an Al-Cu-Mg-Si phase (Al$_5$Cu$_2$Mg$_8$Si$_6$) continues to grow from 1.50 to 2.50 wt%.
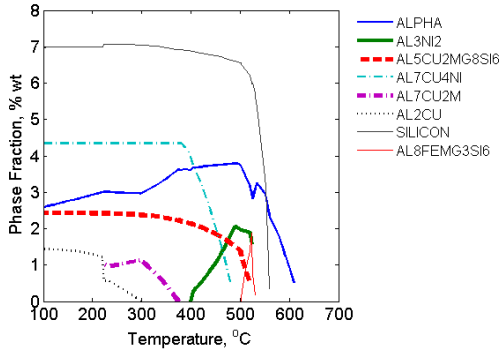
Fig. 4. Changes in intermetallic phases in master alloy
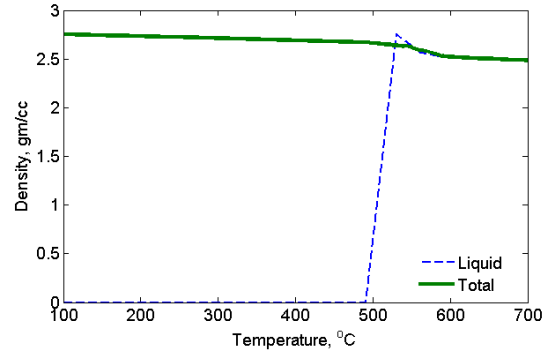
Fig. 5. Condition of mushy zone in master alloy

Using thermodynamics approach, solidification simulation in Scheil-Gulliver condition is also possible. Such modelling results are shown in Fig. 5 for density of the liquid and total system. The solidification of the master alloy starts at 620°C and becomes completely solid at 490°C.Aluminium alloys typically show considerable shrinkage and dendrite formation. The density of the liquid phase increases up to about 2.75 g/cm^3 due its enrichment with Cu and other elements.

From modelling of the second alloy, the formation of same phases as in the first alloy in step temperature calculation predicted is shown in Fig. 6. However, the amount of Al-Cu phases increased considerably due to increased copper content, compared to the master alloy. The transformation of Al-Ni phase to Al-Cu-Ni phase is seen for a very brief period here (between 520-515°C). In addition, the Al-Fe-Mg-Si phase does not form as occurred in master alloy.
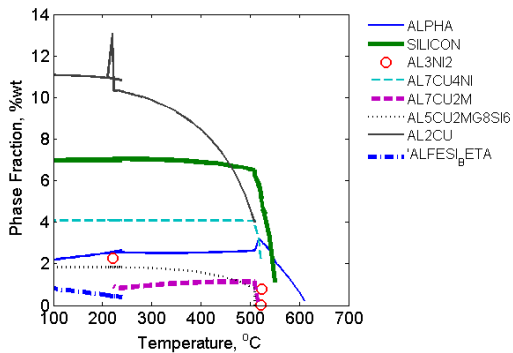
Fig. 6. Changes in intermetallic phases in second alloy
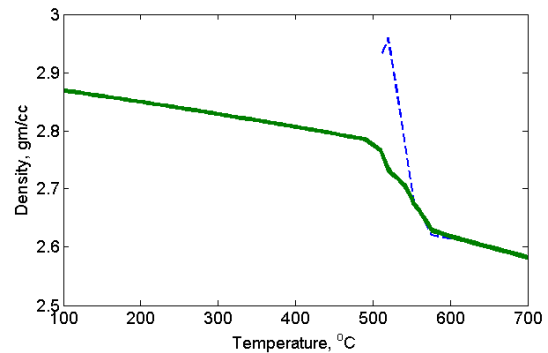
Fig. 7. Condition of mushy zone in second alloy

From solidification Scheil-Gulliver modelling, it can be seen that the alloy starts to solidify at 615°C and solidifies completely at 490°C. The density change observation in Fig. 7 shows that the liquid density increased like before with lowering temperature, but to a greater value of 2.95 g/cm^3, compared to 2.75 g/cm^3 for master alloy. The total density is also increased, which is an influence of copper content. From modelling, it was ascertained that copper content in liquid increases to 24 wt% in second alloy, compared to only 14 wt% for master alloy. This explains that the liquid enrichment is mostly caused by copper content.

Effects of phases in hardness

The hardness of the master alloy was found to be only 27.62 HRB, which increased significantly to 45.2 HRB by an increase in Cu content from 3.5 to 8.46 wt% as shown in Fig. 8.
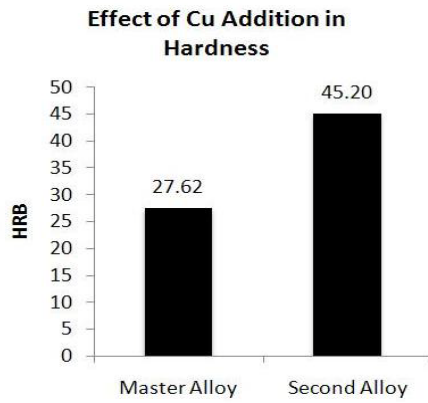
Fig. 8. Effect of cu addition in hardness
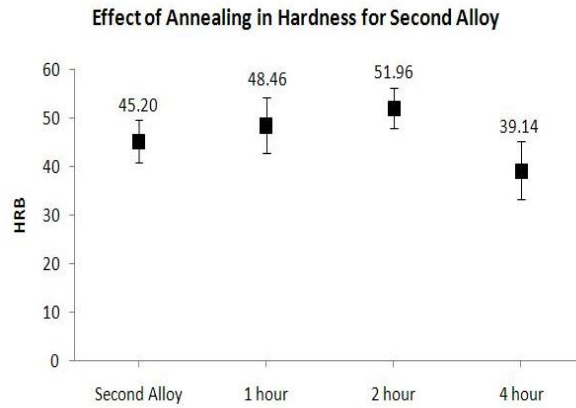
Fig. 9. Effect of homogenisation in hardness

Homogenisation of the second alloy developed gradual increase in hardness after heating at 300°C for 1 and 2 hours due to precipitation-hardening of the alloy. Nonetheless, it decreased considerably after heating for 4 hours as can be seen in Fig. 9. This is attributed to over-ageing.

The change in hardness by homogenisation is related to the precipitation of particular phases, which is confirmed by thermodynamic modelling. From single temperature calculation at homogenisation temperature (300°C) and room temperature (25°C), as shown in Fig. 10, it is evident that Al_3Ni_2 phase is stable at 300°C. Moreover, amount of Al_2Cu phase increased at 300°C. Since this microstructure is retained by quenching followed by homogenisation treatment, these two phases are apparently responsible for such increment of hardness of the second alloy.
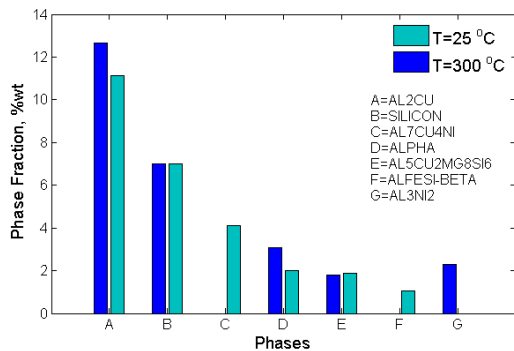
Fig. 10. Phases of second alloy at 300°C
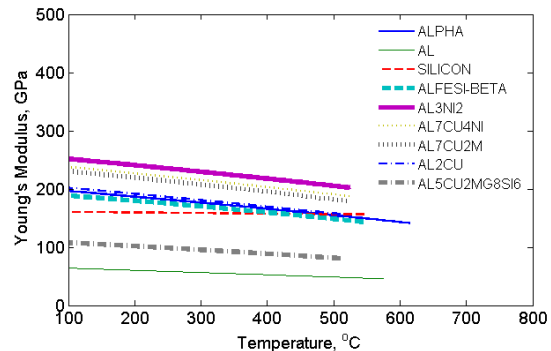
Fig. 11. Young's modulus of phases

Furthermore, up to 1 and 2 hours of homogenisation, Al_3Ni_2 and Al_2Cu phase continues to precipitate out of the matrix and results in precipitation-hardening phenomenon due to their fine size and coherency in the matrix, which provides resistance to dislocation motion. However, longer exposure to heat allows more diffusion to occur and particle coarsening of the phases reduces the Zener pinning effect of the particles and release of the dislocations which is considered as the reason for reduction of hardness of the second alloy.

This is further confirmed from property modelling of the phases of the second alloy (Fig. 11). The Al_3Ni_2 phase is predicted to provide maximum young's modulus amongst the phases. Therefore, presence of this phase is considered to be beneficial for strengthening apart from Al_2Cu phase alone.

4. Conclusion

a. The presence of copper lowers the solidification temperature significantly. Addition of copper increases the range of mushy zone, enriches the liquid and causes segregation and dendrite formation. Increasing copper causes higher hardness values. The microstructural study revealed the formation of several intermetallic phases. Modelling of these alloys confirmed the increased amount of intermetallic phases due to copper addition.

b. Homogenisation of the second alloy caused the removal of dendrites, and gradual increase in size of the particles and their growth throughout the matrix. The hardness values increased by precipitation-hardening process up to 2 hour homogenisation at $300^{o}C$ and lowered considerably after 4 hour homogenisation. With increase of homogenisation time, diffusion accelerates phase coarsening, which affects dislocation distribution adversely and results in lower hardness values observed.

c. Thermodynamic modelling shows that increase in copper content promotes formation of Al_2Cu and Al_3Ni_2 phases at $300^{o}C$ which apparently contributes to observed higher hardness which was confirmed by the higher Young's modulus of Al_3Ni_2 phase.

5. Acknowledgement

6. References

[1] L.A. Dobrzanski, R. Maniara and J.H. Sokolowski, "The Effect of Cooling Rate on Microstructure and Mechanical Properties of AC AlSi9Cu Alloy", *Archives of Materials Science and Engineering*, Vol. 28, No. 2, pp. 105-112, 2007.

[2] G. Mrowkwa-Nowotnik, J. Sieniawski and M. Wierzbinska, "Analysis of Intermetallics Particles in AlSiMgMn Aluminium Alloy", *Journal of Achievement in Materials and Manufacturing Engineering*, Vol. 20, pp. 155-158, 2007.

[3] L. Backerud, E. Krol and J. Tamminen, "Solidification Characteristics of Aluminium Alloy 1", *Proc. of the American Foundries Society,* Des Plaines, Illinos, American Foundries Society, Inc., 1986.

[4] L. Backerud, G. Chai and J. Tamminen, "Solidification Characteristics of Aluminium Alloy 2", *Proc. of the American Foundries Society.,* Des Plaines, Illinos, American Foundries Society, Inc., 1992.

[5] L. Backerud, G. Chai and J. Tamminen, "Solidification Characteristics of Aluminium Alloy 3", *Proc. of the American Foundries Society,* Des Plaines, Illinos, American Foundries Society, Inc., 1992.

[6] L.A. Dobrzanski, R. Maniara, M. Krupinski and J.H. Sokolowski, "Microstructure and Mechanical Properties of AlSi9Cu Alloys", *Journal of Achievement in Materials and Manufacturing Engineering*, Vol. 24, pp. 51-54, 2007.

[7] J.G. Kauffman and E. L. Rooy, "Aluminum Alloy Castings", ASM Metals Handbooks, Ohio ASM International, 2005.

[8] A.K. Dahle, "Heat Treatment of Aluminum Alloys", Encyclopedia of Materials: Science and Technology, pp. 111-113, 2010.

[9] N Saunders, Z Guo, X Li, A P Miodownik and J Ph Schille, "Using JMatPro to Model Materials Properties and Behavior." JOM, Vol. 55 No. 12, pp. 60-65, 2003.

[10] Metals Handbook, ASM International: Metals Park, Ohio, 1990.

[11] N. Roy, A.M. Samuel and F.H. Samuel, "Porosity Formation in Al-9wt%Si-3wt%Cu Alloy Systems: Metallographic Observations" Metall. Mater. Trans. A., Vol. 27A, pp.415-29, 1996.

[12] R.H. Stevens, "Aluminum Alloys: Metallographic Techniques and Microstructures, in Metallography and Microstructures", ASM International, 1992.

Improved Dielectric Properties of La/Mn Codoped Bismuth Titanate Ceramic

M. S. Parvez[1], M. Bodiul Islam[2,*]

[1]Department of Materials Science and Engineering (MSE), University of Rajshahi, Rajshahi-6205, Bangladesh
[2]Department of Glass and Ceramic Engineering (GCE), Rajshahi University of Engineering & Technology (RUET), Rajshahi-6204, Bangladesh
Corresponding author, E-mail: mbislam_mst@yahoo.com

Abstract

Undoped bismuth titanate, $Bi_4Ti_3O_{12}$ (BIT), La doped bismuth titanate, $Bi_{3.25}La_{0.75}Ti_3O_{12}$ (BLT) and La/Mn codoped bismuth titanate $Bi_{3.25}La_{0.75}Ti_{3-x}Mn_xO_{12}$ (BLTM) (x = 0.005, 0.01, 0.02) ceramic samples were prepared by solid state reactions. The influence of La/Mn cosubstitution in the crystal structure of BIT was investigated by XRD and IR spectroscopic studies. The XRD results show that all samples are polycrystalline and almost single phase with a bismuth-layered structure belonging to the crystalline phase of BIT. In IR spectra, three absorption peaks appeared at 814, 592 and 379 cm^{-1}, which were for the formation of titanate structure. In addition, two shoulders appeared at 313 and 470 cm^{-1} in support of the monoclinic symmetry of pure BIT. A new and relatively broad absorption peak appeared around 1015 cm^{-1} due to Mn doping in BLT corresponding to the stretching vibration of Mn-O bond. Dielectric measurements showed that the dielectric constant of the prepared samples decreased with increasing frequency and remained almost constant after 10 KHz. It was found that dielectric constant was increased and dielectric loss was reduced on La-doping. The effect of Mn codoping on the dielectric properties of BLTM was studied and it found that the optimum codoping concentration of Mn was 0.01 mol%.

Keywords: Codoping, Solid-state reaction, Dielectric constant, Dielectric loss, XRD, IR.

1. Introduction

Dielectric ceramic materials are useful in optical applications and device components such as filters, transmitters, reflectors, lenses and optical waveguides. They are also utilized widely in electronic devices such as capacitors, actuators, etc. These materials are usually characterized by their refractive indices, dielectric constants and dielectric losses. Dielectric materials with high values of refractive indices and dielectric constants but low dielectric losses can markedly reduce the size of devices, which is highly desirable in integrated circuits, optical systems, electronic systems, and electro-optical systems [1].

Bismuth titanate ($Bi_4Ti_3O_{12}$, BIT) is a well-known member of the Aurivillius family of bismuth-based ferroelectric compounds with a layered structure $(Bi_2O_2)^{2+}(Bi_2Ti_3O_{10})^{2-}$ [2]. BIT has attracted more and more attention recently because it is considered to be a potential candidate for lead-free dielectric and ferroelectric ceramics [3]. BIT ceramics have been used in multilayer ceramic capacitors, ultrasonic generators, actuators, ferroelectric random access memory, and so on as it has strong anisotropic character, low dielectric dissipation factor, high dielectric breakdown strength, low aging rate and electro-optic switching behavior, high temperature coefficient of resonant frequency [4-6]. Although BIT is considered to be a potential candidate for lead-free chemical composition, high $2P_r$, and other good electrical properties, it suffers from a strong fatigue failure after 10^{12} cycles and high processing temperature [7]. Recently, it has been reported that A-site modification in BIT by Lanthanides (La, Pr, Sm and Nd) improves fatigue behavior significantly [8]. Among them, the La doped BIT, namely $Bi_{3.25}La_{0.75}Ti_3O_{12}$, ceramic is fatigue free under repeating switching cycle but in this case the $2P_r$ is decreased largely from 50 $\mu C/cm^2$ to 30 $\mu C/cm^2$ while the coercive field ($2E_c$, 100 KV cm^{-1}) is reasonable [7]. In this investigation, Mn ion is chosen for the B-site modification of La doped BIT because Mn ion shows a peculiar behavior for its variable valencies. In the present work, pure BIT, La doped BIT and La/Mn codoped BIT ceramics have been prepared by the conventional solid-state reaction method. The phase assemblages and dielectric properties of the ceramic samples have been investigated and compared with those of BIT.

2. Sample Preparation and Experimental Setup

Pure BIT, La-doped BIT and La/Mn codoped BIT samples have been prepared by solid-state reaction. A reagent grade Bi_2O_3 (Merck, Germany), La_2O_3 (Wako Pure Chemical Industries Ltd., Japan), TiO_2 (Merck, India) and MnO_2 (Wako Pure Chemical Industries Ltd., Japan) powders have been used as the starting materials. Sample preparation has been completed by the following steps:

```
┌─────────────────────────────────┐         ┌─────────────────────────────┐
│  Grinding and Mixing in Ethanol  │ ──────► │  Settling down and Drying   │
└─────────────────────────────────┘         └─────────────────────────────┘
                                                           │
                                                           ▼
┌──────────────────────────────────────────┐   ┌─────────────────────────┐
│ Pellet formation (60 KN) and Sintering    │ ◄─│   Calcining (800 °C)    │
│ (1050 °C)                                  │   └─────────────────────────┘
└──────────────────────────────────────────┘
```
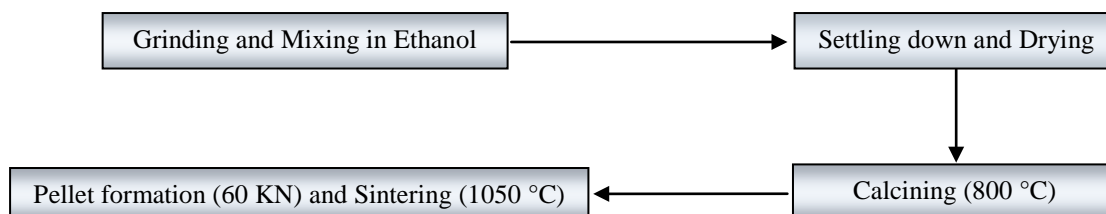
Fig. 1. Different steps of sample preparation

Stoichiometric amounts of starting materials were weighed out, mixed and milled in ethanol for 24 h in a ball mill. After ball milling, the mixture was kept in a beaker for 24 h to settle down the mixed powder. The ethanol was decanted out and the slurry was put into an oven for drying. The dried powder was again grounded in a mortar and calcined at 800 °C for 4 h. The rate of temperature raising and cooling was maintained at 10 °C/min. The calcined powders were mixed with 2.5% PVA solution in a mortar and then pressed at 60 KN to form pellet. The prepared pellets were then sintered at 1050 °C for 1 h. After sintering the color of $Bi_4Ti_3O_{12}$, $Bi_{3.25}La_{0.75}Ti_3O_{12}$, $Bi_{3.25}La_{0.75}Ti_{2.995}Mn_{0.005}O_{12}$, $Bi_{3.25}La_{0.75}Ti_{2.99}Mn_{0.01}O_{12}$ and $Bi_{3.25}La_{0.75}Ti_{2.98}Mn_{0.02}O_{12}$ samples were white shadow, white shadow, brown shadow, light brown and brown respectively.

A natural convection oven (JSR, JSON-100), a Carbolite furnace (ELF 11/6B) and a Shimadzu hand pressure gauge machine were used for drying, calcining and sintering, and making pellet. The XRDs were taken by an X-ray diffractometer (X'Pert-PRO, Philips, Japan). For measurements of frequency dependent capacitance, impedance and dielectric constant, a Precision Impedance Analyzer (model 4294A, range 40 Hz to 110 MHz, Agilent Technologies, Japan) was used. The frequency dependent capacitance was taken in the frequency range (1 KHz to 1 MHz) for all samples. A FTIR spectrophotometer (Spectrum 100, Perkin Elmer, resolution =1 cm^{-1}) was used to take spectra within 2000 – 300 cm^{-1}.

3. Results and Discussion

The experimental results on characterization and dielectric properties measurements of the samples are given and discussed below:

Structural Study

The structures and phases of the sintered BIT, BLT and BLTM samples were characterized by X-ray diffraction patterns (X-ray diffractometer, X'Pert-Pro, Philips, Japan using Cu $K\alpha$ ($\lambda = 1.5405$Å) radiation). The XRD patterns of the ceramic samples are shown in Fig. 2. All the peaks are indexed according to the reference code 36-1486, which indicates that the obtained BIT ceramic is polycrystalline in nature and it contains single phase of bismuth-layered perovskite structure with preferred (117) and (00*l*) orientations [7]. However, in the XRD patterns there are three unknown peaks observed at (27.9198°), (28.7277°) and (49.3098°). These peaks indicate that a trace amount of another phase is present in the sample. This phase could be pyrochlore ($Bi_2Ti_2O_7$) phase [9]. In addition, the slim width of the diffraction peaks indicates the large crystallite size of the ceramic [10].

Fig. 3 shows the FTIR spectra of the calcined powders within 2000 – 300 cm^{-1}. From the spectra of BIT, it is found that two sharp absorption peaks appear at 814 and 592 cm^{-1} which correspond to stretching vibrations of Bi-O and Ti-O bonds, respectively [11]. Another sharp absorption peak appears at 379 cm^{-1} that is related to the bending vibration of Ti-O bond [12]. In addition, two shoulders are observed at 470 and 313 cm^{-1}. The absorption peaks at 814, 592 and 379 cm^{-1} is a characteristics feature of the formation of titanate structure [13]. It is found that the IR spectra of BLT powder were similar to those of BIT powder, except small shifts of the absorption peaks with reduction of the intensities. The adsorption peaks at 592 cm^{-1} and 379 cm^{-1} were shifted to 607 cm^{-1} and 392 cm^{-1}, respectively, in FTIR spectra of BLT, while the intensity of the band at 814 cm^{-1} is significantly decreased [12]. It is also found that shoulders at 470 and 313 cm^{-1} in BIT are disappeared on La

doping (at 0.75). It is well known that crystal structure of pure BIT is monoclinic [15]. The monoclinic phase undergoes a structural phase transition to orthorhombic due to La doping at 0.66 doping level [14]. Therefore, the disappearance of shoulders at 470 and 313 cm^{-1} could be related to the monoclinic to orthorhombic phase transition.
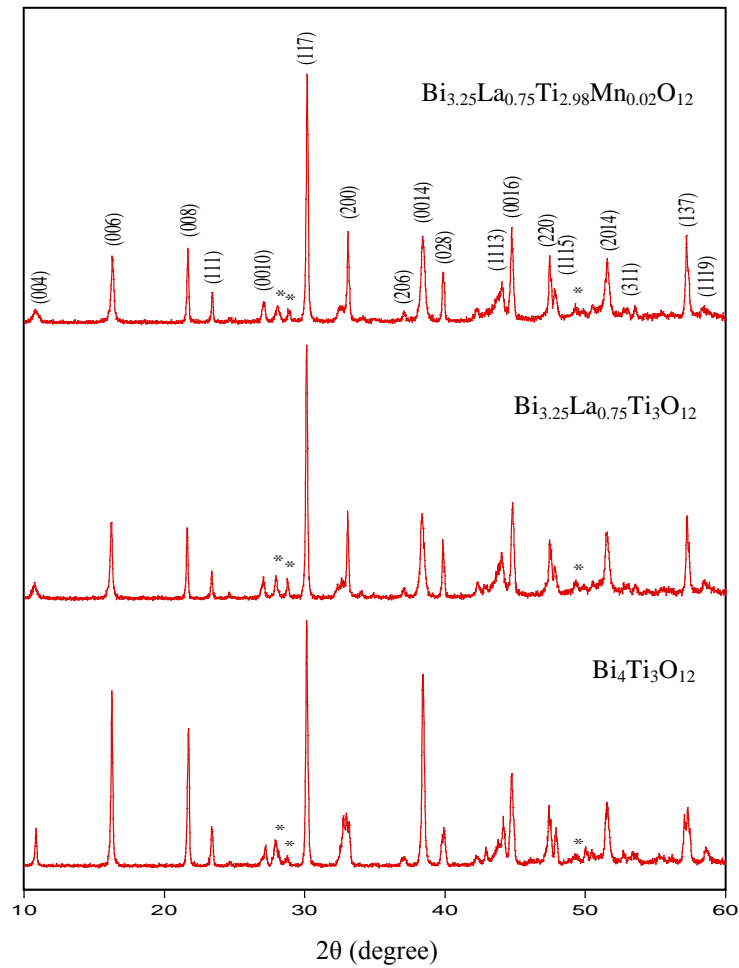
Fig. 2. X-ray diffraction patterns of BIT ceramic samples sintered at 1050 °C for 1 hour (∗Pyrochlore phase)
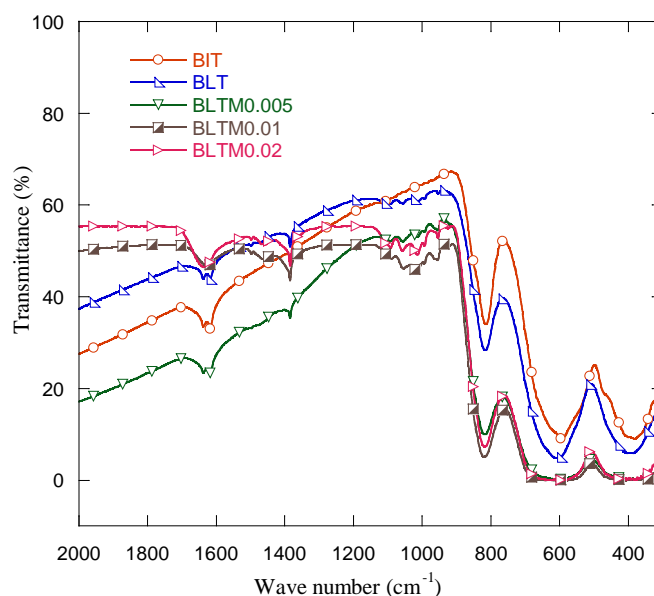
Fig. 3. Combined FTIR spectra of BIT, BLT and BLTM (x = 0.005, 0.01, 0.02) powder calcined at 800 ºC for 4 hours

From figure it is noticed that with increasing doping level of Mn in BLT, a dramatic change in FTIR spectra is observed. The absorption peaks at 607 cm^{-1} and 392 cm^{-1} become defused. Moreover, a new and relatively broad absorption peak appears at ~1015 cm^{-1}, which may related to the stretching vibration of Mn-O bond [15]. Therefore, it is reasonable to speculate that the new absorption peak resulting from the Mn-O vibrational mode could be due to the replacement of Ti by Mn in the TiO$_6$ octahedron [16]. The intensity of this peak gradually increases with the increase of Mn doping level. The gradual enhancement of the new absorption peak with the increase of Mn doping level further confirms the Mn substitution at the *B* site in BLTM ceramic samples [16].

Study of Dielectric Properties

Fig. 4 shows the variation of dielectric constant with frequency at room temperature for BIT, BLT and BLTM samples. It is seem that the dielectric constant of the sample is relatively high at lower frequency region in comparison to that in higher frequency region and the value becomes constant after 10 KHz for all samples. The dielectric constant of La doped BIT is higher than that of pure BIT. The increment of dielectric constant due to La doping can be explained as follows: It is known that defects such as Bi vacancies accompanied by oxygen vacancies degrade the dielectric properties in BIT [17]. These vacancies arise during sintering process due to the high volatility of Bi ions [18]. La doping improves the dielectric properties of bismuth titanate as it suppresses the volatility of Bi during sintering and reduces the oxygen vacancies in the ceramics [19]. It is also found that the dielectric constant of Mn doped BLT is increased with the increase of Mn doping level to a certain content (up to x = 0.01) and then decreased with the increase of Mn doping level. The increment of dielectric constant can be explained as follows: Mn doping at a suitable level improved the dielectric properties of the BLT samples by producing extrinsic oxygen vacancies that reduced the number of intrinsic bismuth vacancies [20]. The optimum Mn doping level in BLT towards the better dielectric performance is 0.01 mol%.
In addition the ionic radius of Mn^{4+} (0.060 nm) is a little smaller than that of Ti^{4+} (0.068 nm). When host Ti ions are replaced by small substitutional Mn ions, these ions may be located in the off-centered positions, which enhances the ionic dispalcement or distortion of TiO$_6$ octahedron, thus improving the dielectric property [16]. Excessive Mn doping reduced the dielectric properties of BLT ceramic. This can be explained by the ways: when Mn content is higher in BLT, ion-doped crystal lattice have not entered the interior in the grain, it gather in the grain boundary which impede the motion of the domain wall in the electric field. The domain wall motion has an important role to dielectric properties. By impeding domain wall motion excessive Mn doping reduced the dielectric constant [21].
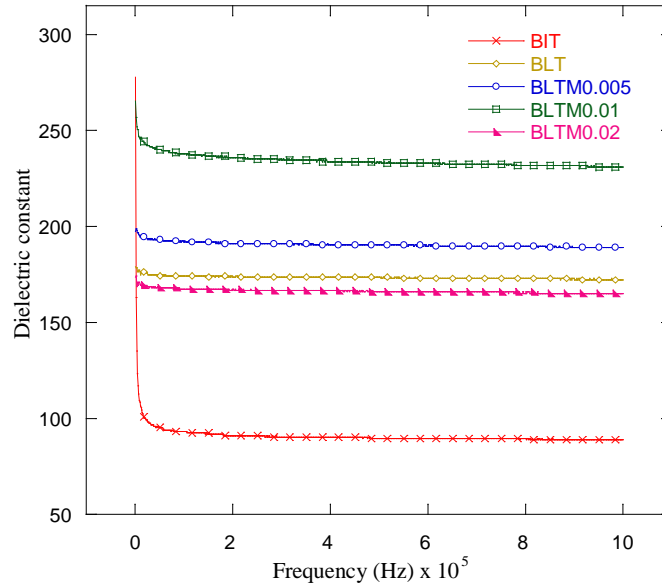
Fig. 4. Dielectric constant of BIT, BLT and BLTM (x = 0.005, 0.01, 0.02) samples as a function of frequency

Fig. 5 shows the dielectric losses of BIT, BLT and BLTM samples. It is seen that the loss tangents of BLT and BLTM ceramics are lower than that of pure BIT. This reduction of loss tangent could be due to the reduction of free charge, like oxygen vacancy, bismuth vacancy, etc.
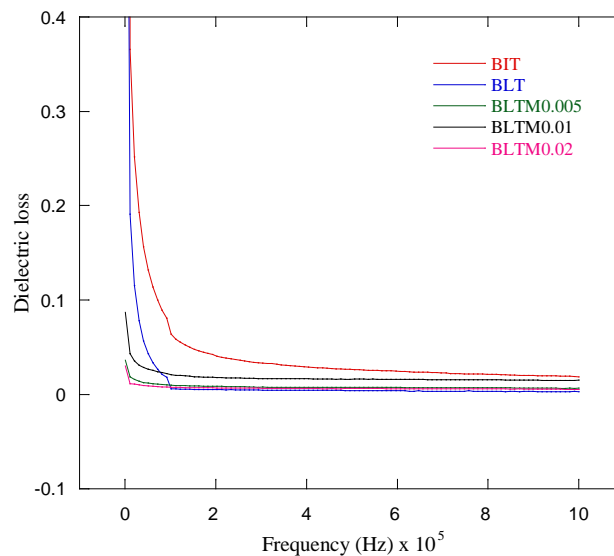
Fig. 5. Dielectric loss of BIT, BLT and BLTM samples as a function of frequency

4. Conclusions

BIT, La doped BIT and La/Mn codoped BIT ceramic samples fabricated by the solid-state reaction method exhibit polycrystallinity and almost single phase of bismuth-layered structure belonging to the crystalline phase $Bi_4Ti_3O_{12}$. The appearance of three absorption peaks at 814, 592 and 379 cm^{-1} in IR spectra of the prepared samples confirms the formation of titanate structure. Dielectric constant of the prepared samples decreases with the increase of applied frequency and then remains more or less constant after 10 KHz. The incorporation of La

in BIT suppressed the volatilization of Bi^{3+} during sintering and reduces the oxygen vacancies in the sintered sample. As a result, the dielectric constant increases and the dielectric loss are significantly reduced with La doping. The dielectric constant of Mn doped BLT increases with increasing Mn doping up to x = 0.01 and then decreases due to the domain wall pinning. From these results it is observed that BLTM sample shows the best dielectric properties for the Mn doping level at 0.01 mol%.

Acknowledgements

References

[1] W. F. Su, J. F. Lee, M. Y. Chen, and R. M. Ho, "Bismuth titanate nanoparticles dispersed polyacrylates", *J. Mater. Res.,* Vol. 19, No. 8, pp. 2343-2348, 2004.

[2] M. Krapchanska, Y. Dimitriev, and R. Iordanova, "Phase Formation in the System Bi_2O_3-TiO_2-SiO_2", *Journal of the University of Chemical Technology and Metallurgy*, Vol. 41, No. 3, pp. 307-310, 2006.

[3] X. Du, Y. Xu, H. Ma, J. Wang, and X. Li, "Synthesis and Characterization of Bismuth Titanate by an Sol-Gel Method", *J. Am. Ceram. Soc.,* Vol. 90, No. 5, pp. 1382-1385, 2007.

[4] R. Bharat, "Electron Microscopy of Barium Bismuth Titanate Multilayer Ceramic", *Mater. Sci. Res.,* Vol. 14, pp. 401-409, 1981.

[5] M. Kobavashi, C. K. Jen, Y. Ono, and S. Kruger, "Lead-free Thick Piezo-electric Films as Miniature High Temperature Ultrasonic Transducers", *Proc. of the IEEE,* UFFC-S, Vol. 2, pp. 910–913, 2004.

[6] N. V. Giridharan, M. Subramanian, and R. Jayavel, "Enhancement of Polarization in Bismuth Titanate Thin Films Co-Modified by La and Nd for Non-Volatile Memory Applications", *Appl. Phys. A*, Vol. 83, No. 1, pp. 123–126, 2006.

[7] X. L. Zhong, J. B. Wang, L. Z. Sun, C. B. Tan, X. J. Zheng and Y. C. Zhou, "Improved Ferroelectric Properties of Bismuth Titanate Films by ND and Mn Cosubstitution", *Appl. Phys. Lett.,* 90, 2007.

[8] M. Osada, M. Tada, M. Kakihana, T. Watanabe, and H. Funakubo, "Cation Distribution and Structural Instability in Bi4-xLaxTi3O12", *Jpn. J. Appl. Phys.,* Vol. 40, pp. 5572-5575, 2001.

[9] W. F. Yao, H. Wang, X. H. Xu, J. T. Zhou, X. N. Yang, Y. Zhang, and S. X. Shang, "Photocatalytic property of bismuth titanate $Bi_2Ti_2O_7$" *Applied Catalysis A: General*, Vol. 259, No. 1, pp. 29-33, 2004.

[10] W. Li, A. Chen, X. Lu, and J. Zhu, "Collective domain-wall pinning of oxygen vacancies in bismuth titanate ceramics", *J. Appl. Phys.,* Vol. 98, No. 2, pp. 024109, 2005.

[11] Z. Chen, Y. Yu, J. Hu, A. Shui, and X. He, "Hydrothermal synthesis and characterization of $Bi_4Ti_3O_{12}$ powders", *Journal of the Ceramic Society of Japan,* Vol. 117, No. 1363, pp. 264-267, 2009.

[12] Y. Kan, X. Jin, G. Zhang, P. Wang, Y. B. Cheng, and D. Yan, "Lanthanum modified bismuth titanate prepared by a hydrolysis method", *J. Mater. Chem.,*Vol. 14, pp. 3566-3570, 2004.

[13] N. Pavlovic, D. Kancko, K. M. Szecsenyi, and V. V. Srdic, "Synthesis and characterization of Ce and La modified bismuth titanate", *Processing and Application of Ceramic*, Vol. 3, No. 1-2, pp. 88-95, 2009.

[14] M. Iwata, C. H. Zhau, R. Aoyagi, M. Maeda, and Y. Ishibashi, "Splitting of Triggered Phase Transition in $Bi_{4-x}La_xTi_3O_{12}$ Mixed Crystals", *Jap. J. Appl. Phys.,* Vol. 46, pp. 5894-5900, 2007.

[15] F. I. Ezema, and U. O. A. Nwankwo, "Effect of Concentration of Mn Dopant Ions on the Structural and Optical Properties of Zinc Oxide Crystals", Digest Journal of Nanomaterials and Biostructures, Vol. 6, No. 1, pp. 271-278, 2011.

[16] Y. Wu, X. Wang, C. Zhong, and L. Li, "Effect of Mn Doping on Microstructure and Electrical Properties of the $(Na_{0.85}K_{0.15})_{0.5}Bi_{0.5}TiO_3$ Thin Films Prepared by Sol–Gel Method", *J. Am. Ceram. Soc.,* Vol. 94, No. 11, pp. 3877–3882, 2011.

[17] S. H. Shah and P. D. Bristowe, "*Ab Initio* Energetics of Lanthanum Substitution in Ferroelectric Bismuth Titanate", *J. Phys.: Condens. Matter,* Vol. 23, No. 15, pp. 155902, 2011.

[18] A. Z. Simoes, R. F. Pianno, C. S. Riccardi, L. S. Cavalcante, E. Longoa, and J. A. Varela, "Dielectric Properties of Pure and Lanthanum Modified Bismuth Titanate Thin Films", *Journal of Alloys and Compounds,* Vol 454**,** No. 1-2, pp. 66–71, 2008.

[19] N. Pavlovic, V. Koval, J. Dusza, and V. V. Srdic, "Effect of Ce and La Substitution on Dielectric Properties of Bismuth Titanate Ceramics", *Ceramics International*, Vol. 37, No. 2, pp. 487-492 (2011).

[20] J. Y. Choi, C. H. Choi, K. H. Cho, T. G. Seong, S. Nahm, C. Y. Kang, S. J. Yoon, and J. H. Kim, "Effect of Oxygen Vacancy and Mn-doping on Electrical Properties of $Bi_4Ti_3O_{12}$ Thin Film Grown by Pulsed Laser Deposition", *Acta Materialia*, Vol. 57**,** No. 8, pp. 2454–2460, 2009.

[21] P. Yongping, W. Jinfei, Y. Wenhu, Y. Gongan, and L. Yunhe, "Microstructure and Electric Properties of Dy and Sm-Doped Bismuth Titanate Ceramics", *Journal of Rare Earths*, Vol. 25, pp. 432-435, 2007.

Paper ID: MS-09

Structural Analysis and Mechanical Testing of Single Fiber from Ladies Finger Plant

S. Imam Hossain and MahbubHasan
Department of Materials and Metallurgical Engineering,
Bangladesh University of Engineering and Technology, Dhaka, Bangladesh
Email:*imam_raihan94@yahoo.com*

Abstract

The use of natural fiber as a reinforcement material is increasing day by day due its low cost, easy availability and bio-degradability compared to other fibers such as synthetic fiber. In present research, raw fiber from ladies finger plant was characterized using structural analysis and mechanical testing. Under structural analysis, Fourier Transform Infrared Spectroscopic (FTIR) analysis and Scanning Electron Microscopic (SEM) imaging were performed. Tensile test of ladies finger single fiber was also conducted by varying the span length. The FTIR analysis showed broad picks for –OH group and hemicelluloses in raw ladies finger fiber. SEM imaging revealed a rough fiber surface. The Young's modulus increased, whereas the tensile strength and strain to failure decreased with increase in span length.

Keywords: Ladies Finger Plant; Single Fiber; FTIR; SEM, Tensile Test

1. Introduction

Increased awareness on the environmental protection and the interest in long term sustainability of construction materials have led to the development of environmental friendly alternatives to fiber reinforced plastic composites. In this regard, significant efforts were directed to investigate the use of natural fibers as reinforcement in thermoplastics. Typical reinforcements for composites with plastic matrix are various synthetic fibers such as glass, graphite, boron, metallic and ceramic materials. These materials are heavy, expensive and harmful to environment. Natural fibers such as wood, wheat, straw, jute and bagasse have several benefits viz., low cost, low density, high toughness, acceptable specific strength properties, enhanced energy, recovery and biodegradability. The use of natural fibers in plastic matrix leads to many benefits such as low volumetric cost, increase of heat deflection temperature, increase of stiffness of thermoplastics and improvement of fiber surface appearance [1].Wide range of research has been carried out on fiber reinforced polymer composites in recent years [2-9].

Fibers from ladies finger plant are extracted in a similar way to jute fiber. It has so far been used to produce ropes and mats which performs satisfactorily. In appearance, it is very much similar to jute. The objective of present research is to characterize raw ladies finger natural fiber by finding out their structural and mechanical properties.

2. Experimental Procedure

2.1. Tensile Test of Ladies Finger Single Fiber

Tensile test of single ladies finger fiber was carried out by varying span length at 5, 15, 25 and 35 mm using a tensile testing machine. The fibers were glued in a paper frame (**Fig. 1**) to ensure a good gripping and straight direction to the test clamps. Diameter of single fiber was measured by using a scanning electron microscope (SEM). The paper frame was carefully placed in between the jaws of the load cell. Load cell of 50N was used and cross-head speed was 4mm/min.
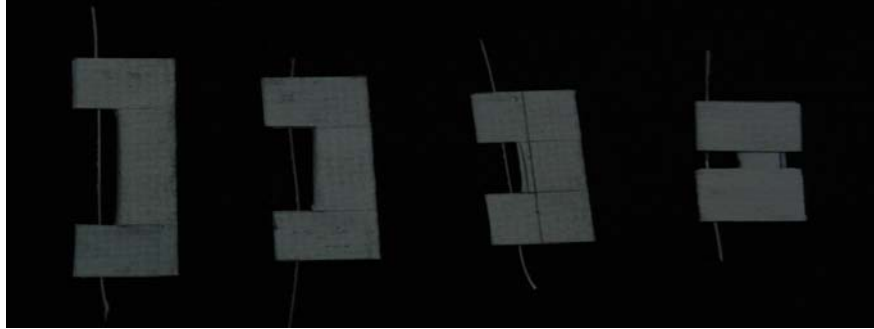
Fig. 1. Specimen for Tensile Test of Fiber

2.2. FTIR Spectroscopy

FT-IR stands for Fourier Transform Infra-Red, the preferred method of infrared spectroscopy. In infrared spectroscopy, IR radiation is passed through a sample. Some of the infrared radiation is absorbed by the sample and some of it is passed through (transmitted). The resulting spectrum represents the molecular absorption and transmission, creating a molecular fingerprint of the sample. Like a fingerprint no two unique molecular structures produce the same infrared spectrum. This makes infrared spectroscopy useful for several types of analysis.

Some powder sample was collected from the fiber surface and mixed properly with Potassium Bromide (KBr) at a ratio of KBr:sample =100:1. A pellet was made using that mixture and placed in a sample holder. After that the holder along with the pellet placed into the IR spectrograph.

2.3. Scanning Electron Microscopy

Surface morphology of fibers was observed under a scanning electron microscope. The diameter of the fiber was also measured using the same microscope. Gold sputtering was carried out to make the fiber surface conductive.

3.   Results and Discussion

3.1. Tensile Properties

The raw ladies finger fiber had been characterized using 5mm, 15mm,25mm and 35mmspan length separately. For each span length several samples were tested and the Young's modulus and tensile strength were measured. Due to the occurrence of slip during test, the Young's modulus seemed to increase with the increase in span length as percentage of slip is higher for smaller span length (Fig. 2). The Young's modulus values were corrected by correcting strain using the following formulas [10]:

1. $\Delta L_{total} = \Delta L_{fiber} + \Delta L_{grip}$

2. $\alpha_i = \Delta L_{total} / F - L_0 / E_0 . A_i$

3. $\Delta L_{total} / F = \varepsilon . L_0 / \sigma . A_i$
$= 1 / E. L_0 / A_i$
4. $\Delta L_{grip} / L_o = \alpha_1 (A_i . \sigma) / L_o$
5. $\Delta L_{fiber} / L_o$ (Corrected)$= (\Delta L_{Total} / L_o - \Delta L_{grip} / L_o)$

Where $L_0$is original length of fiber, A_i is cross- section area of each fiber and $E_0$is extrapolated modulus.

The variation of the corrected Young's modulus and tensile strength are shown in Figures 3 and 4 respectively. The tensile strength decreased with increase in span length [11,12]. As mentioned by

Bledskiand Gassan [13], the longer the stressed distance of the natural fiber, the more inhomogenities (flaws) will be in the stressed fiber segment that weakening the structure. Thus increasing fiber length inevitably reduces the strength of the fiber.
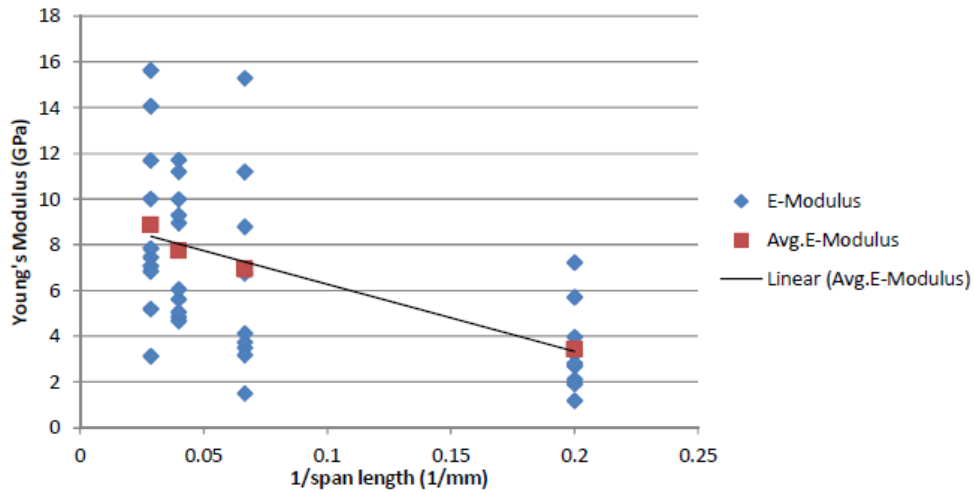
Fig. 2. Young's modulus vs 1/span length curve for ladies finger fiber (uncorrected).
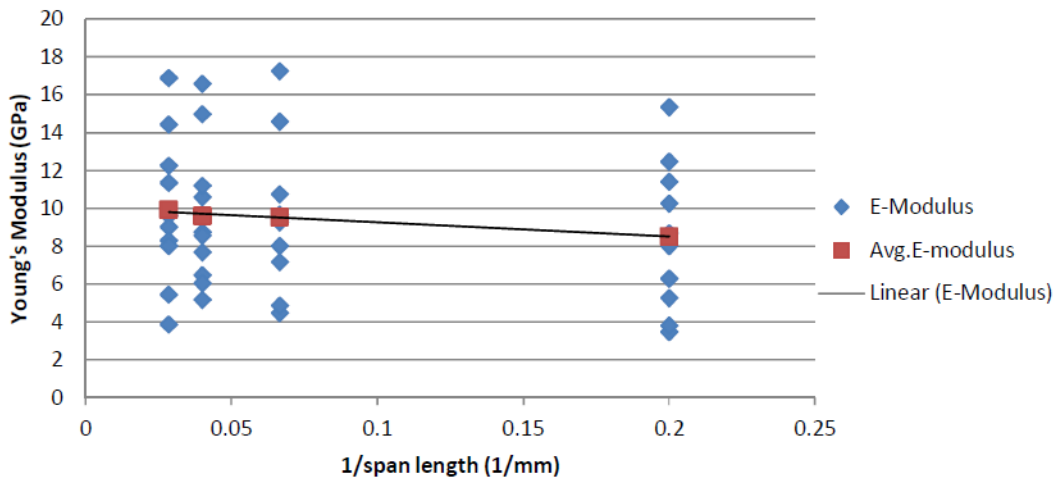
Fig. 3. Young's modulus vs 1/span length for ladies finger fiber (corrected)

Page | 597
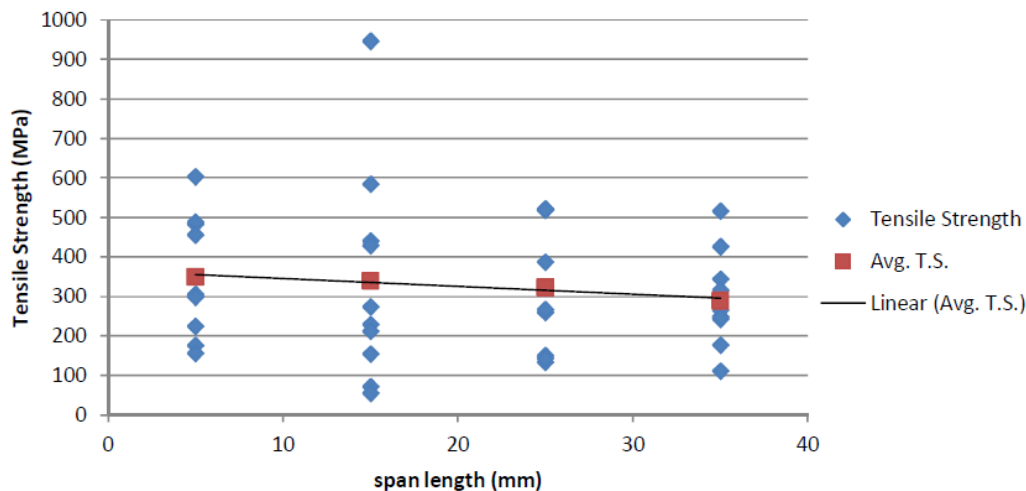
Fig. 4. Tensile strength vs span length curve for raw ladies finger fiber

3.2. FTIR Spectroscopic Analysis

The IR spectrum for raw ladies finger fiber (**Fig. 5**) clearly shows the characteristics band of (OH) broad, strong band from the constituents of fiber at the regions of 3600-3200 cm^{-1}, lignin and hemicelluloses at near about 1731.5 cm^{-1} ,(C-H) aromatic rings and alkane at 2920.5 cm^{-1} [14].
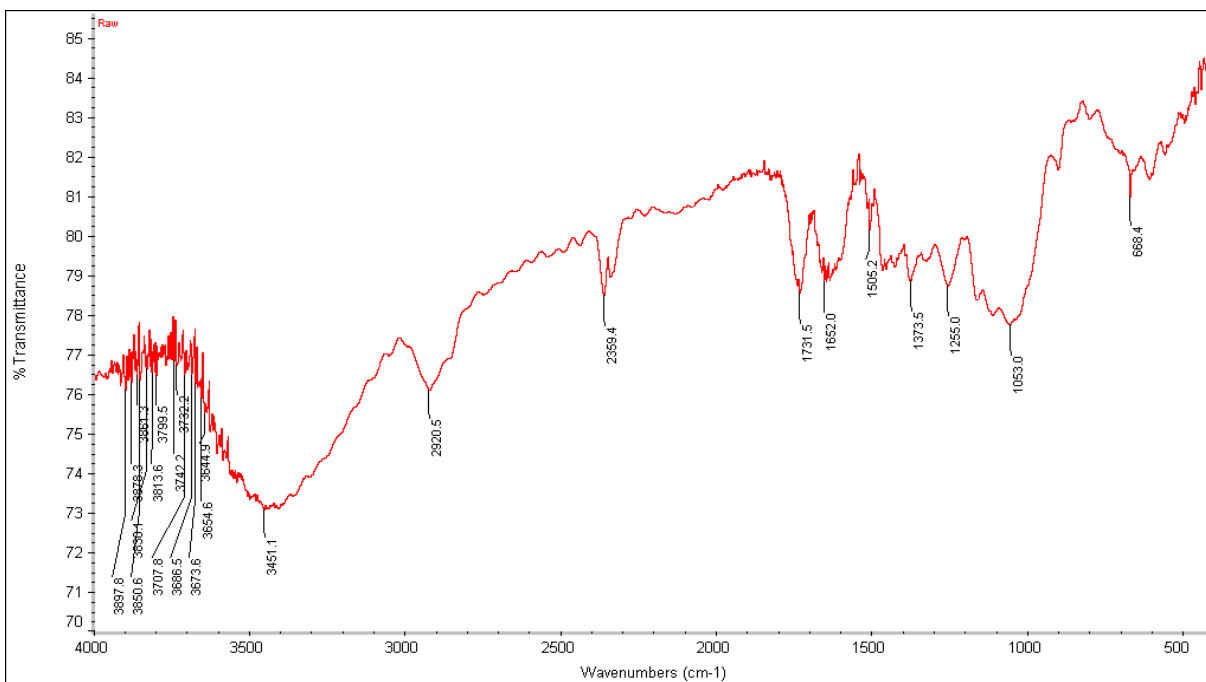
Fig. 5. FTIR analysis of ladies finger fiber

3.3. Surface Morphology

SEM imaging revealed the surface morphology of the fiber, which was a bit rough.
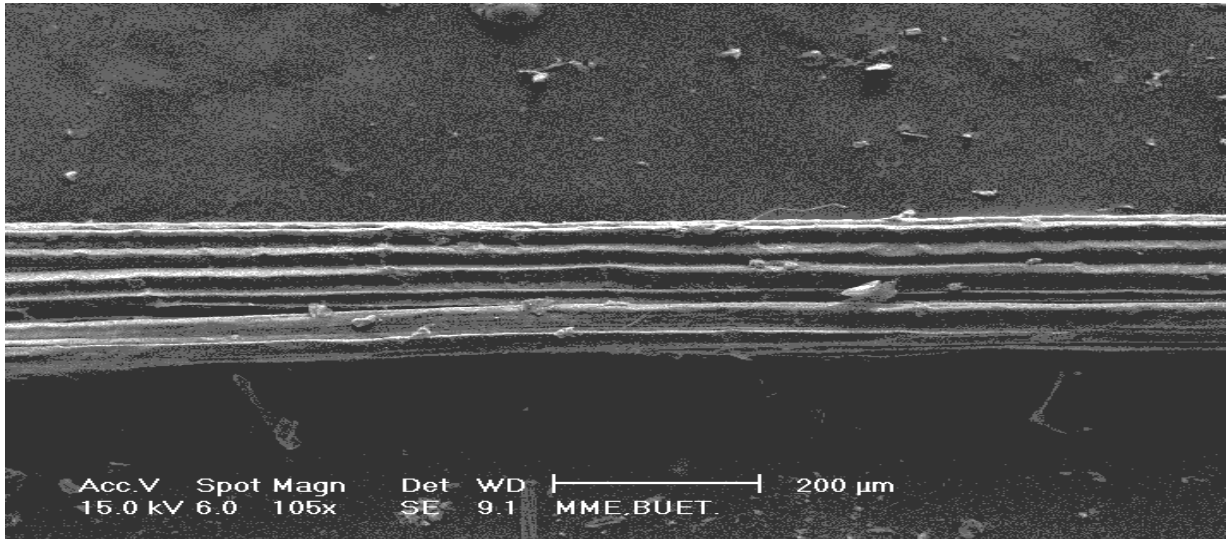
Fig. 6.SEM micrograph of ladies finger fiber.

4. Conclusion

The tensile strength of the fiber seemed to decrease with the decreasing span length. FTIR analysis of the fiber evidenced the presence of hemicellulose in fiber structure which is the main reason of hydrophilic nature of the natural fiber. It may cause problems like poor adhesion and therefore poor mechanical properties when combined with hydrophobic matrix. However, with proper treatment, this problem can be solved.

Reference

1. J. Jayaramudul, D. J. P. Reddy, B. R. Guduri and A. V. Rajulu, "Tensile Properties of Polycarbonate Coated NaturalFabric *SterculiaUrens*: Effect of Coupling Agent" (introduction, FTIR)
2. B. C. Mitra; R. K. Basak; M. Sarkar; *Journal of Applied Polymer Science*, 67, 1093-1100 (1998).
3. A. N. Netravali; "Natural Fibers, Plastics and Composites", Kluwer Academic Publisher, USA (2004).
4. A. Kelly; *Journal of Ceramic Processing Research*,2, 147-154 (2004).
5. P. Wambua; J. Ivensand; I. Verpost; *Composite Science and Technology*, 63, 1259-1264 (2003).
6. C. N. Singleton; *Composite: Part B*, 34, 519-526 (2003).
7. M. T. Moe;, K. Liao; *Composite Science and Technology,*63, 375-387 (2003).
8. E. M. F. Aquino;, L. P. S. Sarmento;, W. Oliveira; *Journal of Reinforced Plastics and Composites*, 26, 219-233 (2007).
9. M. T. Moe; *Composite: Part A*, 33, 43-52 (2002).
10. S. Biswas; "Characterization and Performance Analysis of Natural Fibers as Reinforcement in Polymer Composite", M.Phil Thesis, Bangladesh University of Engineering and Technology, Bangladesh, (2010).
11. S. Biswas; Q. Ahsan; I. Verpoest; M. Hasan; *Advanced Materials Research*, 264-265, 445-450 (2011).
12. S. S. Mir; M. N. Hasan; Md. J. Hossain; M. Hasan**;** *Engineering Journal*, 16, 73-83 (2012).
13. K. Bledzki; J. Gassan; *Progress in Polymer Science*, 24, 221-274 (1999).
14. N. Nafsin, Manufacturing and Characterization of Coir Fiber Reinforced Polypropylene Composites, Bachelor Thesis, Dept. of MME, BUET.

Pyrolized Growth of (Al, N) dual doped CdO Thin Films and Study of Structural, Surface Morphology and Opto-electrical Properties.

A.F.M. Faizullah[1] M.K.R.Khan, M.Mozibur Rahman
[1]Department of Physics, University of Rajshahi, Bangladesh
E-mail: afmfaizullah07@gmail.com

Abstract

Thin films of undoped and (Al, N) dual doped CdO were prepared on glass substrate at substrate temperature 350 ℃ by spray pyrolysis method. The films are characterized by XRD, AFM, Double beam Spectrophotometer and Van der Pauw's methods. The films are highly poly crystalline and found to be cubic. AFM images show the surface properties of the film. It increases with increasing concentration of Al & N in the CdO samples. Optical transmittance is made at room temperature within the wavelength range 400 nm to 1100 nm. Direct band gap of undoped CdO has been measured and found to be 2.58 eV and it decreases with (Al, N) dual doping in CdO thin film upto 2.52 eV. The resistivity of undoped CdO shows the metallic behavior upto 370 K and then followed by semiconducting behavior. (Al, N) dual doping shows the carrier compensation during temperature range (355 - 375) K.

Keywords: spray pyrolysis, Dual doped, CdO, grain size.

1. Introduction

Transparent conductive oxides (TCO) are a type of nonstoichiometric semiconductor oxides of high conductivity arising from structural metal interstitials and oxygen vacancies. They have widespread use in many advanced technology applications. It is essential to investigate the means for improving the function of TCOs since they could have an enormous impact on the next generation flat panel displays and solar energy systems, and any progress in the field will require a dedicated, multidisciplinary effort [1]. It is well known that high carrier mobility is essential for TCOs with good quality electro-optical properties. From other side sometimes it is necessary to hybridize TCO in order to get some magnetic or other properties for various applications.
CdO is an n-type semiconductor with a rock-salt crystal structure (fcc) and possesses a direct band gap of 2.2 eV [2]. Its high electrical conductivity and high optical transmittance in the visible region of solar spectrum along with a moderate reflective index make it useful for various applications, photodiodes, gas sensors, etc [3, 4]. Undoped, mono-doped and dual doped CdO thin films have been prepared by various techniques such as spray pyrolysis [5], ion beam sputtering [6], sol-gel [7] etc.
In this study, undoped and (Al, N) dual doped CdO thin films have been deposited by spray pyrolysis method using cadmium acetate dehydrate, aluminium chloride and ammonium acetate as the solvent and the structural, morphological, optical and electrical properties of the films has been studied. We have chosen the spray pyrolysis method because of low cost, easy to control growth parameters, large area of fabrication.

2. Experimental Details

CdO thin films have been deposited on glass substrates at substrate temperature 350° C using spray pyrolysis technique. Cadmium acetate dehydrate $[Cd(COOCH_3)_2.2H_2O]$ with constant concentration of 0.15 M, Aluminium chloride and Ammonium acetate were taken as the source of cadmium oxide, aluminium and nitrogen respectively. The distance between the spray nozzle and substrate was maintained at 20 cm to obtain maximum coverage throughout the film with substrate temperature 350 ℃. Al and N were implanted at different ranges of 0, 1, 2, 3, and 4%. To study the structural property X-Ray Diffraction (XRD) patterns were obtained from Cu-Kα radiation (λ = 1.54056 A^0) with scanning range of 2θ from 30° to 65° to detect the possible peaks.

Surface properties of the film were studied using AFM. Optical properties were taken by UV 1601PC double beam Spectrophotometer. Electrical properties were studied through the standard four probe technique. Fig. 1 shows the experimental setup for preparation of (Al, N) dual doped CdO thin film by using spray pyrolysis technique.
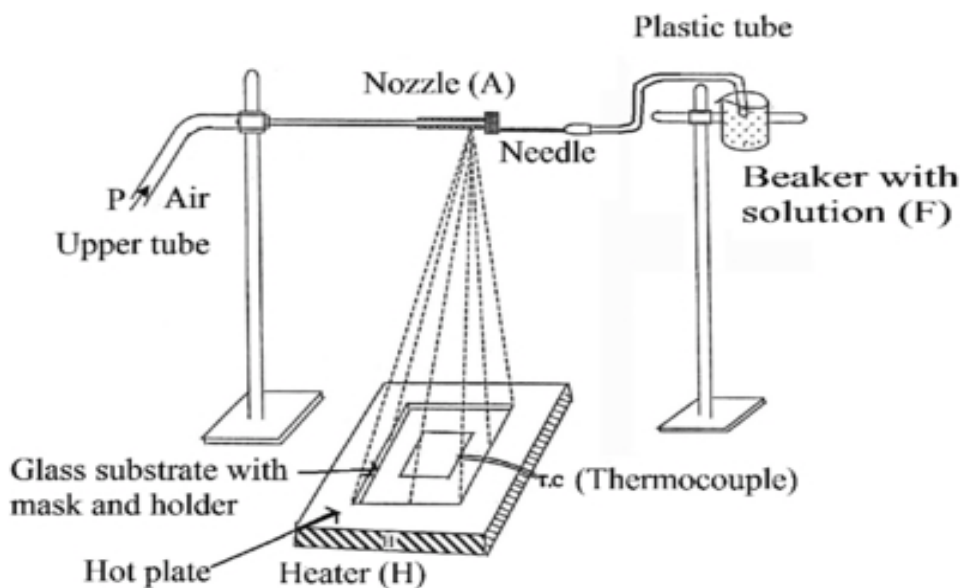
Fig. 1. Experimental setup

3. Results and Discussion

Structural analysis: XRD patterns were obtained for undoped, Al doped and (Al, N) dual doped CdO thin film and are given in Fig.2. The diffracted peaks showed that it has polycrystalline nature with cubic crystal structure were confirmed from JCPDS (Joint Committee on Powder Diffraction Standards) file No. 05-0640 which indicates the formation of CdO sample. Both undoped and dual doped films show the preferential orientation along (200) plane. There are no additional peaks without CdO upon doping indicates the solubility of the dopant in the crystal structure. The grain size of the undoped film was found to be 27.15 nm which decreased to 26.873 nm for (Al, N) dual doping CdO. The values of peak angle, grain size and lattice parameter obtained from undoped and dual doped CdO films are given in Table 1.
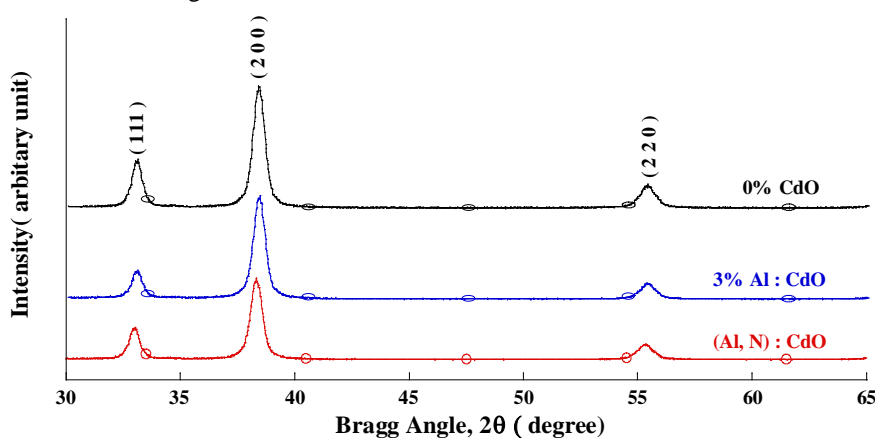
Fig. 2 XRD patterns of undoped, Al doped and (Al, N) dual doped CdO

Surface analysis: Fig. 3 shows the AFM (Atomic force microscopy) images obtained for undoped and (Al, N) dual doped CdO films. The roughness of the surface was estimated by calculating the Root Mean Square (RMS) value. The surface of (Al, N) dual doped CdO seems to be rougher than the undoped CdO. Doping of (Al, N) in CdO thin films increases the surface roughness with the increase of (Al, N) wt. % concentration.

Optical properties: Fig. 4 shows the optical transmittance spectra with wavelength from 400 nm to 1100 nm of the undoped, Al doped and (Al, N) dual doped CdO thin films. It is seen from Fig. 4 that the films are transparent in the visible region. The optical transmittance increases with increasing (Al, N) doping concentration (Fig. 4).

The optical band gap of undoped and doped CdO thin films is determined from the data of transmittance and reflectance using the relations given below. The absorption coefficient (α) is given by

$$\alpha = \frac{1}{t}\ln\left[\frac{(1-R)^2}{T}\right] \qquad (1)$$

where, 'T' is transmittance and 't' is film thickness. The relation between the absorption coefficient and the incident photon energy (hν) is given by the equation,

$$\alpha = \frac{A(h\nu - E_g)^n}{h\upsilon} \qquad (2)$$

where 'A' is a constant and 'Eg' is optical band gap. The undoped CdO film shows a band gap of 2.58 eV. The band gap decreases with doping concentration and acquires a minimum of 2.52 eV. Fig. 5 shows the variation of $(\alpha h\nu)^2$ versus hν for direct transitions of the CdO thin films.

Electrical properties: The variation of resistivity with temperature is shown in Fig. 6. Resistivity measurements were done from room temperature to 470 K by Van der Pauw's method. The resistivity of undoped and Al doped CdO thin film were slightly increases with temperature which shows the semi-metallic behavior (up to 378 K) and with the further increase of temperature the resistivity falls and shows the semiconducting behavior. But for (Al, N) dual doped CdO thin film the resistivity remains almost constant with temperature from 300 K to 360 K and after that the resistivity is sharply increases (at around 365 K) due to the effect of N doping which creates holes in the system. In this case compensation of charge is occurred and this compensation stops at nearly 380 K. And resistivity decreases with the further increase of temperature and shows the semiconducting nature. Finally it remains constant from 450 K to 470 K. This may be due to the spinning of Fermi energy.

Table 1. XRD data obtained for undoped and (Al, N) dual doped CdO

Types of samples	2θ (deg.)	Grain size (nm)	Observed d value (Å)
Undoped CdO	33.002	27.150	2.7109
3% Al doped CdO	33.000	27.578	2.7111
(Al, N) doped CdO	33.014	26.873	2.7100

(a)   **(b)**
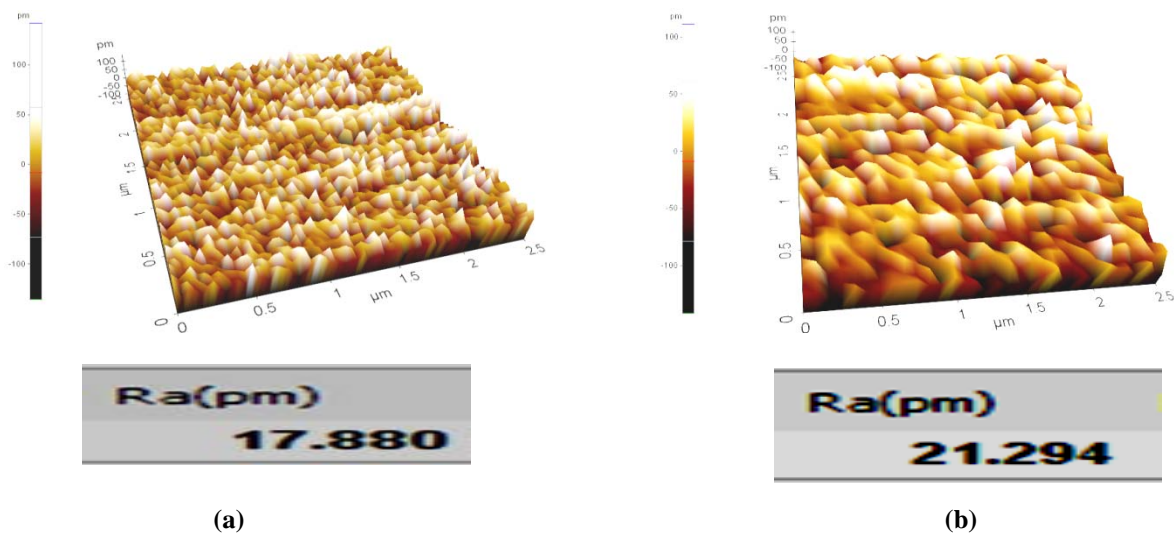
Fig. 3. (a-b): AFM images of (a) undoped and (b) 3% Al & 1% N dual doped CdO
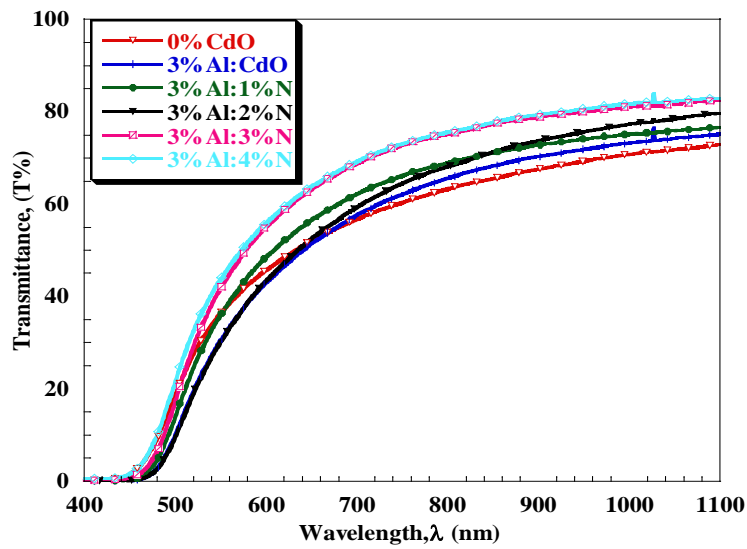
Fig. 4 Optical transmittance spectra of (Al, N) dual doped CdO thin films.
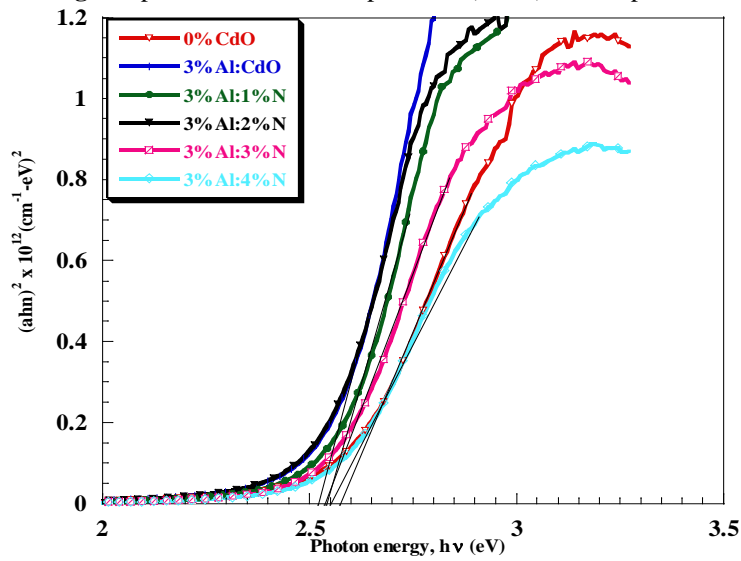
Fig. 5 The plot of $(\alpha h\nu)^2$ against $h\nu$ of CdO thin films.
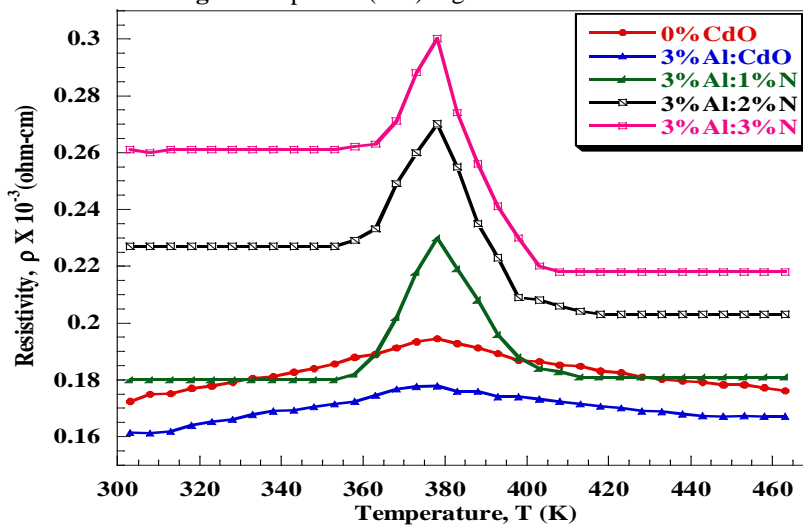
Fig. 6 The plot of resistivity against temperature of CdO thin films

4. Conclusions

(Al, N) dual doped CdO films are fabricated by spray pyrolysis technique. XRD patterns shows that it has polycrystalline nature with cubic crystal structure with (2 0 0) plane as preferential orientation. The grain size of undoped CdO film is 27.15 nm which increase for Al doped CdO thin film while it decreases with dual doping of Al and N. The optical band gap values were found to decrease from 2.58 eV to 2.52 eV for direct transitions with dual doping of (Al, N) in CdO. Electrical studies revealed that for dual doping compensation of charges (electron and hole) are occurs at certain temperature range (360- 380) K.

5. Acknowledgement

6. References

[1] S. Canan, A. N. Tiwari, High mobility transparent conducting oxides for thin film solar cells 518 (2010) 1839.
[2] M. Ortega, G. Santana, A. Morales-Acevedo, Preparation of nanostructure Ni doped CdO thin films by sol gel spin coating method 44 (2000) 1765.
[3] R. Ferro, J.A. Rodriguez, Optical and Structural Studies of Sol-Gel Deposited Nanostructured CdO Thin Films: Annealing Effect 64 (2000) 363.
[4] T.K. Subramanyam, S. Uthanna, B. Srinivasulu Naidu, Matter. Lett. 35 (1998) 241.
[5] O. Vigil, F. Cruz, A. Morles-Acevedo, G. Contreras-Puene, L. Vaillant, G. Santana, Matter. Chem. Phys. 68 (2001) 249.
[6] T.L. Chu, S.S. Chu, J. Electronchem. Soc. 110 (1963) 548.
[7] *Hobert, H.*; *Seltmann*; *B*. Infrared study of SiO2/TiO2/CdO layers on glass prepared by the sol-gel method. *J. Non-Cryst. Solids 195*(*1996*)*54*-63.

Corrosion Behavior of Different Percentage Al-Zn Galvanized Steel.

AzrinAkhterChowdhury
*Department of Materials and Metallurgical engineering. Bangladesh University of Engineering and Technology.*Corresponding email: azrin.chowdhury@yahoo.com

Abstract:

Galvanizing or zinc coating is a method of protecting iron and steel against corrosion. When aluminum (Al) is added with zinc (Zn) in galvanizing process, properties of zinc coating varies. It effects on corrosion behavior, appearance, thickness, hardness and other physical or mechanical properties. Structure of the coating also varies. So by adding aluminum in zinc various types of properties can be analyzed for the better improvement of zinc coating. In this project effect of aluminum on corrosion behavior of hot dip galvanized steel, is mainly analyzed. The method of galvanization was done by hot dipping process. Here corrosion in different solution is also observed. Corrosion rate in 20% NaCl solution is higher than 10% NaCl solution. Varying the aluminum percentage in zinc shows different corrosion behavior on different solution.

Keywords:Hotdipping, Galvanization,Transpassive,Corrosion, Moltenbath.

1. Introduction

Galvanizing is an attractive and economical because of its corrosion protection for a wide variety of commercial and industrial steel articles. Hot Dip Galvanizing is a process in which an adherent, protective coating of zinc and zinc compounds is developed on the surfaces of iron and steel products by immersing them in a bath of molten zinc [1]. The usefulness of zinc coatings depends, first on the relatively slow rate of corrosion of zinc as compared with that of iron and the much less objectionable appearance of the white, nonstaining corrosion products of zinc as compared with iron rust, second on the electrolytic protection afforded to iron by zinc [2].
Zinc coating have the longest life under conditions of rural exposure where the air is free from sulfur gasses and other industrial fumes [3]. They have satisfactory service in salt air, also. They are more rapidly attacked in highly in acid industrial atmosphere. Galvanized coatings are applied to iron and steel primarily to provide protection against corrosion of the base metal. Some major applications of hot dip galvanized coatings include: Marine pilings and rails, Bridge structural members, culverts, corrugated steel pipe etc. Rather that Corrosion appearance, Abrasion resistance, High temperature Exposure, Surface reflectivity also enhance the importance of galvanized [4]. Adding Aluminum on Zinc bath enhance the corrosion properties of the galvanized steel. Resistivity of corrosion is much higher Al-Zn coating compares to pure zinc. This coating has good corrosion resistive property also. In this project, the effect of aluminum on corrosion behavior of hot dip galvanized steel is work on.

2. Experimental Procedure

In this experiment mild steel strips are galvanized by batch hot dipping process .The sample is dipped in various percentages of Al –Zn bath. Then the corrosion properties of this galvanized sample are examined in NaCl solution. The substrate that was taken in this experiment is 6 cm by 2 cm in size. Before dipping it the molten bath, it has gone through different type of cleaning procedure and protection from air as well. Here galvanization is done by dry galvanizing process where samples are degreased, pickled and immersed in an aqueous flux solution, dried and then immersed in the molten zinc bath.Work pieces must be handled properly until the coating has completely solidified, which was accomplished by air cooling. The whole procedure has been

illustrated in Fig 1. Although degreasing, pickling, water rinsing, and other cleaning procedures remove most of the surface contamination and scale from iron and steel, small amounts of impurities in the form of oxides, chlorides, sulfates, and sulfides are retained. Unless removing, these impurities will interfere with the iron-zinc reaction when the iron or steel part is immersed in molten zinc.
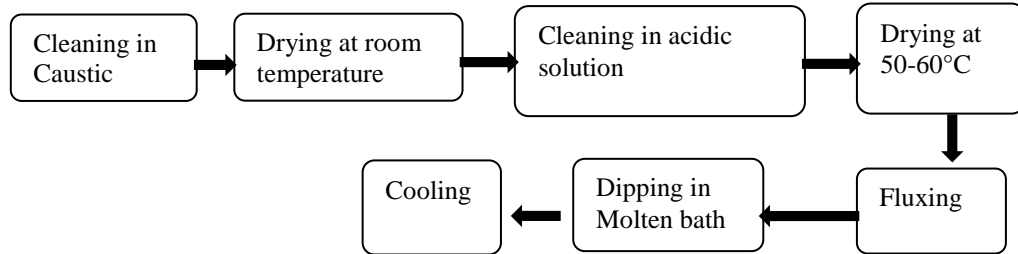
Fig. 1. Experimental procedure

In this experiment samples were dipped in various bath compositions. The temperature is maintained within the range of 600-650°C. The immersion time for all samples was 1 minute. The bath compositions for this experiment are in table 1. For corrosion test samples were immersed in different % of NaCl solution bath at various time ranges. In this paper 10% and 20% NaCl solution had been used for corrosion test. Corrosion rate of different composition of samples has also been depicting on.

Table. 1. Compositions of molten bath solution

Bath Compositions	% of Al in Zn	Notations
Pure Zn	0	Pure Zn
3.97% Al-Zn	3.97	3 Al-Zn
8.4 % Al-Zn	8.4	8 Al-Zn
15.56 % Al-Zn	15.56	15 Al-Zn

3. Results

Fig. 2a) illustrated 20% and 10 % of NaCl test of different samples. Except the sample maintained in solution for 5 hr, rest of all are in similar pattern. In other samples corrosion rate decreases up to 8.4% aluminum added sample. Then corrosion rate increases with increasing the percentage of aluminum. This behavior is observed for increasing percentage aluminum up to 10.94% Then again corrosion rate decreases. Some exceptionality has been noticed for the sample maintained for 5 hr.
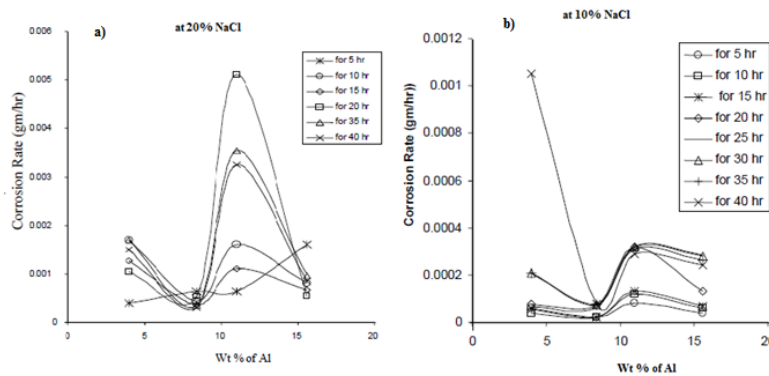
Fig. 2. Weight % of Al Vs Corrosion rate at a) 20% NaCl b) 10% NaCl

Fig. 2b) illustrated thatsamples maintained in solution for 5 to 35 hr are in similar pattern. At first corrosion rate decreases up to about 8.4 % aluminum then again increases up to about 10.94 % finally again corrosion rate decreases. But the sample which is maintained in solution 40 hr in first portion corrosion rate decreases drastically. Corrosion rate for the samples from 5 hrs to 20 hrs is comparatively higher than others samples in 35 hrs and 40 hrs. Corrosion rate for 40 hours sample is slower. From this phenomenon we can conclude that with increasing Al upto 8% corrosion rate decreases as some oxides formation occur during immersion of this solution. These oxides scale act as protective layer for further oxidation. That's why it reduces the corrosion rate. With increasing the thickness of the oxide layer, the oxide scale get off which is responsible for further oxidation.

Corrosion rate of 8.84% Al- Zn samples at different time is observed from following figure. This test is done at various NaClsolutions. From the graph it is observed that corrosion behavior of 5% and 20% NaCl test are in similar pattern. The corrosion rate decreases slowly with time. But for 10% NaCl test corrosion rate increases slowly with time upto 20 hr, after that corrosion rate increases somewhat.
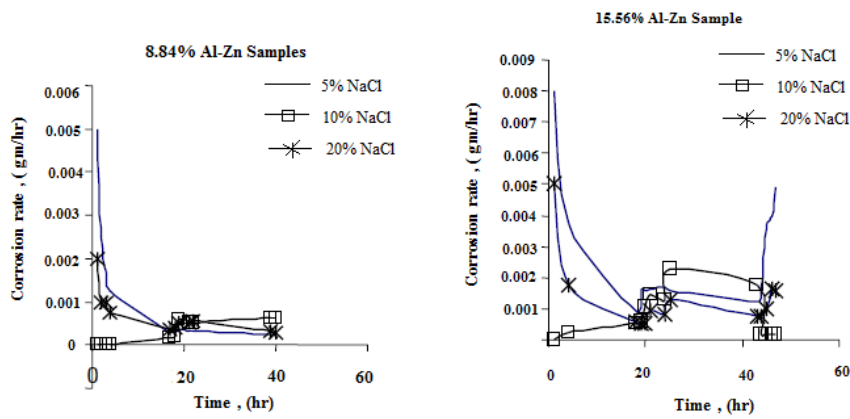
Fig. 3. Corrosion rate Vs time for a) 8.84%Al-Zn Sample b) 15.56% Al-Zn Sample

From the following figure it is observed that corrosion rate behavior for 5% NaCl and 20% NaCl are similar pattern. In both case corrosion rate at first decreases with time, then constant for some time, then again increases. 10% NaCl test shows different pattern, at first corrosion increases slowly with time. After 20hr it increases rapidly, and then it is constant with time.

4. SEM analysis

From the SEM picture it can be shown that coating is very uniform, homogenous microstructure. The coating thickness varies in between 59- 60 µm.
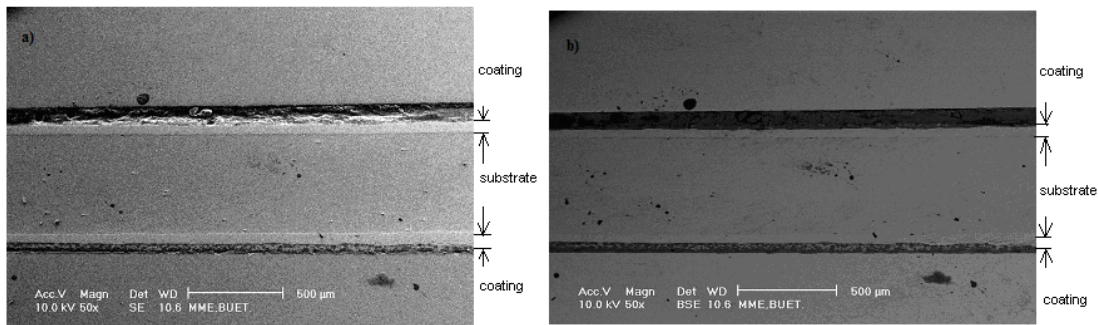
Fig.4.SEM images a) Secondary electron image b) Backscattered electron image

5. Conclusion

In this paper corrosion experiment has been done at different types of NaCl solution medium and different composition of Aluminum as well. In all cases corrosion rate decrease with increasing the Aluminum content after that it again increases. High concentrated NaCl solution increases corrosion rate.Coating from increased amount of aluminum in zinc bath shows good resistive properties of corrosion. At the very beginning corrosion rate decreases slowly with time then constant for some time and increases again. It can be concluded that the total corrosion effect can be divided into three parts active, passive and transpassive. . In the active region the behavior of this material is identical to that of a normal metal. Increasing the time weight loss increases rapidly, then at a time reached when weight losses slightly. This is passive region. Overcoming this passive region weight loss again increases with time. That means corrosion rate increases .This region known as transpassive region.

6. Acknowledgement

7. Reference

[1]. W.L.Hall, "Corrosion Prevention", *Anti-corrosion Methods and Materials*, Vol. Iss: 7,pp. 173-182.

[2]. J.L.Rodda, H.bablic, "Galvanizing" *E & F.N. Spon, ltd, London,* 3rd Ed, 1950.

[3]. G.Vourlias,N.Pistofidis, D. Chaliampalias, E. Pavlidou, G. Stegioudis, E.K. Polychroniadis, D. Tsipas , "Zinc deposition with pack cementation on low carbon steel substrates", *Journal of Alloys and Compounds*, Vol. 416, Iss 1-2, pp. 125-130,2006.

[4]. J.R. Daesen, "Galvanizing Handbook", *Reinhold Publishing Corp, New York*, 1946.

Phase Evolution & Characterization of Spinel Ferrite (Oxide) Nanocomposite material Prepared by Chemical Route

Soumya Mukherjee, Abhigyan Datta, Mrinal Saha, Siddhartha Mukherjee[1]

[1] Department of Metallurgical & Material Engineering, Jadavpur University, Kolkata-700032, India

Corresponding E-mail: sm_n4@yahoo.co.in, smmukherjee3@gmail.com

Abstract

Nanocomposite of Nickel Ferrite-Zinc Ferrite (Spinel Oxide ferrites) was prepared by co-precipitation route from metal nitrate precursors using 1:1 molar ratio. DSC-TGA of the mixed powder was studied to observe thermal behaviour and crystallization temperature for proper phase development. Heat treatment was carried out at 700^0, $750^0 C$ for 3, 4 and 5hrs for synthesizing the nanocomposite. XRD analysis was done to determine the phases, plane of orientation of respective phases of the nanocomposite while crystallite size was measured by Scherrer's formula. Highly pure samples with proper orientation of phases developed for the nanocomposite was obtained at 700^0, $750^0 C$ for 5hours soaking period. SEM (Scanning electron Microscope) was taken to obtain the morphology and structural analysis. Interconnected agglomerates with spherical and polygonal shape particulate morphology was obtained in the nanocomposite material. The materials were characterized by FTIR to determine the stretching and vibration of bonds with proper co-ordination required followed by UV-VIS spectral analysis. Bandgap was evaluated from the spectra using Tauc relation.

Keywords: Nickel Ferrite-Zinc Ferrite, Nanocomposite, XRD, FTIR, HRSEM, UV-VIS.

1. Introduction

Nanocrystalline spinel ferrites have been the subject of interest due to their enhanced optical, magnetic, and electrical properties, in compare to bulk counterparts. Nanospinel ferrites have variety of applications, like electrodes in energy storage devices, catalysts, and magnetic storage devices. Among various ferrites, which form a major constituent of the magnetic ceramic materials, nanosized nickel ferrite possesses attractive properties for the application as soft magnets, core materials in power transformers and low loss materials at high frequencies. High permeability in the radio frequency region, high electrical resistivity, high Curie temperature and low eddy current loss are important properties of nickel ferrites, which make them suitable for wide range of applications. Nickel ferrite has inverse spinel structure. The crystal structure is face centred cubic with the unit cell containing 32 O^{2-}, 8 Ni^{2+} and 16 Fe^{3+} ions. The oxygen ions form 64 tetrahedral and 32 octahedral sites, where 24 cations are distributed. The eight Ni^{2+} and eight Fe^{3+} cations occupy half of the octahedral sites and the other eight Fe^{3+} ions occupy eight tetrahedral sites. Ferrimagnetic property of the material arises from magnetic moments of anti-parallel spins between Fe^{3+} ions at tetrahedral sites and Ni^{2+} and Fe^{3+} ions at octahedral sites. $ZnFe_2O_4$ is a promising semiconductor photo-catalyst for various processes, due to its ability to absorb visible light and its high efficiency shows potentially wide applications in photoinduced transformer, photoelectrochemical cells and photochemical hydrogen production. It is known that bulk zinc ferrite represented by the chemical composition $ZnFe_2O_4$ crystallizes in the normal spinel structure with Zn^{2+} ions in the tetrahedral A-sites and Fe^{3+} ions in the octahedral B-sites and it is antiferromagnetic with a Neel temperature of about 10K due to the B–B interactions, and above that temperature, they are paramagnetic. It is therefore likely that in nanocrystalline zinc ferrite due to strain, the cation distribution changed from normal to mixed spinel type. Thus, a small number of Fe^{3+} ions occupy the tetrahedral A-sites and these ions switch on the A–B super-exchange interaction, leading to a larger magnetization. In other words, the magnetic ordering introduced in nanocrystalline zinc ferrites occurs because of strong A–B interaction between Fe^{3+} ions in the octahedral B-sites and Fe^{3+} ions in the tetrahedral A-sites, which are forced into these respective positions during the synthesis of nanoparticles. Synthesis and magnetic studies on Ni-ferrite and Zn-ferrite as well as Ni-Zn ferrite has been carried out for over a decade. $Ni0.5Zn0.5Fe_2O_4$ nano-particles were synthesized via sol-gel route in a silica matrix followed by calcinations at 700-900^{0}C. The absence of saturation magnetization at 10 kOe and Mossbauer spectra confirm super-paramagnetism of Ni-Zn Ferrite.[1] Effect of preparation method on structure and properties of Nickel ferrite were studied by producing $Ni0.8Zn0.2Fe_2O_4$ via the conventional

ceramic route (oxide precursors) and also through co-precipitation route (metal nitrate precursors and ammonium hydroxide precipitation).[2] Nanosized Ni-Zn ferrites were also prepared using reverse micelle route using AOT/iso-octane at room temperature without requiring any subsequent firing of the material.[3]

However, not much work has been reported on preparation of composites of Ni-ferrite and Zn-ferrite nano-particles instead of Ni-Zn intermetallic ferrite. In this endeavor we have synthesized Ni ferrite- Zn ferrite nanocomposite via coprecipitation method. Coprecipitation method was used due to its distinct advantages such as high production rate, small particle size, lower temperatures than conventional ceramic route and low cost of starting material (TEOS used in sol-gel is costly). Since composite exhibits properties as volume fraction of the constituent phases, we can get the advantages of Ni-ferrite as a super-paramagnetic material and Zn-ferrite as a photocatalyst, chemical sensor in the same composite. Nanocomposite synthesized was characterized by XRD for phase identification, morphology by SEM along with structural information, bandgap evaluation using Tauc relation from UV-VIS spectra and FTIR spectra determining the bond co-ordination of the nanocomposite.

2. Experimental procedure

Chemical coprecipitation route was performed to synthesize nanocomposite of Nickel Ferrite-Zinc Ferrite. AR grade Nickel nitrate, Ferric Nitrate, Zinc Nitrate and Ammonium Hydroxide (Merck India) was used as precursors for synthesizing the nanocomposite material. At first hydroxides of Ni, Fe and Zn, Fe were obtained by dissolving the respective nitrate salts in 1:2 molar ratio in double distilled water with constant stirring at about 70-80°C, followed by addition of ammonium hydroxide to obtain the precipitate of respective (Ni,Fe & Zn,Fe) hydroxides. Hydroxides obtained were filtered and dried at 80°C for certain period till all hygroscopic matters were eliminated. The dried respective hydroxide powders were then mixed properly in agate mortar in 1:1 molar ratio. A part of powder was put in DSC-TGA analyzer (Perkin Elmer, Pyris Diamond 480) for thermal analysis and to observe the zone of crystallization. Mixed powders were then put in furnace for heat treatment in air atmosphere at temperatures of 700°C, 750°C for 3, 4 and 5hrs respectively. Phases were determined from the developed powder crytallites by means of X-ray Diffraction (Rigaku, Ultima III Cu K_α of 1.54Å source). The crystallite size was calculated using Scherrer's formula $t=0.9\lambda/\beta\cos\theta$ and plane of orientation was also identified. Morphology was observed by means of HRSEM (Jeol, JSM-6360 Scanning Electron Microscope). FTIR analysis (IR Prestige-21, Shimadzu) was done to observe the vibration and stretching of the required bond formed in the nanocomposite. UV-VIS spectroscopy (Perkin Elmer, Lamda 35) was performed to evaluate the bandgap of the nanocomposite.

3. Results & Discussions
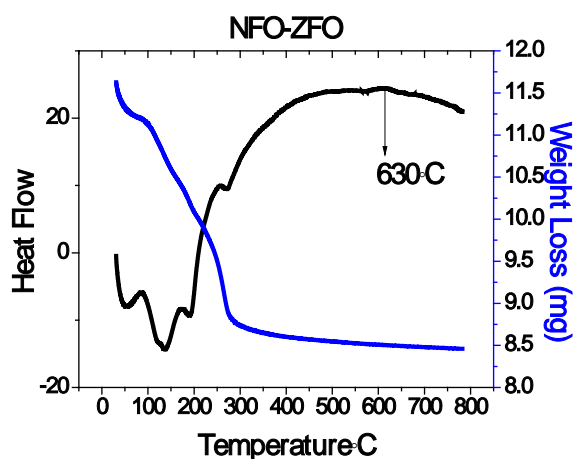
Fig1. DSC-TGA plot of NFO-ZFO for nanocomposite formation

From thermal analysis plot of DSC-TGA (Fig1), it was observed that upto 300°C there was drastic weight loss accompanied with one prominent endothermic trough at about 130°C. After 300°C, weight loss was found to be negligible followed by a broad exothermic hump. Weight loss may be due to loss of water of crystallization and residual ammonium hydroxide used for precipitation to synthesize the nanocomposite. The broad exothermic hump was found to initiate at about 450°C. Broad exothermic peak corresponds to crystallization zone/sintering range for phase development of the required nanocomposite material. Ferrite was found to form at about 630°C. From this thermal analysis, heat treatment schedule was selected to develop the spinel ferrite nanocomposite.

Heat treatment was carried out in air at 700°C, 750°c for 3, 4 and 5 hours for the synthesis of nanocomposite material.
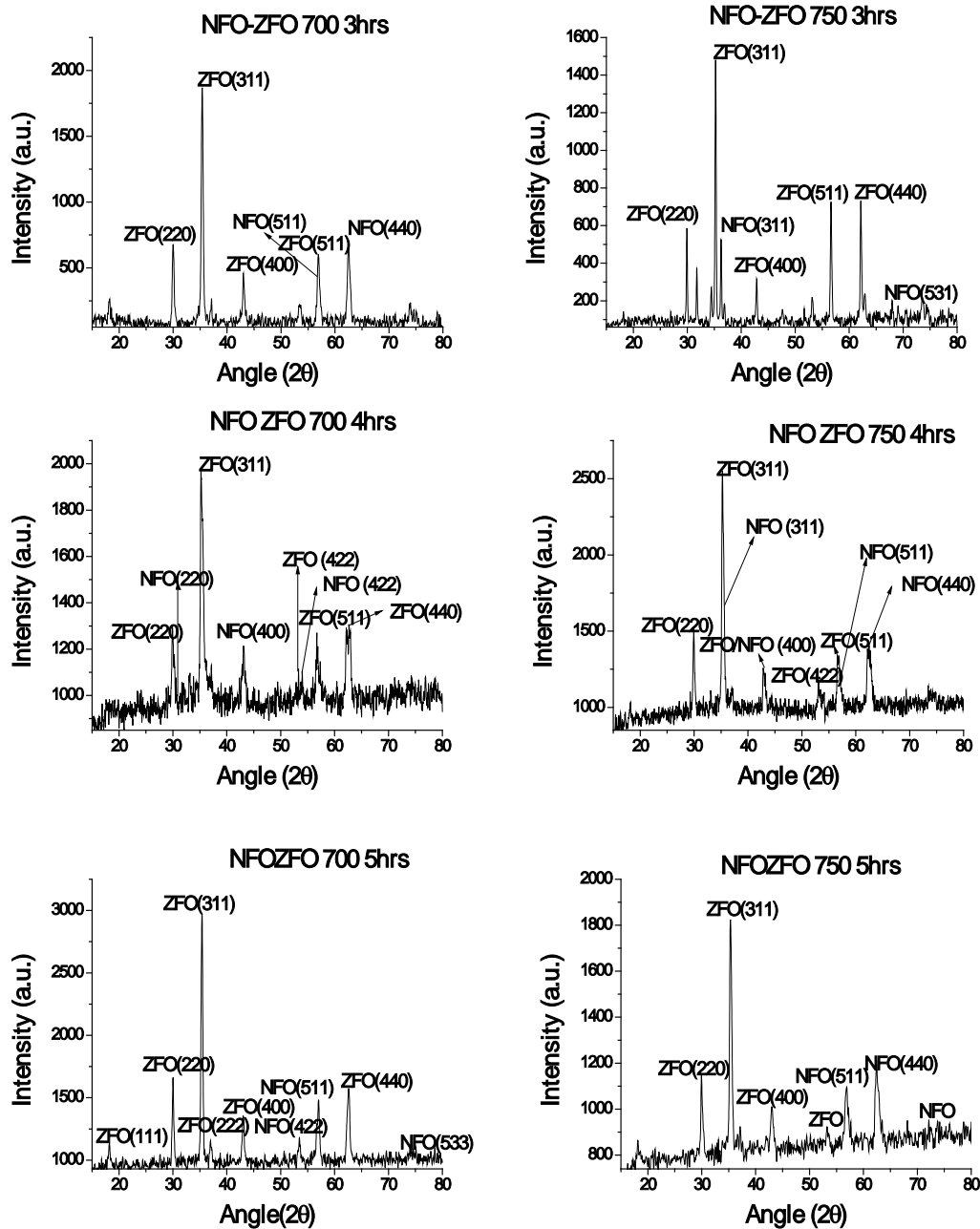
Fig 2. XRD plots of NFO ZFO nanocomposite after heat treatment at 700 and 750 for 3, 4 and 5 hours

The phases developed after heat treatment within the nanocomposite was determined by using XRD (X-ray Diffraction) with Cu Kα source of 1.54A° wavelength (Fig-2). In all the cases, Zinc ferrite (ZFO) spinel was formed within the nanocomposite with highest peak along (311) plane. Crystallite size was measured using Scherrer's formula $t=0.9\lambda/\beta\cos\theta$ for ZFO phase. Crystallite size of ZFO was found to be maximum at 750^0C, 3hrs (among 750 series) and at 700^0C, 4 hrs (among 700 series) having values 44.32nm & 70.6nm respectively. Other prominent peaks of Zinc ferrite were found to be oriented along (220), (400), (511) plane. Inverse-spinel Nickel ferrite was found to be prominent along (311), (440), (220) and (511) plane. Both inverse-normal spinel ferrites with their high intense peak along (311) plane was obtained after heat treatment at 750°C for 3 and 4 hours respectively. Highest crystallite size for nickel ferrite was found to be 70.7nm at 750°C at 4hours soaking period. At 700°C, for 4 hours soaking period treatment leads to formation of both ferrites having closest

crystallite size. A comparative study of nanocomposite samples treated at different temperature, time and evaluation of crystallite size was shown below in Table1.

Table1. Nanocomposite synthesized at different temperatures, soaking period with variation in crystallite size

Sample Name	Heat treatment temperature	Soaking time	Crystallite size (nm) & Planes of orientation
NFOZFO	700	3	29.6 nm for ZFO (311) plane & 65.85 nm for NFO (440) plane
NFOZFO	750	3	44.32 nm for ZFO (311) plane & 55.96 nm for NFO (311) plane
NFOZFO	700	4	70.6 nm for ZFO (311) plane & 69.7 nm for NFO (220) plane
NFOZFO	750	4	35.5 nm for ZFO (311) plane & 70.7 nm for NFO (311) plane
NFOZFO	700	5	23.61 nm for ZFO (311) plane & 23.23 nm for NFO (440) plane
NFOZFO	750	5	20.13nm for ZFO (311) plane & 49.39nm for NFO (440) plane

From the Table-1, it was observed that there were no certain trends for better crystallite growth with the effect of temperature and time of individual ferrites formation.
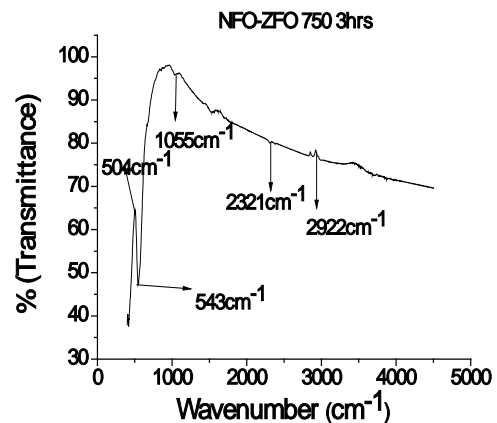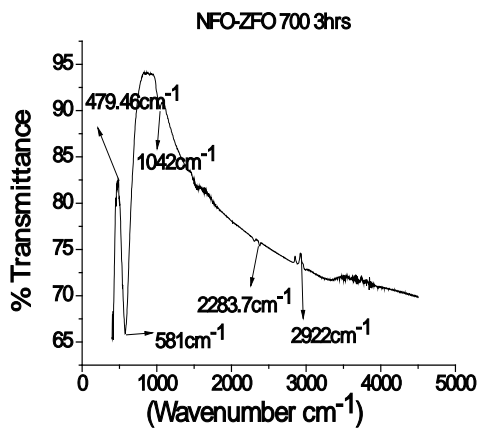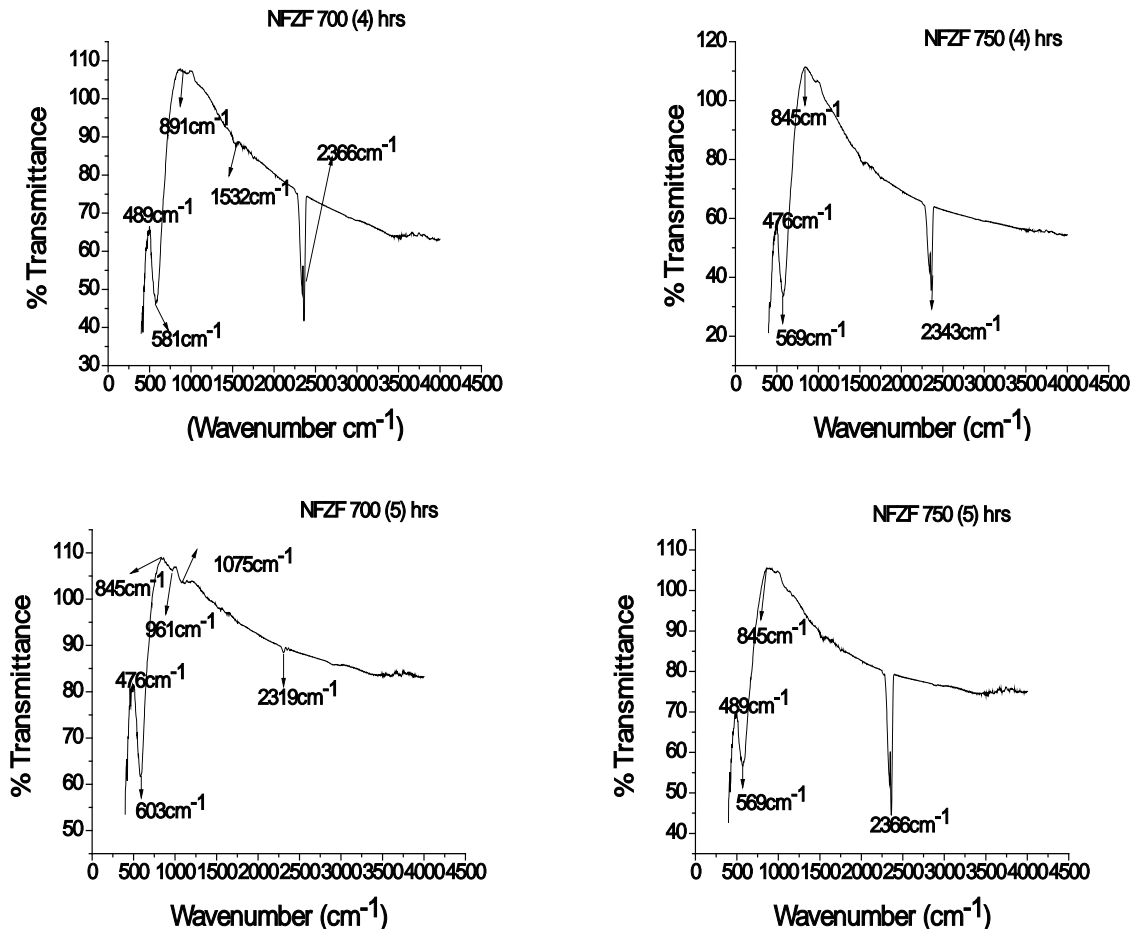
Fig 3 . FTIR spectra plots of NFO ZFO after heat treatment at 700 and 750 for 3, 4 and 5 hours

From FTIR spectra (Fig-3) in transmittance mode, stretching and vibration of bonds for the nanocomposite was observed. Here the mid IR spectra of the samples synthesized at 700°C, 750°C for 4, 5 hours were noted. Frequency bands were found to be sensitive to the co-ordination of cation-anion in octahedral and tetrahedral positions, which were found in the range of 600-540 and 450-400cm^{-1} [4], [5]. In our experiment, absorption bands were observed at about 480cm^{-1} and 569-603cm^{-1}, thus confirming with the results of the previous workers. Hence, proper phase development from XRD study coupled with stretching and vibration of the required bonds as per the co-ordination of cations in octahedral and tetrahedral positions confirm the successful synthesis of nanocomposite of ferrite spinel system.
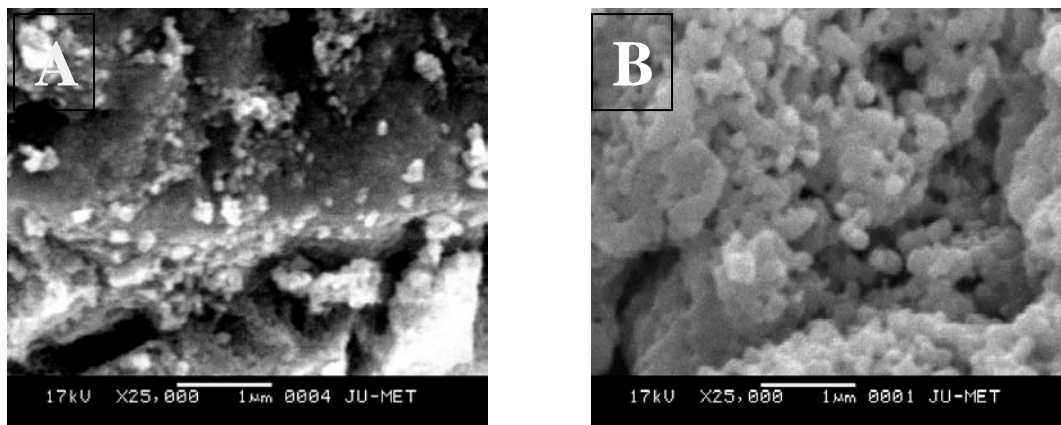
Fig4. Morphology from SEM at 25000X for the nanocomposite of NFO-ZFO synthesized at 700^{0}C, 5 hrs and at 750^{0}C, for 3hrs

Fig-4 shows the Morphology of the prepared nanocomposite studied using SEM (Scanning Electron Microscope) at magnification of 25,000 with 1μ resolution . Powdered samples were coated with Pd in Jeol (JFC-1600 Autofine spin coater) to make it conducting to generate the image properly by backscattered electrons. Interconnected agglomerates were obtained for the prepared nanocomposite sample. Agglomerates were also found to have spherical shape and irregular slightly elongated particulates being dispersed throughout the matrix. Particle sizes of the agglomerates were found to be around 160nm.
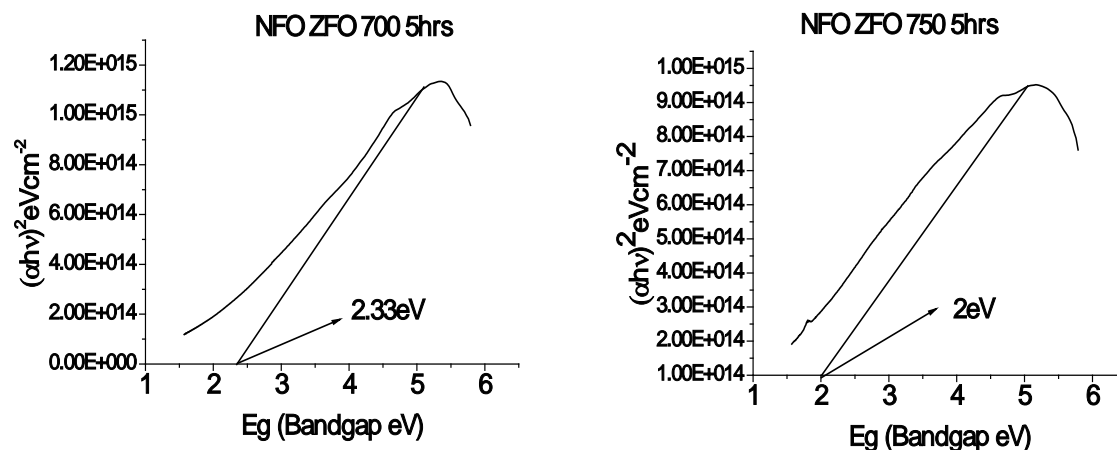
Fig5. Bandgap of the nanocomposites of NFO-ZFO heat treated at 700°C, 750°C for 5hours.

Bandgap of the nanocomposite of inverse spinel-normal spinel Nickel ferrite-Zince ferrite was calculated using Tauc relation [$(\alpha h\nu) = B(h\nu - E_g)^2$] from the UV-VIS spectra (Fig-5) at transmission mode within the scan range of (200-700) nm wavelength. Bandgap evaluated for the nanocomposite (2.33eV for NFO-ZFO 700 5hrs, 2eV for NFO-ZFO 750 5hrs) was found to lie in the energy band transition range for semiconductor materials. Bandgap of nanocrystalline Zinc ferrite was found to be about 2.7eV (Direct Eg) [6], while that of nanocrystalline Nickel ferrite was found to be around 5eV [7]. Thus, the bandgap evaluated was found to be close to direct bandgap of nanocrystalline Zinc ferrite. Thus, the material may have some potential applications in the field of catalysis (i.e. degradation of organic wastes or pollutants from industries, dyes) in the visible range and also applicable to remove iron based pollutant from water bodies using the magnetic property of the material.

3. Conclusions

Nanocomposite of spinel ferrites were synthesized using chemical coprecipitation route. Phase developed were identified by XRD analysis and crystallite size was calculated using Scherrer formula. Crystallite size of ZFO were found to be within 23.6 to 70.6 nm and for NFO 23.23-70.7nm. SEM studies reveal interconnected agglomerates with particle size about 160nm. Bandgap of the nanocomposites of NFO-ZFO were evaluated using Tauc relation and found to be 2eV and 2.33eV for 700^0C, 5hr and 750^0C, 5hr heat treatment. The prepared nanocomposites have bandgap close to semiconductor and can be applied as catalyst for decomposition of complex hydrocarbons; dyes in visible range coupled with removal of iron based polluting species from water bodies.

4. References

[1] A. Chatterjee, D. Das, S.K. Pradhan, and D. Chakraborty, "Synthesis of nanocrystalline Ni-Zn ferrite by the sol-gel method", Journal of Magnetism and Magnetic Materials, Vol.127, pp. 214-218, 1993.

[2] Tania Jahabin, Mansor Hashim, and Khamirul Amin Mantori, "Comparative studies on the structure and electromagnetic properties of Ni-Zn ferrites prepared via co-precipitation and conventional ceramic processing routes", Journal of Magnetism and Magnetic Materials, Vol.322, pp. 2684-2689, 2010.

[3] Shanon A. Morrison, Christopher L. Cahill, Everett E. Carpenter, Scott Calvin, Raja Swaminathan, Michael e. McHenry, and Vincent G. Harris,Journal of Applied Physics, Vol.95,Number 11, pp. 6392-6395, 2004.

[4] Markutty Thomas, and K.C. George, "Infrared and magnetic study of nanophase zinc ferrite", Indian Journal of Pure and Applied Physics, Vol.47, pp. 81-86, 2009.

[5] N.M.Deraz, and A.Alarifi, "Synthesis and Physiochemical properties of Nanomagnetic Zinc Ferrite system", International Journal of Electrochemical Science, Vol.7, pp. 3798-3808, 2012

[6] Zhibin Wu, Masayuki Okuya, and Shoji Kaneko, "Spray pyrolysis deposition of Zinc ferrite films from metal nitrates solutions", Thin Solid Films, Vol.385, pp. 109-114, 2001.

[7] Manish Srivastava, Animesh K. Ojha, S.Chaubey and A.Materny, "Synthesis and optical characterization of nanocrystalline $NiFe_2O_4$ structures", Journal of Alloys and Compounds, Vol.481, pp. 515-519, 2009

Effect of Composition and Sintering Temperature on The Microstructure and Theoretical Density of TiO_2 Stabilized Al_2O_3 Cutting Tool.

Abu Naser Rashid Reza[1,a], Tashneem Ara Islam[2,b],
Md. Fakhrul Islam[3,c], Md. Mohar Ali Bepari[4,d].

[1]Department of Materials and Metallurgical Engineering, BUET, Dhaka.
[2]Post Graduate Student, Department of Bionics, Rhine-Waal University of Applied Science, Germany.
[3]Professor, Department of Glass and Ceramic Engineering, BUET, Dhaka.
[4]Professor, Department of Materials and Metallurgical Engineering, BUET, Dhaka.
[a]amit_buet@yahoo.com,[b]nipun32@yahoo.com,[c]fislam@mme.buet.ac.bd,[d]mohar@mme.buet.ac.bd

Abstract

Cutting tool samples of three different compositions such as 2% TiO_2 -, 5% TiO_2 - and 8% TiO_2 stabilized Al_2O_3 were made by pressing the prepared powder at a pressure of 175-180 MPa and sintered at three different temperatures of 1350^oC, 1400^oC and 1450^oC for 2 hours. The microstructure of the sintered cutting tool samples were studied by scanning electron microscope. The theoretical densities of the prepared cutting tool samples were also studied. It was found that as sintering temperature increases grain size increases for all three compositions of Al_2O_3 cutting tools but with higher % of TiO_2 the extent of grain coarsening decreases. With increasing sintering temperature and higher % TiO_2 content high degree of densification has been achieved. The maximum % theoretical density of 95.18% has been obtained at 1450^oC for 8% TiO_2 stabilized alumina cutting tool.

Keywords: TiO_2, Nano-scale Al_2O_3, Microstructure, Pinning effect, Ceramic tool materials.

1. Introduction

Alumina base ceramic cutting tool is one of the most wide used cutting tool [1] materials in the industrial levels. The reason behind is, it contains good physical properties such as high hardness [2] and good wear resistance [3]. It also contains good chemical properties such as high melting point and excellent chemical stability. They are more stable than high-speed steels and carbides, thus having fewer tendencies to adhere to metals during machining and less tendency to form built-up edge. This results in good surface finish and dimensional accuracy in machining steels.

These properties of alumina materials are mainly related to the density and microstructures. Highly dense and fine grained structures provide the best mechanical properties [4]. Ceramic cutting tools should have % theoretical density more than 90% for good performance. In order to achieve high density, alumina has to be sintered over 1600-1700^oC. But highly dense and fine grain microstructure can also be achieved if alumina is stabilized with other materials such as TiC, ZrO_2, TiB_2, SiC, NbC etc in lower temperature than conventional sintering temperature. Likewise this, an attempt has been made to produce Al_2O_3 ceramic cutting tool of highly dense and fine grained microstructure, stabilizing it with different composition of TiO_2 at lower temperatures.

2. Experimental

Samples were prepared from commercial alpha Al_2O_3 powder [~40nm; purity: 99.87%] mixed with 2, 5 & 8 weight% TiO_2 [~40nm; purity: 99.9%] by the conventional ceramic processing technique. Powders were at first weighted in electronic weighted balance. Raw materials were then ball-milled at 150 rpm for 18~20 hours in acetone medium in presence of zirconia balls. After proper mixing, extraction of the powder was done with the help of acetone. The wet powder was kept in the oven at 110-120^oC for 24 hours to dry out. A binder was made with PVA (Poly vinyl alcohol) and water (10gm in 100 ml) in 100^{0}C with continuous stirring. After drying out of the raw powder mix, 5~8% PVA binder was mixed with the powder before compaction. Cutting tool samples

were prepared using the pressure of 175-180MPa and 2 minutes holding, using a uniaxial hydraulic or mechanical press. The prepared samples were around 13 mm in diameter and 2 mm thick. These green samples were again dried for one day at 110^0C. After that, the samples were taken for sintering. Sintering was done in a single stage sintering process. Samples were placed in the furnace and the temperature was raised very slowly (3^oC/min) in order to avoid crack formation. Binder was removed by holding the samples at 500^oC for 1 hr and then temperature was again raised slowly to the desired sintering temperature and held at that temperature for 2 hours for all three composition of Al_2O_3- TiO_2. For every composition of Al_2O_3 and TiO_2 (2, 5 and 8%) sintering were done for three different temperatures respectively (1350^0C, 1400^0C and 1450^oC). Finally upon completion of sintering process, percent theoretical densities were calculated. It was done after the measurement of the density with precision electronic balance and slide calipers. Microstructure observation along with grain sizes measurement was also done using SEM (Scanning Electron Microscope).

3. Result and Discussions
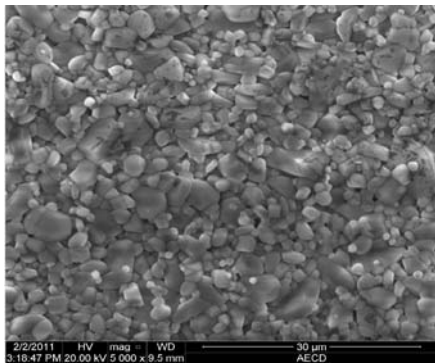
Fig.1. SEM of 2% TiO_2-98% Al_2O_3 sintered at 1350^0C 1400^0C   (5000X)
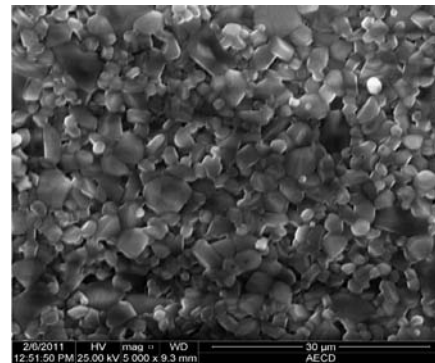
Fig.2. SEM of 2% TiO_2-98% Al_2O_3 sintered at (5000X)
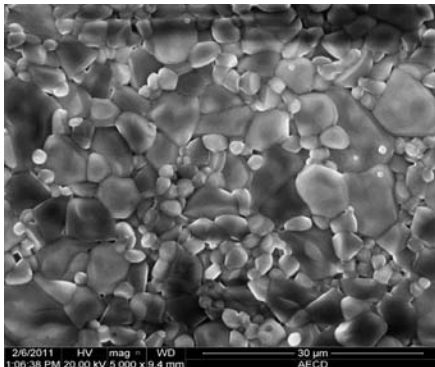
Fig.3. SEM of 2% TiO_2-98% Al_2O_3 sintered at 1450^0C 1350^0C
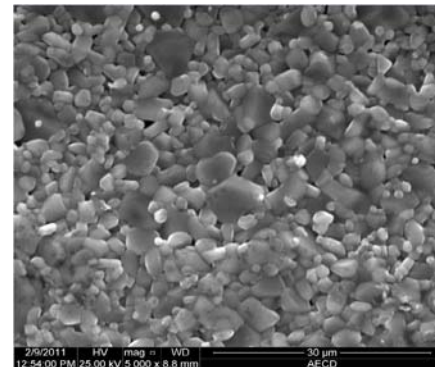
(5000 X)

Fig.4. SEM of 5% TiO_2-95% Al_2O_3 sintered at
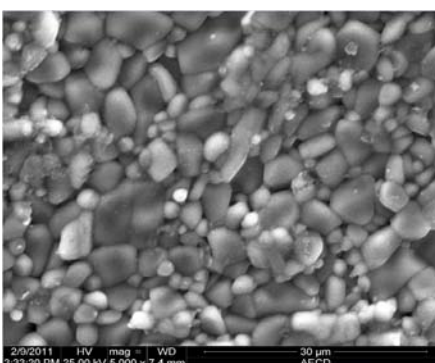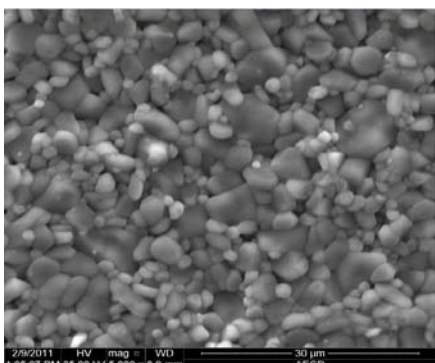
(5000 X)

Fig.5. SEM of 5% TiO_2-95% Al_2O_3 sintered at 1400^0C 1450^0C (5000X)
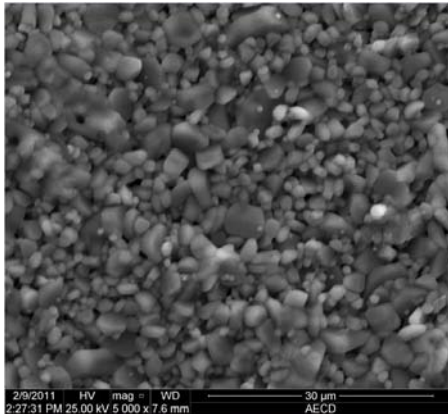
Fig.6. SEM of 5% TiO_2-95% Al_2O_3 sintered at (5000X)
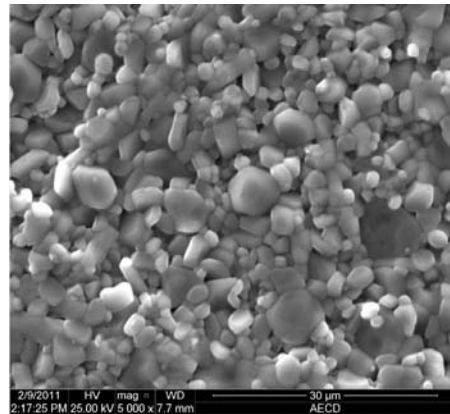
Fig.7. SEM of 8% TiO_2-92% Al_2O_3 sintered at 1350^0C 1400^0C
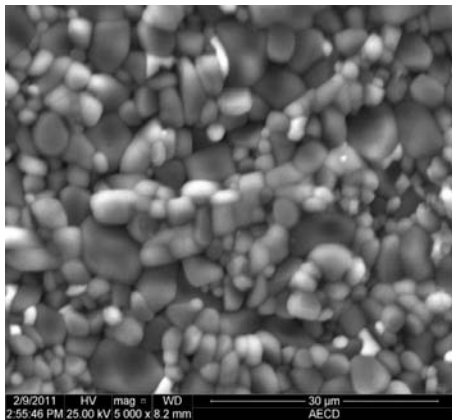
(5000X)

Fig.8. SEM of 8% TiO_2-92% Al_2O_3 sintered at
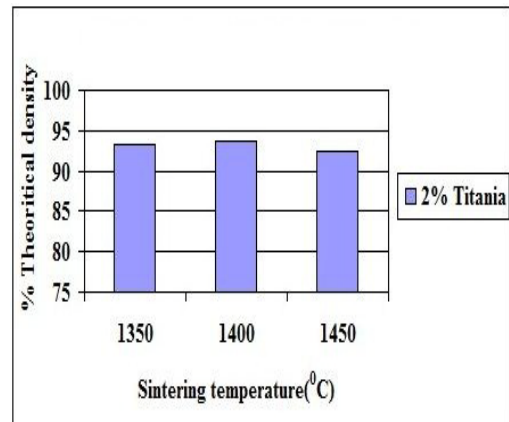
(5000X)

Fig.9. SEM of 8% TiO_2-92% Al_2O_3 sintered at 1450^0C density (5000X)

Fig.10. Sintering temperature vs. % theoretical of 2% TiO_2 stabilized Al_2O_3
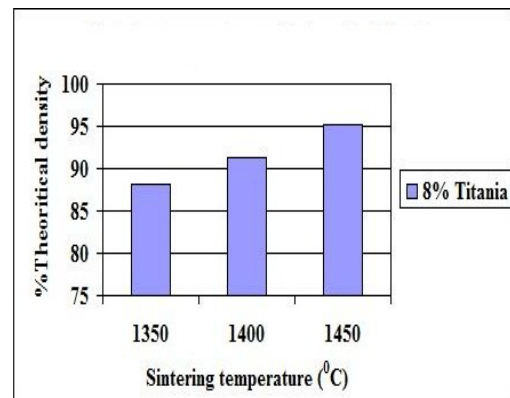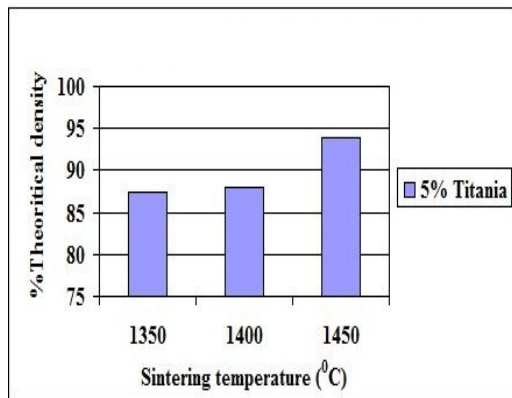
Fig.11. Sintering temperature vs. % theoretical density of 5% TiO_2 stabilized Al_2O_3

Fig.12. Sintering temperature vs. % theoretical density of 8% TiO_2 stabilized Al_2O_3

From the microstructural study it was found that grain structures of the Al_2O_3 cutting tool samples were different due to the effect of different % TiO_2 and variable sintering temperature. Usually, grain coarsening or exaggerated grain growth occurs in Al_2O_3 with increase in sintering temperature. But in the presence of little amount of TiO_2, sufficient pinning [5] effect can be generated which can successfully inhibit grain coarsening to a useful degree. TiO_2 act as grain growth inhibitor and stops Al_2O_3 grain growth. So increase in %TiO_2 in Al_2O_3 has a prompt effect on Al_2O_3 grain structures. It is quite evident from the microstructures that are shown here. From figures 1-3 it was showed that, with increase in sintering temperature from 1350-1450^{0}C, gradual grain coarsening of Al_2O_3 occurred in a normal way for 2%TiO_2. The grain sizes were 2.1µm, 2.35µm and 3.81µm respectively. So 2% TiO_2 cutting tool samples showed very negligible pinning effect on Al_2O_3. From figures 4-6 it was observed, that the grain sizes of Al_2O_3 were 2.42µm, 2.97µm and 2.98µm for 5% TiO_2 stabilized Al_2O_3. Though the grain coarsening occurred here as well but compared to the grain coarsening of 2% TiO_2, rate of grain coarsening of 5% TiO_2 composition was less and slow. In a similar way, (figures 7-9) for 8% TiO_2 stabilized Al_2O_3, the grain sizes of Al_2O_3 were found 2.39µm, 2.82µm and 2.84µm respectively. In this case the grain coarsening rate was much more slower compared to 2% and 5% TiO_2 stabilized Al_2O_3. So very fine grain microstructure was achieved as the % TiO_2 increased up to 8%.

With the increase of % TiO_2 and temperature, higher degree of densification was achieved in Al_2O_3. From figure 10 it was found that at low %TiO_2 (2%), the density at first started to increase then drops at higher temperature. With the increase in temperature though compaction of the TiO_2 - Al_2O_3 samples occurs but due to grain coarsening as it was showed in figures 1-3 the density drops at higher temperature. As percentage of TiO_2 is very small it could not provide sufficient pinning effect during densification process. But it was observed in figures 11 and 12 the density gradually increased as the %TiO_2 increases from 5% to 8% with increasing temperature. TiO_2 provides pinning effect which inhibits grain coarsening of Al_2O_3 at higher sintering temperature and helps to achieve high degree of densification [6-7]. It was seen that 8% TiO_2 stabilized Al_2O_3 cutting tools sintered at 1450^{0}C showed maximum theoretical density of 95.18%.It was also found that from the figures 10-12 an average % theoretical density about 91.5% was achieved.

4. Conclusion

The main purpose of TiO_2 addition in Al_2O_3 ceramic cutting tool is to achieve high degree of densification at relatively lower temperature. The average theoretical density for all the composition is 91.5% and maximum theoretical density of 95.18% was observed for 8% TiO_2 stabilized Al_2O_3 at 1450^{0}C temperature. The grain coarsening inhibition and densification were occurred due to the pining effect of TiO_2 in Al_2O_3. So with the addition of the higher percent of TiO_2 in Al_2O_3, highly dense and fine grained Al_2O_3 can be produce at relatively lower temperature.

5. Acknowledgement

6. References

[1] Sidney H. Avner, "Introduction to Physical Metallurgy", Ch. 10 in Tool Steel. McGraw-Hill Book Company, New York, 1974.
[2] A. Krell, "Grain Size Dependence of Hardness in Dense Submicrometer Alumina," J. Am.Ceram. Soc, 78 [4] 1118–20(1995).
[3] A. Krell, "Improved Hardness and Hierarchic Influences on Wear in Submicron Sintered Alumina," Mater. Sci .Eng. A, 209 [1–2] 156–63 (1996).
[4] Fei Xiong, Rafael R. Manory, Liam Ward, and Mircea Terheci, "Effect of Grain Size and Test Configuration on the Wear Behavior of Alumina" *J. Am.Ceram. Soc.,* 80 [5] 1310–12 (1997)
[5] W. J.Smothers and H. J Reynolds, "Sintering and Grain Growth of Alumina" J. Amer. Ceram. SOC.,Vol. 37, No.12.
[6] H. N. Baumann, Jr., and R. C. Benner, "Alumina Solid Solution," U. S. Pat2,418,496, April 8, 1947.
[7] W. D. McKee, Jr., and Eugene Aleshin, "Aluminum Oxide- Titanium Oxide Solid Solution," J. Amer. Ceram. SOC.46[l] 54-58 (1963).

Corrosion of Galvanized Steel and its Substitutes in Various Environments

M.Merajul Haque, S.Alam Limon, M.Moniruzzaman and Md.Mohar Ali Bepari
Department of Materials and Metallurgical Engineering   Bangladesh University
of Engineering and Technology, Dhaka-1000, Bangladesh.
E-mail: haque_meraj@yahoo.com

Abstract

Corrosion test of galvanized steel has been carried out in three different aqueous environments (NaCl solution, sea water and rain water) by weight loss measurement technique by exposing them from one to five days in the selected environment. Corrosion rate is measured in mdd (milligram/decimeter^2/day) units. Aluminium and copper is considered as a possible alternative of galvanized steel. Aluminium and copper is treated in same manner for substitution of galvanized steel. Corrosion characteristics of the corroded samples are also investigated by XRD, XRF and SEM analysis to understand the corroded surface morphologies. Copper is better than galvanized steel in NaCl and rain water environments. On the contrary, Aluminium can be easily used as a substitute material for galvanized steel in industrial structure (Roofing sheets) and water distribution system considering all these aqueous environment. Aluminium is better corrosion resistant than galvanized steel in liquid environments. So, aluminium can use as a substitute material for galvanized steel in industrial structure (Roofing sheets) and water distribution system considering these entire aqueous environments.

Key words: *Corrosion rate (mdd), NaCl solution, Sea water, rain water.*

1. Introduction

Galvanized steel is used in aqueous environments in many indoor and outdoor applications. Galvanized steel is widely used in applications where rust resistance is needed. Galvanized steel is also used in underground pipeline under sea water, frames to build houses and several household appliances. On the contrary, aluminium is used in buildings for a wide spectrum of applications, rainwater goods and replacement windows. Copper tube is the highest quality material available today for a variety of building applications including plumbing, fire sprinklers and harsh marine environments such as petroleum pipelines. For many years a lot of research work has been carried out all over the world. In one study, it has been found that Al is very low resistant to the corrosive environment(3%NaCl) in static regime and corrosion processes onto the Al surface take place[1].

In another study, the effect of rain on Al alloy and galvanized steel roofing sheets was studied as well as their relative corrosion resistance [2]. The corrosion behavior of the pure Al after different immersion intervals in 3.5% NaCl solutions was also carried out and it indicates that the corrosion rate of Al is decreased with increasing immersion time due to the growing thickness of the corrosion product [3]. On the other hand, American Galvanizers Association (AGA) conducted tests of corrosion of galvanized steel in water collected from marine environments all over USA and it has been found that soft water, tropical sea water, high oxygen content causes higher corrosion in Zinc coating of galvanized steel [4]. In another study of copper the experimental determined that the weight loss of copper due to NaCl effect is significantly less than that of atmospheric condition by 0.002g[5]. In Bangladesh, roofing system in maximum houses of rural areas and few houses of urban areas involve using galvanized steel sheet. Usage of Cu and Al is very few as roofing sheet. Using of galvanized steel or substituting it with Al or Cu as roofing sheet or in plumbing applications is another field of interest in this research work. In this research paper, corrosion behavior of galvanized steel, Al and Cu has been investigated in three different types of aqueous environments.

2. Experimental Details

Galvanized steel sheet as well as the Al and Cu sheet of 4.5×2.0 cm size was taken as a main substrate and substitute substrate respectively. All the substrates were cut from the main sheet by hand shear cutting machine. The thickness of all substrates was 0.4mm. Area [A(decimeter^2)] of all the substrates was measured by slide calipars. All the substrates were cleaned with detergent, washed with acetone and dried. Initial weight [w_i(miligram)] of all the substrates were measured using electronic weighing balance machine. All the conditions were measured between 25^0C to 28^0C. After that all substrates were immersed in liquid environments (NaCl solution, Sea water and Rain water) respectively. For every liquid environment; five samples were dipped in five beakers containing the liquid and kept for 1,2,3,4 and 5 days (T) respectively. Then all the substrates were cleaned again with detergent, washed with acetone and dried. Finally, all the substrates final weight [w_f (miligram)] were measured. The weight loss is determined as difference between the initial and final losses after removal of the corrosion product by using electronic measuring device and hence calculation is used to measure the corrosion rate. CORROSION RATE= $\frac{Wi-Wf}{T*A}$; this formula is used to calculate corrosion rate. Corroded surface characteristics were observed using different types of test. XRD (X-ray diffractometer), XRF(x-ray fluorescence) test was undertaken. Finally, Scanning electron microscope (SEM) was employed to inspect the surface morphology of the base and corroded samples.

3. Results and Discussion

3.1 Corrosive Environment: NaCl Solution

Galvanized steel exposed to NaCl solution shows decreasing corrosion rate with increasing exposed time. The value of corrosion rate or mdd for Al sample in NaCl environment is much lower than Galvanized steel. Al also shows decreasing corrosion rate with increasing exposed time [fig.1]. Chlorides are severely corrosive to zinc. So initially corrosion rate was high. As most of the zinc corrodes early; decreasing its concentration with time, decreases corrosion rate.

In the XRD pattern Zinc and chloride peaks were found [fig .2]. In XRF test , the amount of Zn (47.14%). So some Zn coating corrodes leaving behind residue in the beaker and also exposed Fe (32.25%) of the sample . Chlorides are severely corrosive to Al as its reactivity is high . So initially corrosion rate was high. As most of the Al corrodes early; decreasing its concentration with time, decreases corrosion rate. The XRD pattern [fig.3] of corroded sample shows only Al peak and a little disturbance or deviation from the standard one.

XRF indicates that Al (62%) whereas O (36.71%) and also some other impurities in minor amounts. O_2 and CO_2 come from distilled water [6] which forms protective film of aluminium oxide to resist further corrosion . Chlorides ions are very aggressive ions to copper and its alloys due to the tendency of the chloride ion to form an unstable film (CuCl)and soluble chloride complexes($CuCl_2^-$ and $CuCl_3^{2}$)[7].The formation of this CuCl film does not protect copper from dissolution in the chloride media. So initially corrosion rate was high. As most of the copper corrodes early; decreasing its concentration with time, decreases corrosion rate.

In Cu-O-H system, Cu and CuO_2 are the only stable solid phases if the fugacity of molecular hydrogen is maintained at a very low level. The XRD pattern shows[fig.5] the presence of Cu peak and CuO_2 peak. Maximum intensity for Cu occurs at ($2\theta=43^0$) and for CuO_2 it occurs at ($2\theta=36^0$).The ultimate reaction product on exposure of Cu to water is Copper hydroxide which is not well characterized using X-ray diffraction. Cupric ion (Cu^{2+}) is the most important state and is the oxidation state generally encountered in water and that's why copper oxide peak has found. So the corrosion product in NaCl solution is copper oxide. The reaction is given below:-

$$Cu+OH^-{\rightarrow}Cu(OH)(ads)+e+$$
$$Cu+OH(ads) \rightarrow CuO_2+H_2O$$
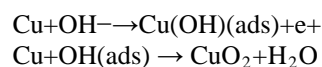
XRF test indicates Cu(97.9194%) and Na(1.3692%),Cl(0.36345%).No free O found as it forms compound(CuO_2).
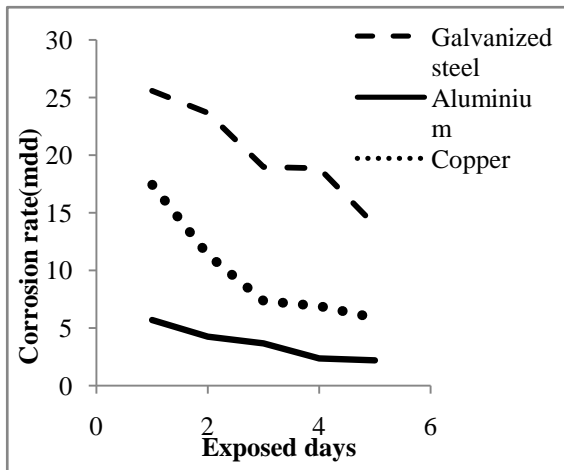
Figure 1. Corrosion rate vs exposed days   **Figure 2.**XRD analysis of Galvanized steel
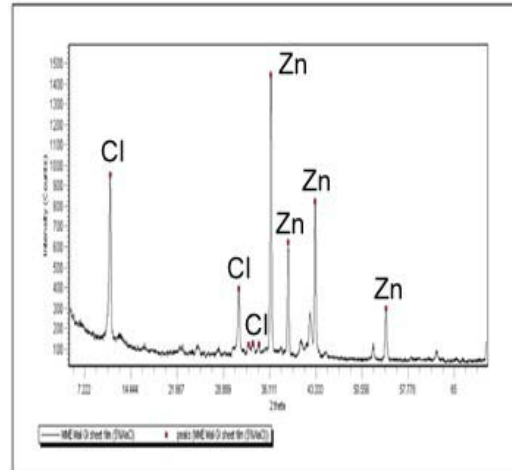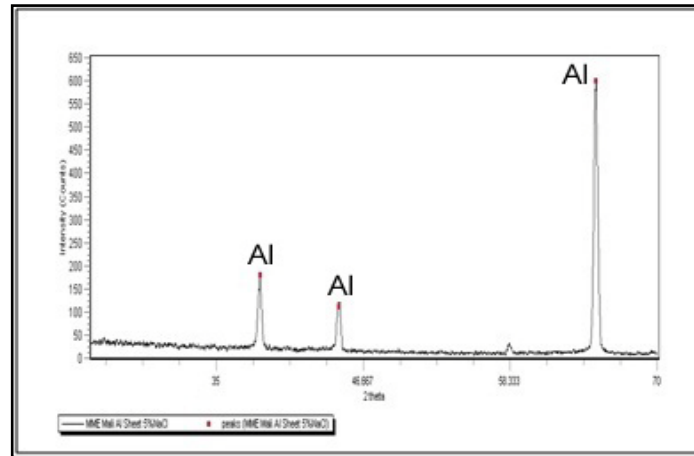
Figure 3.XRD analysis of Aluminium

3.2 Corrosive Environment: Sea Water

Sea water is high in salt content in the form of various chlorides and often sulfide is also detrimental [8]. It is a good electrolyte and corrosion is affected by oxygen content, temperature and biological organisms but it also contains carbonates. Carbonates form protective film on Zn surface . It also forms protective film on Al [8]. So corrosion rate in sea water is much lesser than NaCl solution in both samples[fig.4]. The presence of Ca and Mg ions also inhibits corrosion in the sea water because they form protective flim of carbonates .

XRD test of the galvanized steel sample ensures several peaks of Zn like in NaCl environment whereas XRD test of Al shows only Al peaks [fig.3]. XRF test of that sample ensures Zn (82.43%) so lesser amount of Zn corrodes than NaCl solution and exposed Fe (14.13%). For Al, XRF indicates Al (85.23%) and O (13.58%). Although corrosion curve in sea water shows increasing trend the value of mdd or corrosion rate is much lower. Corrosion of pure copper to sea water is believed to occur according to the following reaction:

Anodic reaction: $Cu \longrightarrow Cu^+ + e^-$

Cathodic reaction: $O_2 + 2H_2O + 4e^- \longrightarrow 4OH^-$
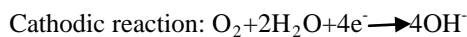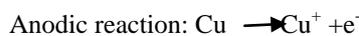
Followed by the formation of cuprous complex,

$$Cu^+ + 2Cl^- \longrightarrow CuCl_2^-$$
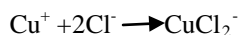
Then cuprous oxide will be formed as:

$$CuCl_2^- + OH^- \longrightarrow CuO_2 + H_2O + Cl^-$$

According to the above equations the movement of O_2, OH^-, Cu^+ and $CuCl_2$ to and from the corroding surfaces will control the corrosion of Cu[10]. According to the mixed potential theory, increased transport of Cl^- or $CuCl_2$ to and from the surface will accelerate the anodic reaction, while the increase of O_2 transport will increase the cathodic reaction, so that corrosion rate will increase[fig.4] and vice versa.

The XRD pattern shows several number of CuO_2 peak [fig.5] whereas some Cu peak. Stable corrosion product(CuO_2) confirmed by XRD built up in the surface and reduce the mass transfer of O_2 and other agents to the metal surface resulting in the reduction of the kinetic of the cathodic reactions. Therefore, the increase in the corrosion product thickness decreases the corrosion rate.XRF test indicates Cu(99.3972%) and Cl(0.3970%) and no free O element as it forms stable CuO_2 compound.
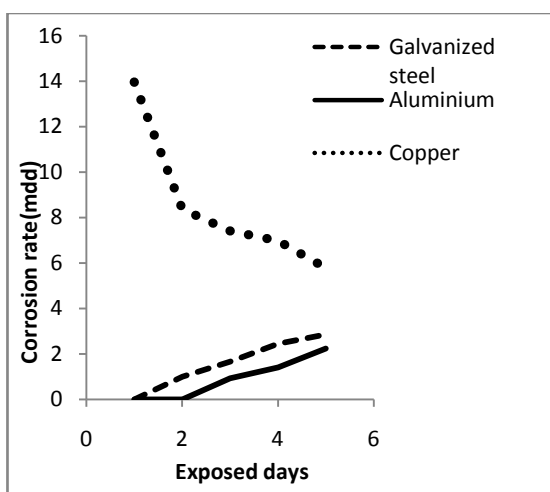
Figure 4. Corrosion rate vs exposed days
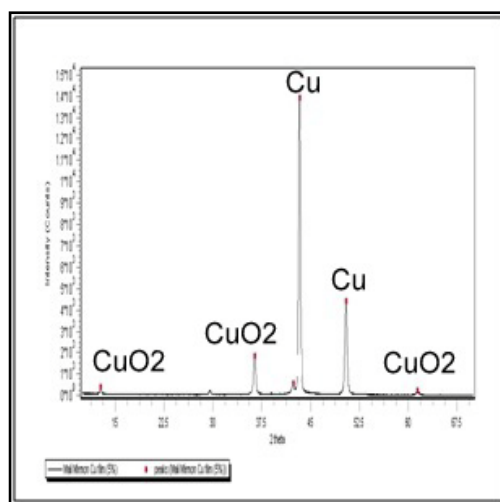
Figure 5.XRD analysis of Copper

3.3 Corrosive Environment: Rain Water

Rain water causes higher corrosion than that of the sea water. Rain water falls through atmosphere so it collects oxygen gas from atmosphere and dissolved in rain water which increases corrosion rate. The rain water is collected from Dhaka city. As the pollution is high in the Dhaka city, the rain is acidic in nature i.e. acid rain . So, corrosion rate is high. In the case of galvanized steel initially the amount of reactants is high but with increasing exposed day its amount decreases so inhibits corrosion rate[fig.6]. XRD test [fig. 7] ensures several peaks of Zn.

The XRD pattern shows more disturbance because of the formation of amorphous phase on the surface. The amorphous phase is Simonkollite [$Zn_5(OH)_8Cl_2.H_2O$]. XRF test ensures Zn (77.01%) so more Zn corrodes than sea water and exposed Fe is (12.33%).In the case of Al corrosion rate increases [fig6] but the mdd values are very small. XRD shows only Al peak like that of NaCl solution and XRF indicates less aluminium deterioration (aluminium is 98.8% in corroded sample). Rain water causes higher corrosion. The XRD (Figure12.) pattern shows only Cu peak and no peak for stable compound CuO_2 .As a result with increasing time the rate of corrosion is increased. XRF test indicates Cu(99.6441%) and Cl (0.1127%) although the value of mdd is lower than that of sea water.
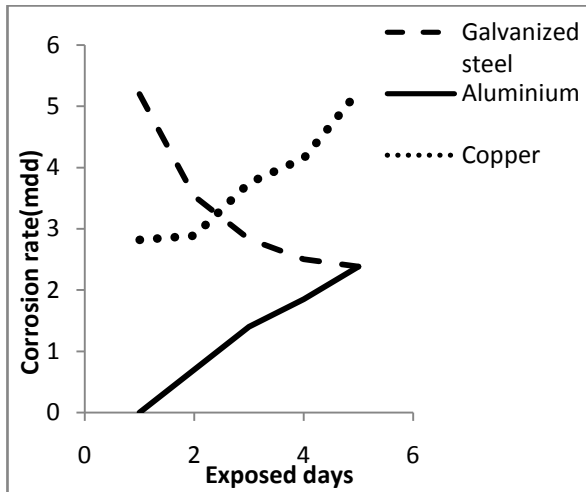
Figure 6. Corrosion rate vs exposed days
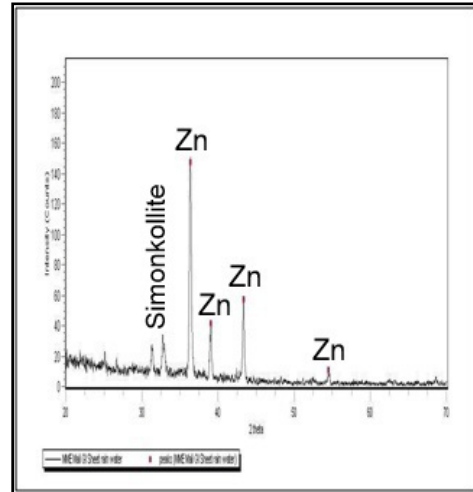
Figure 7. XRD analysis of galvanized steel

3.4 SEM Analysis for surface Morphology

SEM image of corroded galvanized steel sample is shown in figure 8. The sample was exposed five days in corrosive environment. The SEM image of sample immersed in NaCl solution shows some white corrosion product or nodules which are randomly arranged over the corroded surface to inhibit corrosion so corrosion rate decreased and also shows a separate layer on the surface. SEM image of corroded Al sample is shown in figure 9. These samples were also exposed five days in corrosive environments. This SEM shows corrosion product embedding on the surface which inhibits further corrosion of Al sample in these environment. Corrosion products wedging action causes the propagation of exfoliation attack [11] which increases the corrosion rate as time goes or number of days increased. The SEM image of the corroded copper sample is shown in figure 10. It shows numerous or several point defects or holes which are randomly distributed over the entire surface due to corrosion and some regions are not affected due to the formation of corrosion product (CuO_2).

Figure 8. SEM of Galvanized Steel   **Figure 9.** SEM of Aluminium   **Figure10.** SEM of Copper

5. Conclusion

Corrosion test of Galvanized steel, aluminium and copper has been conducted. Compositional variation, corroded surface characteristics and surface morphology has been studied. Based on the experimental results and analysis, the following conclusions have been drawn:

1. The highest corrosion rate is found for galvanized steel (25.59) in NaCl environment whereas lowest value found in sea water (0).

2. Aluminium is the best material among the three considering all these aqueous environments.

3. Copper is better than galvanized steel only in NaCl solution and in rain water environments.

4. Corroded samples shows mainly small white nodules of corroded product ,corrosion products embedded on the surface and numerous point defects, holes randomly orientated for galvanized steel ,Al and Cu samples respectively.

6. References

[1]   Petrica hagioglu, Constantin gheorghies, Alina mihaela cantaragiu and Strul moisa :"The Accelerated Corrosion Behaviour in Saline Environments of Some Samples Made of Tombac, Copper and Aluminium*" Journal of Science and Arts-Year* 20, No. 1(12),pp. 153-160, 2010.

[2]   Bala isah abdulkarim1, Yusuf ahmed Abdullah and Kamoru adio salam:"Corrosion Resistance of Commercial Roofing Sheets to Acid Rain Water in Eleme, Rivers, Nigeria*" International Journal of ChemTech Research-*Vol.1, No.4, pp 802-806*.*

[3]   El-Sayed M. Sherif ,A. A. Almajid , Fahamsyah Hamdan Latif and Harri Junaedi :" Effects of Graphite on the Corrosion Behavior of Aluminum-Graphite Composite in Sodium Chloride Solutions*" Int. J. Electrochem. Sci-* 6 (2011) 1085 – 1099.

[4]   "American Galvanizers Association"

   http://www.galvanizeit.org/about-hot-dip-galvanizing/how-long-does-hdg-last/in-water

[5]   Abdul maruf, S. and Dajab, D.D:"Corrosion Behavior of Copper Immersed in Different Environment*" Materials society of Nigeria(MSN)Zaria Chapter Book of Proceedings*,3rd Edition,2007.

 [6]   T.E.Larson:"Corrosion by Domestic Waters" isws-75-bul59 bulletin 59 state of Illinois department of registration and education.

[7]   Zhang Peng, Guo Bin1, Jin Yong-ping and Cheng Shu-Kang:" Corrosion Characteristics of Copper in Magnetized Sea Water"*Trans.Nonferrous Met.Soc.China*1792007)s189-s193.

[8]   http://www.Proceedings_of_the_indian_academy_of_sciences__vol33b(2)"_92-99_2 .

[9]   W. B. Wan nik1, o. Sulaiman, a. Fadhli and r. Rosliza :" Corrosion Behaviour of Aluminum Alloy in Seawater" *the international conference on marine technology*,11-12 december 2010, buet, dhaka, bangladesh.

[10] A.M.Nagiub:''Evaluation of Corrosion Behaviour of Copper in Chloride Media Using EIS*"Portugaliae Electrochimica Acta* 22(2005)301-314.

[11] "Aluminium and corrosion"- UK Aluminium Industry Fact Sheet 2-by Aluminium federation.

[12]   Fontana, M.G. (1967), "Corrosion Engineering" 2nd edition Mc-Graw-Hill Books, New York, pp.2-2.

Studies on the Mechanical Properties of Woven Jute Fabric Reinforced Poly(L-Lactic Acid) Composites

G. M. Arifuzzaman Khan[1], M. A. Gafur[2] and Md. Shamsul Alam[1]

[1]Department of Applied Chemistry and Chemical Technology, Islamic University, Kushtia-7003, Bangladesh
[2]PP and PDC Division, BCSIR, Dhaka, Bangladesh
E-mail: gm_arifuzzaman@yahoo.com or arif@acct.iu.ac.bd

Abstract

The plain woven jute fabric reinforced poly(L-lactic acid) (PLLA) composites were prepared by hot press molding method and their mechanical properties i.e. tensile, flexural and impact properties were investigated. The average tensile strength (TS), tensile modulus (TM), flexural strength (FS), flexural modulus (FM), and impact strength (IS) of untreated woven jute composite in warp direction of untreated woven fabric composite were about103, 211, 95.2, 42.4 and 85.9%, respectively better compared to unreinforced PLLA and strain at maximum tensile stress for composite samples was enhanced 11.7%. It was found that the strengths and modulus of composites in warp direction is higher than weft direction. Woven jute fabric composites in both directions presented superior mechanical properties than non woven fabric composite. Chemical treatment of jute fabric through benzoylation showed positive effect on the properties of composites. Morphological studies by SEM demonstrated that better adhesion between the treated fabric and PLLA was achieved.

Keywords: Woven jute fabric, PLLA, jute modification, mechanical properties.

1. Introduction

Woven fabrics have received extensive study as reinforcements since they provide acceptable mechanical properties, simple processing and conformability for advanced structural applications [1]. Woven fabric composites recommend more balanced properties than unidirectional laminas. The weaving of the fiber gives an interlocking that increases strength higher than fiber-matrix binding strength. Since fibers are attached together tightly in woven fabrics, pull-out is quite impossible, consequently need more strength to breakdown the fabric reinforced composites [2]. Very few reports on woven fabric composites have found so far. Sapuan et al. [3] investigated the mechanical properties of woven banana fiber reinforced with epoxy composites. The tensile stress was found greater in X-direction (warp) than Y-direction (weft). Weaving patterns such as plain, twill, satin, basket, leno etc. are crucial factor in determining the response of the composites [4]. The properties of plain woven fabric reinforced polymer composites were found to have tremendous potential for improving the performance of composite structures due to longer stability, high porosity, symmetrical properties and low manufacturing cost of plain woven fabric. Lai et al. [5] studied betel palm woven hybrid composite characteristics and testing features. They found the mechanical properties of the woven composites made from alkali treated fibers were superior to the untreated fibers. However, Jacob et al. established that tensile strength and tensile modulus of sisal fabric reinforced natural rubber composites were decreased with chemical modifications (mercerization and silanation) [6]. Therefore, the good adhesion between fiber and matrix give better mechanical strength in natural fiber/fabric reinforced composites which depend not only on fiber modification but also nature of matrix.

Recent research efforts are being harnessed in developing a new class of fully biodegradable composites (biocomposites) by combining natural fabric with biodegradable polymer [7]. The main advantages of the use of biocomposites that they are environmentally friendly, fully degradable and sustainable. A large number of these biodegradable polymers are commercially available such as PHA-polyhydroxyalkanoate, PLLA-poly(L-lactic acid), PCL-polycaprolactone, PEA-polyesteramide etc. In the class of biodegradable polymers, PLLA appears to be one of the most attractive materials in the structural and packaging industries because of its facile

availability, good biodegradability and high mechanical properties [8]. PLLA is a strong competitor in the plastics market having similar properties to PET which make it suitable for the food packaging sector.

In the present study, plain woven jute fabric reinforced PLLA composites is subjected for mechanical test include the tensile, flexural and impact properties. The effects of chemical treatment (benzoylation) of fabric on the properties of composite have also been investigated.

2. Materials and Methods

The PLLA polymer used in this study was synthesized in melt polycondensation methods having molecular weight above 110000g.mol^{-1}. Jute fabrics used as the form of a plain woven mat of weight basis (~200g.m^{-2}) and raw jute (unidirectional mat) were collected from local market of Jhenidha, Bangladesh.

The PLLA was converted into film approximately 0.2-0.3mm in thickness using a hot press moulding machine. Mould was kept 10min at 180°C thereafter it was cooled by tap water. A square woven mat of (15×15)cm^2 in dimensions and the average mass of this was 2.0g was cut and dried in an oven at 60°C for 24h to remove moisture. The prepared PLLA films also cut into the same dimension like fabric. Then the woven and non woven fabrics were placed in between the PLLA films maintaining 10wt% fabric with respect to blend. For non woven fabric/PLLA composites, fibers were placed unidirectional. The specimens were then placed on stainless steel open mould and composite was fabricated as like PLLA film making. A mould releasing spray (BONEY-Mould release silicon spray, manufacturer-London chemicals Ind. England) used to easy opening the mould. The specimens for tensile (dimensions: 110×15×0.5-1.0 mm^3) and flexural (dimensions: 79×10×0.5-1.0 mm^3) tests were made using cutting machine.

Tensile tests were conducted according to ASTM D882 (E) using a Universal Testing Machine (Hounsfield UTM 10KN). Three-point flexural tests of composites were carried out using Hounsfield UTM 10KN according to the standard method used for flexural properties (ASTM D790-98). Notched Charpy impact tests (according to ASTM D6110-97) were carried out using a universal impact tester. All the results were taken as the average value of 10 samples.

Scanning electron microscopy (SEM) was used to observe the tensile fractured surface morphology of composites. The instrument (Philips XL-30) was operated with an excitation voltage 30 kv. The samples were coated with 3nm gold layer using a vacuum sputter coater.

3. Results and Discussion
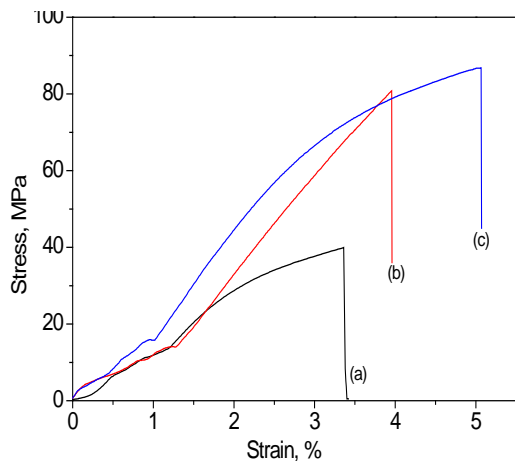
Fig. 1. Tensile stress-strain diagrams of (a) PLLA, (b) untreated woven jute fabric/PLLA and (c) treated jute fabric/PLLA composites in warp direction
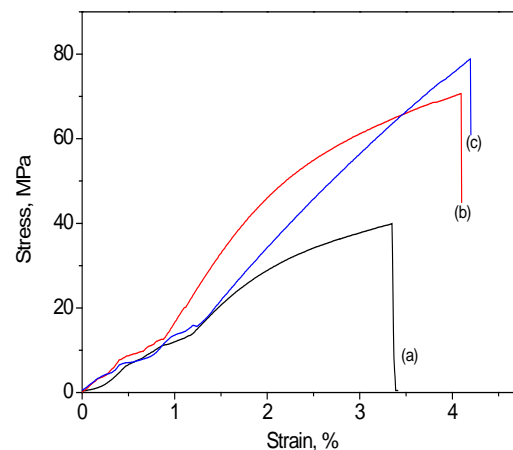
Fig. 2. Tensile stress-strain diagrams of (a) PLLA, (b) untreated woven jute fabric/PLLA and (c) treated jute fabric/PLLA composites in weft direction

Fig. 1 and 2 represent the tensile stress–strain diagrams of unreinforced PLLA, untreated and treated woven jute fabric/PLLA composites in warp and weft direction, respectively. The initial portion of the curve of untreated woven jute fabric/PLLA composites is linear at low strain rates followed by change in the slope of the curve

indicating nonlinear behavior of the material. The start of nonlinearity in the curve is an indication of the initial matrix cracking followed by progressive failure of the fibers. TM was determined by the slope of the initial portion of stress–strain curve. A significant improvement in the TS and TM of PLLA was obtained by the reinforcement with untreated woven jute fabric; in warp direction their respective values were increased to 102.5 and 211.1%. In weft direction, TS and TM were also found 77.5 and 105.6% higher than unreinforced PLLA samples, respectively. The strain at maximum tensile stress for untreated fabric composite samples ranged from (1.7–5.9)% in warp direction and (3.4–4.8)% in weft direction. It has been noticed that TS, TM and elongation properties of untreated fabric composite is higher in warp direction than weft direction. This is because more number of fibers in warp direction offers greater resistance to crack propagation than in weft direction.
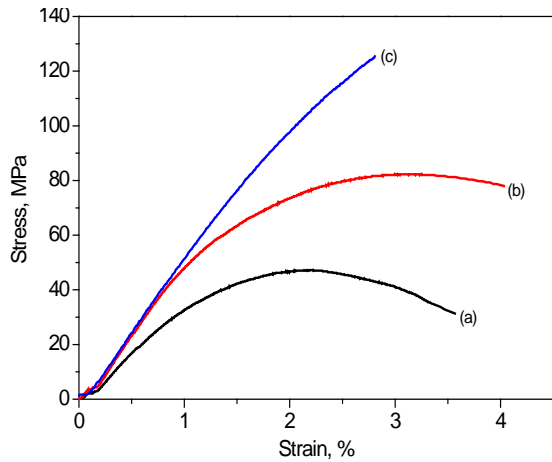
Fig. 3. Flexural stress-strain diagrams of (a) PLLA, (b) untreated woven jute fabric/PLLA and (c) treated woven jute fabric/PLLA composites in warp direction
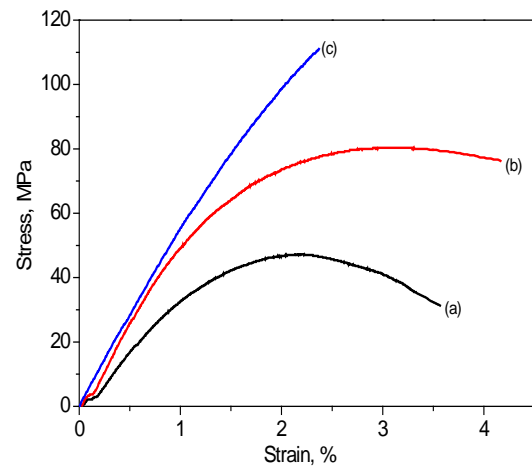
Fig. 4. Flexural stress-strain diagrams of (a) PLLA, (b) untreated woven jute fabric/PLLA and (c) treated woven jute fabric/PLLA composites in weft direction

Table 1. Mechanical properties of jute fabrics/PLLA composites

Fabric/PLLA composites	Tensile strength (MPa)	Tensile Modulus (GPa)	Elongation (%)	Flexural Strength (MPa)	Flexural Modulus (GPa)	Impact strength (KJ/m^2)
Unreinforced PLLA	40±6.3	0.36±0.001	3.4±0.4	42±9.7	3.02±0.8	8.82±0.91
Non woven jute	55±11.5	0.867±0.02	6.01±1.1	67±8.4	2.83±1.1	12.98±1.05
Woven fabric composites at warp direction						
Untreated jute	81±13.5	1.12±0.034	3.8±2.1	82±12.0	4.3±0.10	16.4±1.8
Treated jute	87±8.5	1.42±0.047	5.1±0.5	121±13.4	5.3±0.095	18.1±2.3
Woven fabric composites at weft direction						
Untreated jute	71±8.7	0.78±0.063	4.1±0.7	81±9.4	3.62±0.077	14.3±1.46
Treated jute	79.2±9	0.91±0.057	4.2±0.5	111±8.1	4.72±0.046	16.6 ±1.8

The flexural modulus is a measure of the resistance to deformation of the composite in bending. The flexural behavior of jute fabric composite is presented in Fig. 3 and 4. Under the flexural loading, the surfaces of the specimen are subjected to greater strains than the sample center. Hence, FS and FM are controlled by the strength of the extreme layers of reinforcement [9]. The average FS and FM of untreated jute fabric composite was found to be 95.2 and 42.4% higher than the unreinforced PLLA in warp direction. As like tensile properties, flexural behavior of woven fabric composite is found higher in case of warp direction than weft direction.

The effect of woven jute fabric on impact strength of PLLA is presented in Table 1. The average impact strength of untreated fabric composite (16.4 KJ/m^2) is 85.9% higher than the impact strength of unreinforced PLLA in warp direction. This indicates that woven fabric plays an important role in the impact resistance of the composite as they interact with the crack formation in the matrix and act as stress-transferring medium.

It is also seen that the tensile properties of woven jute fabric composites is higher than non-woven jute fabric composites (Table 1). In woven fabric, fiber yarns of warp direction crossover and under the fiber yarns of weft

direction to create an interlocking structure. Under tensile loading, these crimped fibers tend to straighten out, which create high stresses in the matrix. As a result, the strength of the woven fabric composite is greater than the strength in the non-woven fabric composite.

Fig. 1-4 and Table 1 show that benzoylated woven jute reinforced PLLA composites possessed higher TS, TM, FS, FM and IS compared with those of untreated counterparts. It indicates that for the composites which possess better interfacial bonding due to fiber surface treatments. Untreated woven jute reinforced PLLA, which had poor interfacial bonding between the fabric and the matrix, showed a lower tensile strength due to the fact that a lower load is needed to break and pull-out the fiber from the matrix (Fig. 5). However, the poor interfacial bonding property between the fabric and the matrix made it easier for the fiber to debond from the matrix. The crack was somewhat blunt and the composites showed brittle properties. For treated woven jute reinforced PLLA composites, due to the improved interfacial bonding properties, the pull-out the fiber from the matrix is rare and a good fracture resistance property was achieved.
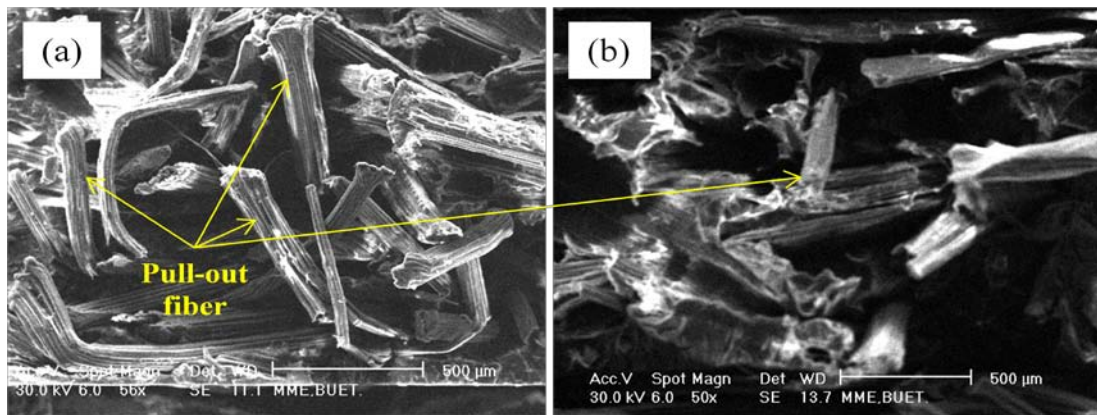
Fig. 5. SEM photographs of tensile fracture surface of (a) untreated and (b) treated woven jute fabric/PLLA composites in warp direction

4. Conclusion

The excellent mechanical behaviour of PLLA based woven jute fabric biocomposites was shown under tensile, flexural, and impact loadings. Chemical modified jute fabric composite offered better tensile, flexural, and impact strength than untreated woven jute fabric composites. Finally, it may be concluded that PLLA based woven jute composite can be molded into a value added composite material by using hot press molding method. Further investigations have to be carried out to determine the thermal and biodegradability of these composites.

5. Acknowledgement

6. References

[1] N. Jekabsons, and N. Bystrom, "On the effect of stacked fabric layers on the stiffness of a woven composite" *Composites: Part B*, Vol. 33, No.8, pp. 619, 2002.

[2] S.V. Lomov, A. Willems, I. Verpoes, Y. Zhu, M. Barburski, and T. Stoilova T, "Picture frame test of woven composite reinforcements with a full-field strain registration", *Textile Research Journal,* Vol. 76, No. 3, pp. 243, 2006.

[3] S.M. Sapuan, A. Leenie, M. Harimi, and Y.K. Beng, "Mechanical properties of woven banana fiber reinforced epoxy composites", *Materials Design,* Vol. 27, pp. 689, 2006.

[4] L.A. Pothen, S. Thomas, and G. Groeninckx, "The role of fiber/matrix interactions on the dynamic mechanical properties of chemically modified banana fiber/polyester composites" *Composites: Part A,* Vol. 37, pp. 1260, 2006.

[5] W.L. Lai, and M. Mariatti, "The properties of woven betel palm (*areca catechu*) reinforced polyester composites"' *Journal of Reinforced Plastics and composites,* Vol. 27, pp. 925, 2008.

[6] M. Jacob, K.T. Varughese, and S. Thomas, "Novel woven sisal fabric reinforced natural rubber composites: Tensile and swelling characteristics", *Journal of Composite Materials,* Vol. 40, pp. 1471, 2006.

[7] A.N. Netravali, and S. Chabba, "Composites get greener", *Materials Today,* Vol. 6, pp. 22, 2003.

[8] L. Liu, S. Li, H. Garreau, and M. Vert, "Selective enzymatic degradations of Poly(L-lactide) and poly(3-caprolactone) blend films", *Biomacromolecules,* Vol. 1 No. 3, pp. 350, 2000.

[9] G.T. Munikenche, A.C.B. Naidu, and R. Chhaya, "Some mechanical properties of untreated jute fabric-reinforced polyester composite", *Composites: Part A,* Vol. 30, pp. 277, 1999.

Influence of Surface Treatments on the Physical Properties of Jute Fiber

G. M. Arifuzzaman Khan, S. M. Abdur Razzaque, Mahmudur Rahman Tusar,
and Md. Shamsul Alam

Dept. of Applied Chemistry and Chemical Technology, Islamic University, Kushtia-7003, Bangladesh
E-mail: gm_arifuzzaman@yahoo.com

Abstract

The aim of the study is the chemical modification of jute fibers using bleaching, acrylonitrile (AN) grafting, and diphenylmethanediisocyanate (DPMIC) treatment, to confer hydrophobicity, higher mechanical and thermal properties to jute fiber. The extent of modification reaction was evaluated by FTIR measurement. Morphologies of jute fibers were investigated by scanning electron microscopy (SEM). Tensile properties such as maximum stress at break, extension at break and Young's modulus of untreated, bleached, AN grafting and DPMIC treated fibers were evaluated and compared. AN grafted and DPMIC treated fibers showed substantial increase in tensile properties. Based on findings of hydrophobicity, the DPMIC treated fiber has been showed better properties than bleached and AN grafted fibers. Thermal stability also improved by AN grafting and DPMIC treatments.

Keywords: Jute, surface modification, characterization, physical properties, thermal property.

1. Introduction

Jute, the golden fiber of Bangladesh gained considerable attention in composite industries as an environmental friendly reinforcement. The fiber has a high aspect ratio, high strength to weight ratio, low energy conversion and has good insulation properties. However, poor compatibility between the hydrophilic jute fiber and the hydrophobic polymer matrix is usually the weakest point in a composite, which makes the performance of the final composite limited by fiber pull-out rather than fiber break. Thus, full strength of the jute fiber as reinforcing material is not utilized, the optimal properties of the composite are not obtained as well as the full commercial potential is not achieved. To improve the compatibility between the fiber and the polymer matrix, the jute fiber should be modified either physically or chemically.

Surface chemical modification with coupling agents is usually applied to optimize the wetting of the natural lignocellulosic fibers by the polymeric matrix and to improve the interaction and adhesion between the non-polar matrix and the polar reinforcement. The chemical surface modification techniques such as alkali treatments [1], bleaching [2], acetylation [3], and graft co-polymerization [4], has also been reported to overcome the incompatible surface polarities between the natural fiber and polymer matrix. Though, surface chemical modification is usually applied to improve the interaction and adhesion between the non-polar matrix and the polar lignocellulosic fibers, the presence of surface impurities such as pectin and waxy substance of the fiber sometime hinder the modification process. Surface pretreatment is necessary before perform chemical modification. $NaClO_2$ bleaching is very efficient pretreatment method to remove wax, pectin and lignin. Therefore, acrylonitrile (AN) grafting and diphenylmethanediisocyanate (DPMIC) treatments were used on bleached jute fiber. The chemical and physical properties of treated fiber was also been studied.

2. Experimental

Jute fiber was collected from local market of Jhenidha, Bangladesh. Sodium carbonate, acetic acid, sodium acetate, sodium chlorite, sodium metabisulfite, chloroform, toluene, acrylonitrile, and diphenylmethanediisocyanate (DPMIC), were purchased from Merck, Germany. Other chemicals used were analytical reagent grade.

About 20 g of untreated jute fiber was bleached in 1 L $NaClO_2$ ($7gL^{-1}$) solution buffered at pH 4. The reaction was carried out at 90-95°C for 90 min maintaining the fiber to liquor ratio 1:50. After completing the bleaching reaction, the fiber was treated with 0.2 (w/v)% sodium metabisulphite solution for 15 min to reduce chlorite action and then washed thoroughly with distilled water [2]. 1 g bleached jute fiber was taken in 100 ml

stoppered conical flask. Aqueous solution of acrylonitrile monomer (50 wt% of fiber), $K_2S_2O_8$ as initiator (1 wt% of fiber) and $FeSO_4$ as catalyst (1 wt% of fiber) was taken for grafting reaction. Fiber to liquor ratio was maintained 1:50. The reaction was continued at 70ºC in a water bath for 90 min. After completing the reaction fiber was washed with methanol and then distilled water to removed adhering homopolymer from jute surface. The grafted fiber was dried in air and finally in oven [2]. Bleached jute fiber was dipped in toluene solution containing DPMIC (5wt% of fiber) for 1 h at 70°C. The fiber was then decanted, washed and dried in an air oven at 70°C for 2 h.

The FTIR spectroscopy of jute samples were taken using Perkin Elmer Spectrum One spectrometer. Samples were taken with KBr to make a transparent pellet. For each sample 5 scans were taken at a resolution of 4 cm^{-1}. The surface morphology of jute samples were observed by scanning electron microscope (FEI QUANTA 200 3D) with an accelerating voltage 10 kv. WAXD patterns were obtained with a BRUKER D8 ADVANCE wide angle X-ray diffractometer using Cu Kα radiation (α = 0.154 nm), voltage of 50 kV, and current of 40 mA with 2θ ranges from 5 to 45° increased in steps of 2°/min. The thermogravimetry of fiber was conducted by thermal gravimetric analyzer (TG/DTA 6300, Seiko Instrument Inc., Japan). Tensile tests were conducted according to ASTM D638-01 using a Universal Testing Machine (Hounsfield UTM 10KN).
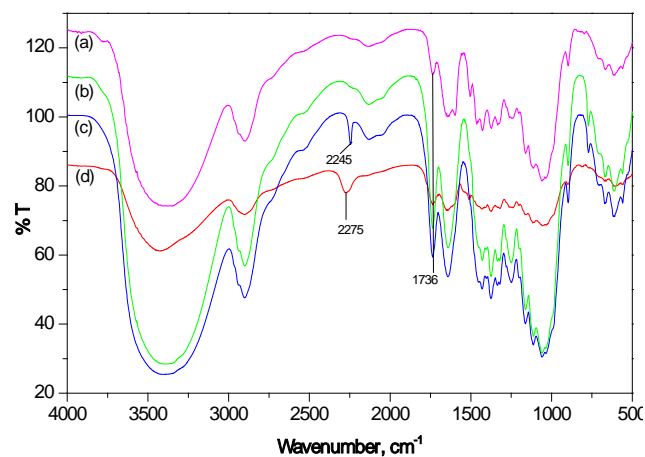
Fig. 1. FTIR spectra of (a) untreated, (b) bleached, (c) AN grafted and (d) DPMIC treated jute fibers

3. Results and Discussion

FTIR spectra of untreated and treated jute fibers are shown in Fig. 1. The FTIR spectra of fibers contain the typical vibration bands of the components mainly corresponding to cellulose, hemicellulose, and lignin. The hydrophilic tendency of jute fibers is reflected in the broad absorption band in the 3700–3100 cm^{-1} region, which is related to the –OH groups present in their main components. In the 1600–900 cm^{-1} region, it is possible to appreciate in fibers vibrations of chemical components of the lignin at frequencies of 1514 cm^{-1} for guaiacyl [5] and 1468, 1433, and 1214 cm^{-1} associated with syringyl [5]. Almost the same absorption peaks as shown in the untreated jute fibers were observed in the spectrum of the treated jute fibers. This indicated that the structure of cellulose had not been damaged after the treatments. The drop in the peak of bleached jute fiber found at the range of 1597, 1503 and around 1374 cm^{-1} indicated the removal of lignin. In the spectrum of bleached jute fibers, the reduction in the peak intensity found at 1372 and 1244 cm^{-1}, indicated the partial removal of hemicellulose. The peak at 1632 cm^{-1} becomes less intense because of the removal of oils and other impurities. In Fig.1(c), the band at 2243 cm^{-1} arising from the stretching vibration of C≡N was used for characterization of the AN grafted jute. The peak at 1460 cm^{-1} is due to the CH_2 deformation intensified upon grafting [6]. The FTIR spectrum of the DPMIC treated bleached jute exhibited the characteristic urethane peaks at 2275 cm^{-1} for =N=C=O asymmetric stretching and 1720 cm^{-1} for –C=O stretching (amide -NH=CO-O-) vibrations. The introduction of the cardanol moiety was indicated by the presence of a –C=C peak at 1620 cm^{-1}, –CH aromatic at 3020 cm^{-1} and –C–H aliphatic at 2980 cm^{-1}. The FTIR spectrum of the DPMIC also showed peaks at 1440 and 1590 cm^{-1} due to the C=C aromatic ring stretching.

In order to observe the changes in morphological structure of the jute fibers on chemical treatments were observed by SEM (Fig. 2). The surface of the untreated jute fiber was covered by a number of impurities like hemicellulose, lignin, pectin, waxy substances, and so on. However, the treatment creates a lot of modification on the fiber surface. On comparison of Fig. 2(a) and 2(b), the drastic difference in the surface morphology

between the untreated and the bleached fiber can be easily visualized. The multi-cellular nature of a fiber filament is more clearly revealed in Fig. 2(b). Unlike the untreated fiber the surface of bleached fibers seems to be free from surface debris and overgrowths. This is undoubtedly due to the removal of lignin and also a part of hemicellulose during the bleaching from both the surface and the intercellular spaces. On AN grafting, bleached jute fiber became defibrillated (Fig. 2(c)). The deposition of the polymer onto the fiber makes a film and it fills the gap between the fibrils and making it more hydrophobic [6]. Comparison of the micrographs of the bleached and DPMIC treated jute shows that a considerable amount of –ICN groups is grafted onto the jute surface. The intercellular gaps are also reduced due to crosslinking of cellulose.
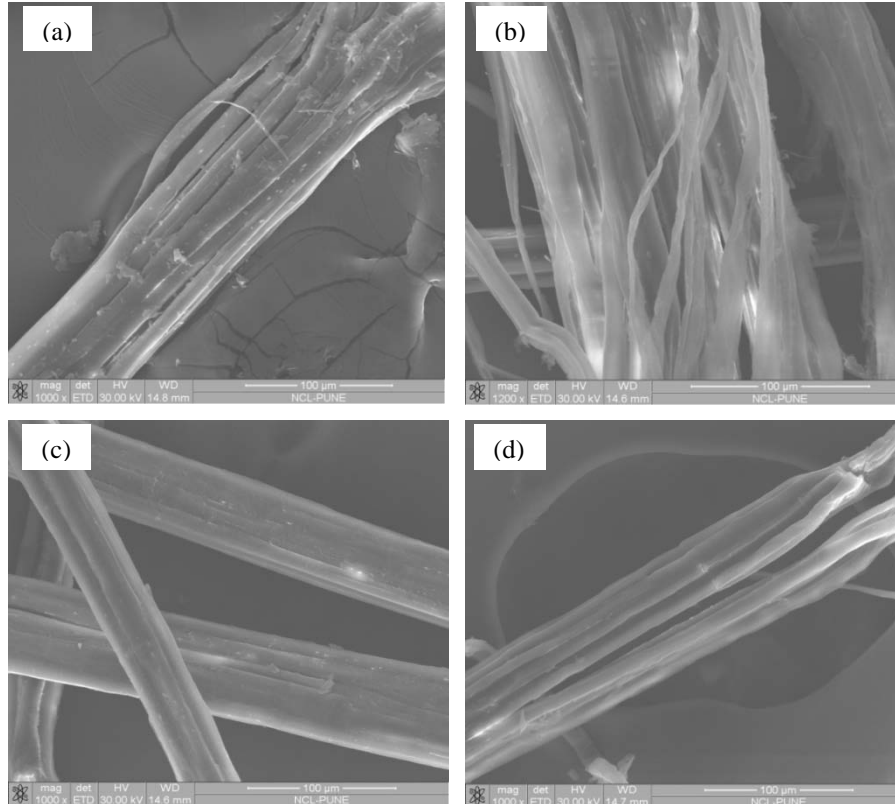
Fig. 2. SEM topography of (a) untreated, (b) bleached, (c) AN grafted and (d) DPMIC treated jute fibers

The wide angle X-ray diffractograms (WAXD) and the crystallinity index of untreated and treated jute fibers are shown in Fig. 3 and Table 1, respectively. The bleached fiber showed highest crystallinity. This may be due to removal of amorphous hemicelluloses and lignin. The reduction of crystallinity index was observed in X-ray diffractogram of AN grafted and DPMIC treated fibers. This result suggests that a degree of crystallinity of cellulose decreased with AN grafting and DPMIC treatment which is because of deposition of amorphous components on cellulose surface [7].

Table 1. The crystallinity index of the untreated and treated jute fibers

Types of jute	Peaks at $2\theta=15.7°$ angle			Peaks at $2\theta=22.6°$ angle			Crl
	Area	Width	Height	Area	Width	Height	%
Untreated	32481	4.637	5588.8	40442	2.667	12098	70.00
Bleached	37258	4.430	6711.1	45983	2.597	14129	73.07
AN grafted	32718	4.449	5868.2	38880	2.622	11832	68.75
DPMIC treated	39127	4.567	6836.0	44479	2.524	14060	70.99

The effect of chemical treatment of the jute fibers on the physical properties and density values are given in Table 2. The quality of jute fiber largely depends on its physical properties, such as fineness, moisture regain and densities. Splitting of the cemented fibers causes a reduction in the fiber diameter. Further modification through AN grafting and DPMIC treatment given of jute surface coating hence increase the fiber diameter slightly. The densities of untreated, bleached, AN grafted and DPMIC treated fibers were 1.15, 1.40, 1.32 and

1.25 gcm^{-3}, respectively, showing that the surface treatments have significant affect on density [8]. As seen in Table 2, jute contains 5.01% of moisture, while 60 min is sufficient to dry the fiber. For bleached fibers the moisture content is increased to 6.8%. This may be due the removal of hemicellulose, pectin, waxes and fats, fiber become floppy i.e. contain more pore. Therefore, moisture can easily diffuse in these pore result in moisture regain increase. A significantly decrease in moisture affinity of jute modified by AN grafting and DPMIC treatments.
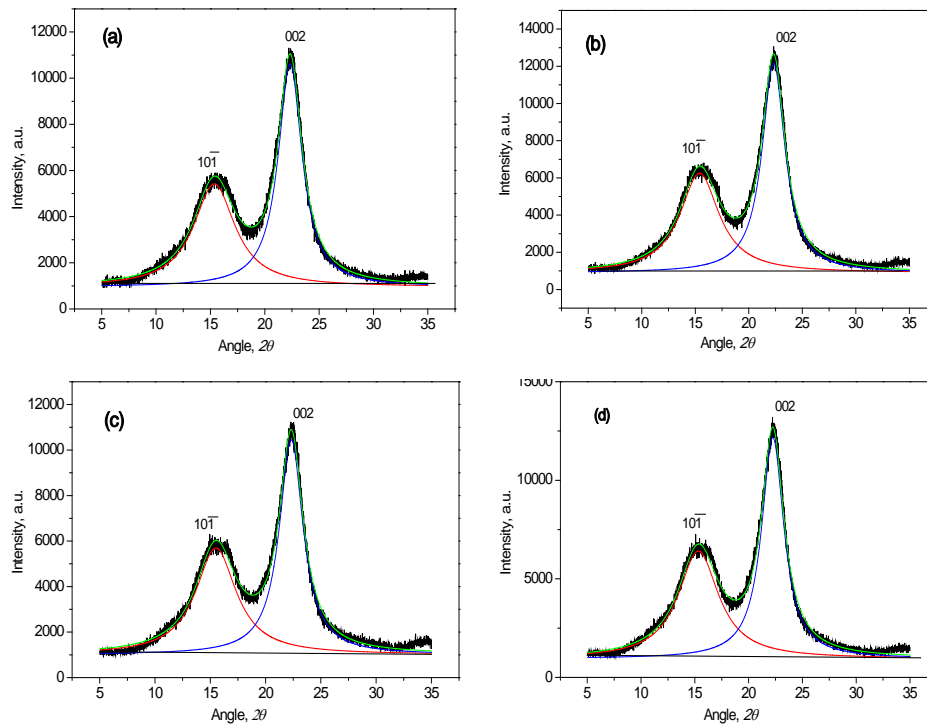
Fig. 3. WAXD and fitted data of (a) untreated, (b) bleached, (c) AN grafted and (d) DPMIC treated jute fibers

The tensile properties of untreated and treated jute fibers are shown in Table 2. Bleached fibers show an appreciable decrease in the tensile strength. This decrease may be attributed to substantial delignification and degradation of cellulosic chains during the chemical treatment. The extension at break in these fibers does not change much. AN and DPMIC treated fibers brings about a substantial increase in tensile strength (TS) and tensile modulus (TM). This may be attributed to the fact that AN and DPMIC treatments may create orderly arrangement jute fibrils by surface coating via crosslinking reaction [9].

Table 2. Physical properties of untreated and treated jute fibers

Types of jute	Density (g.cm^{-3})	Diameter (μm)	TS (MPa)	TM (GPa)	Elongation, (%)	Moisture (%)
Untreated	1.15	67.6-75.6	483±11	3.30±1.3	3.85	5.01
Bleached	1.40	30.0-38.4	523±13	4.29±1.1	2.67	6.80
AN grafted	1.32	36.8-45.7	717±15	4.36±1.5	3.20	3.20
DPMIC treated	1.25	31.9-38.7	537±13	4.13±1.6	2.88	3.90

The TG, DTA and DTG curves of the untreated and treated jute fibers are shown in Figure 4. In all the cases, initial weight loss at temperature between 30 to 150°C indicates removal of moisture from the fiber. The weight loss below 250°C is negligible; above that temperature the fibers begin to degrade fast and at 400ºC, only residual char is obtained due to loss of hydroxyl groups and depolymerization of cellulose to anhydroglucose units**.**

The initial stage decomposition of untreated, bleached, AN grafted and DPMIC treated jute are 5.8, 7.7, 3.8, and 3.8% respectively. It evident that bleached fiber reduces more moisture than others. The final decomposition of untreated, bleached, acetylated, AN grafted and DPMIC treated jute are 76.1, 66.6, 75.1 and 72.2% respectively and corresponding final decomposition temperature (FDT) are 361.0, 363.7, 380.8 and 372.0°C. It has been

observed from above results that AN grafting and DPMIC treatment enhanced the thermal stability of jute fibers. Maximum thermal stability was presented by AN grafted, fiber followed by DPMIC treated jute fibers.
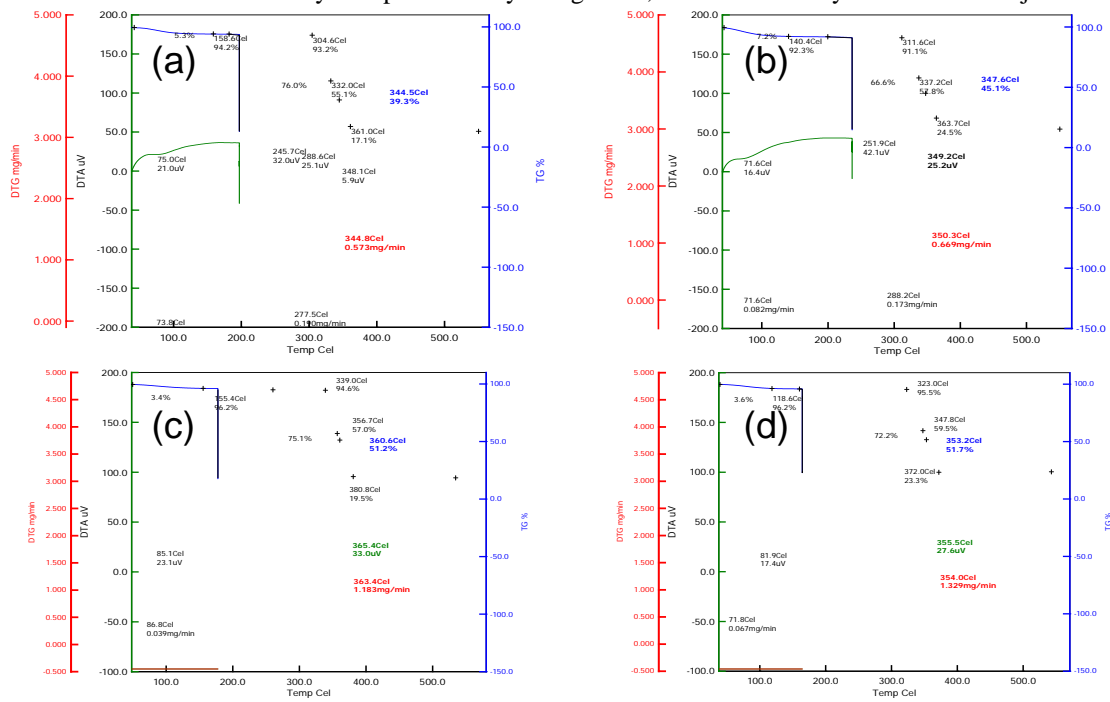
Fig. 4. TG, DTA and DTG thermograms of (a) untreated, (b) bleached, (c) AN grafted and (d) DPMIC treated jute fibers

Table 3. TG data of untreated and treated jute fibers

Types of jute	Weight loss % at temperature (°C)			FDT (°C)	Residual Char, (%)
	0-150	150-230	230-400		
Untreated	5.8	1.0	76.1	361.0	17.1
Bleached	7.7	1.2	66.6	363.7	24.5
AN grafted	3.8	1.6	75.1	380.8	19.5
DPMIC treated	3.8	0.7	72.2	372.0	23.3

*FDT- Final decomposition temperature

Table 4. DTG of untreated and treated jute fibers

Types of jute	Peak I		Peak II		Peak III	
	Temperature (°C)	Rate (mg/min)	Temperature (°C)	Rate (mg/min)	Temperature (°C)	Rate (mg/min)
Untreated	73.8	0.065	277.5	0.190	344.8	0.573
Bleached	71.6	0.082	288.2	0.173	350.3	0.669
AN grafted	86.6	0.039	--	--	363.4	1.183
DPMIC treated	71.8	0.067	--	--	354.0	1.329

Table 5. DTA data of untreated and treated jute fibers

Types of jute	Temperature, °C		
	Peak I (endo)	Peak II (exo)	Peak III (endo)
Untreated	75.0 (endo) (21.0uV)	245.7 (exo) (32.0uV)	348.1 (5.9uV)
Bleached	71.6 (endo) (16.4uV)	251.9(exo) (42.1uV)	349.2(endo) (25.2uV)
AN grafted	85.1 (endo) (23.1uV)	--	365.4 (endo) (33.0uV)
DPMIC treated	81.9 (endo) (17.4uV)	--	355.5(endo) (27.6uV)

The residual char left at 550°C highest in the case of bleached fiber and thereafter DPMIC treated fiber (Table 3). Saha et al. [10], explained that by reduced the hemicellulose to a considerable extent, giving rise to a lignin–cellulose complex, thereby making the product more stable than the untreated sample, and this was reflected in the increased amount of residual char. The treatment on jute fiber decreased the weight loss during pyrolysis,

and enhanced the residual char formation with a lowering in the formation of the flammable volatiles, and thus concluded that the thermal stability was decreased in the case of the treated fibers.

In the DTG curve of the untreated jute fiber, the peak I below at 73.8°C was the result of evaporation of moisture (Table 4). The peak II at 277.5° and peak III at 344.8°C were caused by hemicellulose and α-cellulose degradation, respectively. In the case of bleached fiber, moisture loss peak shifted to a lower temperature. This tendency toward releasing moisture at a lower temperature might be caused by an increase in the surface area of the split `fibers (Fig. 4), facilitating easier evaporation of moisture at a lower temperature. The degradation peak of the α-cellulose and the hemicelluloses shifted to higher temperatures in all the treated fibers. The disappearance of peaks for hemicellulose degradation observed for AN grafted and DPMIC treated fiber. It may say that the degradation temperature of hemicelluloses affected by AN grafting and DPMIC treatment of bleached jute fiber.

An endothermic peak below 100°C was observed, resulting from moisture loss. The exothermic peak at 240-290°C and the endothermic peak at 330-380°C were caused by the hemicellulose and α-cellulose decomposition, respectively. It is apparent that the exothermic peak II was disappeared for AN and DPMIC treated jute may be due to hemicelluloses removal or blocked by those treatments. In the case of AN or DPMIC treatment, where only the hydroxyl groups took part in the chemical reaction, no such inversion was observed.

4. Conclusion

Modification of jute fiber by NaClO$_2$ bleaching, AN grafting and DPMIC treatment were carried out in this study to obtain better surface properties, while maintaining good inherent mechanical properties. The remarkable morphology changes of treated fiber were observed by FTIR and SEM micrograph. WAXD was used to investigate the crystalline development. The results showed the positive change of degree of crystallinity of treated fiber. The tensile strength, modulus, elongation, hydrophobicity, and the fineness were improved when jute was treated through AN grafting and DPMIC treatments. On the contrary, the breaking strength and moisture regain decreased for bleached fibers. Thermal stability also improved by AN grafting and DPMIC treatments.

References

[1] A.K. Bledzki, H.P. Fink HP, and K. Specht, "Unidirectional hemp and flax EP- and PP-composites: Influence of defined fiber treatments", *Journal of Applied Polymer Science,* Vol. 93, No. 5, pp. 2150, 2004.

[2] B. Sikdar, R.K. Basak, and B.C. Mitra, "Studies on graft copolymerization of acrylonitrile onto jute fiber with permanganate ion initiation system in presence of air", *Journal of Applied Polymer Science,* Vol. 55, No. 12, pp. 1673, 1995.

[4] S. Mishra, M. Mishra, S.S. Tripathy, S.K. Nayak, and A.K. Mohanty, "Graft copolymerization of acrylonitrile on chemically modified sisal fibers", *Macromolecular Materials and Engineering,* Vol. 286, No. 2, pp. 107, 2001.

[3] S. Mohanty, S.K. Nayak, S.K. Verma, and S.S. Triphacy, "Effect of MAPP as a coupling agent on the performance of jute–PP composites", *Journal of Reinforced Plastics and Composites,* Vol. 23, pp. 625, 2004.

[5] K.K. Pandey, "A study of chemical structure of soft and hardwood and wood polymers by FTIR spectroscopy", *Journal of Applied Polymer Science,* Vol. 71, No. 2, pp. 1969, 1999.

[6] A.K. Mohanty, S. Parija, and M. Misra, "Ce (IV)-N-Acetylglycine initiated graft copolymerisation of acrylonitrile onto chemically modified pineapple leaf fibers", *Journal of Applied Polymer Science,* Vol. 60, pp. 931,1996.

[7] V. Tserki, N.E. Zafeiropoulos, F. Simon, and C. Panayiotou, "A study of the effect of acetylation and propionylation surface treatments on natural fibers", *Composites: Part A,* Vol. 36, pp. 1110, 2005.

[8] A.K. Bledzki, and J. Gassan, "Composites reinforced with cellulose based fibers", *Progress in Polymer Science,* Vol. 24, No. 2, pp. 221, 1999.

[9] J. Rout, M. Misra, and A.K. Mohanty, "Surface modification of coir fibers I: studies on graft copolymerization of methyl methacrylate on to chemically modified coir fibers", *Polymers for Advanced Technologies*, Vol. 10, No. 6, pp. 336, 1999.

[10] S.C. Saha, P.K. Ray, S.N. Pandey, and K. Goswamy, "IR and X-ray diffraction studies of raw and chemically treated pineapple leaf fiber (PALF)", *Journal of Applied Polymer Science,* Vol. 42, No. 10, pp. 2767, 1991.

Preparation and Properties of Chemically Reduced Cu and Ag Nanoparticles

M. Julkarnain*, Arup Kumar Mondal, Md. Mizanur Rahman and Md. Sohel Rana
Department of Applied Physics and Electronic Engineering, University of Rajshahi
Rajshahi-6205, Bangladesh.
E-mail: jnain.apee@ru.ac.bd

Abstract

Metallic nanoparticles like copper (Cu) and silver (Ag) were prepared by simple chemical reduction method. The synthesis of Cu nanoparticles was performed by the reduction of copper sulfate ($CuSO_4$) with hydrazine hydrate in aqueous solution under atmospheric air in the presence of sodium dodecyl sulfate (SDS) as capping agent. Likewise, Ag nanoparticles were reduced by $NaBH_4$ from the solution of $AgNO_3$ in water. The synthesized nanoparticles were characterized by UV-Visible absorption spectra, FT-IR and optical microscopic images.

Keywords: *nanoparticles, chemical reduction, hydrazine hydrate, SDS, UV-visible spectra.*

1. Introduction

Nanotechnology has become one of the most interesting areas of scientific research in recent years, particularly in the area of material research, including the synthesis, characterization and application of nanometer-sized metals, oxides, semiconductors and ceramics [1]. Nanoparticles (NPs) exhibit electronic and optical properties different from those displayed by their bulk-material counterparts. These properties can further be tuned by altering the dimensions and their mutual interactions [2-5]. Gold, silver and copper stable dispersions of nanoparticles are useful in areas such as microbiology, surface-enhanced Raman scattering (SERS) detection, photography, catalysis, biological labeling, photonics and optoelectronics [3]. The antifouling properties of copper and silver are well known and their effectiveness at reducing the growth of various microorganisms has been reported [6-8].

Nanoparticles are small and not thermodynamically stable for crystal growth. Therefore, the nanoparticles must be protected during the reaction either by adding surface-protecting agents such as organic ligands and inorganic capping materials or by placing in inert environment such as inorganic matrix and polymers.

A variety of preparation routes have been reported for the preparation of metallic nanoparticles [9, 10]; notable examples include, metal vapour deposition, electrochemical reduction, radiolysis, thermal decomposition, ultrasonic irradiation, mechanical attrition and chemical reduction. Among these methods, the solution method is found to be simple and most versatile for metal nanoparticles [11]. In this paper, we report the synthesis and properties of SDS capped copper and silver nanoparticles by chemical reduction method.

2. Experimental details

2.1. Materials

The chemical materials of Cupper Sulfate (>99.98% $CuSO_4$), Silver Nitrate (>99.5% $AgNO_3$), Sodium Borohydride ($NaBH_4$) and Hydrazine Hydrate were purchased from Merck (Germany) and NaOH & SDS were from Merck (India). All of the chemicals were analytical grade and used as purchased without further purification. Redistilled water was used to prepare all of the solutions.

2.1. Preparation of Cu and Ag nanoparticles

The copper NPs were prepared in aqueous phase by chemical reduction of $CuSO_4$ with hydrazine hydrate in the presence of SDS as capping agent. NaOH was used to adjust the p^H of the solution and accelerate the reduction reaction in water. In a typical experiment, 1ml of 0.5M NaOH was added with 100 ml of 10 mM $CuSO_4$ solution and stir for a time period of 10 minutes. 1 ml of 0.1 M SDS solution was then added drop-wise to the solution under a continuous stirring. After 10 minutes 2 ml of 80% hydrazine hydrate was added drop-wise to the above solution under constant stirring. The color of the reaction solution changed to reddish black on complete addition of reducing agent indicating the formation of copper nanoparticles.

On the other hand, Ag NPs were prepared according to K.C. Song et al.[12]. Here Ag nanoparticles were synthesized from $AgNO_3$ precursor by using $NaBH_4$ and SDS as reducing agent and stabilizer, respectively. $AgNO_3$ solution was prepared by dissolving the required amount of $AgNO_3$ in distilled water. Separately, the $NaBH_4$ solution was prepared by dissolving $NaBH_4$ and SDS in 45 ml distilled water for a period of 20 minutes together. After that 5 ml of $AgNO_3$ solution added drop-wise into the $NaBH_4$ solution with SDS slowly. After all solutions were added, the mixed solutions were stirred for a half an hour more.

2.3. Characterization

The surface plasmon absorption spectra of Cu and Ag nanoparticles were measured with a SHIMADZU UV-1650PC UV-visible spectrophotometer. During the experiment, the colloidal sample was filled in clean quartz cell for measurement. The scanning region was from 300 to 700 nm. To investigate the morphology and shape of the nanoparticles high resolution optical microscope (Olympus-IX-71) was used. Fourier Transform Infrared (FT-IR) spectroscopic measurements were done using Perkin Elmer 100E spectrophotometer.

3. Results and discussion

3.1. UV-visible Spectroscopy

UV–visible absorption spectra and color of copper nanoparticles are shown in Fig. 1. From the figure it is reveal that chemically synthesized copper nanoparticles solution appears as reddish black in color and has the characteristic absorption peak at around 575nm which is well reported signature of copper nanoparticles formation [13-15]. The strong surface-plasmon band may depend on the individual particle property including sizes, shapes, solvents and reducing agents employed. The strong surface-plasmon absorption band observed at 575nm may due to the formation of non-oxidized copper nanoparticles. The broadness of the absorption band (Fig. 1) probably arises from the wide size distribution of copper nanoparticles.

Figure 2 shows the UV-visible absorption spectra of Ag nanoparticles prepared with different initial $AgNO_3$ concentrations. All the other conditions were constant as 0.01M $NaBH_4$ and 0.01M SDS. The color of the solutions depends on the concentrations of added $AgNO_3$ solutions. With increasing the initial concentration, the color of the solution changed from light yellow to brown. A minor blue shift observed at the absorption peak with increasing the initial $AgNO_3$ concentrations. This may be due to formation of smaller size nanoparticles with higher $AgNO_3$ concentrations. The absorption peak at around 405nm in Fig. 2 is attributed to the surface plasmon excitation of silver nanoparticles, indicating the formation of silver nanoparticles [9,12,16]. From this figure, it also observed that the peak intensity of the samples increases with increasing $AgNO_3$ concentrations which could be attributed to the generation of highly dense and smaller particles.
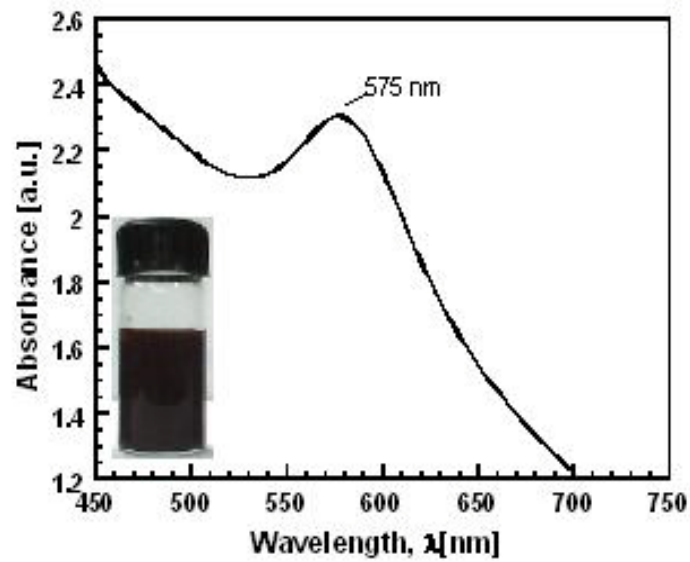
Fig. 1. UV-visible absorption spectrum and color of copper nanoparticles
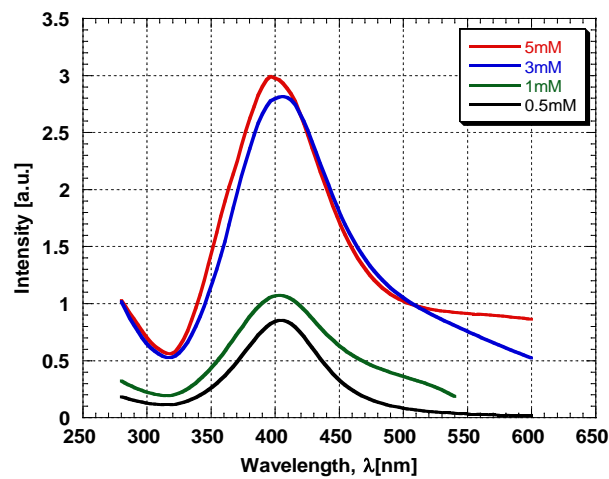
Fig. 2. UV-visible absorption spectra of Ag nanoparticles with varying initial $AgNO_3$ concentrations

(a)

(b)
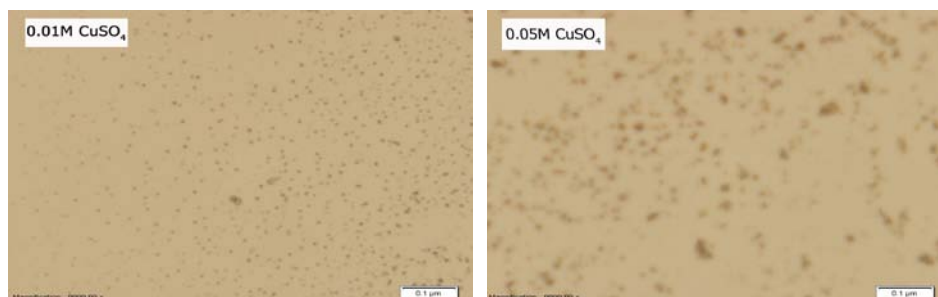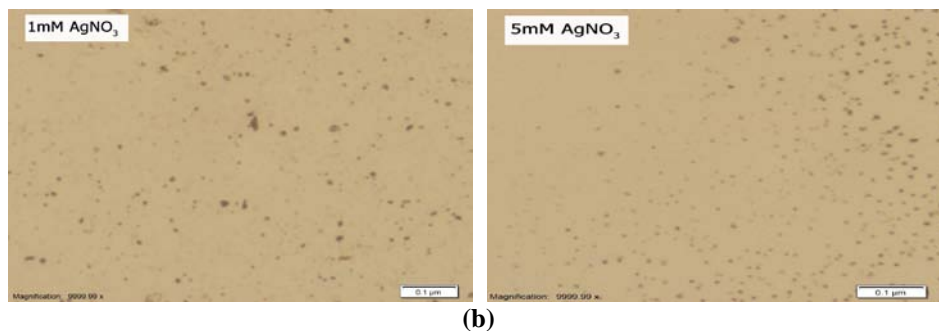
Fig. 3. Microscopic images of (a) Cu NPs having initial precursor concentration of 0.01M and 0.05M, and (b) Ag NPs with initial precursor concentration of 1mM and 5mM.

3.2. Optical Microscopy

Copper and silver nanoparticles were characterized by high resolution advanced optical microscope to determine the morphology and size of the prepared nanoparticles. Fig. 3 shows the microscopic images of Cu and Ag nanoparticles. From this figure it is seen that the size of the nanoparticles changes with concentrations and the average sizes of the particles are less than 40nm with spherical structure.

3.3. Study of FT-IR

To examine the interaction between the SDS and copper nanoparticles, FT-IR spectra were recorded for SDS alone and SDS capped copper nanoparticles respectively. FT-IR spectrometry is useful for understanding the role of the organic molecules in this study. Fig. 4 shows the IR spectra of pure SDS and the copper nanoparticles coated with SDS in the range of 400–4000cm^{-1}. For pure SDS (Fig. 4(a)), the peak at 590 cm^{-1} due to the O-H out-of-plane bending and the peaks in the range of 610–1000cm^{-1} are attributed to the C–H bending vibration. The two absorption peaks that appear at 1081.23 and 1223.61cm^{-1} are due to the SO_3 stretching vibrations. The peaks at 1383.79 cm^{-1}, 1468.41 cm^{-1} and 1637.78 cm^{-1} are corresponding to CH_2 wagging, CH_3 and HOH bending vibrations, respectively. The CH_3 asymmetric (2957.03 cm^{-1}), the CH_2 asymmetric (2918.10 cm^{-1}), CH_3 symmetric (2873 cm^{-1}), CH_2 symmetric (2850.43 cm^{-1}) and OH (3461.96 cm^{-1}) stretching bands are also observed in the figure.
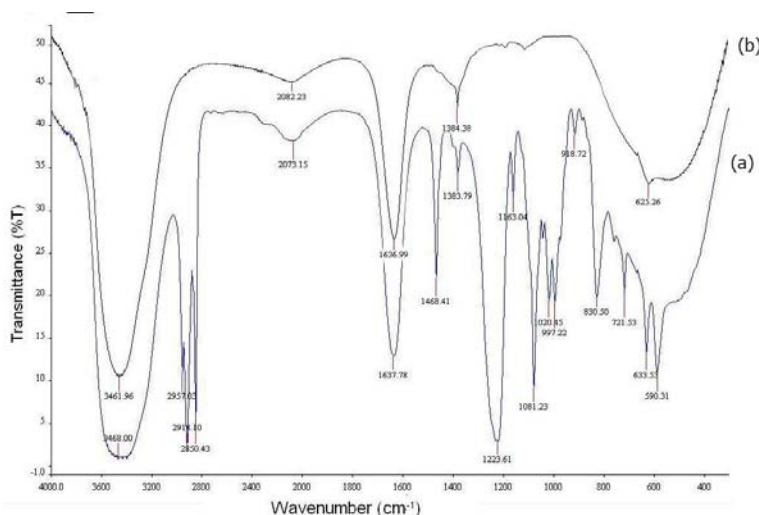
Fig. 4. The FT-IR spectra of (a) pure SDS and (b) SDS capped copper nanoparticles

Comparing Fig. 4(a) and (b), it observed that all the peaks in Fig. 4(b) are weaker, the stretching vibration of O–H bands at 3468.00 cm^{-1} and bending vibration of C–H band at 633.53 cm^{-1} in the spectrum of pure SDS is shifted to 3461.96 and 625.26 cm^{-1}, respectively, in the spectrum of the copper coated with surfactant. The HOH bending vibration band at 1637.78cm^{-1} and CH_2 wagging band at 1383.79 cm^{-1} are shifted slightly for coated copper nanoparticles. These peak shifts reveal that there exist an interaction between Cu nanoparticles and SDS. All other peaks that present in the spectrum of pure SDS are disappeared in the spectrum of the copper coated

with SDS. These dramatic differences indicate that a chemical bond could have been formed between SDS and Cu atoms on the surface of the copper nanoparticles.

4. Conclusions

Metallic nanoparticles were successfully synthesized by chemical reduction method. UV-visible absorption spectra of Cu and Ag nanoparticles give absorbance maxima at about 575 and 405nm, respectively. Sizes of the nanoparticles were changed with changing initial precursor concentrations. FT-IR study of Cu nanoparticles shows that a chemical bond could have formed between SDS and Cu atoms on the surface of the copper nanoparticles.

5. Acknowledgement

6. References

[1]   S.I. Bozhkoa, A.N. Chaikaa, G.A. Emelchenkoa, V.M. Masalova, A.M. Ionova, A.N. Gruzintsevb, G.M. Mikhailovb and B.K. Medvedev, "Mono- and multilayered opalline superlattices: application to nanotechnology of 2D ordered array of nanoobjects and 3D metalattices", *Appl. Surf. Sci.* Vol. 234, pp. 93-101, 2004.

[2]   G. Walters and I.P. Parkin, "The incorporation of noble metal nanoparticles into host matrix thin films: synthesis, characterisation and applications", *J. Mater. Chem.* Vol. 19, No. 5, pp. 574-590, 2009.

[3]   M.C. Daniel and D. Astruc, "Gold Nanoparticles: Assembly, Supramolecular Chemistry, Quantum-Size-Related Properties, and Applications toward Biology, Catalysis, and Nanotechnology", *Chem. Rev.* Vol. 104, pp. 293-346, 2004.

[4]   S. Basu, S. Jana, S. Pande and T. Pal, "Interaction of DNA bases with silver nanoparticles: Assembly quantified through SPRS and SERS", *J. Colloid Interface Sci.* Vol. 321, No. 2, pp. 288-293, 2008.

[5]   B.C. Sih and M.O. Wolf, "Metal nanoparticle-conjugated polymer nanocomposites", *Chem. Commun.* Vol. 27, pp. 3375-3384, 2005.

[6]   N. Cioffi, N. Ditaranto, L. Torsi, R. A. Picca, E. D. Giglio, L. Sabbatini, L. Novello, G. Tantillo, T. Bleve-Zacheo and P. G. Zambonin, "Synthesis, analytical characterization and bioactivity of Ag and Cu nanoparticles embedded in poly-vinyl-methyl-ketone films", *Anal. Bioanal. Chem.* Vol. 382, pp. 1912-1918, 2005.

[7]   Z.H. Chohan, K.M. Khan and C.T. Supuran, "Synthesis of antibacterial and antifungal cobalt(II), copper(II), nickel(II) and zinc(II) complexes with bis-(1,1-disubstituted ferrocenyl)thiocarbohydrazone and bis-(1,1-disubstituted ferrocenyl)carbohydrazone", *Appl. Organomet. Chem.* Vol.18, pp. 305–310, 2004.

[8]   V. Acharya, C.R. Prabha and C. Narayanamurthy, "Synthesis of metal incorporated low molecular weight polyurethanes from novel aromatic diols, their characterization and bactericidal properties", *Biomaterials*, Vol. 25, 4555-4562, 2004.

[9]   Pal A., Shah S., Devi S. "Preparation of silver, gold and silver–gold bimetallic nanoparticles in w/o microemulsion containing TritonX-100", *Colloids and Surfaces A,* Vol. 302, pp. 483-487, 2007.

[10] M.J. Rosemary and T. Pradeep, "Solvothermal synthesis of silver nanoparticles from thiolates", *J. Colloid and Interface Science,* Vol. 268, pp. 81-84, 2003.

[11] P.K. Khanna, S. Gaikwad, P.V. Adhyapak, N. Sing and R. Marimuthu, "Synthesis and characterization of copper nanoparticles", *Mat. Lett.* Vol. 61, pp. 4711-4714, 2007.

[12] K.C. Song, S.M. Lee, T. S. Park and B.S. Lee, "Preparation of colloidal silver nanoparticles by chemical reduction method", *Korean J. Chem. Eng.* Vol. 26, No.1, pp. 153-155, 2009.

[13] S.H. Wu and D.H. Chen, "Synthesis of high-concentration Cu nanoparticles in aqueous CTAB solutions", *J. Colloid and Interface Science,* Vol. 273, No. 1, pp. 165-169, 2004.

[14] M.A.A. Mamun, Y. Kusumoto and M. Muruganandham, "Simple new synthesis of copper nanoparticles in water/ acetonitrile mixed solvent and their characterization", *Mat. Lett*. Vol. 63, pp. 2007-2009, 2009.

[15] S.S. Joshi, S.F. Patil, V. Iyer and S. Mahumuni, "Radiation induces synthesis and characterization of copper nanoparticles", *Nanostructured Materials,* Vol. 10, No. 7, pp. 1135-1144, 1998.

[16] S.D. Solomon, M. Bahadory, A.V. Jeyarajasingam, S.A. Rutkowsky and C. Boritz, "Synthesis and Study of Silver Nanoparticles", *J. Chem. Edu.* Vol. 84, No. 2, pp. 322-325, 2007.

Studies on the Artificial Ageing and Microstructure of the Al-6Si-0.5Mg Alloys with Copper Addition at Various Levels

A. Hossain[1], M. S. Kaiser[2] and A. S. W. Kurny[1]

[1]Department of Materials and Metallurgical Engineering, [2]Institue of Appropriate Technology, Bangladesh University of Engineering and Technology, Dhaka-1000, Bangladesh
E-mail: aswkurny@mme.buet.ac.bd

Abstract

The influence of Cu content on the artificial age hardening and microstructure of Al-6Si-0.5Mg-xCu (x = 0.5%, 1%, 2% and 4%) was investigated. Different amounts of copper were added to molten Al-Si-Mg master alloy. Molten alloys at 700°C were cast in a metal mold. The solution treatment was performed at 540°C for 2h and then the specimens were quenched in ice salt water. The samples were aged isochronally for 60 minutes at temperatures up to 400°C and isothermally at 225°C for different periods in the range 15 to 360 minutes. Hardness of the alloys was measured to study the age hardening effect due to copper addition. Resistivity changes with annealing time at 225°C were measured to understand the precipitation behaviour of the alloys. The microstructure was examined using an optical microscope and a scanning electron microscope. Maximum hardness of the solution treated alloys increased with an increase in Cu content. However, copper in amounts of more than 2% did not cause significant increase in hardness during artificial ageing at 225°C. The hardness of matrix increases due to precipitation hardening. The microstructural investigations show that the shape of the eutectic Si particles changes to granular type in all alloys after heat treatment.

Keywords: Al-Si-Mg-alloys, Cu content, Hardness, Age hardening, Resistivity.

1. Introduction

Aluminium-silicon cast alloys are widely used in the automotive industry due to their outstanding castability, good wear resistance and low thermal expansion, together with their low specific weight. These properties lead to the application of Al-Si alloys in automotive industry, especially for cylinder blocks, cylinder heads, pistons and valve lifters [1-3].

The quality of microstructure of Al-Si alloys depends on chemical composition, alloying elements, melting process, casting process and solidification rate. The mechanical properties of cast Al-Si alloy parts largely depend on grain size and its morphology, dendrite arm spacing (DAS), size and distribution of secondary phases [4]. As DAS decreases, structural refinement takes place which leads to improvement in mechanical properties [5]. Addition of Mg and Cu to Al–Si alloys increases strength and reduces ductility [6, 7]. For Al–Si–Mg and Al–Si–Cu–Mg alloys, a heat treatment consisting of solution treatment, quenching and ageing is often used to increase the strength by precipitating nanometer particles, which provide excellent obstacles for the dislocation movement [8]. For Al–Si–Mg alloys, the age hardening is caused by the precipitation of β'' and/or β' phases (precursor of Mg_2Si phases) [2]. For Al–Si–Mg–Cu alloys, the precipitation behaviors are rather complicated and several phases such as β (Mg_2Si), $\theta(CuAl_2)$, $S(CuMgAl_2)$ or Q ($Cu_2Mg_8Si_6Al_5$) in metastable situations may exist [9].

Heat treatment is generally carried out to obtain an optimum combination of strength and ductility in Al-Si-Cu-Mg alloys. The steps for the heat treatment consist of solution treatment, quenching and artificial aging [3]. The age-hardening mechanisms responsible for strengthening are based on the formation of intermetallic compounds during decomposition of a metastable supersaturated solid solution obtained by solution treatment and quenching. The mechanical properties of these alloys are significantly influenced by the presence of precipitates. $W(Al_xCu_4Mg_5Si_4)$ and $S(Al_2CuMg)$ phases coexist with $\theta(Al_2Cu)$ and $\beta(Mg_2Si)$ phases in aged Al-Si-Cu-Mg alloys. θ phase preferentially precipitates on the dislocations introduced around eutectic Si particles in the Al-Si-Cu based alloys, while $\lambda(Al_5Cu_2Mg_8Si_5)$ phase homogenously precipitates in the α matrix, regardless the sites of dislocations and therefore these precipitates significantly raise the age-hardening

ability. Q($Al_5Cu_2Mg_8Si_6$) phase exhibiting an effect on age-hardening may exist in aged Al-Si-Cu-Mg alloys [7, 10].

In this study, the effect of Cu content at various levels on the age hardening, precipitation behavior and microstructure of Al-6Si-05Mg alloys was studied.

2. Experimental Procedures

Calculated amounts of commercially pure aluminium (99.7% pure) and Al-7.1Si-0.3Mg master alloy were melted in a gas fired clay-graphite crucible under suitable flux cover (degasser, borax etc). Magnesium ribbon (99.7% pure) was added to the molten solution. Copper, in the form of wire (99.98% purity) was then added by plunging. The final temperature of the melt was always maintained at 950±15°C with the help of an electronic temperature controller. Before casting, the melt was homogenized by stirring at 700°C. Casting was done in cast iron metal moulds preheated to 200°C. Mould sizes were 15mm x 150mm x 300mm. All the alloys were analysed by wet chemical and spectrochemical methods simultaneously. The chemical compositions of the alloys are given in Table 1. The cast samples were first ground properly to remove the oxide layer from the surface. All the alloys were then homogenised by heating in an electric muffle furnace for 24 hours at 500°C. The homogenised samples were solution treated at 540°C for 120 minutes and quenched in salt iced water solution. As-cast and quenched samples were aged isochronally for 60 minutes at different temperature up to 400°C. The samples were also isothermally aged at 225°C for different ageing times ranging from 15 to 360 minutes. Hardness of different alloys processed with different schedules and aged at different temperatures was measured in Rockwell hardness testing machine with 60 kg load and 1/16$^{//}$ steel ball indenter [F scale]. An average of seven consistent readings was accepted as the representative hardness value of an alloy. Electrical conductivity of the heat treated alloys was determined with an Electric Conductivity Meter, type 979. Pieces of the alloy measuring 15 mm x 20 mm x 5 mm were ground and polished prior to the electrical conductivity measurement. Electric resistivity was calculated from the conductivity data. All the samples were observed under an optical microscope. The specimens for metallographic observation were prepared using standard techniques, final polishing was done with very fine alumina. The etching was done in Keller's reagent (HNO_3 – 2.5 cc, HCl – 1.5 cc, HF – 1.0 cc and H_2O – 95.0 cc). The washed and dried samples were observed carefully in an OPTIKA Microscope (Model: B-600 MET) at different magnifications and some selected photomicrographs were taken. Scanning Electron Microscopy of the selected samples was carried out by a Scanning Electron Microscope type Inspect^{TM} S50 FEI Quanta at various magnifications.

Alloy synthesis and production of samples for aging studies

Table 1. Chemical Composition of the Experimental Alloys (wt %)

Alloy	Si	Mg	Cu	Ni	Fe	Zn	Mn	Pb	Cr	Sn	Ti	Sb	Al
1	5.902	0.461	0.007	0.005	0.146	0.004	0.002	0.003	0.001	0.004	0.099	0.008	Bal
2	6.033	0.517	0.558	0.006	0.129	0.006	0.003	0.002	0.001	0.001	0.094	0.005	Bal
3	6.105	0.555	1.185	0.029	0.334	0.005	0.005	0.002	0.004	0.001	0.088	0.005	Bal

| 4 | 5.801 | 0.497 | 1.980 | 0.003 | 0.300 | 0.004 | 0.004 | 0.002 | 0.005 | 0.001 | 0.094 | 0.005 | Bal |
| 5 | 5.884 | 0.532 | 3.800 | 0.014 | 0.181 | 0.003 | 0.003 | 0.001 | 0.010 | 0.001 | 0.086 | 0.007 | Bal |

Remarks: Alloy 3 Al-6 wt% Si-0.5% Mg-1 wt% Cu
Alloy 1 Al-6 wt% Si-0.5 wt% Mg   Alloy 4 Al-6 wt% Si-0.5% Mg-2 wt% Cu
Alloy 2 Al-6 wt% Si-0.5 wt% Mg-0.5 wt% Cu Alloy 5 Al-6 wt% Si-0.5% Mg-4 wt% Cu

3. Results and Discussion

3.1. Optical and SEM micrographs:

Microstructure Al-6Si-0.5Mg alloy in T6 condition is presented in Fig. 1. Analyzing the micrographs of the alloy after solution treatment at 540°C for 2h, it had been found that during solution heat treatment the morphology of primary eutectic Si changes from relatively large needle like structure to the more refined "Chinese script" and spherical in shape particles.

The optical microstructure of solution treated alloy 1 shows dendrites with black second phase particles within inter-dendritic spaces (Fig. 1). Addition of copper to the base alloy by 0.5 wt% shows a diminution in the amount of second phase particles. It further appears that dendrite arm spacing is decreased in Alloy 2 with the consequent refinement of dendrites (Fig. 2).
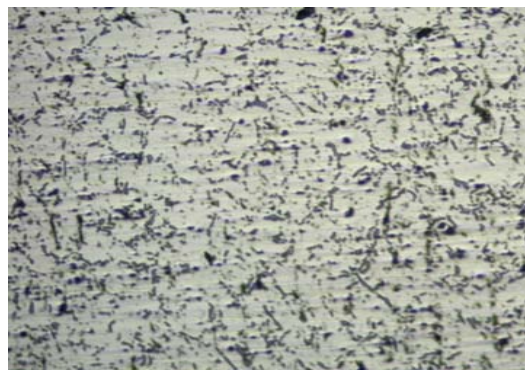
Fig. 1. Optical micrograph of solution treated alloy 1
$\overline{100\mu m}$
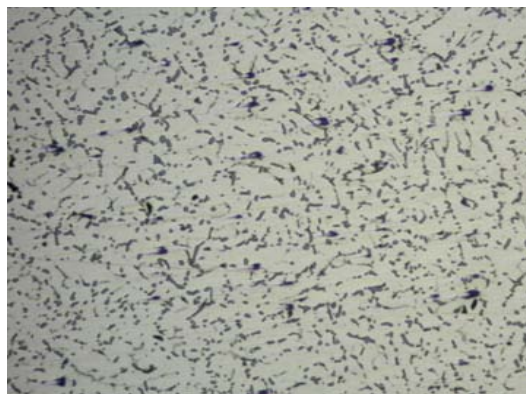
$\overline{100\mu m}$
Fig. 2. Optical micrograph of solution treated alloy 2
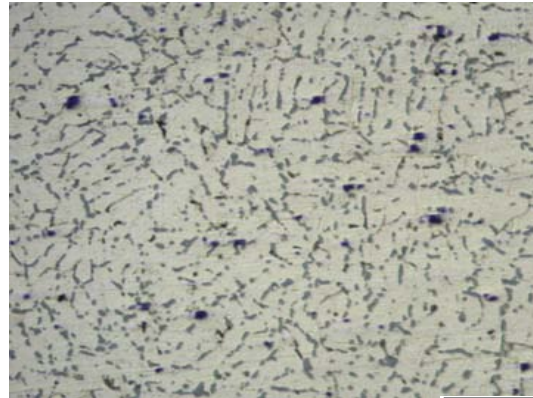
Fig. 3. Optical micrograph of solution treated alloy 4

The structural fineness is seen to increase with increasing copper content. In the alloys with 2 wt% Cu and 4 wt% Cu the amount of second phase particles is reduced to a great extent. The dendrite fragments are seen to have refined remarkably (Figs. 3 and 4).

Where the alloys are aged at 300°C for 1 hour, noticeable change in microstructures results. Alloy 1 shows relatively coarse grain structure with somewhat less amount of second phase constituent (Fig. 5). Alloy with 2 wt% Cu has not been able to refine grain structure to any greater extent (Fig. 6)
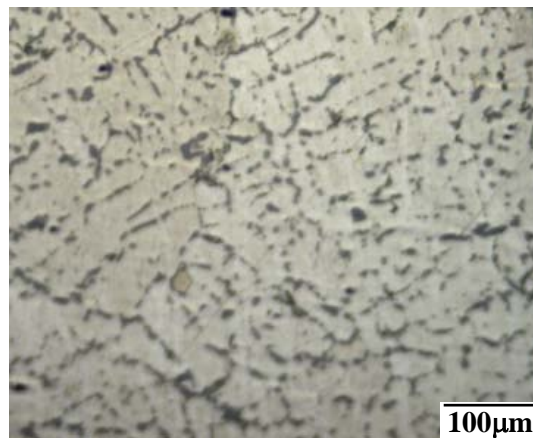
Fig. 4. Optical micrograph of solution treated alloy 5
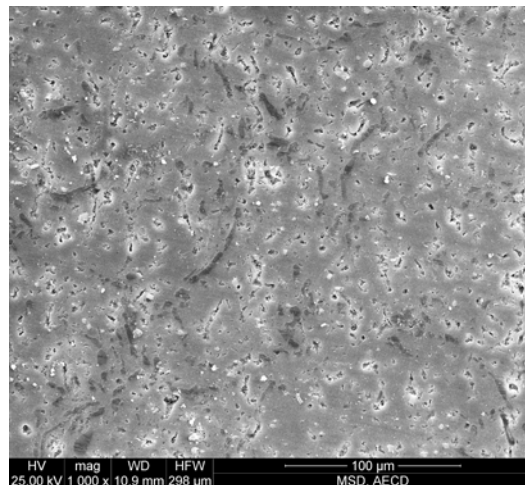
Fig. 5. SEM micrograph of alloy 1 aged at 300°C for 1 hour
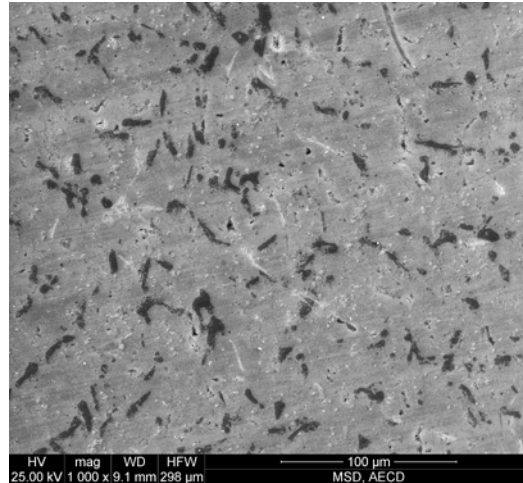
Fig. 6. SEM micrograph of alloy 4 aged at 300°C for 1 hour

3.2. Isochronal Ageing:

Figure 7 shows the isochronal aging behavior of the different alloys. For all the alloys, the peak aging condition is attained at 225°C. Although hardness of the base alloy is lower than the Cu-bearing alloys in the solution treatment. The decrease in hardness became more pronounced with increasing aging temperature beyond 250°C. However, the Cu-bearing alloy exhibits stronger resistance to softening in comparison with the base alloy. Hardness in both of the as quenched conditions and peak-aged conditions increases strongly with increase of Cu content. The increase of hardness in as quenched conditions with increase of Cu content indicates that the solid-solution strengthening of the alloys is enhanced with increase of Cu content. This indicates that addition of Cu increases the age hardening ability slightly; moreover Cu addition decreases the age hardening rate. The strong increase of maximum hardness during ageing with increase of Cu content is mainly the results of solid-solution strengthening of Cu on a (Al) matrix.
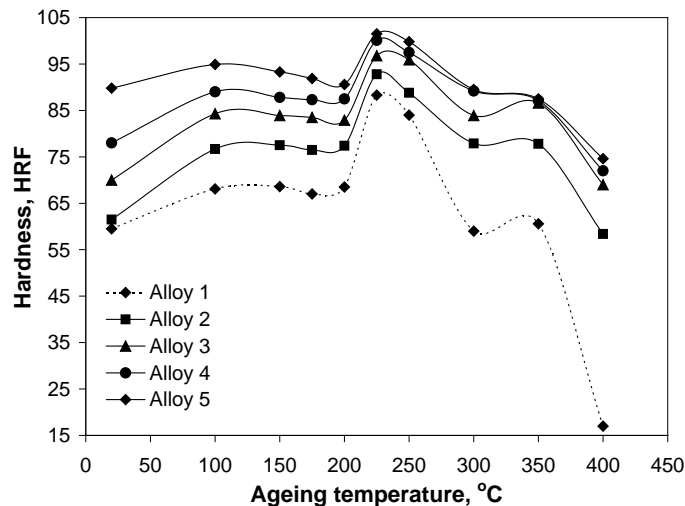
Fig. 7. Isochronal ageing curve of the alloys, aged for one hour

3.3. Isothermal Ageing:

Fig. 8 shows the isothermal aging behavior of different alloys at 225°C, all the alloys attain the peak condition after 60 min. In the case of Cu-bearing alloys the peak hardness is maintained without any appreciable softening duration of aging. Fig. 9 shows the effect of the ageing time on the electrical resistivity of the samples isothermal ageing at 225°C. It is clear that the electrical resistivity of the material decreased with increasing holding time of ageing. It can also be seen that the most significant decrease in the electrical resistivity occurs at the first 2 hours of ageing. The electrical resistivity shows a step decrease and then an increase leading to peak or a plateau followed by a decrease until it reaches a nearly constant value.
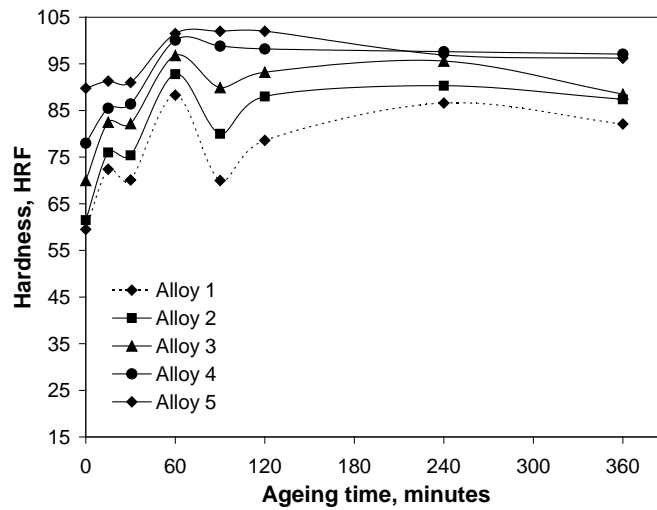
Fig. 8. Isothermal ageing curve of the alloys, aged at 225°C

In the presence of secondary particles, the primary elective parameters on the electrical resistivity are as follows: [8] (1) the volume fraction of fine and coherent particles in the structure, (2) the particle interspacing, and (3) the concentration of elements in solid solution. The formation of dispersoids leads to a decrease in the concentration of the corresponding elements in the matrix. If the elements precipitate out during a thermal process such as homogenization or precipitation hardening, the change in the electrical resistivity of the material depends on the size and the interface of the newly formed particles. If the new particles are small and coherent, the electrical resistivity of the material increases and vice versa. The formation of the plateau in the electrical resistivity curve may be due to the balance of the increase in the concentrations of some elements, namely Si, Mg, and Cu in the matrix. When the rate of the increase in the electrical resistivity due to the dissolution of constitutive particles and therefore, the enrichment of the structure becomes equal to the rate of the decrease in the electrical resistivity due to the formation of dispersoids, a peak or plateau is observed in the electrical resistivity curve.
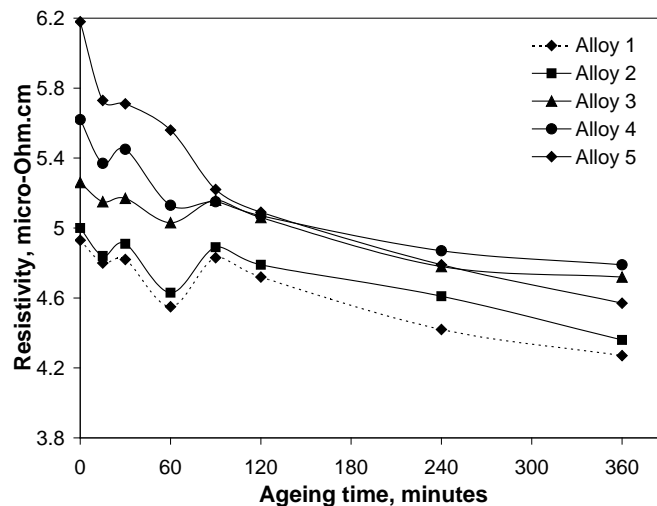
Fig. 9. Variation of resistivity of the alloys, Isothermally aged at 225°C

The effect of grain refinement of the alloys is clearly evident from the resistivity curves, which show a significant difference of resistivity values of the copper added alloy with that of the base alloy. The initial high resistivity of copper treated alloy is indicative of high electron scattering sites viz. grain boundary area to mean that grains in all those alloys are finer. Formation of supersaturated solid solution assures a high precipitation hardening effect upon decomposition of this solid solution with the formation of fine coherent precipitates. The

softening of the alloys at higher temperature may be due to particle coarsening effect. The initial drop in resistivity is due to stress relieving in the alloys during ageing. The steeper drop at the initial period of isothermal ageing at 225°C may be attributed to the formation solute atom vacancy complex. Transition metals are known to bind vacancies strongly. For this reason, the number density of scattering centers is reduced. This causes a sharp fall in resistivity. The subsequent increase in resistivity is due to the appearance of fine precipitates. When the ageing temperature is small, the resistivity continues to increase beyond the peak because the precipitation formation and reordering of atoms continues.

4. Conclusions

Addition of Cu to Al–6Si–0.5Mg alloy decreases the age hardening rate. Maximum hardness could be achieved by artificial ageing for 1h at 225°C. With increase of Cu content, the solid-solution strengthening of the alloys is enhanced, but the age hardening ability increases slightly, moreover it decreases a little with addition of 2 wt% Cu. The strong increase of maximum hardness during ageing with increase of Cu content is mainly the results of solid-solution strengthening of Cu on a (Al) matrix. The microstructural investigations show that the shape of the eutectic Si particles changes to granular type in all alloys after heat treatment.

References

[1] H. Liao, Y Suny and G. Sun, "Correlation between mechanical properties and amount of dendritic α-Al phase in as-cast near-eutectic Al-11.6%Si alloys modified with strontium" Materials Science and Engineering A, Vol. 335, No. 1−2, pp. 62−66, 2002.

[2] M. Zeren, E. Karakulak and S. Gumus, "Influence of Cu addition on microstructure and hardness of near-eutectic Al-Si-xCu-alloys" Transaction of Nonferrous Metals Society of China, , Vol. 21, pp. 1698-1702, 2011.

[3] G. Wang, Q. Sun, L. Feng, L. Huo and C. Jing, "Influence of Cu content on ageing behavior of AlSiMgCu cast alloys" Materias and Design, Vol. 28, pp. 1001-1005, 2007.

[4] H. Kezhun, Y. Fuxiao, Z. Dazhi, and Z. Liang, "Microstructural evoluation of direct chill cast Al-15.5Si-4Cu-1Mg-1Ni-0.5Cr alloy during solution treatment" China foundry, Vol. 8, No. 3, pp. 264-268, 2011.

[5] L. Lasa and J. M. Rodrigues, "Characterization of the dissolution of the Al2Cu phase in two Al-Si-Cu-Mg casting alloys using calorimetry" Materials Characterization, Vol. 48, No. 5, pp. 371-378, 2002.

[6] W. Reif, J. Dutkiewicz, R. Ciach, S. Yu and J. Krol, " Effect of aging on the evolution of precipitate in AlSiCuMg alloys" Materials Science and Engineering A, Vol. 234-236, No. 30, pp. 165-168, 1997.

[7] G. Wang, X. Bian, W. Wang and J. Zhang, "Influence of Cu andminor elements on solution treatment of Al-Si-Mg-Cu cast alloys" Materials Letters, Vol. 57, No. 24-25, pp. 4083-4087, 2003.

[8] A. R. Eivani, H. Ahmed, J. Zhou and J. Duszczyk, "Correlation between Electrical Resistivity, Particle Dissolution, Precipitation of Dispersoids and Recrystallization Behavior of AA7020 Aluminium Alloy" Metallurgical and Material transactions A, Vol. 40A, pp. 2435-2446, 2009.

[9] I. C. Barlow, W. M. Rainforth, H. Jones, " The role of silicon in the formation of the $(Al_5Cu_6Mg_2)$ r phase in Al–Cu–Mg alloys", J Mater Sci Vol. 35, pp. 1413–81.2003.

[10] L. Lasa and J. M. Rodrigues, "Characterization of the dissolution of the Al_2Cu phase in two Al-Si-Cu-Mg casting alloys using calorimetry" Materials Characterization, Vol. 48, No. 5, pp. 371-378, 2002.

Influence of Copper and Nickel Addition on Microstructure and Artificial Ageing of Al-6Si-0.5Mg Alloys

A. Hossain[1], M. S. Kaiser[2] and A. S. W. Kurny[1]

[1]Department of Materials and Metallurgical Engineering, [2]Instiue of Appropriate Technology, Bangladesh University of Engineering and Technology, Dhaka-1000, Bangladesh
E-mail: aswkurny@mme.buet.ac.bd

Abstract

The effects of Cu and Ni on the artificial age hardening behaviour and microstructure of Al-6Si-0.5Mg alloys were investigated. Different amounts of Cu and Ni were added to molten Al-Si-Mg master alloys. The molten alloys at 700°C were cast in metal molds. The solution treatment was performed by heating at 540°C for 2h followed by quenching in iced salt-water. The samples were aged isochronally for 60 minutes at temperatures up to 400°C and isothermally at 225°C for different periods in the range 15 to 360 minutes. Age hardening behaviour was followed by hardness measurements. Resistivity changes with annealing time at 225°C were measured to understand the precipitation behaviour of the alloys. The microstructure was examined using an optical microscope and a scanning electron microscope. Maximum hardness could be achieved by artificial ageing for 1h at 225°C. Cu was found to be more effective than nickel in increasing the hardness and addition of both Cu and Ni resulted in still higher hardness. The hardness of the matrix increased due to precipitation. The particle distribution including eutectic silicon and intermetallic compounds was found to be more homogenous after heat treatment.

Key words: Al-Si-Mg-alloys, Heat-treatment, Age hardening, Resistivity, Microstructure

1. Introduction

Al-Si-Mg wrought and casting alloys have found extensive use in a variety of applications in the automotive, aerospace and defence industries due to their wide range of mechanical and physical properties [1-2]. The accelerated need for weight reduction however calls for improved properties in these alloys. Among the elements added to Al–Si base alloys for increasing strength and to control grain-size, copper has arrested considerable attention. Cu addition reduces the natural ageing rate of Al-Mg-Si alloys but generally increase the kinetics of precipitation during artificial ageing [3]. Addition of Cu to Al-Si alloys leads to the formation of Al_2Cu phases and other intermetallic compounds, which influences the strength and ductility [4,5].

The castings are usually heat treated to obtain the desired combination of strength and ductility. The most common is the T6 heat treatment, which consist of a solution heat treatment, water quench, natural and artificial ageing. A solutionizing treatment in the range 400-560°C dissolve hardening agents in the Al matrix, homogenizes the casting, and modifies the morphology of the eutectic silicon. Castings are quenched from the solution treatment temperature to suppress the formation of intermetallic phases, retain alloying elements in solution to form a supersaturated solid solution and limit their diffusion to grain boundaries, undissolved particles or other defect locations. [6]. A report regarding the properties of the Al_3Ni system indicates that an increased amount of Al_3Ni reinforcement reduces the time of peak ageing [7].

Thus Cu and Ni could strengthen aluminium alloys through precipitation and dispersion hardening respectively. The object of this study is to investigate the individual and combined effects of Cu and Ni on the age hardening properties and microstructure of Al-Si-Mg alloys.

2. Experimental Procedures

Calculated amounts of commercially pure aluminium (99.7% pure) and Al-7.1Si-0.3Mg master alloy were melted in a gas fired clay-graphite crucible under suitable flux cover (degasser, borax etc). Magnesium ribbon (99.7% pure) was added to the molten solution. Copper, in the form of wire (99.98% purity), Ni in the form of chips were then added by plunging. The final temperature of the melt was always maintained at 950±15°C with the help of an electronic temperature controller. Before casting, the melt was homogenized by stirring at 700°C. Casting was done in cast iron metal moulds preheated to 200°C. Mould sizes were 15mm x 150mm x 300mm.

All the alloys were analysed by wet chemical and spectrochemical methods simultaneously. The chemical compositions of the alloys are given in Table 1. The cast samples were first ground properly to remove the oxide layer from the surface. All the alloys were then homogenised by heating in an electric muffle furnace for 24 hours at 500°C. The homogenised samples were solution treated at 540°C for 120 minutes and quenched in salt iced water solution. As-cast and quenched samples were aged isochronally for 60 minutes at different temperature up to 400°C. The samples were also isothermally aged at 225°C for different ageing times ranging from 15 to 360 minutes. Hardness of different alloys processed with different schedules and aged at different temperatures was measured in Rockwell hardness testing machine with 60 kg load and 1/16$^{//}$ steel ball indenter [F scale]. An average of seven consistent readings was accepted as the representative hardness value of an alloy. Electrical conductivity of the heat treated alloys was determined with an Electric Conductivity Meter, type 979. Pieces of the alloy measuring 15 mm x 20 mm x 5 mm were ground and polished prior to the electrical conductivity measurement. Electric resistivity was calculated from the conductivity data. All the samples were observed under an optical microscope. The specimens for metallographic observation were prepared using standard techniques, final polishing was done with very fine alumina. The etching was done in Keller's reagent (HNO_3 – 2.5 cc, HCl – 1.5 cc, HF – 1.0 cc and H_2O – 95.0 cc). The washed and dried samples were observed carefully in an OPTIKA Microscope (Model: B-600 MET) at different magnifications and some selected photomicrographs were taken. Scanning Electron Microscopy of the selected samples was carried out by a Scanning Electron Microscope type Inspect^{TM} S50 FEI Quanta at various magnifications.

Alloy synthesis and production of samples for aging studies

Table 1. Chemical Composition of the Experimental Alloys (wt %)

Alloy	Si	Mg	Cu	Ni	Fe	Zn	Mn	Pb	Cr	Sn	Ti	Sb	Al
1	5.902	0.461	0.007	0.005	0.146	0.004	0.002	0.003	0.001	0.004	0.099	0.008	Bal
2	5.801	0.497	1.980	0.003	0.300	0.004	0.004	0.002	0.005	0.001	0.094	0.005	Bal
3	5.965	0.454	0.007	2.202	0.141	0.006	0.003	0.002	0.005	0.001	0.088	0.008	Bal
4	5.760	0.501	1.968	2.001	0.265	0.001	0.004	0.001	0.010	0.001	0.081	0.005	Bal

Remarks:
Alloy 1: Al-6 wt% Si-0.5 wt% Mg   Alloy 3: Al-6 wt% Si-0.5 wt% Mg-2 wt% Ni
Alloy 2: Al-6 wt% Si-0.5% Mg-2 wt% Cu   Alloy 4: Al-6 wt% Si-0.5 wt% Mg-2 wt% Cu-2 wt% Ni

3. Results and Discussion

3.1. Optical and SEM micrographs:

Figures 1 to 4 show the optical micrograph of the alloys, solution treated for 120 minutes at 540°C. α (Al) face centered cubic solid solution is the predominant phase in the microstructure of the alloys. The matrix of the specimens show equiaxed grain structure. During solution heat treatment primary particles Si- and Cu-containing phases: Al_2Cu and $Al_5Cu2Mg8Si6$ dissolve in the α -Al matrix. The subsequent aging heat treatment leads to formation from the supersaturated solid solution fine intermetallic strengthening particles of α-Mg_2Si and Al_2Cu.
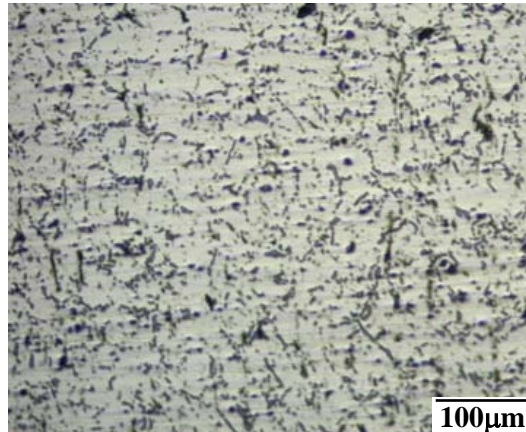
Fig. 1. Optical micrograph of solution treated alloy 1
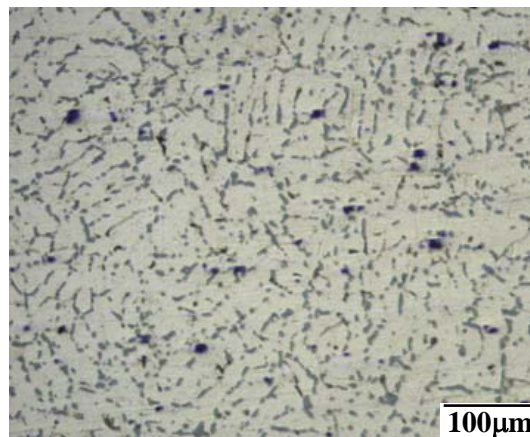
Fig. 2. Optical micrograph of solution treated alloy 2
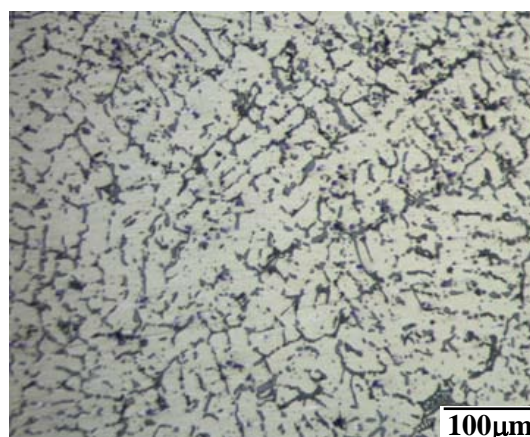
Fig. 3. Optical micrograph of solution treated alloy 3
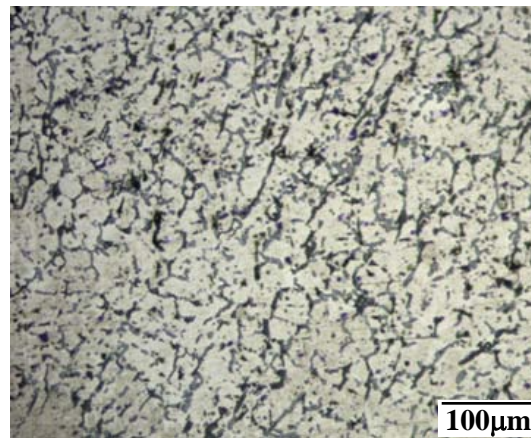
Fig. 4. Optical micrograph of solution treated alloy 4

The scanning electron micrographs of the aged samples show the presence of the intermetallic compounds (Figures 5-6). According to the chemical compositions of the samples the precipitated particles should contain Cu, Mg and Si. It can thus be inferred that the hard phases in Alloy-1 is Mg_2Si, in Alloy -2: Mg_2Si and Al_2Cu, in Alloy-3: Mg_2Si and Al_3Ni and in alloy-4 : Al_2Cu, Mg_2Si and Al_3Ni.
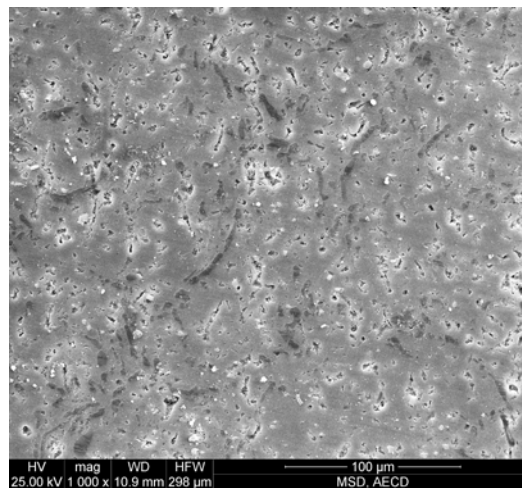
Fig. 5. SEM micrograph of alloy 1 aged at $300^{o}C$ for 1 hour
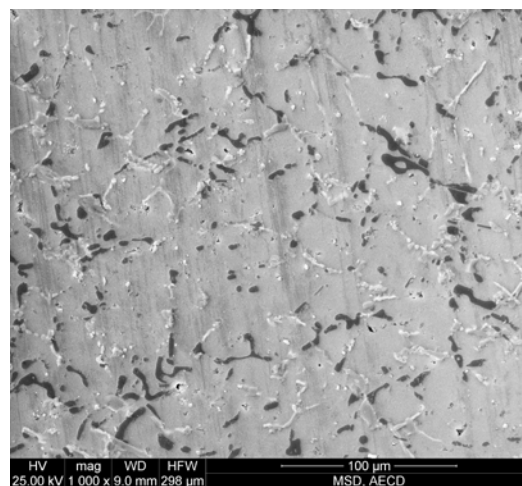
Fig. 6. SEM micrograph of alloy 4 aged at $300^{o}C$ for 1 hour

3.2. Isochronal Ageing:

Fig. 7 shows the plots of hardness against ageing temperature during isochronal ageing for 1h of the as-quenched samples of Al–6Si–0.5Mg with additions of Cu or of Ni or of both the elements. The addition of both Cu or of Ni to the base alloy (alloy-1) strongly increases the hardness in both the as-quenched and the peak aged conditions. Peak aged (maximum hardness) condition is achieved at 225 °C for 1h artificial ageing for all alloys. Hardness value of Alloy-2 (2% Cu) is greater than that of Alloy-3 (2% Ni). Thus the effect of Cu on precipitation hardening of the base alloy is higher than that of Ni. When both Cu and Ni has been added (Alloy-4), the hardness value is slightly higher than that of Alloy-3 (containing 2%Ni).
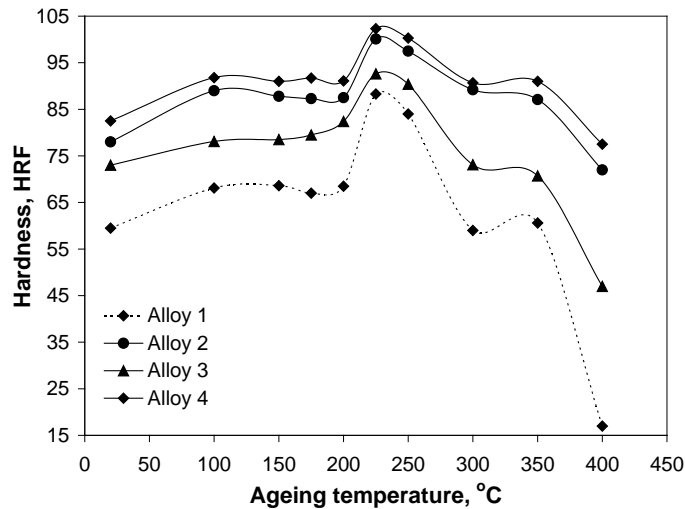
Fig. 7: Isochronal ageing curve of the alloys, aged for one hour

For Al-Si-Mg alloys, the precipitation sequence is α_{ss} ⟶clusters/GP zones⟶ β'' ⟶ β' ⟶ β (Mg$_2$Si) [8]. The age hardening is caused by the precipitation of β'' and/or β' phases (precursor of Mg$_2$Si phases) [9]. For Al-Si-Mg-Cu alloys, the precipitation behaviors are rather complicated and several phases such as β (Mg$_2$Si), θ(CuAl$_2$), S(CuMgAl$_2$) or Q(Cu$_2$Mg$_8$Si$_6$Al$_5$) in metastable situations may exist [10]. If Ni is added to the Al–Si–Mg alloy or Al–Si–Mg-Cu alloy systems at first the eutectic Si and Al$_3$Ni hard phases are formed [7]. The hard phases in the eutectic is completely continuous for the as cast and as well as for the solution treated samples and increases the hardness of the alloy.

3.3. Isothermal Ageing:

Hardness of all the alloys (Alloys 1, 2, 3 and 4) was found to vary with time of isothermal ageing at 225°C (Figure 8). All the alloys, except Alloy 3, attained the peak hardness after 60 minutes of ageing. Softening due to overageing was not very pronounced in alloys containing copper. Noticeable decrease in hardness in alloys containing copper (Alloy 2 and Alloy 4) could not be detected during aging for 90 – 360 minutes. Attainment of peak hardness in Alloy 3 (containing 2% Ni) required a little more time. At the same time softening due to overageing was found to begin earlier in Alloy 3 than in alloys containing copper.

With continued ageing beyond peak aged condition hardness in age-hardenable alloys decreases due to growth of the precipitate particles. Softening in alloys containing copper could not be noticed within the time period of investigation. The hardness of the alloy containing only 2% Ni, on the other hand, showed significant decrease in hardness. It thus appears that addition of copper not only enhance the maximum attainable hardness, but also retards overageing.

The chemical compositions of the sample indicate that the precipitate particles contain Cu, Ni and Mg. Therefore the hardening was caused by the precipitation of the Al$_2$Cu, Al$_3$Ni and Mg$_2$Si particles. From the experimental results it can be state that artificial ageing of 60 minutes is sufficient to achieve the hardness and microstructure compared to the other ageing times.

Figure 9 shows the changes of electrical resistivity during aging at 225°C in all the alloys under investigation. It also shows that the electrical resistivity in the solution treated condition depends on the chemical composition of the samples. The resistivity increases as the amount of alloying element increases. It can also be seen that the electrical resistivity of the alloys decreased rather rapidly during the initial period of ageing. The most

significant decrease in the electrical resistivity occur during the first 2 hours of ageing. The electrical resistivity shows a step decrease and then an increase leading to peak or a plateau followed by a decrease until it reaches a nearly constant value.
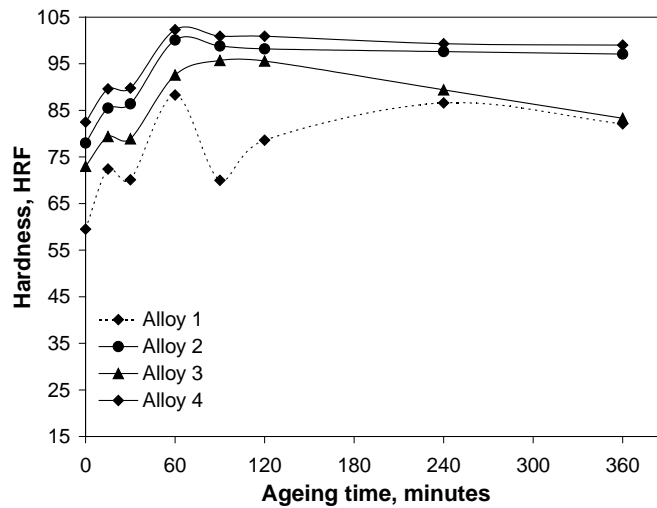
Fig. 8. Isothermal ageing curve of the alloys, aged at 225°C
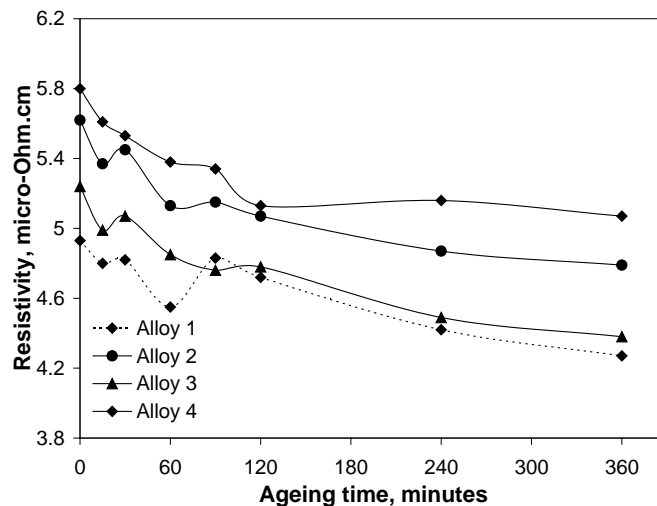
Fig. 9. Variation of resistivity of the alloys, Isothermally aged at 225°C

In the presence of secondary particles, the primary effective parameters on the electrical resistivity are as follows: (1) the volume fraction of fine and coherent particles in the structure, (2) the particle interspacing, and (3) the concentration of elements in solid solution. It is well-known that the presence of alloying elements or impurities in solid solution increases the electrical resistivity of aluminum alloys. The formation of dispersoids leads to a decrease in the concentration of the corresponding elements in the matrix. If the elements precipitate out during a thermal process, the change in the electrical resistivity of the material depends on the size and the interface of the newly formed particles. Regardless of the interface of the dispersoids formed, it is expected that, if the particle interspacing is greater than the required free-passing distance of the electrons (i.e., for precipitate interspacing of 100 nm and larger in aluminum alloys), the effect of particles is negligible. The distances between the dispersoids vary depending on the extent of growth of the precipitate particles. The hardness in the copper containing samples remained more or less unchanged indicating that the size and distribution of the precipitate particles did not vary much. Thus the inter particle spacing and also the resistivity did not changed.

4. Conclusions

Maximum hardness could be achieved by artificial ageing for 1h at 225°C. Cu was found to be more effective than nickel in increasing the hardness and addition of both Cu and Ni resulted in still higher hardness. The hardness of the matrix increased due to precipitation. The particle distribution including eutectic silicon and intermetallic compounds was found to be more homogenous after heat treatment.

References

[1] H. Kezhun, Y. Fuxiao, Z. Dazhi and Z. Liang, "Microstructural evoluation of direct chill cast Al-15.5Si-4Cu-1Mg-1Ni-0.5Cr alloy during solution treatment" China foundry, Vol. 8, No. 3, pp. 264-268, 2011.

[2] M. Zeren, E. Karakulak. and S. Gumus, "Influence of Cu addition on microstructure and hardness of near-eutectic Al-Si-xCu-alloys" Transaction of Nonferrous Metals Society of China, Vol. 21, pp. 1698-1702, 2011.

[3] I. J. Polmear, "Light Alloys, Metallurgy of the Light Metals' 2ND Ed., Edward Arnold, London, p. 95, 1989.

[4] L. He, H. Zhang and J. Cui, "Effects of Pre-Ageing Treatment on Subsequent Artificial Ageing Characteristics of an Al-1.01Mg-0.68Si-1.78Cu Alloy" Materials Science and Technology, Vol. 26, No.2, pp. 141-145.2010.

[5] K. Matsuda, S. Ikeno, Y. Uetani and T. Sato, "Metastable phases in an Al-Mg-Si alloy containing copper" Metallurgical and Materials Transactions A, Vol. 32, No. 6, pp 1293-1299.2001.

[6] R. S. Rana, R. Purohit and S Das "Reviews on the Influences of Alloying elements on the Microstructure and Mechanical Properties of Aluminum Alloys and Aluminum Alloy Composites" International Journal of Scientific and Research Publications, Vol. 2, No.6, pp. 1-7.2012.

[7] J. Song, T. Lin and H. Chuang, "Microsrtuctral Characteristics and Vibration Fracture Properties of Al-Mg-Si Alloys with Excess Cu and Ni" Materials Transaction, Vol. 48, No. 4, pp. 854-859.2007.

[8] J. Song, J, T. Lin. and H. Chuang, "Microsrtuctral Characteristics and Vibration Fracture Properties of Al-Mg-Si Alloys with Excess Cu and Ni" , Materials Transaction, Vol. 48, No. 4, pp. 854-859, 2007.

[9] Y. Yang, K. Yu, Y. Li, D. Zhao and X. Liu, " Evolution of nickel-rich phases in Al–Si–Cu–Ni–Mg piston alloys with different Cu additions", Materials & Design, Vol. 33, pp. 220–225, 2012.

[10] I. C. Barlow, W. M. Rainforth and H. Jones, " The role of silicon in the formation of (Al$_5$Cu$_6$Mg$_2$) σ-phase in Al-Cu-Mg alloys, J Mater Sci, Vol. 35, pp. 1414-81, 2000.

Formation of Perovskite Structure and Microstructure Development of Nb Doped BaTiO₃ Based Ceramics

A. N. Ahmed[1] and H.M.M.A. Rashed[2]

[1,2]Department of Materials and Metallurgical Engineering, Bangladesh University of Engineering and Technology, Dhaka – 1000, Bangladesh

E-mail:[1]adhi88bd@yahoo.com, [2]hrashed@mme.buet.ac.bd

Abstract

Barium Titanate is a ceramic material having ferroelectric, photorefractive and piezoelectric properties. It is used as dielectric materials in capacitors. In this work, formation and microstructure development of niobium (Nb) doped barium titanate ($BaTiO_3$) was investigated through the mixed oxides route via the process of calcination, starting with based on the formula $BaTi_{1-x}Nb_xO_3$; x=.004, .008, .016. XRD data confirmed the formation of provskite structures when Nb doped $BaTiO_3$ patterns were compared with standard $BaTiO_3$ pattern. Above 90% of theoretical density was achieved for samples having different doping level and different sintering temperature ranged from 1425 to 1475 °C. Consistency in the grain growth behavior was observed when microstructures were studied by scanning electron microscope SEM.

Keywords: Barium Titanate, Perovskite Structure, Niobium Oxide, X-ray Diffraction, Scanning Electron Microscopy.

1. Introduction

Barium Titanate is a dominating material in the field of elecroceramics. Many applications of barium titanate in electronic devices come from its diversified properties. It is used extensively as dielectric materials in capacitors especially in MLCCs (Multi Layer Ceramics Capacitor). Moreover, its applications as thermistor, transducer, actuators and ferroelectric random access memory are also remarkable. Ferroelectrocity and piezoelectricity resulted from barium titanate due to its crystal structure and composition. The type of crystal structure that is possessed by barium titanate is termed as perovskite structure formulated by ABX_3 having two cations A, B, and one anion X. Two cations Ba and Ti and O anion are the main constituents of Barium Titanate perovskite where Ti^{4+} is located at the octahedral site of the lattice surrounded by O^{2-} at the octahedral position and Ba^{2+} at the corners of the lattice forming a face-centered cubic structure Fig. 1.
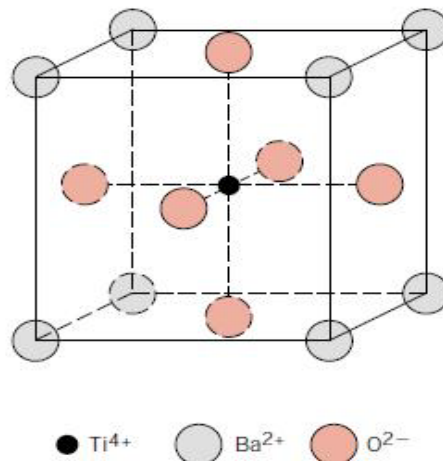
Fig. 1. Crystal structure of barium titanate [1]

Barium Titanate is large enough compared to the Ti^{4+} ion for its shifting into six possible minimum energy positions around it when an electric field is applied resulting spontaneous polarization and high dielectric constant. Moreover, crystal structure of $BaTiO_3$ changes from cubic to tetragonal below the Curie temperature 120 °C resulting an off-centered position of Ti ion leading to a formation of permanent dipole [2].

Barium titanate is an insulating material and substantial change in properties can be achieved if it is doped with donor dopants such as Nb^{5+}, Ta^{5+} replacing the octahedral Ti ion. However, diffusion of Nb is very sluggish even at high temperature into the octahedral site. That is why an attempt has been made to introduce Nb into the octahedral site by the process of calcination starting with $BaCO_3$, TiO_2 and Nb_2O_5, and simultaneously producing perovskite structure of Nb doped $BaTiO_3$. In addition to that, microstructure development with variable sintering temperature has also been observed.

2. Experimental

Nb doped $BaTiO_3$ was prepared on the basis of the formula $BaTi_{1-x}Nb_xO_3$, where x=0.004, 0.008 and 0.016 were taken. Nano-sized $BaCO_3$, TiO_2 and Nb_2O_5 were weighed in electronic balance and then were ball milled with yttria stabilized zirconia ball with a milling media of acetone for 18 hours. Milled powders were then dried and calcined at a temperature of 1300 °C for 2 hours in order to form the $BaTi_{1-x}Nb_xO_3$ perovskite. After calcination powders were milled again for 6 hours. Afterwards, mixture was dried and PVA binder was added followed by pressing into pellets. Green pellets were dried prior to sintering and then sintered from 1425 to 1475 °C for 2 hours with an intermediate heating stage at 500 °C in order to remove the binder. Perovkite structure formation was ensured with X-ray diffraction (XRD) patterns analyzed by Bruker D8 Advance diffractometer with $Cu_{k\alpha}$ λ=1.5406 Å radiation. Microstructures of the samples were observed with a Philips Scanning Electron Microscope (SEM). Density was measured with precision electronic balance and slide calipers and was compared with theoretical density in order to obtain the percent theoretical density.

3. Results and Discussion

(a)

(b)

(c)
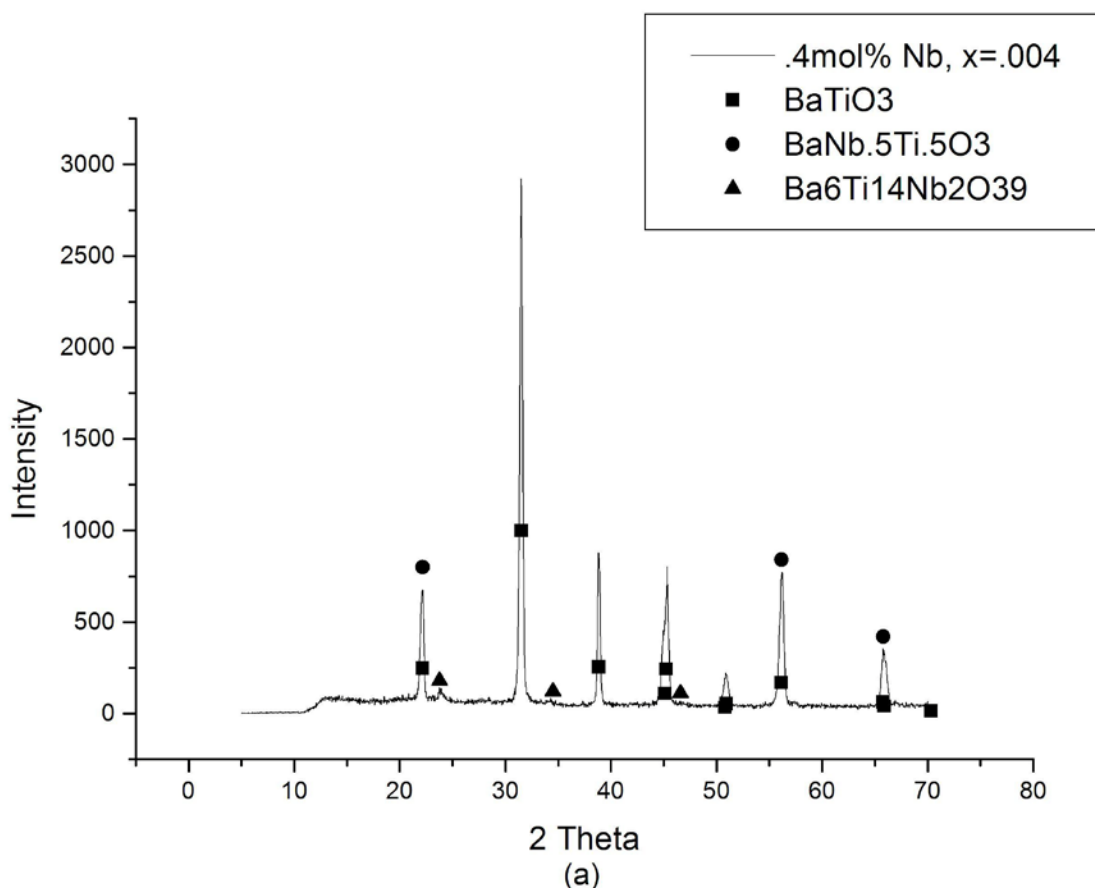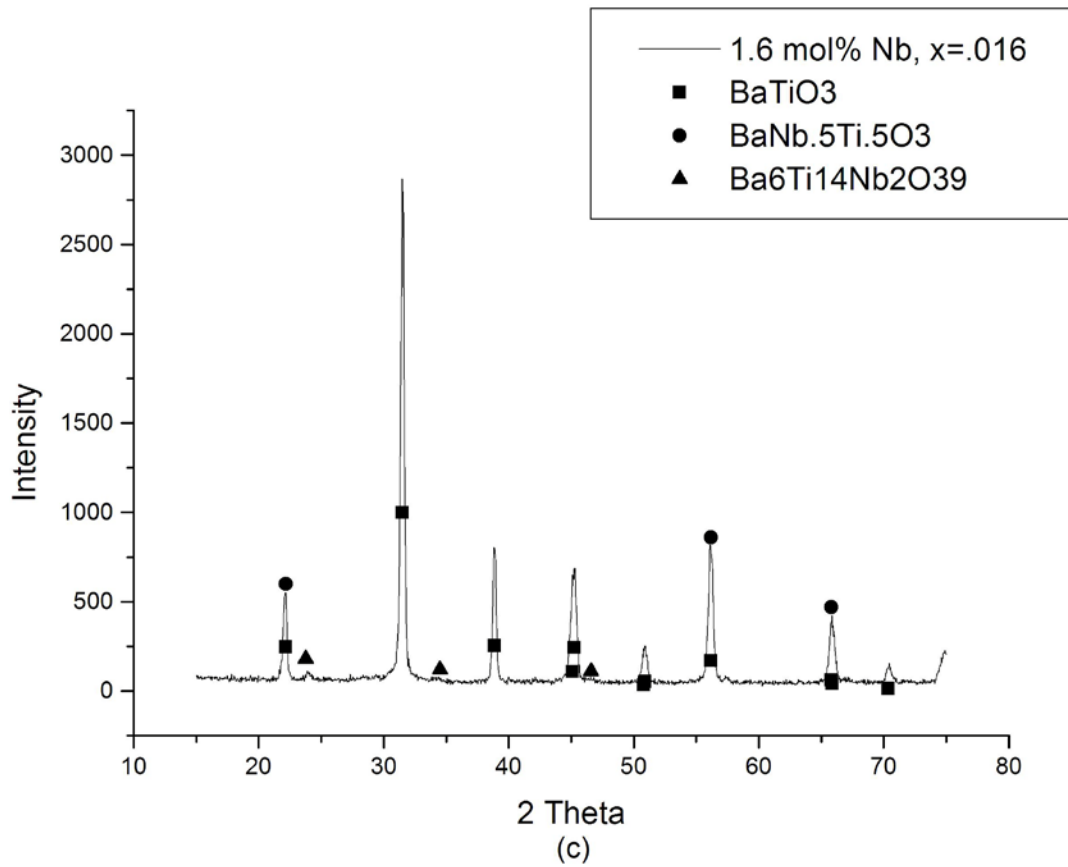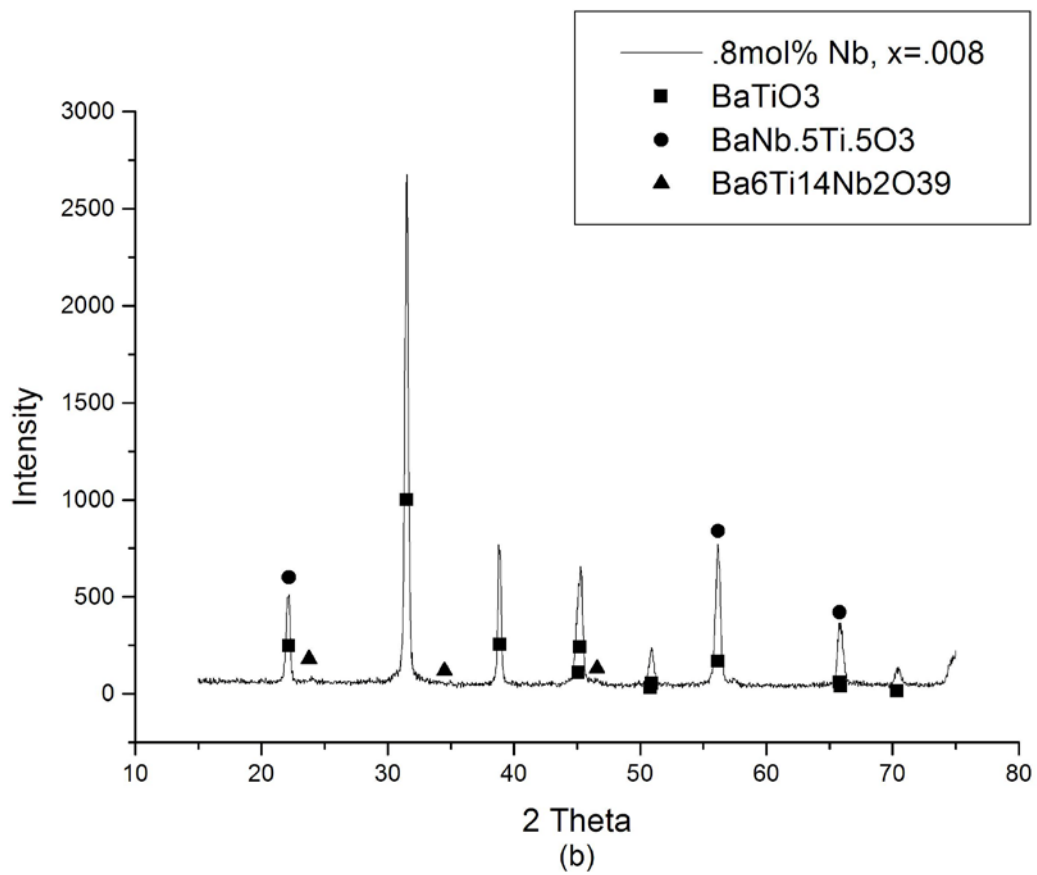
Fig. 2. XRD patterns compared with standards (a) .4mol% (b) .8mol% and (c) 1.6 mol% Nb

Initially it was confirmed with the XRF data shown in Table 1, whether calculated and experimental achievement was consistent or not. The formation of Nb doped $BaTiO_3$ or $BaTi_{1-x}Nb_xO_3$ perovskite in the case of different doping level x=.004, .008 and .016 was ensured with XRD data as shown in Fig. 2. Formation of perovskite structure was ensured as the position of the standard $BaTiO_3$ having perovskite structure indicated by solid square marks in figure 2 nearly superimposed on the peaks generated from the samples. The existence of double square on the peak corresponding to the 2θ value of 45° resulted due to the presence of twin peak in standard perovskite $BaTiO_3$ (Fig. 2). In addition, pattern positions indicated by solid circle correspond to the pattern of $BaNb_{.5}Ti_{.5}O_3$ [3] from which it can be realized that substitution of Ti ion by Nb ion has been occurred in the octahedral sites. Formation of new phase has also been identified, indicated by solid triangle in figure 2 in the form of $Ba_6Ti_{14}Nb_2O_{39}$ [4]. Since Nb content is very low, the peak height of secondary phase is too low to observe.

Table 1. XRF data of sample of .4mol% Nb sintered at 1475°C

Calculated Weight Percent Initially Added	Weight Percent After Sintering by XRF
$BaCO_3$ 55.276	BaO 61.9858
TiO_2 28.679	TiO_2 36.874
Nb_2O_5 .19166	NbO 0.2576
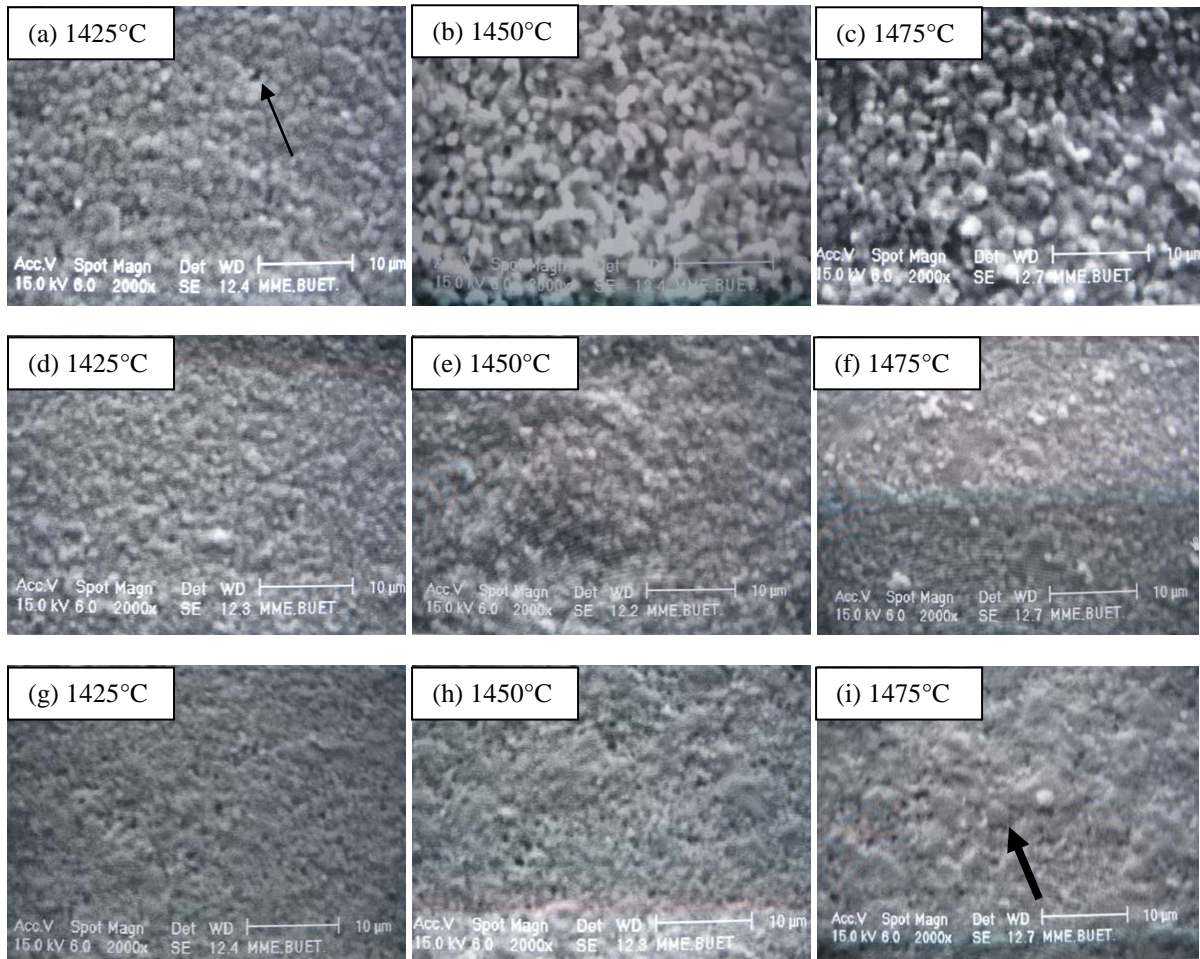
Fig. 3. SEM micrograph of $BaTi_{1-x}Nb_xO_3$ samples with different sintering temperature and doping level (a, b, c) .4mol% Nb, (d, e, f) .8mol% Nb and (g, h, i) 1.6 mol% Nb

Table 2. Density data of Nb doped BaTiO$_3$

Nb mol%	Sintering Temperature °C	Density gm/cc	% Theoretical Density Achieved
.4	1475	5.83±0.06	96.63±1.01
.8	1475	5.95±0.01	98.49±0.17
1.6	1475	5.83±0.11	96.19±1.87
.4	1450	5.91±0.12	97.97±1.78
.8	1450	5.67±0.06	93.94±0.98
1.6	1450	5.73±0.06	94.57±0.99
.4	1425	5.95±0.06	98.72±1.03
.8	1425	5.99±0.02	99.15±0.25
1.6	1425	5.51±0.04	90.91±0.66

In Table 2 the density data of the samples is shown. For all the samples percent theoretical density that has been achieved is more than 90%. High density material is with finer grain size is always required for achieving better dielectric properties.

In Fig. 3 micrographs of the samples are shown, where Fig. 3-a,b and c corresponds to the samples containing .4mol% Nb; d,e and f corresponds to the samples containing .8mol% Nb and g, h and i representing 1.6 mol% Nb. Sintering temperatures of the samples are indicated on micrographs.

From Fig. 3, existence of porosity has been observed in the microstructure indicated by arrow for sample (a) sintered at 1425°C doped with 0.4mol% Nb. Minimum porosity was found for figs. 3(d-f) compared with other microstructures. Distinct and developed grain formation with few porosities was observed for samples doped with 0.4 mol% Nb, Figs. 3(a-c). An increase in holding time may be required to remove the remaining porosities.

In figs. 3 (d–f), finer grains with low porosity are evident. In figs. 3 (g–i), structure with some coarse grains (indicated by arrow in Fig. 3-i) and porosities can be found which is thought to be not the optimum microstructure required for better dielectric properties. It is therefore essential that more energy is required to remove the pores in terms of holding time or sintering temperature. In this scenario, the issue of fine grain microstructure may need to be compromised. Second stage sintering can be a solution in this situation so that shorter holding at higher temperature and longer holding at lower temperature can restrict the grain growth with minimum porosity.

There are six transport mechanisms that may occur during sintering: surface diffusion, volume diffusion, evaporation-condensation, grain boundary diffusion, volume diffusion and plastic flow [5]. Transport of material is required into the pores in order to reduce the same. It is the dominating mechanism or combination of mechanisms corresponding to the sintering parameter and doping agent that decide the amount and size of pore. On the other hand, driving force for densification that acts during sintering is the reduction of excess surface free energy of the particles and it may be reduced by reducing the total surface area with increasing average size of the particle thus grain coarsening [6]. The dominant phenomena between these matter transport and grain coarsening decides the final microstructure of ceramics.

As the sintering temperature range is narrow, only 50 °C starting from 1425 to 1475 °C, the effect of sintering temperature on grain size is not so significant for 0.4 and 0.8 mol% Nb concentration, but for 1.6 mol% Nb, increasing number of coarse grains have been observed with increasing sintering temperatures which has been indicated by arrow in Fig. 3-i. Higher temperature and higher Nb content may be responsible for the grain growth of the samples. Grain growth due to higher Nb content has also been reported earlier [3].

4. Conclusion

Successful formation of Nb doped $BaTi_{1-x}Nb_xO_3$ perovskite was observed for doping levels of 0.4, 0.8 and 1.6 mol% Nb after calcianing at 1300 °C with the presence of secondary phases. Over 90% of the theoritical density was achieved for these compositions. In addition, fine-grain microstructure was obtained with less porosity for samples containing 0.8 mol% Nb and with some porosity for 0.4 mol% Nb. Coarse grains along with some fine grains were observed for samples containing 1.6mol%. Nb.

5. Acknowledgement

6. References

[1] Willium D. Callister Jr., Fundamentals of Material Science and Engineering-An Interactive, *John Willey and Sons Inc.*, Fifth Edition, pp. 44, 2001.

[2] D.W. Richarson, Modern Ceramic Engineering-Properties, Processing and Use in Design, *H C Malone Books*, Second Edition Revised and Expanded, pp. 264-265, 1992.

[3] Y. Zhang, J. Hao and J. Qi, "The Effect of Nb_2O_5 addition on the dielectric properties of BaTiO3-based Ceramics", *Advanced Materials Research*, Vol. 287-290, pp 1108-1111, 2011.

[4] Y. Yuan, S.R. Zhang, X.H. Zhou and B. Tang, "Effects of Nb_2O_5 doping on the microstructure and the dielectric temperature characteristics of barium titanate ceramics", *J Mater Sci*, Vol.44, pp. 3751–3757, 2009.

[5] C.C. Barry, Norton M. Grant, Ceramic Material-Science & Engineering, *Springer*, pp. 430, 2007.

[6] M.W. Barsoum, Fundamentals of Ceramics, *IOP Publishing Ltd.*, pp. 304, 2003.

Micro Responses of Sheared Granular Materials using 3D DEM

Md. Mahmud Sazzad[1], Toufiq-E-Alahy[2] and Shashanka Biswas[3]

[1]Associate Professor, Department of Civil Engineering, Rajshahi University of Engineering & Technology, Rajshahi-6204, Bangladesh
E-mail:mmsruet@gmail.com

[2]Undergraduate Student, Department of Civil Engineering, Rajshahi University of Engineering & Technology, Rajshahi-6204, Bangladesh
E-mail:Toufiq.shiam@gmail.com

[3]Undergraduate Student, Department of Civil Engineering, Rajshahi University of Engineering & Technology, Rajshahi-6204, Bangladesh
E-mail:biswas.shashanka@gmail.com

Abstract

This study presents the macro- and micro-mechanical responses of a sheared granular system using the three dimensional (3D) discrete element method (DEM). Spheres of different sizes were first generated in a cubic frame in such a way that they were not in contact with their neighbors. This sparse sample was compressed isotropically with a constant confining pressure of 100 kPa. The isotropically compressed sample was subjected to shear deformation with a small strain rate under strain controlled condition. The numerical data were recorded at regular interval to carry out the macro-micro analysis. The numerical result depicts that the simulated stress-strain-dilative responses are in good agreement with the experimental result in a qualitative sense. Different micro parameters were monitored and recorded as well during the numerical simulation. The evolution of these micro-parameters is reported.

Keywords: Granular Materials, Micro-parameter, DEM.

1. Introduction

Granular materials are discrete in nature and their mechanical behavior is complex. Still today, there remain many experimentally observed phenomena that are not clarified and well understood. Specifically, the internal processes that take place during the laboratory experiments are not well known. This is because; these internal processes can not be explored using the traditional experimental devices. Advanced experimental techniques such as the photo imaging analysis [1], X-ray tomography [2], wave velocity measurement [3], magnetic resonance imaging [4] etc. can be employed to understand the internal processes and extract the micro-mechanical data. However, they are sophisticated, expensive and time consuming. Besides, it is not possible to extract all the internal (i.e., micro level) data using these advanced experimental devices or methods. The understanding of these micro-processes is important to develop physically sound models. These micro data is also necessary to explain the physically observed phenomena from the micro-mechanical point of view. The above fact suggests that a comprehensive study is necessary to understand the micro-mechanical characteristics of a granular system. Since it is difficult to conduct experimental study using the conventional experimental facilities, the only alternative is the numerical approach that can model the discrete nature of a granular system. Discrete element method (DEM), pioneered by Cundall and Strack [5], is a numerical method that enables one to model the discrete nature of the granular media. Indeed, the micro-mechanical characteristics have been studied using DEM [e.g., 6-10]; it is still not sufficient and requires further study. In the current paper, the micro-mechanical characteristics of a sheared granular system have been studied in details using 3D DEM. For this purpose, a cubic sample consisting of spheres was generated and compressed isotropically. The isotropically compressed dense sample was subjected to shear under the strain controlled conditions. The digital macro- and micro-mechanical data were recorded at regular interval and their evolution were reported.

2. Numerical method and computer program

The current simulation was carried out using the DEM. The basic idea used in DEM is simple. Each particle in DEM is considered as an element. Each element can make and break contact with its neighbor. The particles can translate and rotate. Newton's second law of motion is employed to obtain the acceleration of the particle. This acceleration is integrated over time twice to get the displacement. Then the force displacement law is used to get the force using the displacement of the particle calculated earlier. Thus the cycle continues for the next step. For details of DEM, readers are referred to Cundall and Strack [5]. Both the translational and rotational accelerations of the particles are computed as follows:

$$m\ddot{x}_i = \sum F_i \qquad i = 1, 3 \tag{1}$$

$$I\ddot{\theta} = \sum M \tag{2}$$

where F_i are the force components on each particle, M is the moment, m is the mass, I is the moment of inertia, $\ddot{x}_i$ are the components of translational acceleration and $\ddot{\theta}$ is the rotational acceleration of the particle.

The DEM has been incorporated in the computer code YADE and it has been used to conduct the numerical simulation. The code is written in C++ with Object Oriented Programming and consists of software, libraries and necessary plug-ins. In YADE, one can add new numerical models by only plugging in the corresponding formulas. 3D models of spherical shape particles can be simulated using YADE. It runs on Linux platform. One of the important points in YADE is that it has graphical user interface which allows one to monitor the simulation process during the program run. For details of YADE, readers are referred to Kozicki and Donze [11].

3. Sample preparation

A sparse sample was first generated in a cubic frame such that the particles in the cube were not in contact with each other. Spheres were used as particles as it reduces the computational cost. More than 3800 particles were generated randomly in the cube. The sample was then isotropically consolidated by moving the six rigid boundaries inward with all around confining pressure of 100 kPa. The rate of consolidation was chosen in such a way that the unbalanced forces generated during the consolidation remained fairly small. The consolidation continued for several thousand steps until the confining pressures reached 100 kPa and the porosity of the sample became constant for the last few thousand steps. The interparticle friction angle was assigned zero degree at this stage of consolidation to obtain a dense sample. The state of consolidation simulation was saved in the xml-file format. In the next stage, the xml-file was opened and the interparticle friction angle was replaced by 26.5 degree and the file was saved. The saved file was reloaded and the consolidation continued for the next few thousand steps. When the isotropic consolidation completed, a final state of simulation condition was saved for shear deformation. The porosity of the dense sample at the end of isotropic compression was 0.38. The configurations of the isotropically compressed dense samples with reference axes are depicted in Fig. 1.
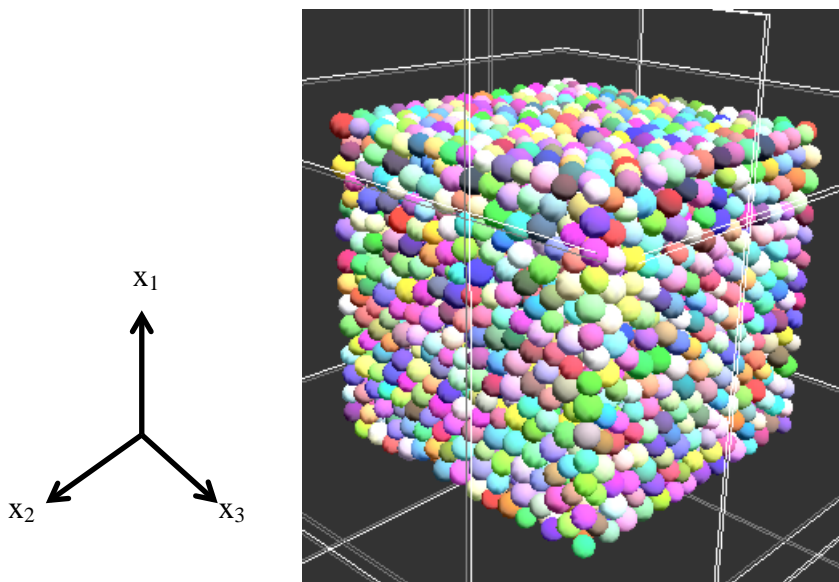
Fig. 1 Configurations of the isotropically compressed dense sample

4. Numerical simulation

Simulation of triaxial compression test was accomplished by moving the top and bottom boundaries inward the sample at a small strain rate of 0.1 while maintaining the confining stresses in other four boundaries 100 kPa. The confining stresses are maintained 100 kPa by continuously adjusting the position of the boundaries. The stresses in three axial directions and the corresponding strains are measured. The DEM parameters used in the simulations are tabulated in Table. 1.

Table. 1 DEM parameters used in the simulations

DEM parameters	Value
Young's Modulus (MPa)	60
Stiffness ratio (K_s/K_n)	0.50
Mass density (Kg/m^3)	2600
Inter particle friction angles (degree)	26.50
Damping coefficients	0.20

5. Stress-strain-dilative response

Fig. 2 depicts the stress-strain response of the sheared granular system in strain controlled simulation condition under triaxial compression test for a dense sample. Note that the deviatoric stress q [$= \sigma_1 - \sigma_3$] increases with axial strain ε_1 till the peak and then decreases until it reaches the residual state. Here σ_1 and σ_3 represent the stresses in x_1 - and x_3 - direction, respectively. This tendency is consistent with the laboratory based experimental studies [e.g., 12] in a qualitative sense. This also demonstrates the versatility of the current simulation using the DEM. The evolution of volumetric strain ε_v with axial strain ε_1 is shown in Fig. 3. Volumetric strain is defined here as $\varepsilon_v = \varepsilon_1 + \varepsilon_2 + \varepsilon_3$, where ε_1, ε_2 and ε_3 are the strains in x_1-, x_2- and x_3- direction, respectively. In Fig. 3, a positive value of ε_v represents compression while a negative value represents dilation. Note that dilation is the dominant characteristic during the shearing of a dense granular system. This tendency is also qualitatively consistent with the laboratory based experimental studies [e.g.,12]. The evolution of the dilatancy index DI defined here as $DI = -d\varepsilon_v / d\varepsilon_1$ is depicted in Fig. 4.
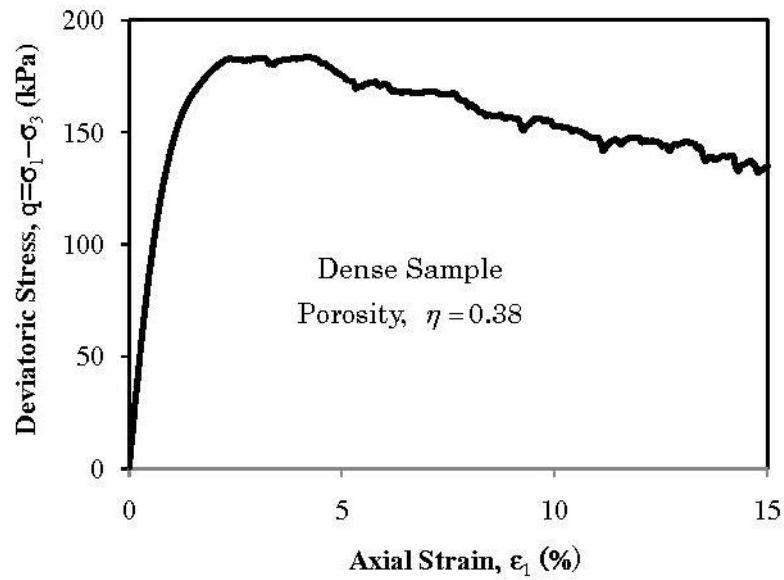
Fig. 2 Stress-strain relationship for a dense granular assembly sheared under strain controlled simulation conditions
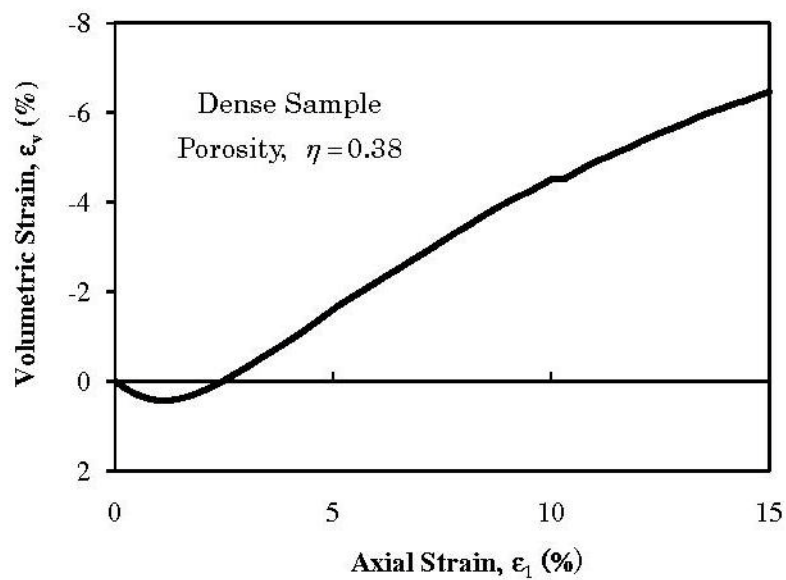
Fig. 3 Evolution of volumetric strain with axial strain for a dense granular assembly sheared under strain controlled simulation conditions
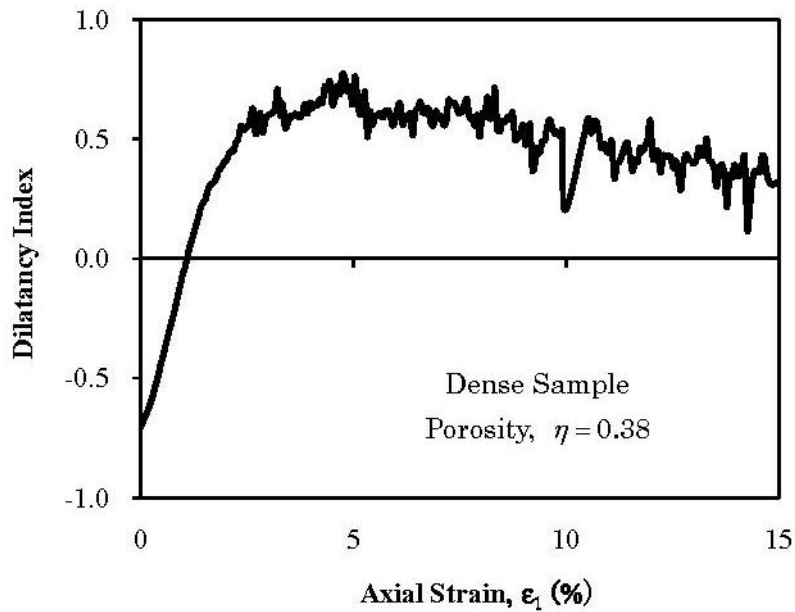
Fig. 4 Evolution of dilatancy index with axial strain for a dense granular assembly

6. Evolution of micro parameter

In this section, the evolution of different micro parameters is discussed. The evolution of the average velocity at any given strain normalized by the average velocity at the end of the isotropic consolidation of the dense sample, V_i^a / V_{iso}^a , with axial strain is depicted in Fig. 5. Here, V_i^a is the magnitude of the average translational velocity at any given strain and V_{iso}^a is the magnitude of the average translational velocity at the end of the isotropic consolidation of the dense sample. The average velocity is measured from 1% to 10% of axial strain. It is noted that the normalized average velocity has a scattered tendency. Although V_i^a / V_{iso}^a has a scattered behavior, the maximum value of V_i^a / V_{iso}^a is observed at 4% axial strain which is close to the peak stress state.
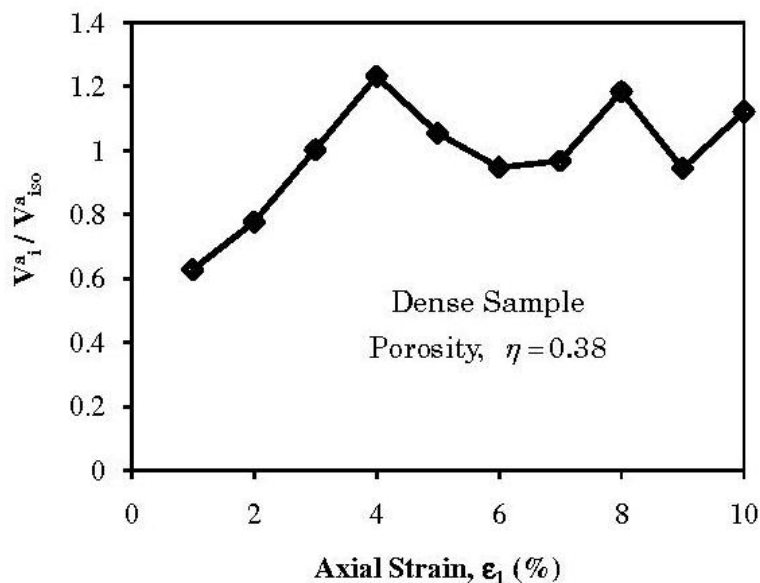
Fig. 5 Evolution of V_i^a / V_{iso}^a with axial strain for a dense granular assembly

Fig. 6 depicts the relationship between the number of contacts (that carry forces) per particle. It is noted that the contact number per particle sharply decreases at the beginning stage of simulation and later, it becomes almost steady. The loss of contact is due to the dilation of the sheared sample. During dilation, the lateral four boundaries move outward the sample and consequently contact loss takes place.
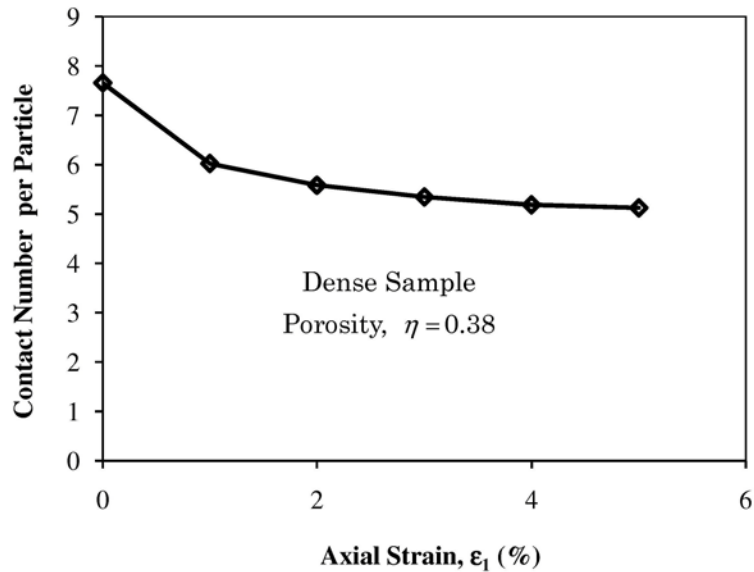
Fig. 6 Relationship between the contact number per particle with axial strain for a dense granular assembly

7. Conclusions

The numerical experiment was conducted under strain controlled simulation condition. Conventional Triaxial Compression (CTC) test was simulated using the DEM. A cubic dense sample consisting of spheres was sheared and the macro and micro-mechanical behaviors were observed. The stress-strain-dilative responses have nice agreement with the experimental tendencies. This reveals the versatility of the current simulation using DEM. The micro-mechanical responses were studies as well. It is noted that the normalized average velocity of the dense assemble is maximum near the peak stress state. It is also noted that the contact number per particle sharply decreases at the begging state of the simulation and later this decrease rate reduces as the strain increase for a dense sample.

8. References

[1]   M. Oda, and J. Konishi, "Microscopic deformation mechanism of granular material in simple shear", *Soils and Foundation*, Vol.14, No.4, pp.25–38, 1974.
[2]   X. Lee, W. C. Dass, and C.W.Manzione, "Characterization of granular material composit structures using computerized tomography" *Proc. of 9th Engng. Mechnical. Conference ASCE, New York*, pp. 268–271, 1992.
[3]   J.C. Santamarina, and G. Cascante, "Stress anisotropy and wave propagation: a micromechanical view" *Canadian Geotechnical Journal*, Vol.33, No.5, pp.770–782, 1996.

[4]   T.-T. Ng, and C. Wang, "Comparison of a 3-D DEM simulation with MRI data." *Int. J. Numer. Anal. Mech. Geomech.*, Vol.25, No.5, pp.497–507, 2001.

[5]   P.A.Cundall, and O.D.L. Strack, "A discrete numerical model for granular assemblies." *Geotechnique*, Vol.29, No.1, pp. 47-65, 1979.

[6]   F. Radjai,, S. Roux, and J.J .Moreau, "Contact forces in a granular packing." *Chaos*, Vol.9, No.3, pp.544-550, 1999.

[7]   M.R. Kuhn, "Structured deformation in granular materials", *Mech. Mater.*, Vol.31, No.6, pp.407-429, 1999.

[8]   T.-T. Ng, "Fabric evolution of ellipsoidal arrays with different particle shapes", *J. Engng. Mech., ASCE,* vol.127, No.10, pp.994-995, 2001.

[9]   E. Azema, F. Radjai, R. Peyroux, and G. Saussine, "Force transmission in a packing of pentagonal particles", *Phys. Rev. E*, Vol.76 No. 1, 011301:1-13, 2007.

[10] M.M. Sazzad, and k. Suzuki, "Micromechanical behavior of granular materials with inherent anisotropy under cyclic loading using 2D DEM", *Granular Matter*, Vol.12, No.6, pp.597–605, 2010.

[11] J. Koziki, and F.V. Donze, A new open-source software developed for numerical simulations using discrete modeling methods", *Computer Methods in Applied Mechanics and Engineering*, Vol.197, No.49-50, pp. 4429–4443, 2008.

[12] K. A. Alshibli, S.N. Batiste, and S. Sture, "Strain localization in sand: plane strain versus triaxial compression", *Journal of Geotechnical and Geoenvironmental Engineering*, Vol.129, No.6, pp. 483-494, 2003

Surface Alloying of CP-Ti Using preplaced Fe-C-Si powder by Tungsten Inert Gas Torch Technique

M.A Maleque[1] and S.A. Adeleke[2]

[1,2]Advanced Materials and Surface Engineering Research Unit
Department of Manufacturing and Materials Engineering
International Islamic University Malaysia, P.O. Box 10, 50728, Kuala Lumpur, Malaysia
maleque@iium.edu.my[1], adelekeshakiru@gmail.com,[2]
[*] Corresponding author: Tel.: +6011-1514023;adelekeshakiru@gmail.com

Abstract

Surface alloyingcan play an important role for the protection of metallic components against wear and fric-tion.In this study, the surface alloying of CP-Ti material was performed using pre-placed powder mixture of carbon,silicon and iron under TIG arc techniques at an energy of 945 J/mm. The melt geometry, topogr-aphy, microstructure and hardness were investigated on the surface modified Cp-Ti alloy. The results indicated that the TIG torch produced at the energy input of 945 J/mm gave melt pool is in hemispherical shape.Pores were seen to be concentrated at the bottom of the melt pool where low melting energies are promin-ent entrapped escaped gases upon fast melt solidification. The melt pool microstructures glazed contained variation of dendritic and armed type of TiC to be precipitated in the presence of longer solidification time. TiC precipitation were higher in population and bigger in sizein the middle of the melt pool compared to the track edges. Surface modified Cp-Ti alloy exhibited hardness values ranging from 600 Hv to 780 Hv which was 3 to 3.5 times higher than base metal hardness. The higher hardness observed at particular areas are attributed to high population and big sizes of dendritic microstrucutres of TiC.

Keywords: Surface alloying, TiC, TIG, dendrites, microhardness

1. Introduction

Due to the high specific strength-to-weight ratio, excellent corrosion and high temperature resistance, titanium alloys are widely employed as a suitable material for aeronautical, chemical, petrochemical and marine applications. However, owing to their low wear resistance and hardness values, their potential application is restricted.One of the ways to overcome this problem is to modify the surface on the substrate material by melting process via high energy input. Since then, research works showed improvement in surface hardness under this processing technique [1,2] thus allowing the modified material to be a suitable candidate for aggressive wear application. Subsequent rapid solidification of the melted layer might lead to the formation of structures which are not achieved under equilibrium condition [3]. Azmi and Shamanian [4] studied the effect of silicon on the microstructures and properties of Fe-Cr-C and reported that effect of silicon exhibited increase in microhardness and better wear resistance. Mridha [5] found that the hard titanium nitride layer that is processed in the pure nitrogen environment under TIG arc gave maximum hardness of about 2000 Hv.HajbagheriAdibet. al. [6] studied the wear resistance of CP-Ti by surface alloying with silicon under TIG torch melting technique and they found that the created layer achieved hardness values of approximately 4 to 5 times higher than the substrate material. Several research works found in literatures focusing on melting different alloying powders by using state of art processing techniques such as laser and plasma welding which are generally known to give higher in production price [7, 8]. Yet, no study has been carried out to melt the mixture of Fe-Si-C ternary material system by using the conventional and cheaper TIG method for surface modification. As such, the objective of this work is to investigate the quality of the melt pool layer using Fe-Si-C powders on CP-Ti substrate melted at the energy input of 945 J/mm. Melt pool geometry, topography, microstructure and microhardnessresults are presented in this paper. The success of this work will provide new opportunities for coating manufacturers to use this cheaper TIG technique rather than using laser or plasma beam processes and ternary powder mixtures with cost effective manner

Experimental

In this work, commercial purity titanium (CP-Ti) substrate with the dimension of 100 mm x 40 mm x 10 mm was thoroughly cleaned using acetone to remove contaminants such as dirt and grease on the surface. Weighed iron powder was added with carbon and silicon powder at given weight ratio as shown in Table 1. The mixed powders were blended using ball milling process for 1 hour with ball-to-powder weight ratio of 10:1. The blended powder weighed at 1 mg/mm^2 was mixed with Polyvinyl acetate solution before it was evenly spreaded across the titanium substrate surface. The amount of binder was restricted within limit in order to prevent excessive pores formation to be embedded in the re-solidified melt tracks [9]. The powder coated samples were heated in the oven at 80 ^{o}C for 1 hour to remove excessive moisture and for ensuring the layers are well adhered on the substrate surface. Single tracks were produced at energy input of 945 J/mm using TIG 165 welding machine with 2.4 mm in diameter of tungsten thoriated electrode. The arc energy input was calculated using a simple mathematical expression which can be found elsewhere. Fig.1 shows the schematic diagram of the surface melting process under the TIG torch. Pure argon gas with the flowing rate of 20 lit/min was purged into the melt pool to protect the tracks against excessive oxidation. The sectioned track layers were grounded on emery papers to the grit size of 2000 followed by polishing process that uses alumina paste with the size of 1 micron in diameter on the polishing pad cloth. The Kroll's reagent at the mixture 50 % HF, 30 % H_2O_2 and 20 % distilled water by volume was used to etch the surface of the sectioned layers. The sample microstructures and topographies were observed by scanning electron microscope and Nikon measuring microscope respectively while experimental analysis was carried out using energy dispersive x-ray. The Vickers microhardness test across the melt depth was conducted using Wilson Wolpert testing machine at the load of 500 gf with 10 seconds delay.
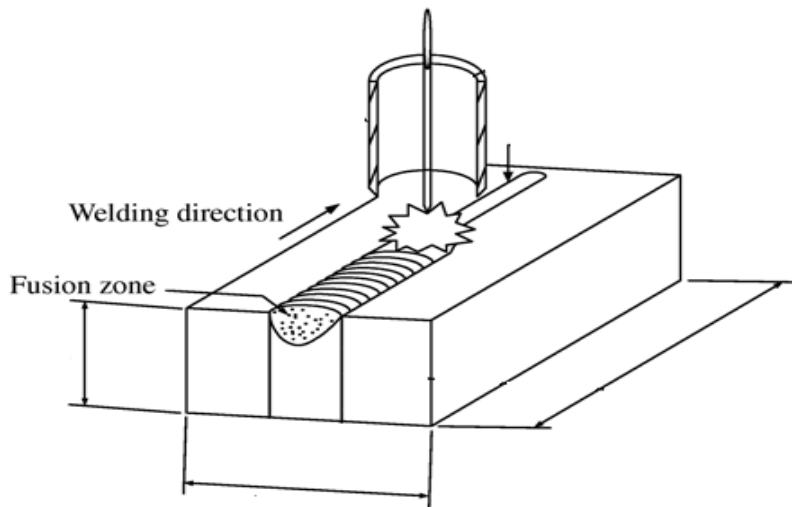
Fig.1 Schematic representation of TIG torch glazing features

Table. 1. Processing conditions and alloy powder ratio

Processing conditions			Powder ratio
Energy (J/mm)	Depth(mm)	Width(mm)	Fe:C:Si ≡ 94 : 4 : 2
945	1.03	6.16	

3. Results and Discussion

3.1 Surface topography

The surface topography of modified Cp-Ti alloy with ternary alloy of Fe-C-Si using TIG torchtechnique at an energy input of 945 J/mm depicted in Fig 2.Rippling marks on the glazed sample was found to form in two

different directions which are along and perpendicular to the electrode traversing direction. The radial rippling formations along the electrode traverse direction showed that solidification of molten melt pool was taken place near the base metalhowever, it solidified finally near the arc source. This low heat input energy produces a small radial mark along the electrode traversing direction on the noticeable re-solidified melt waves of the rippling marks that are perpendicularly to the direction of electrode movement (Fig. 2). The thick melt solution that formed slightly above melting temperature fused at this energy input created the surging fluid greater in penetration resistance and upon little solidification time, this high viscosity melt wave freezes as perpendicular rippling marks on the substrate surface. Previous works have showed that greater in ripples marks were formed by greater convection force that stirs the melt liquid in the presence of longer solidification time and fast solidification using low heat input caused rough and undulated surface which are the sign of incomplete melting at the beneath of surface layer [10, 11].
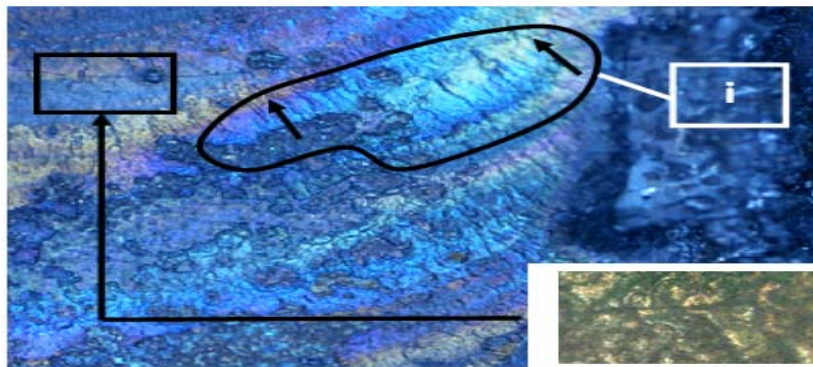
Note:Perpendicular rippling marks indicated by (i)

Fig.2.Topography of the processed tracks showing perpendicular rippling marks and the radial marks along electrode traversing direction by black arrows.Cracks are indicated at the insets.

3.2 Melt Microstructure

The micrographs of the resolidified melt layer fused showed hemispherical melt pool shape layer embedded on the surface of the substrates (Fig. 3) The Gaussian energy distribution which is known to provide greater heat intensity in the middle of the melt and gradually decreases to both edges are responsible to give such hemispherical in shape behaviour upon solidification. This phenomenon was also explained by other researchers using lasers and TIG melting process for composite coating where the hemispherical melt pool shapes are formed by the Gaussian energy distribution [1, 10, 12]. Continuous fusion line observed between the coating layer and the substrate in Fig. 2proved that good metallurgical bonding was incurred in this region from extensive mixing of dissolved reinforcing material with an amount of diluted substrate. Pores were seen to be entrapped at thelow energy area which are the edges due to fast solidification (Fig. 3). In the pre-placing technique, pores are reported due to escaped gases from the burnt binder which does not efficiently released to the environment upon solidification [2, 17].However, the microstructure showed little dilution of the base metal with smaller amount of dissolved reinforced powders especially carbon which permitted to the precipitation of the new dendritic armed TiC phase in the presence of longer solidification time (Fig. 4). It is worth noting that the diffusion of carbon in titanium in presence of higher carbon content (4 wt%) via diffusion hardening process assists the formation of dendritic TiC as shown in Fig. 4. Fig. 5 shows the EDX elemental analysis on the SEM micrograph and it is clear from the results that modified metal faceconsists of both Ti and C. The high affinity of carbon for titanium than other elements is significant to develop such populated TiC phase. In the previous work, the re-precipitated TiC consist of iron, titanium and carbon using pre-placed TiC particulates melted on the low alloy steel substrate by high TIG energy input [1].   At this low energy input of 945 J/mm, the melt fluid is thick and as such, the solidification time for the melt to freeze isvery short and this retarded the possibility for greatamount and sizes of TiC to be precipitated. In the previous work, the low energy at the edges fused by TIG arc showed poor dissolution efficiency thus giving high un-melted and partially melted particulates to be agglomerated with minimal re-precipitation of TiC microstructures [1] and this was also observed in other research works [14].
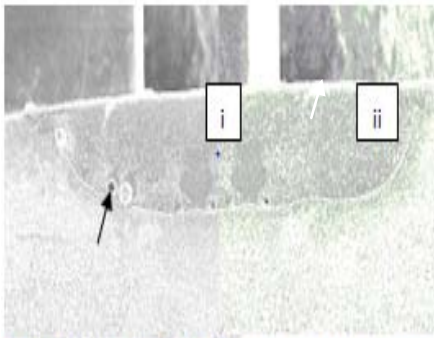
Fig. 3. Micrograph of Fe-C-Si coated surface with the arrow showing porosities
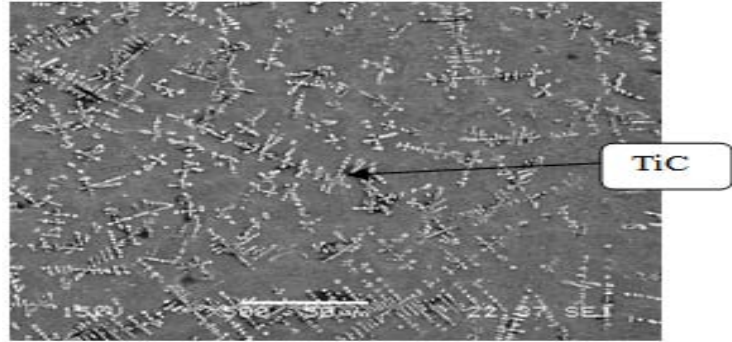
Fig. 4. SEM micrograph of modified surface showing dendritic TiC observed in Fig. 3 (i)
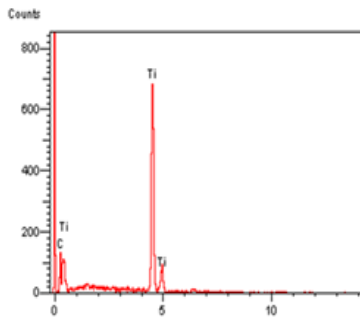
Fig. 5. Elemental analysis in the dendrite (Fig 4) showing Ti and C.
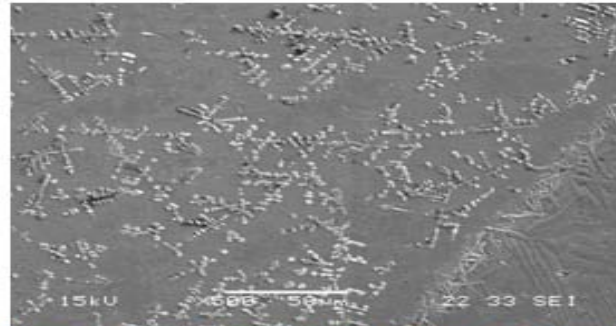
Fig. 6. Lesser and smaller dendritic TiC precipitation observed in Fig.3 (ii).

3.3 Microhardness Profile

Themicrohardness profile of the ternary alloy prep-placed powder modified Cp-Ti alloy processed under the energy input of 945 J/mm is presented in Fig. 7. The microhardness recorded for modified surface were found ranging from 600 to around 780 Hvwhile the Cp-Ti substrate microhardness value was 200 Hv.In this work, the main contribution to the increase of microhardness value areprecipitation of the new dendritic armed TiC microstructure that were mainly populated near the arc source. The enrichment of TiC dendrite attained maximum hardness of approximately 780 Hv and this value decreases to the lowest of about 600 Hv at the depth of 200 micron. The variation of hardness is attributed by the gradient distribution of variety TiC types and population across the depth of the track layer [2, 14]. Emamian et al. [15]reported that fluctuation in hardness result normally occurs due to the difference in hardness value of matrix and reinforcement particles. Greater in basemetal dilution by melting using high energy input may reduce the microhardness value in the re-solidified melt layer. However, allowing the new hard phase of TiC to be precipitated at the expense of longer solidification time via high this energy input may overwhelm the poor hardness properties in the re-solidified melt layer.
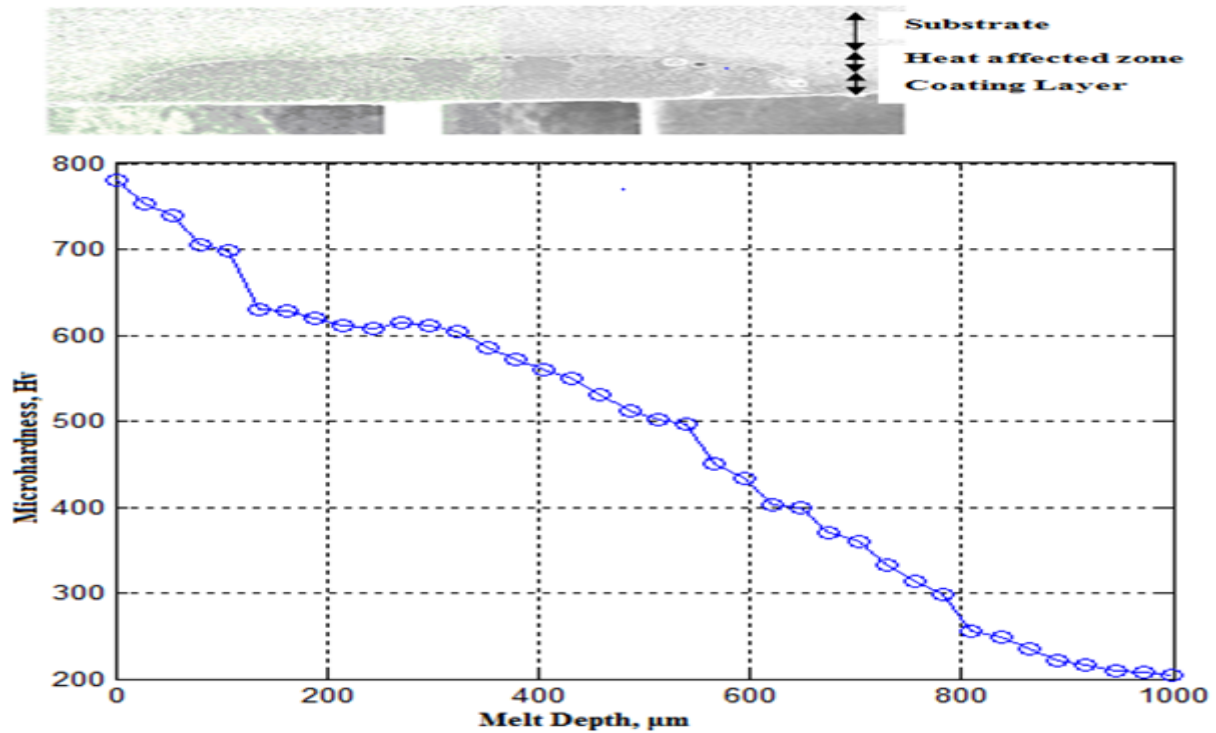
Fig.7. Microhardness profile of the processed track layer at energy input 945 J/mm

4. Conclusions

The surface of CP-Titanium has been successfully modified with Fe-Si-C ternary powders that is preplaced on the substrate via TIG torch technique. The melt pool obtained was hemispherical in shape and populated with precipitationof the new dendritic armed TiC microstructure that was almost homogeneously distributed within the melt pool. Pores were prominent to be embedded at the edges due to fast melt solidification from the viscous liquid during melting process. The maximum hardness in the surface modified area is about 3 to 4times higher than the base metal hardness. The increase of microhardness value within the ternary alloy on the substrate suggest that this processed material is suitable to be used in the aggressive wear environment where low material removal rate is likely to take place on the surface.

5. Acknowledgements

6. References

1. S. Mridha, "Incorporation of TiC particles on AISI 4340 low alloy steel surfaces via tungsten inert gas arc melting," *Advance Material Research*, pp. 665, 2012.
2. S. Mridha, A.N. Md Idriss, M.A. Maeque, Suryanto, and A. Souad, "Effect of voltage on the consolidation of TiC particulates on steel substrate fused by TIG welding arc," *International Journal of Mechanical and Materials Enigneering*, Vol.7**,** No.1, pp. 48-53, 2012.
3. V.Ardavan, H.S. Mahmoud, and S. Abdolghayoom, "Liquid phase surface alloying of CP-titanium with aluminium in an atmosphere of argon and nitrogen," *Surface and Coating Technology*,Vol.206, pp.3788-3794, 2012.
4. G. Azmi, and M. Shamanian, "Effect of silicon content on the microstructure and properties of Fe-Cr-C hardfacig alloys," *Journal Material Science*, Vol. 45, pp. 842-849, 2010.
5. S. Mridha, and S. Dyuti, "Formation of TiN Dispersed Composite Layer on Steel Surfaces by Titanium Powder Preplacement and TIG Surface Melting Processes," *Advanced Materials Research*, Vol.264, pp. 1415-1420, 2011.
6. F. HajbagheriAdib, S.F. KashaniBozorg, and A.A Amadeh, "Microstructure and wear assessment of TIG surface alloying of CP- titanium with silicon," *Journal Material Science*, Vol. 43,pp. 5720-5727, 2008.

7. J. B. Lu, P. Meng, F. Tang, B. Zhao, & J.X. Gong, "Microstructure Analysis of TiC Reinforced Fe-Based Composite Coating by Plasma Cladding,". *Advanced Materials Research,* Vol.472, pp. 297-301, 2012.

8. X. Wang, M. Zhang, X. Liu, S. Qu, & Z. Zou, "Microstructure and wear properties of TiC/FeCrBSi surface composite coating prepared by laser cladding," *Surface and Coatings Technology,* Vol. 202, No.15, pp. 3600-3606, 2008.

9. S. Mridha, and B.S Ng, "Addition of ceramic particles to TIG melted titanium surfaces," *Surface Engineering,* Vol. 15, No. 3, pp. 210, 1999.

10. S. Mridha, and T.N. Baker, "Incorporation of 3 μm SiCp into Titanium surfaces using a 2.8 kW laser beam of 186 and 373 MJ m−2 energy densities in a nitrogen environment," *Journal of Materials Processing Technology,*Vol.185, No. 1-3, pp. 38-45, 2007.

11. S. Dyuti, S. Mridha, and S. Shaha, "Surface Modification of Mild Steel Using Tungsten Inert Gas Torch Surface Cladding,"*American Journal of Applied Sciences*, Vol.7, No. 6, pp. 815-822, 2010.

12. J. Limei Wang, J.L.a.C.Y., "Fe-Cr-C-TiC high chromium Fe-based composite coating prepared by PTA weld surfacing process".*Materials Science Forum,* Vol. 675-677, pp. 783-787, 2011.

13. J.H. Abboud, and D.R.F. "West, microstructure of titanium injected with SiC particles by laser processing.*Journal of Materials Science Letters*, Vol. 10, No. 19, pp. 1149-1152, 1991.

14. X. Wang, S. Song, Z. Zou, & S. Qu, "Fabricating TiC particles reinforced Fe-based composite coatings produced by GTAW multi-layers melting process." *Materials Science and Engineering: A,* Vol. 441, No.1, pp. 60-67. 2006.

15. A. Emamian A, S.F. Corbin, and A. Khajepour, "Effect of laser cladding process parameters on clad quality and in-situ formed microstructure of Te-TiC composite coatings," *Surface and Coatings Technology*, Vol. 205, pp. 2007-2015. 2010.

Design and Fabrication of an Experimental Set-Up to Measure Carbon Content of an Alloy

Md. Yousuf Mia[1*], Juwel Chandra Mojumder[1], Md. Saifur Rahman[2], Anamul Hossain[3], Romel Barua[4].

[1*, 1, 5] Graduate students in Department of Mechanical E ngineering, Chittagong University of Engineering and Technology (CUET),Chittagong, Bangladesh

[3, 4] M. Sc student in Department of Petroleum Engineering, Bangladesh University of Engineering and Technology (BUET), Dhaka, Bangladesh

E-mail: *yousufme07@yahoo.com[1*]* ,

Abstract

Steel and steel alloys are essential ingredient to build nation and quality of steels depend on chemical composition especially on carbon. Nowadays, we perceive how important the quality of steels for construction. In steel, carbon exists in combined and uncombined conditions and in Ferro-alloys, it only in combined state. To measure carbon content is an important criterion to select the quality of steel. Therefore, different methods are used worldwide to do that. This project deals with the measurement of carbon content by combustion process. The objective of this procedure is to determine the total amount of carbon content in all types of iron, steel, cast iron and Ferro-alloys. When regulated oxygen is passed over the heated metal, the oxygen is oxidized with carbon and produced carbon dioxide as well as a small amount of Sulphur dioxide and ferrous oxide. At the end of combustion, carbon dioxide is adsorbed by activated carbon powder inside an airtight jar. The amount of carbon increases with the increasing the weight of airtight gas jar.
.

Key words: Steel, Carbon, Chemical composition, Combustion, Adsorption, Measurement etc.

1. Introduction

Generally, carbon is the most important commercial steel alloy. Increasing carbon content increases hardness and strength and improves harden ability. But carbon also increases brittleness and reduces weld ability because of its tendency to form Martensite. This means carbon content can be both a blessing and a curse when it comes to commercial steel.
 Where there are steels that have up to 2 percent carbon content, they are the exception. Most steel contains less than 0.35 percent carbon. To put this in perspective, keep in mind that's 35/100 of 1 percent.
Carbon, the sixth most abundant element in the universe, has been known since ancient times. Carbon is most commonly obtained from coal deposits, although it usually must be processed into a form suitable for commercial use. Three naturally occurring allotropes of carbon are known to exist: amorphous, graphite and diamond.
Amorphous carbon is formed when a material containing carbon is burned without enough oxygen for it to burn completely. This black soot, also known as lampblack, gas black, channel black or carbon black, is used to make inks, paints and rubber products. It can also be pressed into shapes and is used to form the cores of most dry cell batteries, among other things.
Graphite, one of the softest materials known, is a form of carbon that is primarily used as a lubricant. Although it does occur naturally, most commercial graphite is produced by treating petroleum coke, a black tar residue remaining after the refinement of crude oil, in an oxygen-free oven. Naturally occurring graphite occurs in two forms, alpha and beta. These two forms have identical physical properties but different crystal structures. All artificially produced graphite is of the alpha type. In addition to its use as a lubricant, graphite, in a form known as coke, is used in large amounts in the production of steel. Coke is made by heating soft coal in an oven without allowing oxygen to mix with it. Although commonly called lead, the black material used in pencils is actually graphite. Diamond, the third naturally occurring form of carbon, is one of the hardest substances

known. Although naturally occurring diamond is typically used for jewelry, most commercial quality diamonds are artificially produce.

Carbon is often added to steel to increase its hardness. Adding as little as 0.5% carbon can make a huge difference in the hardness of the steel. However, the increased hardness comes with a disadvantage -it is much less ductile. Careful control of the heat treatment allows one to control the tradeoff between hardness and ductility - but if you make a mistake you can end up with a blade that won't hold an edge or one that shatters if you drop it. Very high quality Japanese steel tools often laminate a piece of high ductility, low carbon steel to a thin layer of low ductility, high carbon steel to give a blade with a hard cutting edge and a reasonably ductile body. Cast irons listed as having 2 to 5% carbon are generally too brittle to make good cutting tools. However, they do make wonderful machine tools since they are extremely dimensionally stable.

In case of stainless steel that does not contain much carbon to make sure that it remains stainless. What is the result? Well carbon is responsible for making steels hard so they hold a really nice cutting edge. Therefore, SS is not very hard and makes lousy cutting tools. Well not really. Metallurgists figured that a metal that was both stainless and held a decent cutting edge would be great so they developed some SS that held a fairly good cutting edge. In the US these are the 400 series SS. The key is that through careful control of the composition and heat treatment you can create a metal that is a good compromise between corrosion resistance and hardness. However, it you make a mistake in either one you end up with a material that is too hard (brittle) or too soft (won't hold and edge). Generally cheap SS tools such as knives err on the side of too soft while high quality tools generally are right on or err on the side of too hard. If you look up the composition of most SS you will find that the carbon content is limited to less than 0.1%. Therefore, SS is technically not steel. Why is the carbon content of SS limited? Well, if you mess up the heat treatment the carbon likes to combine with the Cr to form chromium carbide which has the formula $Cr_{23}C_6$. This compound forms along the grain boundaries (not defined here) and robs the regions along the grain boundaries of Cr. However, Cr was added to the material to make it corrosion resistant so if you remove it the SS is no longer stainless. That is why the carbon concentration of SS is limited. Now, any steel in the 0.35 to 1.86 percent carbon content range can be hardened using a heat-quench-temper cycle. Most commercial steels are classified into one of three groups.

    i. Plain carbon steels
   ii. Low-alloy steels
  iii. High-alloy steel

2. Objectives of the project

The main objectives of this project are as follows.
    i. Design and fabrication of an experimental set-up
   ii. To determine the total amount of carbon in a metal.

3. Importance of carbon in metal

Some basics concerning the iron-carbon-steel relationship and it has influences on welding and metal alloys. Next time we'll look at influences of some key alloying elements and the effects of welding on metallurgy. Iron is the fourth most abundant element and makes up more than five percent of the earth's crust. Iron exists naturally in iron core (sometimes called ironstone). Since iron has a strong affinity for oxygen, iron ore is an oxide of iron; it also contains varying quantities of other elements such as silicon, sulfur, manganese, and phosphorus. Smelting is the process by which iron is extracted from iron ore. When iron ore is heated in a charcoal fire, the iron ore begins to release some of its oxygen, which combines with carbon monoxide to form carbon dioxide. In this way, a spongy, porous mass of relatively pure iron is formed, intermixed with bits of charcoal and extraneous matter liberated from the ore, known as slag. (The separation of slag from the iron is facilitated by the addition of flux, that is, crushed seashells or limestone.) The formation of this bloom of iron was as far as the primitive blacksmith got: he would remove this pasty mass from the furnace and hammer it on an anvil to drive out the cinders and slag and to compact the metallic particles. This was wrought iron ("wrought" means "worked," that is, hammered) and contained generally from .02 to .08 percent of carbon (absorbed from the charcoal), just enough to make the metal both tough and malleable. Wrought iron was the most commonly produced metal through most of the Iron Age.

4. Methodology

In order to getting and determining the amount of carbon, the experiment is properly set up by assembling required instruments. The procedure and method of determining total amount of carbon in a metal is fully based on combustion method. The combustion process is done by burning coal with high flame temperature without losing a little portion of heat energy inside the furnace. Ferrous sample is burnt inside the furnace with the

presence of oxygen. When a regulated of oxygen is passed over the heated ferrous sample, the carbon is oxidized to yield carbon dioxide and Sulphur dioxide that are passed through the metal tube and store in a gas jar or funnel where activated carbon is kept to adsorb hot carbon dioxide gas from combustion chamber. Activated carbon [Fig.1] that is used as a solid adsorbent (powder form) and it is kept inside the jar. Another name of activated carbon is charcoal. Traditionally, active carbons are made in particulate form as powders or fine granules less than 1.0 mm in size with an average diameter between .15 and .25 mm.Thus they present a large surface to volume ratio with a small diffusion distance.

Fig.1: Activated powder carbon

The main function of activated powder carbon is high adsorption capacity of CO_2 as well as with strong adhered. The gas jar is fully airtight since CO_2 is very volatile. In jar a little amount of impurities are presence such as Sulphurous gases, nitrogen, and iron oxide. The increase in weight of the absorbent gives the amount of carbon.

Chemical reaction that is happened during combustion is following:

Ferrous sample + Oxygen = Carbon dioxide +Iron oxide + (Sulphur dioxide) (less amount).

5. Flowchart

```
┌─────────────────┐   ┌─────────────────┐   ┌─────────────────┐   ┌─────────────────┐
│ Scrap of        │──▶│ Purification of │──▶│ Weight          │──▶│ Burning of steel│
│ stainless steel │   │ steel           │   │ measurement of  │   │ in combustion   │
│                 │   │                 │   │ steel           │   │ chamber         │
└─────────────────┘   └─────────────────┘   └─────────────────┘   └─────────────────┘
                                                                           │
                                                                           ▼
┌─────────────────┐   ┌─────────────────┐   ┌─────────────────┐
│ Measurement of  │◀──│ Measurement of  │◀──│ Collection of   │
│ carbon from     │   │ carbon dioxide  │   │ carbon dioxide  │
│ carbon dioxide  │   │                 │   │ in airtight     │
│                 │   │                 │   │ gas jar         │
└─────────────────┘   └─────────────────┘   └─────────────────┘
```
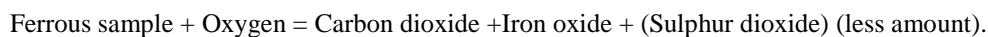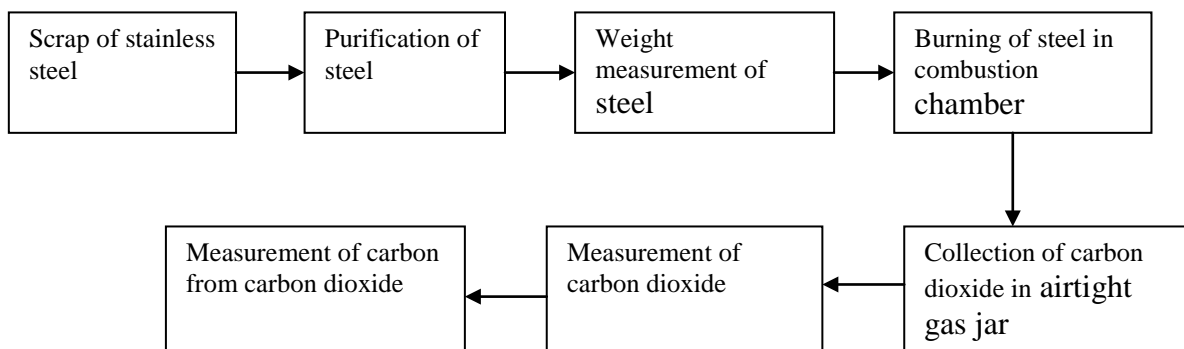
6. Experimental set up
Different types of equipment's are needed for fabricating of an experimental set-up. Lists of equipments use for fabrication of an experimental Set-Up which are given below.

6.1 Oxygen Cylinder
The set-up required for the determination of carbon by the combustion method with combine equipments. Oxygen cylinders one of the major component. The oxygen cylinder contains oxygen at least 99.5 percent purity and should be free from contaminated and carbonaceous matter. But here we used oxygen from natural ambient air since my project furnace has sufficient ventilation of flowing air for complete combustion.

6.2 Safety valve

Safety valve containing mercury is introduced in the line to limit the working value. The valve is connected with two metal tubes where the hot gas is passed and that is totally controlled by it. The main function of safety valve is remaining and storing CO_2 gas in the chamber. As a result CO_2 can't come out in the environment through the metal tube since the gas is high volatile when switch off of valve. After completing combustion I take CO_2 gas in a jar and continuously adsorbing by activated carbon with the help of switch on of the safety valve.

6.3 Furnace

A furnace is an equipment used to melt metals for casting or to heat materials to change their shape (e.g. rolling, forging) or properties (heat treatment). Since flue gases from the fuel come in direct contact with the materials, the type of fuel chosen is important. For example, some materials will not tolerate Sulphur in the fuel. Solid fuels generate particulate matter, which will interfere in the materials placed inside the furnace. For this reason:

   i. Most furnaces use liquid fuel, gaseous fuel or electricity as energy input
   ii. Induction and arc furnaces use electricity to melt steel and cast iron
   iii. Melting furnaces for nonferrous materials use fuel oil
   iv. Oil-fired furnaces mostly use furnace oil, especially for reheating and heat treatment of materials
   v. Light diesel oil (LDO) is used in furnaces where Sulphur is undesirable
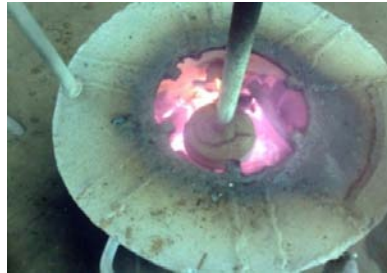
Fig.2: Experimental furnace.

The experimental furnace in [Fig.2] that is made by refractory material as an insulator with high effectively and reliability protecting heat energy. The temperature of the furnace may be developed up to 1550^0 c that is quite enough for melting steel.

Furnace ideally should heat as much of material as possible to a uniform temperature with the least possible fuel and labor. The key efficient furnace operation lies in complete combustion of fuel with minimum excess air. Furnaces operate with relatively low efficiencies (as low as 7 percent) compared to other combustion equipment such as the boiler (with efficiencies higher than 90 percent. This is caused by the high operating temperatures in the furnace. For example, a furnace heating materials to 1200 ^{0}C will emit exhaust gases at 1200 ^{0}C or more, which results in significant heat losses through the chimney.

6.4 Metal melting combustion chamber

The metal melting combustion chamber in [Fig.3] with metal tube is a part of furnace where the scraps or chips of steel are kept. It can take high temperature without deformation. Here we used scrap of steel that is easily melted inside melting chamber under the influence of heat energy.

Fig.3: Metal melting combustion chamber with metal tube.

6.5 Refractory material

Any material can be described as a 'refractory' if it can withstand the action of abrasive or corrosive solids, liquids or gases at high temperatures. The various combinations of operating conditions, in which refractories are used, make it necessary to manufacture a range of refractory materials with different properties. Refractory materials are made in varying combinations and shapes depending on their applications. General requirements of a refractory material are:

  i. Withstand high temperatures
 ii. Withstand sudden changes of temperatures
iii. Withstand action of molten metal slag, glass, hot gases, etc
iv. Withstand load at service conditions

For my experiment we used refractory material as an insulator to protect heat energy inside the furnace. As a result my furnace produces high heat energy with losing a small portion of heat.

6.6 Burning coal

Burning coal in [Fig.4] is used for completing combustion process of furnace because of melting metal and determining the amount of carbon.

Fig.4: Burning coal [7]

6.7 Electronic weighing balance

The electronic weighing balances in [Fig.5] that measure up to milligram since my amount of output CO_2 will be measured in milligram. This type of balance imparts the actual value, incorporating a small portion of fraction what will be measured.

Fig.5: Electronic weighing balance

6.8 The airtight gas jar

The airtight gas jar in [Fig.6] is the most important equipment of this project where the activated carbon is kept inside it. The activated carbon adsorbs the leaving hot CO_2 from the metal melting combustion chamber after opening the safety valve. The main function of airtight is to keep hot gas inside the jar. So that hot gas cannot come out in the environment from the jar.

Fig.6: The airtight gas jar

7. Data collection

The combustion process takes a specific time for completing combustion and reaction when safety valve is fully switched off. When the valve is opened and hot gas from the melting chamber comes out through the metal tube and is accumulated inside the airtight gas jar where it is being absorbed by activated carbon. [***Table 1***] imparts various data of this project.

Table 1: Data collection

Initial reading of jar with cork and activated carbon, m_1 (gm)	Final reading of jar with cork, activated carbon and CO_2 gas, (gm	Average reading of jar with cork, activated carbon and CO_2 gas, m_2 (gm)	Amount of CO_2 gas (m_2-m_1) (gm)	Amount of steel (scrap) that is melted, M (gm)	Amount of available carbon(c) in CO_2 gas, m (gm)	% of carbon(C) in steel= $\{(m \div M) \times 100\}$
183.00	183.50 184.00 183.50	183.667	0.667	550.00	0.1819	0.033

8. Calculation

Amount of steel (scrap) =550 gm.
Initial reading of jar with cork and activated carbon, m_1 = 183.00 gm.
Final reading of jar with cork, activated carbon and hot CO2 gas, w_1 =183.50gm
w_2 =184.00gm
w_3= 183.50gm.
Average final reading of jar with cork, activated carbon and hot CO2 gas, $m_2 = (w_1+w_2+w_3)/3$
$= (183.5+184+183.5)/3$
$= 183.667$ gm.

Therefore, amount of CO_2 gas, $m = (m_2 - m_1)$
$= (183.667-183.00)$ gm
$= 0.667$ gm.
Now, 44.00 gm CO_2 contains = 12.00 gm carbon (c)
0.667 gm CO_2 contains = $(12.00 \times 0.667) \div 44.00$
$= 0.1819$ gm
Therefore, 550.00 gm steel contains 0.667 gmCO_2means = 0.1819 gm carbon (c)
100.00 gm steel contains 0.667 gmCO_2means= $(0.18190 \times 100) \div 550.00$
$= 0.033$ gm carbon

Therefore, amount of carbon in steel = 0.033%.

9. Result and discussion

The concerning matter of my project is to find out how much amount of carbon is available in stainless steel. I have successfully determined the amount of carbon in steel and its amount is 0.033%. The experimental value of carbon varies with actual value since stainless steel contains less than 0.10% that is discussed in limitations.

10. Discussion

In case of steel and cast iron especially carbon has merits and demerits due to the amount of it, I have learnt from this project. During combustion available oxygen is passing inside the furnace. As a result over heated ferrous sample oxidizes with the oxygen due to the reaction of oxidization. Then carbon dioxide is absorbed in an activated carbon. The increase in weight of the absorbent gives the amount of carbon. We know that carbon is most important for both organic and inorganic substance due to its physical and chemical properties. In commercial sphere carbon is very essential. As a result a small amount of carbon can vary physical and chemical properties of metal. The experimental value of carbon is 0.033% of stainless steel but actually stainless steel contains less than 0.10% carbon [Reference 10, (duplex stainless steel)].But duplex stainless steel contains maximum 0.03% carbon. Therefore error is 0.003 %, (0.033-0.03) %, due to a small amount of impurities such as SO_2, FeO are included with CO_2 during measurement.

11. Scope and limitations

With the help of this experimental project we can measure the total amount of carbon from the steel and cast iron by combustion process. The combustion takes place inside a furnace where we use refractory material as an insulator protecting heat energy. The operating and maintenance cost are so effective.

It is quit impossible to find out the exact amount of carbon content of a metal by this experiment since it is analogue system. During the combustion some of the carbon will remain in combustion chamber due to ambient pressure, incomplete reaction and combustion and what not. A little amount of CO_2 will be loss during taking it in gas jar since CO_2 is volatile. Therefore final value of carbon will vary from actual value. But in modern technology the carbon measuring instruments are digital such as spectrophotometer that imparts the proper reading and widely used.

12. Conclusion and recommendation

I have to find out the total amount of carbon finally from the stainless steel by the properly designing and fabricating of an experimental setup. I have become successful to design and fabricate my project. To apply this method in to practical field, it is needed to be modified. Since the carbon measuring instruments are digital in modern technology so it should be digital by proper designing in future with relatively effective cost.

13. References

[1]   Ashton T.S.Iron and Steel in the Industrial Revolution, New York: Augustus M. Kelley, (1968).
[2] Chard, Jack Making Iron and Steel: The Historic Processes, 1700-1900. Ringwood, NJ: North Jersey Highlands Historical Society, (1995).
[3] Fisher, Douglas Alan (1963), the Epic of Steel, New York: Harper and Row.
[4] Sidney H. Avner (1997), Introduction to Physical Metallurgy, Second Edition, professor City University of New York.
[5]   http://www.cofamm.it [Date of access 15/09/2012]
[6]   http://www.iron-foundry.com [Date of access 20/09/2012]
[7]   http://www.shelmetcastings.com [Date of access 23/09/2012]

Friction Coefficient of Copper Mating with Smooth and Rough Mild Steel Counterfaces

[1]Dr. Mohammad Asaduzzaman Chowdhury ,[2]Dr. Dewan Muhammad Nuruzzaman,
[1]Biplov Kumar Roy, [3]Rajib Nandee

[1]Department of Mechanical Engineering, Dhaka University of Engineering and Technology Gazipur,Gazipur-1700, Bangladesh. [2]Faculty of Manufacturing Engineering University Malaysia Pahang, Malaysia ,[3]Esquire Knit Composite Ltd., Narayangonj, Bangladesh
E-mail: asadzmn2003@yahoo.com

Abstract

In the present study, friction coefficient and wear rate of copper sliding against mild steel are investigated experimentally. In order to do so, a pin on disc apparatus is designed and fabricated. Experiments are carried out when smooth or rough mild steel pin slides on copper disc. Experiments are conducted at normal load 10, 15 and 20 N, sliding velocity 1, 1.5 and 2 m/s and relative humidity 70%. Variations of friction coefficient with the duration of rubbing at different normal loads and sliding velocities are investigated. Results show that friction coefficient is influenced by duration of rubbing, normal load and sliding velocity. In general, friction coefficient increases for a certain duration of rubbing and after that it remains constant for the rest of the experimental time. The obtained results reveal that friction coefficient decreases with the increase in normal load for copper mating with smooth or rough mild steel counterface. Moreover, friction coefficient increases with the increase in sliding velocity. The magnitudes of friction coefficient are different depending on sliding velocity and normal load for both smooth and rough counterface pin materials.

Keywords: Friction coefficient; wear rate, copper, mild steel, normal load, sliding velocity

.

1. Introduction

Study of mechanics of friction and the relationship between friction and wear dates back to the sixteenth century, almost immediately after the invention of Newton's law of motion. It was observed by several authors [1-13] that the variation of friction depends on interfacial conditions such as normal load, geometry, relative surface motion, sliding velocity, surface roughness of the rubbing surfaces, type of material, system rigidity, temperature, stick slip, relative humidity, lubrication and vibration. Among these factors normal load and sliding velocity are the two major factors that play significant role for the variation of friction. In the case of materials with surface films which are either deliberately applied or produced by reaction with environment, the coefficient of friction may not remain constant as a function of load. In many metal pairs in the high load regime, the coefficient of friction decreases with load. Bhushan [14] and Blau [15] reported that increased surface roughening and a large quantity of wear debris are believed to be responsible for decrease in friction. It was observed that the coefficient of friction may be very low for very smooth surfaces and/or at loads down to micro-to nanonewton range [16, 17]. The third law of friction, which states that friction is independent of velocity, is not generally valid. Friction may increase or decrease as a result of increased sliding velocity for different materials combinations. An increase in the temperature generally results in metal softening in the case of low melting point metals. An increase in temperature may result in solid-state phase transformation which may either improve or degrade mechanical properties [13]. The most drastic effect occurs if a metal approaches its melting point and its strength drops rapidly, and thermal diffusion and creep phenomena become more important. The resulting increased adhesion at contacts and ductility lead to an increase in friction [13]. The increase in friction coefficient with sliding velocity due to more adhesion of counterface material (pin) on disc.
It was reported [18-21] that friction coefficient of metals and alloys showed different behavior under different operating conditions. In spite of these investigations, the effects of normal load and sliding velocity on friction coefficients of SS 304 mating with smooth and rough couterface are yet to be clearly understood. Therefore, in

this study an attempt is made to investigate the effect of normal load and sliding velocity on the frictional behavior of SS 304 sliding against smooth and rough mild steel counterface.

Moreover, the effects of duration of rubbing on friction coefficient of these materials are examined in this study. It is expected that the applications of these results will contribute to the different concerned mechanical processes.

Within this research, it is sought to better understand the relation between friction/wear and different types of materials under different normal loads and sliding velocities and to explore the possibility of adding controlled normal load and sliding velocity to a mechanical process as a means to improve performance and quality in industry.

2. Experimental

A schematic diagram of the experimental set-up is shown in Fig. 1 i.e. a pin which can slide on a rotating horizontal surface (disc). In this set-up a circular test sample (disc) is to be fixed on a rotating plate (table) having a long vertical shaft clamped with screw from the bottom surface of the rotating plate. The shaft passes through two close-fit bush-bearings which are rigidly fixed with stainless steel plate and stainless steel base such that the shaft can move only axially and any radial movement of the rotating shaft is restrained by the bush. These stainless steel plate and stainless steel base are rigidly fixed with four vertical round bars to provide the rigidity to the main structure of this set-up. The main base of the set-up is constructed by 10 mm thick mild steel plate consisting of 3 mm thick rubber sheet at the upper side and 20 mm thick rubber block at the lower side. A compound V-pulley above the top stainless steel plate was fixed with the shaft to transmit rotation to the shaft from a motor. An electronic speed control unit is used to vary the speed of the motor as required. A 6 mm diameter cylindrical smooth (roughness, R_a, about 0.3 μm) or rough (roughness, R_a, about 3 μm) pins their contacting foots are flat made of mild steel, fitted on a holder is subsequently fitted with an arm. The arm is pivoted with a separate base in such a way that the arm with the pin holder can rotate vertically and horizontally about the pivot point with very low friction.
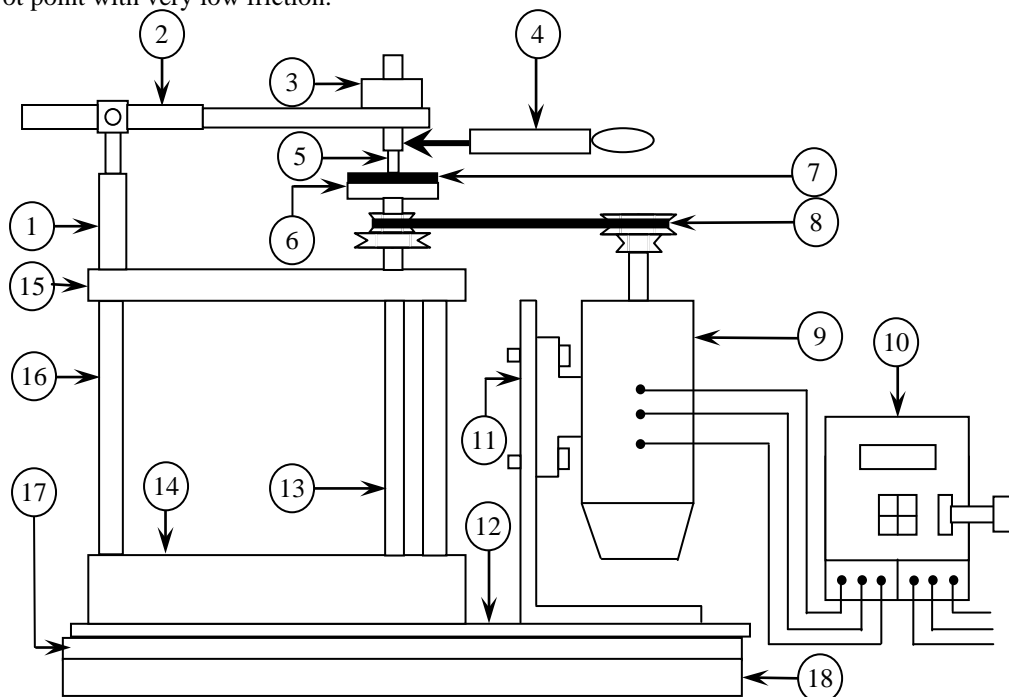
1. Load arm holder 2. Load arm 3. Normal load (dead weight) 4. Spring balance 5. Pin sample
6. Rotating table 7. Test disc 8. Belt and pulley 9. Motor 10. Speed control unit 11. Vertical motor base 12. 3 mm Rubber pad 13. Main shaft 14. Stainless steel base 15. Stainless steel plate 16. Vertical square bar17. Mild steel main base plate 18. Rubber block (20 mm thick)

Fig..1: Block Diagram of the Experimental Set-up

Sliding speed can be varied by two ways (i) by changing the frictional radius and (ii) by changing the rotational speed of the shaft. In this research, sliding speed is varied by changing the rotational speed of the shaft while maintaining 25 mm constant frictional radius. To measure the frictional force acting on the pin during sliding on the rotating plate, a load cell (TML, Tokyo Sokki Kenkyujo Co. Ltd, CLS-10NA) along with its digital indicator (TML, Tokyo Sokki Kenkyujo Co. Ltd, Model no. TD-93A) was used. The coefficient of friction was obtained by dividing the frictional force by the applied normal force (load). Wear was measured by weighing the test sample with an electronic balance before and after the test, and then the difference in mass was converted to wear rate. To measure the surface roughness of the test samples, Taylor Hobson Precision Roughness Checker (Surtronic 25) was used. Before friction tests, the average surface roughnesses of copper test sample was found to be $R_a = 0.5$ μm.. Each test was conducted for 30 minutes of rubbing time with new pin and test sample. Furthermore, to ensure the reliability of the test results, each test was repeated five times and the scatter in results was small, therefore the average values of these test results were taken into consideration. The detail experimental conditions are shown in Table 1.

Table 1. Experimental conditions

Sl. No.	Parameters	Operating Conditions
1.	Normal Load	10, 15, 20 N
2.	Sliding Velocity	1, 1.5, 2 m/s
3.	Relative Humidity	70 (± 5)%
4.	Duration of Rubbing	30 minutes
5.	Surface Condition	Dry
6.	Disc material	Copper
7.	Pin material	Mild steel (smooth and rough)

3. Results and Discussion

Figure 2 shows the variation of friction coefficient with the duration of rubbing at different normal load for copper mating with smooth mild steel counterface. During experiment, the sliding velocity and relative humidity were 1 m/s and 70% respectively. Curve 1 of this figure is drawn for normal load 10 N. From this curve, it is observed that during the starting, the value of friction coefficient is 0.23 and then increases very steadily up to 0.3 over duration of 20 minutes of rubbing and after that it remains constant for the rest of the experimental time.
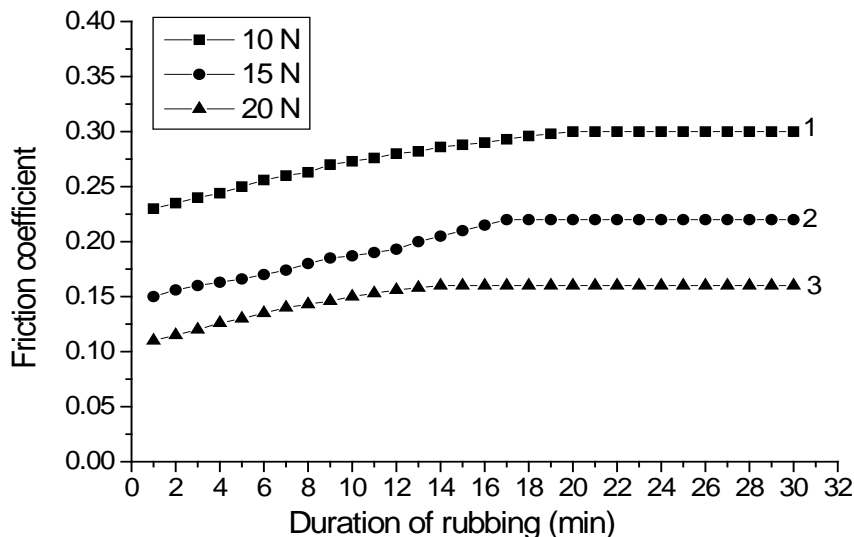
Figure 2: Friction coefficient as a function of duration of rubbing at different normal loads (sliding velocity: 1 m/s, relative humidity: 70%, test sample: Copper, pin: Mild steel,smooth)

At the initial stage of rubbing, friction is low and the factors responsible for this low friction are due to the presence of a layer of foreign material on the disc surface. This layer on the disc surface in general comprises of (i) moisture, (ii) oxide of metals, (iii) deposited lubricating material, etc. Copper readily oxidizes in air, so that, at initial duration of rubbing, the oxide film easily separates the two material surfaces and there is little or no true metallic contact and also the oxide film has a low shear strength. After initial rubbing, the film (deposited layer) breaks up and clean surfaces come in contact which increase the bonding force between the contacting surfaces. At the same time due to the ploughing effect, inclusion of trapped wear particles and roughening of the disc surface, the friction force increases with duration of rubbing. After a certain duration of rubbing, the increase of roughness and other parameters may reach to a certain steady state value and hence the values of friction coefficient remain constant for the rest of the time. Curves 2 and 3 of this figure are drawn for normal load 15 and 20 N respectively and show similar trends as that of curve 1. From these curves, it is also observed that time to reach steady state values is different for different normal load. Results show that at normal load 10, 15 and 20 N, copper-mild steel smooth pair takes 20, 17 and 14 minutes respectively to reach steady friction. It indicates that the higher the normal load, the time to reach steady friction is less. This is because the surface roughness and other parameter attain a steady level at a shorter period of time with the increase in normal load. The trends of these results are similar to the results of Chowdhury and Helali [22, 23].
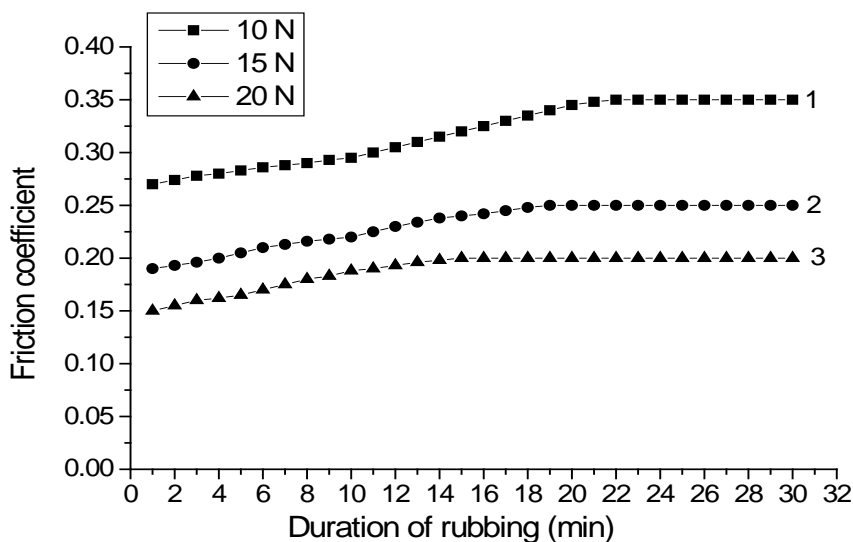
Figure 3: Friction coefficient as a function of duration of rubbing at different normal loads (sliding velocity: 1 m/s, relative humidity: 70%, test sample: Copper, pin: Mild steel,rough)
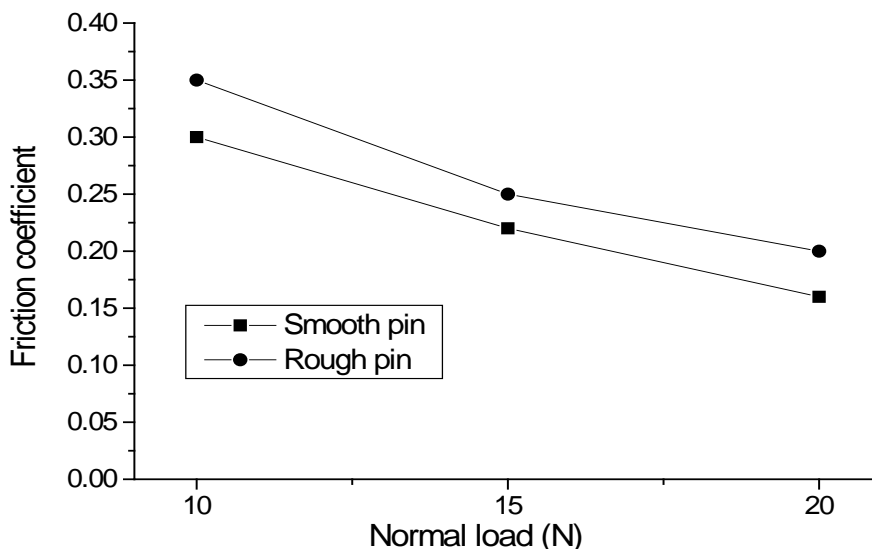
Figure 4: Friction coefficient as a function of normal load for copper (Sliding velocity: 1 m/s, relative humidity: 70%)

Figure 3 shows the effect of the duration of rubbing on the value of friction coefficient at different normal load for copper sliding against rough mild steel counterface at speed of 1 m/s and 70% of relative humidity. Curve 1 of this figure drawn for normal load 10 N, shows that during starting of the experiment, the value of friction coefficient is 0.27 which rises for few minutes to a value of 0.35 and then it becomes steady for the rest of the experimental time. Almost similar trends of variation are observed in curves 2 and 3 which are drawn for load 15 and 20 N respectively. From these curves, it is found that time to reach steady friction is different for different normal load. At normal load 10, 15 and 20 N, copper-mild steel rough pair takes 22, 19 and 15 minutes respectively to reach steady friction That is, higher the normal load, copper-mild steel rough pair takes less time to stabilize.

Figure 4 shows the comparison of the variation of friction coefficient with normal load for copper mating with smooth and rough mild steel couterface. Curves of this figure are drawn for copper under mild steel smooth and rough counerface conditions. It is shown that friction coefficient varies from 0.3 to 0.16 and 0.35 to 0.2 with the variation of normal load from 10 to 20 N for copper-mild steel smooth and copper-mild steel rough pairs respectively. These results show that friction coefficient decreases with the increase in normal load. Increased surface roughing and a large quantity of wear debris are believed to be responsible for the decrease in friction [14,15] with the increase in normal load. Similar behavior is obtained for Al–Stainless steel pair [24] i.e friction coefficient decreases with the increase in normal load. From this figure, it is also found that at identical conditions, the values of friction coefficient of copper mating with smooth counterface is lower that that of copper with rough counterface.
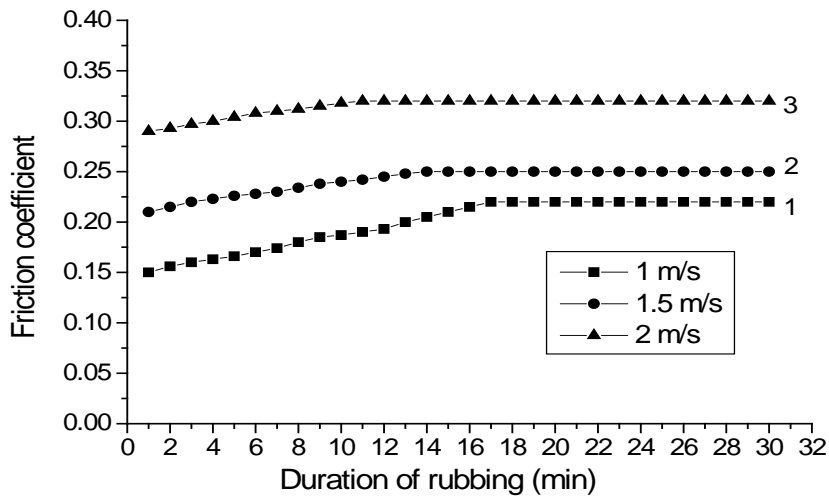
Figure 5: Friction coefficient as a function of duration of rubbing at different sliding velocities (normal load: 15 N, relative humidity: 70%, test sample: Copper, pin: Mild steel,smooth)
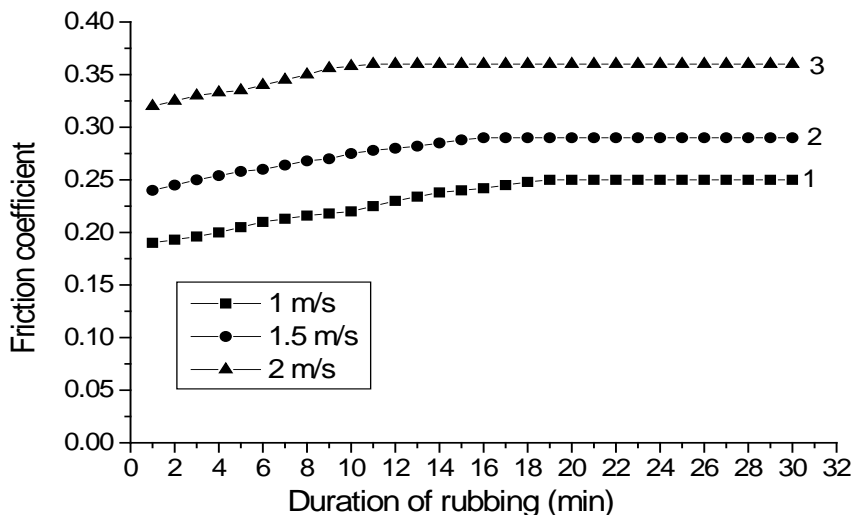
Figure 6: Friction coefficient as a function of duration of rubbing at different sliding velocities (normal load: 15 N, relative humidity: 70%, test sample: Copper, pin: Mild steel,rough)

Figures 5 and 6 show the variation of friction coefficient with the duration of rubbing at different sliding velocity for copper-mild steel smooth and copper-mild steel rough pair respectively at 15 N normal load. Curves 1, 2 and 3 of Figure 5 are drawn for sliding velocity 1, 1.5 and 2 m/s respectively. Curve 1 of this figure shows that during the starting, the value of friction coefficient is 0.15 which increases almost linearly up to 0.22 over a duration of 17 minutes of rubbing and after that it remains constant for the rest of the experimental time. The increase of friction may be associated with ploughing effect and because of roughening of the disc surface. After a certain duration of rubbing the increase of roughness and other parameters may reach to a certain steady value hence the values of friction coefficient remain constant for the rest of the time. Curves 2 and 3 show that for the higher sliding speed, the friction coefficient is more and the trend in variation of friction coefficient is almost the same as for curve 1.
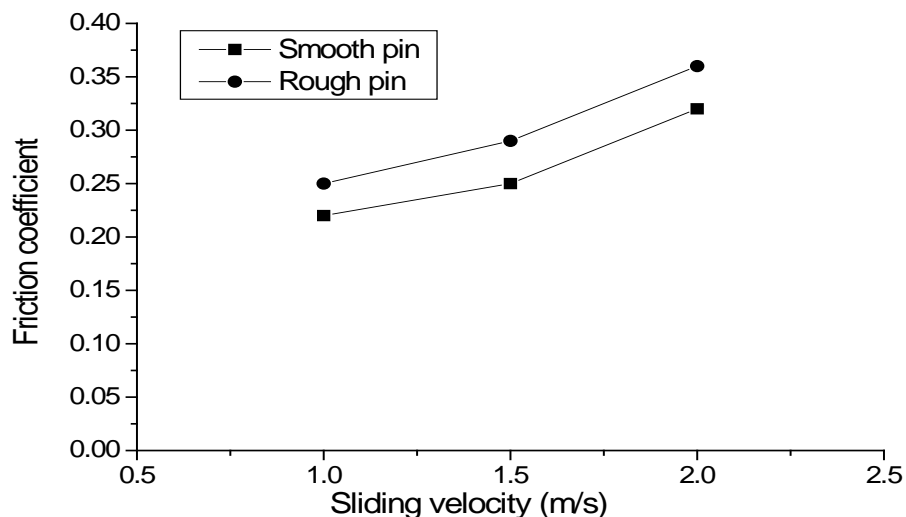
Figure 7: Friction coefficient as a function of sliding velocity for copper (normal load: 10 N, relative humidity: 70%)

From these curves, it is also observed that time to reach steady state values are different for different sliding velocity. From the results it is found that gun metal-mild steel smooth pair at sliding velocity 1, 1.5 and 2 m/s takes to reach constant friction 17, 14 and 11 minutes respectively. It indicates that the higher the sliding velocity, the time to reach constant friction is less. This may be due to the higher the sliding speed the surface roughness and other parameters take less time to stabilize. From Figure 6, it can be observed that the trends in variation of friction coefficient with the duration of rubbing are very similar to that of Figure 5 but the values of friction coefficient are different for copper-mild steel rough pair.

Figure 7 shows the comparison of the variation of friction coefficient with sliding velocity for the above mentioned material pairs. Curves of this figure are drawn for copper-mild steel smooth and copper-mild steel rough pairs. It is shown that the friction coefficient varies from 0.22 to 0.32 and 0.25 to 0.36 with the variation of sliding velocity from 1 to 2 m/s for copper-mild steel smooth and copper-mild steel rough pairs respectively. These results indicate that friction coefficient increases with the increase in sliding velocity. Sliding contact of two materials results in heat generation at the asperities and hence increases in temperature at the frictional surfaces of the two materials. An increase in the temperature generally results in metal softening in the case of low melting point metals. An increase in temperature may result in solid-state phase transformation which may either improve or degrade mechanical properties [13]. The most drastic effect occurs if a metal approaches its melting point and its strength drops rapidly, and thermal diffusion and creep phenomena become more important. The resulting increased adhesion at contacts and ductility lead to an increase in friction [13]. The increase in friction coefficient with sliding velocity due to more adhesion of counterface material (pin) on disc. From this figure, it is also found that at identical conditions, the values of friction coefficient of copper sliding against smooth mild steel counterface is lower that that of copper sliding against rough mild steel counterface.

4. **Conclusion**

The presence of normal load and sliding velocity indeed affects the friction force considerably. The values of friction coefficient decrease with the increase in normal load for copper mating with smooth and rough mild steel counterfac . On the other hand, the values of friction coefficient increase with the increase in sliding velocity for copper sliding against smooth and rough mild steel pins. Friction coefficient varies with the duration of rubbing and after certain duration of rubbing, friction coefficient becomes steady for the observed range of normal load and sliding velocity. At identical conditions, the values of friction coefficient of copper mating with smooth counterface is lower that that of SS 304 with rough counterface.
 As (i) the friction coefficient decreases with the increase in normal load (ii) the values of friction coefficient increase with the increase in sliding velocity and (iii) the magnitudes of friction coefficient are different under smooth and rough counterface conditions, therefore maintaining an appropriate level of normal load, sliding velocity as well as appropriate choice of counterface surface conditions, friction may be kept to some lower value to improve mechanical processes.

References

[1] J. F. Archard, *Wear Theory and Mechanisms, Wear Control Handbook,"M. B. Peterson and W.O. Winer, eds., ASME*, New York, NY, pp. 35- 80, (1980).
[2] D. Tabor, "Friction and Wear – Developments Over the Last 50 Years, Keynote Address, *Proc. International Conf. Tribology – Friction, Lubrication and Wear, 50 Years On*, London", Inst. Mech. Eng., pp. 157-172, (1987).
[3] S. T. Oktay, N. P. Suh, "Wear Debris Formation and Agglomeration, *ASME Journal of Tribology"*, Vol. 114, pp. 379-393, (1992).
[4] N. Saka, M. J. Liou, N. P. Suh, "The role of Tribology in Electrical Cotact Phenomena ", *Wear*, Vol. 100, pp. 77-105, (1984).
[5] N. P. Suh, H. C. Sin, "On the Genesis of Friction and Its Effect on Wear, Solid Contact and Lubrication", *H. S. Cheng and L. M. Keer, ed., ASME*, New York, NY, AMD-Vol. 39pp. 167-183, (1980).
[6] V. Aronov, A. F. D'souza, S. Kalpakjian, I. Shareef," Experimental Investigation of the effect of System Rigidity on Wear and Friction- Induced Vibrations", *ASME Journal of Lubrication Technology*, Vol. 105, pp. 206-211, (1983).
[7] V. Aronov, A. F. D'souza, S. Kalpakjian, I. Shareef," Interactions Among Friction, Wear, and System Stiffness-Part 1: Effect of Normal Load and System Stiffness", *ASME Journal of Tribology*, Vol. 106, pp. 54-58, (1984).
[8] V. Aronov, A. F. D'souza, S. Kalpakjian, I. Shareef, "Interactions Among Friction, Wear, and System Stiffness-Part 2: Vibrations Induced by Dry Friction", *ASME Journal of Tri*bology, Vol. 106, pp. 59- 64, (1984).
[9] V. Aronov, A. F. D'souza, S. Kalpakjian, I. Shareef, "Interactions Among Friction, Wear, and System Stiffness-Part 3: Wear Model", *ASME Journal of Tribology*, Vol. 106, pp. 65-69 (1984).
[10] J. W. Lin, M. D. Bryant," Reduction in Wear rate of Carbon Samples Sliding Against Wavy Copper Surfaces", *ASME Journal of Tribology*, Vol. 118, pp. 116-124 (1996).
[11] K. C. Ludema, Friction, Wear, Lubrication A Textbook in Tribology, CRC press, London, UK. (1996).
[12] E. J. Berger, C. M. Krousgrill, F. Sadeghi, "Stability of Sliding in a System Excited by a Rough Moving Surface", *ASME*, Vol. 119, pp. 672- 680, (1997).
[13] B. Bhushan, Principle and Applications of Tribology, *John Wiley & Sons, Inc.,* New York, (1999).
[14] B. Bhushan, Tribology and Mechanics of Magnetic Storage Devices, *Springer-Verleg*, 2nd edition ,New York, (1996).
[15] P. J. Blau, Scale Effects in Sliding Friction: "An Experimental Study, in Fundamentals of Friction: Macroscopic and Microscopic Processes (I.L., Singer and H. M., Pollock, eds.)", vol. E220, pp. 523-534, Kluwer Academic, Dordrecht, Netherlands (1992).
[16] B. Bhushan, Handbook of Micro/ Nanotribology, *CRC Press*, 2nd edition,Boca Raton, Florida, (1999).
[17] B. Bhushan, A. V. Kulkarni, "Effect of Normal Load on Microscale Friction Measurements", *Thin Solid Films*, vol. 278**,** 49-56; 293, 333, (1996).
[18] M. A. Chowdhury, M. M. Helali, "The Effect of Relative Humidity and Roughness on the Friction Coefficient under Horizontal Vibration", *The Open Mechanical Engineering Journal,* vol. 2, pp. 128- 135, (2008).
[19] M. A. Chowdhury, M. M. Helali, A.B.M. Toufique Hasan "The frictional behavior of mild steel under horizontal vibration", *Tribology International,* vol. 42, pp. 946- 950, (2009).
[20] M. A. Chowdhury, S. M. I. Karim, M. L. Ali, "The influence of natural frequency of the experimental set-up on the friction coefficient of copper", *Proc. of IMechE, Journal of Engineering Tribology,* vol. 224, pp. 293- 298, (2009).
[21] M. A. Chowdhury, D. M. Nuruzzaman, M. L. Rahaman," Influence of external horizontal vibration on the coefficient of friction of aluminium sliding against stainless steel", *Industrial Lubrication and Tribology,* vol. 63, pp. 152- 157, 2011.
[22] M. A. Chowdhury, M. M.. Helali, "The Effect of frequency of Vibration and Humidity on the Coefficient of Friction", Tribology International, 39, pp. 958 – 962. (2006).
[23] M. A. Chowdhury, M. M.. Helali, "The Effect of Amplitude of Vibration on the Coefficient of Friction", Tribology International,41 , pp. 307- 314, (2008).

[24] M. A. Chowdhury,. M. K. Khalil., D. M, Nuruzzaman, M. L.Rahaman, "The Effect of Sliding Speed and Normal Load on Friction and Wear Property of Aluminum", International Journal of Mechanical & Mechatronics Engineering, 11, pp. 53-57. (2011).

Paper ID: MS-32

Evaluation of Stabilized Soil Blocks with the inclusion of 'Plastic Fibre' as Sustainable Building Material: A Complete Review

I. B. Muhit
Department of Civil Engineering, Chittagong University of Engineering & Technology, Chittagong-4349, Bangladesh.
E-mail: imrose_cuet@live.com

Abstract

Now-a-days, huge amount of waste plastics is one of the major and important environmental hazards in Solid Waste Management (SWM) sector. So an efficient and effluent use or management is necessary to recycle these jungles of waste plastics. Through a fundamental research, use of these waste plastics in the specific form of fibres in making block may prove more efficient and undoubtedly a great feedback to Solid Waste Management. The significant effects of Plastic Fibre (which is embedded from waste plastic) on stabilized mud blocks as well as performance effect as a sustainable building material is highlighted and reviewed in this research paper through a systematic investigation process. By adding Portland cement, Lime and their combination was used for preparing stabilized soil. Plastic carry bags (locally known as plastic bazar bags), plastic juice bottles and mineral water bottles in chopped form were the major source of Plastic Fibre. These fibres were added 0.1% & 0.2% by weight of soil as reinforcement. The blocks mix compositions are different in percentage of cement and percentage of lime with different percentage (0.1% by weight of soil & 0.2% by weight of soil) of plastic fibres. The failure patterns of the blocks were analyzed along with tested for density as well as compressive strength in MPa. From investigation it was found that, strength increases about 3% to 10% for different cement and lime percentage for blocks prepared with 0.1% of plastic fibres. From failure pattern observation it was also visible that, uses of fibres reinforcement improve ductility which was compared with raw blocks.

Keywords: Sustainable building materials, Solid waste management, Plastic fibres, Stabilized blocks, Density, Compressive strength, Ductility.

1. Introduction

Earth in the form of mud bricks has been used as the construction material for thousands of years. To improve physical characteristics of compressed soil masonry blocks, moist soil is mechanically compacted. But the key problems arise from the materials, in the presence of water or moisture is low tensile strength with brittle behavior and deterioration. Stabilization with renowned binders like cement or lime can improve the water resisting capacity as well as strength. From H. Binici *et al.* (2007) and A. Mesbah *et al.* (2004) it is clear that, to improve tensile strength, durability and ductility in tension and to reduce shrinkage cracking, natural fibres have been used from long days ago. Theoretical models were also developed on composite soil blocks reinforced with fibres subjected to shear.

The enormous amount of waste plastics is one of the major environmental concerns for recent decades as a part of solid waste management. In mud block making uses of waste plastics in the form of fibres which may term as 'Plastic Fibre-Mud Blocks' is one of the interesting and efficient methods of solid waste management. The efficiency and contribution of this type of solid waste management can be investigated through a fundamental research. Maximum studies on natural fibres are concentrated on cellulose based or vegetable fibres, which may obtain from renewable plant resources and it is evident from the review of the existing literature. But in case of animal fibre, and plastic fibre as well as polystyrene fabric this resource is not valid at all. That's why, to make plastic fibre mud blocks appealing to all and applicable widely, some research on the physic-mechanical properties and characteristics is indispensible. From the preliminary investigation of some systematic study, this paper highlights and represents the key observations on the effect of embedded fibre (the source is plastic waste) on the strength performance of stabilized mud blocks corresponding to different amount of plastic fibre.

2. Key Materials and Experimental Approach

The soil which is being collected for making blocks was carried through standard soil classification. The basic summaries is shown in Table 1

Table 1. Summary of Standard Soil Classification

Sand (%)	Silt (%)	Clay (%)	Specific Gravity	Optimum Moisture Content (%)	Dry Density (g/cc)
58.5	37.5	4.00	2.63	17.5	1.83

Soil was stabilized by combination of cement-lime. The quantity of cement and lime added was 8% & 10% and after several trials 2% & 4% by weight of soil respectively. Similar observations regarding the quantity of stabilizers (7.5% of cement and 2% lime) were made by Jagadeesh, 2007 at *'Building with Stabilised Mud'*. Basically it relies on the type and nature of soil. During making of block, plastic fibre of length 20 mm were added with mixture of 0.1% & 0.2% by weight of soil. The plastic fibre was in chopped form of carry bags having aspect ratio 125 and mineral water bottles having aspect ratio 84. Figure 1 show some chopped plastic fibres which wasn't the actual picture of the experiment but supplied with this paper to identify the types and format of the chopped plastic fibre. Seven types of sample were prepared where one is control block containing only raw soil. The remaining six types of samples were raw soil with 8% cement, raw soil with 8% cement and 2% lime, raw soil with 8% cement and 4% lime, raw soil with 10% cement, raw soil with 10% cement and 2% lime, raw soil with 10% cement and 4% lime respectively, having blocks size 305mm x 143mm x 100mm. These mixture combinations are shown in tabular form in Table 2.

By pressing the prepared soil at OMC, blocks were made and straw as well as gunny bag were used to cover the block stack during curing period. Sprinkling of water on these covers consists the curing. After 3, 7 and 28 days the prepared blocks were tested for compressive strength by using a digital compression testing machine with lowest count of 20 N which ranges up to 1000 kN. In the end, dry density fluctuations and effect on compressive strength were analyzed and finally from the deep observation of failure pattern of the sample blocks the benefits of fibre reinforcement in ductility and crack propagation properties were evaluated.

Fig. 1. Chopped Plastic Fibre

Table 2. Composition of the Blocks

Composition of the Mix	Dimension (mm) L x B x H	Sample Labeling
Raw Soil (Control Block)	305 x 143 x 100	C
Raw Soil with 8% Cement	305 x 143 x 100	C1
Raw Soil with 8% Cement and 2% Lime	305 x 143 x 100	C2
Raw Soil with 8% Cement and 4% Lime	305 x 143 x 100	C3
Raw Soil with 10% Cement	305 x 143 x 100	C4

| Raw Soil with 10% Cement and 2% Lime | 305 x 143 x 100 | C5 |
| Raw Soil with 10% Cement and 4% Lime | 305 x 143 x 100 | C6 |

3. Results and Discussions

3.1 Effects on Density and Specific Gravity

There is a significant effect on density and specific gravity for different mixing proportions. From experiment it is visible that, the density of the soil blocks with different mixing compositions varied from 1800 kg/m^3 to 1898 kg/m^3. Effects of different mix composition with (0.1% by weight of soil & 0.2% by weight of soil) or without plastic fibre, on density is shown in Table 3 in the form of test result. It is also proved from experiment that adding of plastic fibre doesn't create a radical change in density and in almost each cases density falls slightly after adding 0.1% fibre and density falls remarkably after adding 0.2% fibre. It is clearly shown in Figure 2. Most important thing to mention that, the specific gravity of the fibres fluctuates within 1.07 to 1.1.

Table 3. Density (Kg/m^3) for Different Composition

Sample No.	0% Fibre	0.1% Fibre	0.2% Fibre
	Kg/m^3	Kg/m^3	Kg/m^3
C	1889	1825	1800
C1	1892	1888	1841
C2	1883	1854	1829
C3	1855	1847	1831
C4	1898	1882	1834
C5	1885	1865	1823
C6	1866	1860	1822
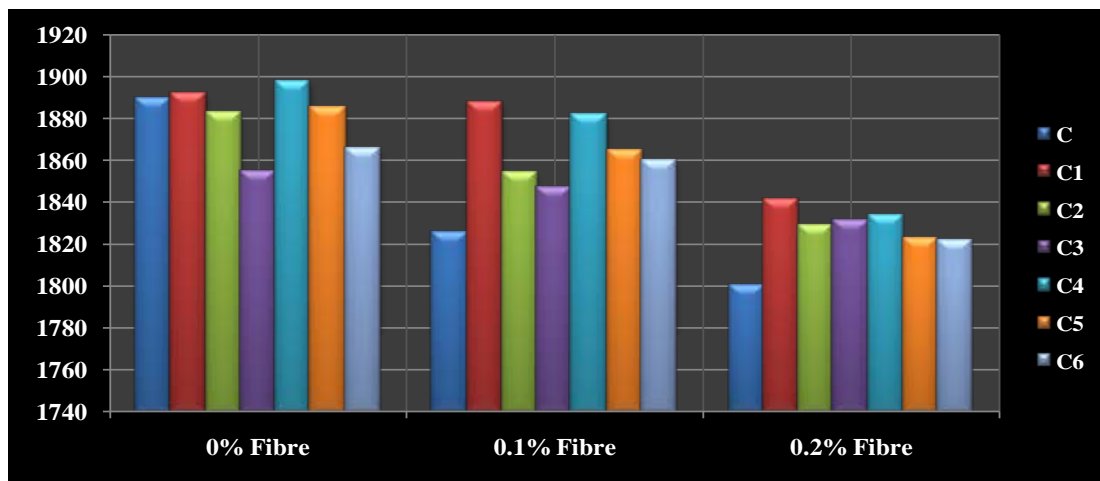
Fig. 2. Fluctuation of Density for Different Composition

3.2 Effects on Compressive Strength

At 28 days curing the compressive strength of the blocks fluctuated from 2.00 to 4.29 MPa depending on different composition of mix and percentage of plastic fibre. If control blocks (C) and blocks stabilized with 8% cement content (C1) compared, it is evident that strength increases approximately 8.5%. Moreover, 29.5% strength increases in case of comparing between control blocks (C) and blocks consists of 10% cement (C4). Again compared to block with 10% cement (C4) there was an increase of 5.6% and approximately 18% in strength when this soil block was stabilized by 2% (C5) and 4% of lime (C6) respectively. The stabilized treated mud blocks exhibits strength values ranges from 2.71 MPa to 4.14 MPa which contains 0% plastic fibre and these may compared with the well burnt brick's compressive strength of 3.5 MPa as per BIS 1077-1992 (Fifth Revision). It is notable that, for all mixing compositions the blocks with 0.2% of plastic fibre the compressive strength were reduced but it was positive for 0.1% plastic fibre. Almost in every case compressive strength was increases significantly for the blocks with 0.1% plastic fibre. Large quantity of fibres distributed non-uniformly

in the blocks and creating weaker plane, which may leads to reduction in strength. The strength in MPa are shown in Table 4 with sample number and Figure 3 shows the fluctuation of strength pattern with respect to different mixing composition for with (0.1% and 0.2%) and without plastic fibre.

Table 4. Strength (MPa) for Different Composition

Sample No.	0% Fibre	0.1% Fibre	0.2% Fibre
	MPa	MPa	MPa
C	2.71	2.90	2.00
C1	2.94	3.36	3.00
C2	3.49	3.95	3.14
C3	2.95	3.60	3.02
C4	3.51	3.99	3.26
C5	3.71	3.97	2.85
C6	4.14	4.29	3.78
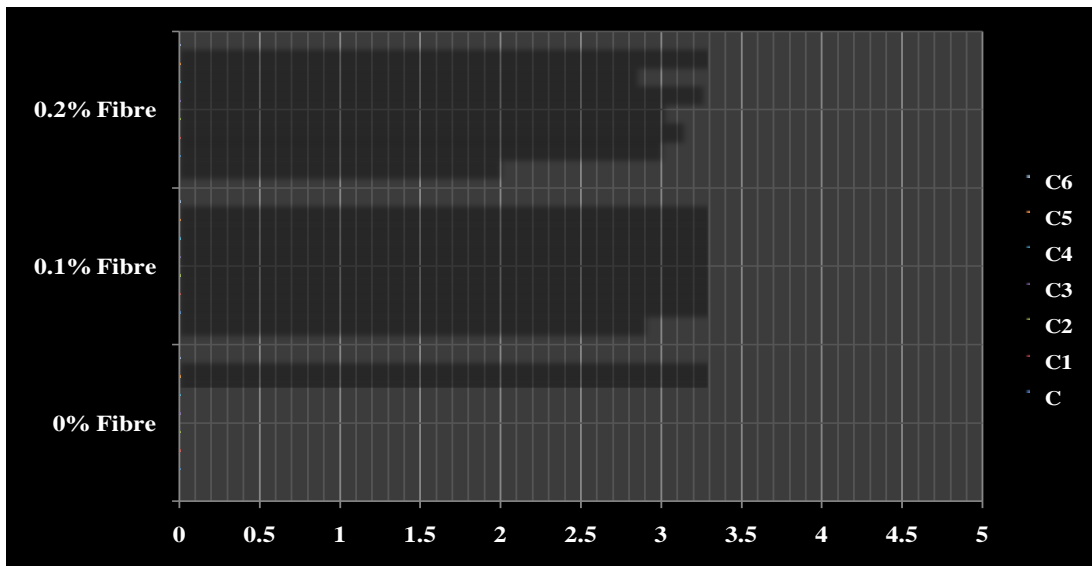
Fig. 3. Fluctuation of Strength for Different Composition

From this experiment and from S.M. Marandi et al. (2008) and C. Galan-Marin et al. (2010) it can be said that during fibre sliding, cement stabilized soil blocks provide some resistance and this leads to the increase in compressive strength at all.

3.3 Effects on Failure Mode and Crack Propagation

The control blocks which contains only raw soil, exhibits an abrupt failure without introducing any symptoms or warning and the mode is quick. On the contrary, the blocks with fibres were quite different in nature from control blocks and these specimens still deformed after the ultimate load was reached and finally crack was observed on the specimen. But these specimens showed fine irregular and distinguishable crack on its surface as like as raw soil control blocks. S.M. Marandi et al. (2008) observed same things in a study on strength and durability of randomly distributed palm fibres reinforced with silty-sand soils. From a complete analysis of failure modes and crack propagation the benefits of plastic fibre was evaluated that it can improve ductility as well as crack propagation after initial formation.

4. Conclusions

This research was conducted to evaluate the density, compressive strength and failure pattern for different stabilized condition with 0% plastic fibre, 0.1% plastic fibre and 0.2% plastic fibre respectively**.** By maintaining and following various standards this study was conveyed.

- ❖ The density of the soil blocks with different mixing compositions varied from 1800 kg/m^3 to 1898 kg/m^3. Adding of plastic fibre doesn't contribute magical change in density and in almost each cases density falls slightly after adding 0.1% fibre and density falls remarkably after adding 0.2% fibre.
- ❖ From comparison of control blocks (C) and blocks stabilized with 8% cement content (C1), it is evident that strength increases approximately 8.5% and 29.5% strength increases in case of comparing between control blocks and blocks consists of 10% cement (C4).
- ❖ There was an increase of 5.6% and approximately 18% in strength when this soil block was stabilized by 2% (C5) and 4% of lime (C6) respectively when compared to block with 10% cement (C4).
- ❖ Large quantity of fibres distributed non-uniformly in the blocks and creating weaker plane, which may leads to reduction in strength.
- ❖ The control blocks which contains only raw soil, exhibits an abrupt failure without introducing any symptoms or warning and the mode is quick
- ❖ The blocks with fibres deformed after the ultimate load was reached and finally crack was observed on the specimen.
- ❖ The chopped plastic fibres from mineral water pet bottle are not consistently sound with soil in improving the compressive strength.

5. Acknowledgement

6. References

[1] S.M. Marandi, M.H. Bagheripour,R. Rahgozar, and H. Zare, "Strength and durability of randomly distributed palm fibres reinforced silty-sand soil", *American Journal of Applied Sciences*, Vol 5(3), pp. 209-220,2008.

[2] C. Galan-Marin,C. Rivera-Gomez, and J. Petric, "Clay based composite stabilised with natural plymer and fibre", *Construction and Building Materials*, Vol 24, pp 1462-1468, 2010.

[3] H. Binici, O. Aksogan, M.N. Bodur, E. Akca, and S. Kapur, "Thermal isolation and mechanical properties of fibre reinforced mud bricks as wall materials", *Construction and Building Materials*.Vol 21; pp. 901-906, 2007.

[4] B.V.V. Reddy, and K.S.Jagadish, "Influence of soil composition on strength and durability of soil cement blocks." *Indian Concrete Journal*. 69(9),pp. 517-524, 1995.

[5] A. Mesbah, J.C. Morel, , P. Walker, P and Kh.Ghavami, "Development of a direct tensile test for compacted earth blocks reinforced with natural fibres". *ASCE Journal of Materials in Civil Engineering*. Vol 16(1); pp. 95 – 98, 2004.

[6] A K Choudhary, "Pressure Moulded Building Blocks with Lateritic Soils", *Institution of Engineers India Journal (CV),*Vol 85, pp.159-162, November 2004.

[7] Chee-Ming Chan., "Effect of Natural fibres inclusion in clay bricks: Physico-Mechanical properties". *International Journal of Civil and Environmental Engineering*. Vol 3(1), pp. 51-57 2011.

[8] K.S. Jagadish, *Building with Stabilised Mud*. LK International Publishimg House Pvt. Ltd., New Delhi, 2007.

[9] BIS 1077-1992 (Fifth Revision), Common burnt clay building bricks, specifications, *Bureau of Indian Standards*, New Delhi.

[10] J.P.Forth, , and S.E.Zoorob. "Masonry units from soil and bitumen", *Proceedings of 6th international masonry conference*, *British Masonry Society*. London, pp. 163-165, 2002.

Analysis of Order of Stress Singularity at a Vertex in 3D Transversely Isotropic Piezoelectric Dissimilar Bonded Joints

Md. Shahidul Islam[1], Md. Golam Kader[2]
[1]Assistant Professor, Department of Mechanical Engineering
[2]Associate Professor, Department of Mechanical Engineering
Khulna University of Engineering & Technology
Khulna-9203, Bangladesh
E-mail:shahidulbitk@gmail.com

Abstract

The order of singularity near the vertex of bonded joints is one of the main factors responsible for debonding under mechanical or thermal loading. The distribution of stress singularity field near the vertex of bonded joints is very important to maintain the reliability of intelligent materials. In this paper, order of stress singularity at a vertex in 3D transversely isotropic piezoelectric dissimilar bonded joints is analyzed. Eigen analysis based on FEM is used for stress singularity field analysis of piezoelectric bonded joints. The Eigen equation is used for calculating the order of stress singularity, and the angular function. The numerical result shows that the angular functions have larger value near the interface edge than the inner portion of the joint. From the numerical result, it was observed that the possibility of debonding at the interface edge of the piezoelectric bonded joints, due to the higher stress concentration at the free edge.

Keywords: Piezoelectric Bonded Joints, Order of Singularity, Transversely Isotropic Material, Smart Structures, Eigen Analysis.

1. Introduction

Piezoelectric materials are being widely used in the electronics industry due to their high functionality. Mechanical stress occurs in piezoelectric material for any electric input. The stress concentrations caused by mechanical or electric loads may lead to crack initiation and extension, and sometimes the stress concentrations may be high enough to fracture the material parts. In the case of multilayer piezoelectric stacks, the electrodes that terminate inside the material body are a source of electric field, which can result in high stress concentrations. Reliable service lifetime predictions of piezoelectric components demand a complete understanding of the debonding processes of these materials. Industrial products such as electronic devices and heat endurance parts are composed of dissimilar materials. A mismatch of material properties causes a failure at the free edge of joint, because a stress concentration occurs along the free edge of interface especially at the vertex of joints [1].

Sosa has suggested a general method of solving plane problems of piezoelectric media with defects [2]. Zak and Williams used Eigen functions for analyzing stress singularity field at a crack tip perpendicular to a bimaterial interface. They found that a real part of Eigen value is within the range of 0 to 1, and expressed a relationship between stress distribution and the order of stress singularity at the crack tip [3]. Aksentian determined Eigen values and Eigen vectors at the singular point in plane intersecting a free edge of the interface in three dimensional dissimilar joints [4]. Yamada and Okumura developed a finite element analysis for solving Eigen value equation to determine directly the order of stress singularity and the angular variation of the stress and displacement fields [5]. Pageau and Biggers determined the order of stress singularity and the angular variation of the displacement and the stress fields around the singular points in plane intersecting a wedge front in the three-dimensional anisotropic material structures using the two dimensional displacement formulation under a plane strain assumption [6].

Thus, at present, no clear picture exits of the effects of stress singularity field near the vertex of three-dimensional transversely isotropic piezoelectric dissimilar bonded joints. Therefore, the purpose of this analysis is to obtain a better understanding of the effect of stress singularity field near the vertex of transversely isotropic

piezoelectric bimaterial joints on interface. In this study, three-dimensional FEM Eigen equation was formulated for analyzing the order of singularity in piezoelectric bimaterial joints.

2. Formula of Analysis

In the absence of body forces and free charges, the equilibrium equations of piezoelectric materials are expressed as follows [7]:

$$\sigma_{ij,j} = 0 \tag{1}$$

$$d_{i,i} = 0 \tag{2}$$

where σ_{ij} represents the stress and d_i the electric displacement.
The constitutive relations are shown as follows:

$$\sigma_{ij} = c_{ijkl}\varepsilon_{kl} - e_{kij}E_k \tag{3}$$

$$d_i = e_{ikl}\varepsilon_{kl} + \chi_{ik}E_k \tag{4}$$

where c_{ijkl} is the elastic constant, e_{ikl} and χ_{ik} are the piezoelectric constant and electric permittivity (dielectric constant), respectively.
The elastic strain-displacement and electric field-potential relations are presented as follows:

$$\varepsilon_{ij} = \frac{1}{2}\left(u_{j,i} + u_{i,j}\right) \tag{5}$$

$$E_i = -\psi_{,i} \tag{6}$$

where ε_{ij} is the strain, and E_i is the eclectic field. u_i is the elastic displacement and ψ is the electric potential.
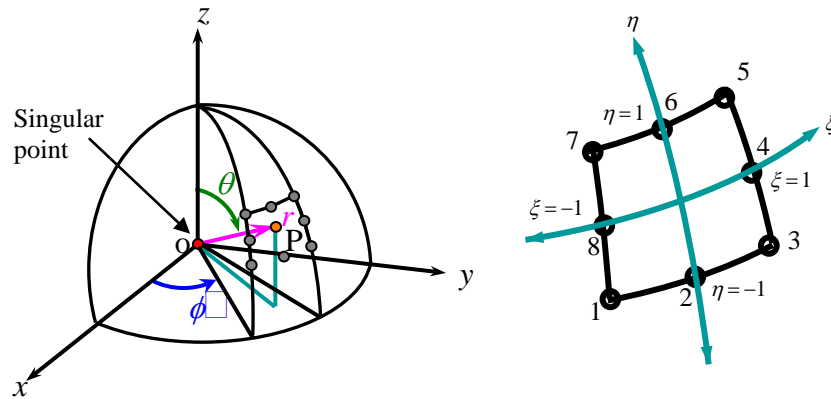
Fig.1 Element geometry and natural co-ordinates at a free edge singular point

Figure 1 represents the geometry of a typical case where a singular stress state occurs at the point o. The region surrounding the singular point is divided into a number of quadratic pyramidal elements with a summit o, with each element being located in spherical co-ordinates r, θ, and ϕ by its nodes 1 to 8. A point P in the element can be located using the singular transformation by the relations.

$$r = r_o\left(\frac{1+\alpha}{2}\right)^{1/p} \quad or, \quad \rho = \frac{r}{r_o} = \left(\frac{1+\alpha}{2}\right)^{1/p}$$

$$\theta = \sum_{i=1}^{8} H_i\theta_i \quad and \quad \phi = \sum_{i=1}^{8} H_i\phi_i \tag{7}$$

where,

$$H_1 = -\frac{1}{4}(1-\eta)(1-\xi)(\eta+\xi+1) \quad H_2 = \frac{1}{2}(1-\eta)(1-\xi^2)$$

$$H_3 = -\frac{1}{4}(1-\eta)(1+\xi)(-\eta+\xi-1) \quad H_4 = \frac{1}{2}(1-\eta^2)(1+\xi)$$

$$H_5 = \frac{1}{4}(1+\eta)(1+\xi)(\eta+\xi-1) \quad H_6 = \frac{1}{2}(1+\eta)(1-\xi^2)$$

$$H_7 = \frac{1}{4}(1+\eta)(1-\xi)(\eta-\xi-1) \qquad H_8 = \frac{1}{2}(1-\eta^2)(1-\xi)$$

θ and ϕ are the nodal values of the angular co-ordinates and α, η, and ξ are natural co-ordinates of the element whose ranges are shown in Fig.1. H interpolation function, p Eigen value, $\rho = r/r_o$, r the distance from the singular point. The elastic displacement and electric potential relations are:

$$\left(\bar{u}-\bar{u}_o\right)=\left(\frac{1+\alpha}{2}\right)\left[\sum_{i=1}^{8} H_i\left(\bar{u}_i-\bar{u}_o\right)\right] \tag{8}$$

$$\left(\bar{\psi}-\bar{\psi}_o\right)=\left(\frac{1+\alpha}{2}\right)\left[\sum_{i=1}^{8} H_i\left(\bar{\psi}_i-\bar{\psi}_o\right)\right] \tag{9}$$

where $\bar{u}_o$ and $\bar{u}$ is the elastic displacement at o and P, respectively, and $\bar{\psi}_o$ and $\bar{\psi}$ is the electric potential at o and P, respectively.

$$u=\left(\bar{u}-\bar{u}_o\right), \qquad u_i=\left(\bar{u}_i-\bar{u}_o\right) \tag{10}$$

$$\psi=\left(\bar{\psi}-\bar{\psi}_o\right), \qquad \psi_i=\left(\bar{\psi}_i-\bar{\psi}_o\right) \tag{11}$$

From the above equation, the elastic displacement and electric potential relations are expressed as follows:

$$u_k = \rho^p\left[\sum_{i=1}^{8} H_i u_{ki}\right] \quad (k=r,\theta,\phi) \tag{12}$$

$$\psi = \rho^p\left[\sum_{i=1}^{8} H_i \psi_i\right] \tag{13}$$

3. Problem Description and Numerical Example

For a transversely isotropic piezoelectric material, taking z to be parallel to the poling axis of the material, by convention, the constitutive relation is expressed in the following form:

$$\{\sigma\}=[c]\{\varepsilon\}-[e]\{E\} \quad and \quad \{d\}=[e]^T\{\varepsilon\}+[\chi]\{E\} \tag{14}$$

where $\{\sigma\}$ and $\{\varepsilon\}$ are the stress and strain which are the mechanical field variables, $\{d\}$ and $\{E\}$ are the electric displacement and electric field, respectively, $[c]$ is the elastic constant, and $[e]$ and $[\chi]$ are the piezoelectric constant and electric permittivity (dielectric constant) respectively.
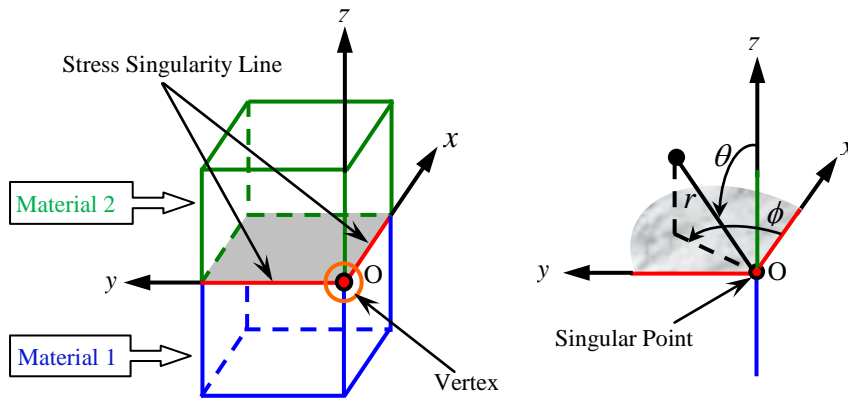
Fig. 2 Singular point of 3D piezoelectric dissimilar bonded joint in *x*, *y*, *z* plane

Table1: Material properties of piezoelectric materials

Material	Elastic Constant, 10^{10} N/m^2					Piezoelectric Constant, C/m^2			Dielectric Constant, 10^{-10} C/Vm	
	c_{11}	c_{12}	c_{13}	c_{33}	c_{44}	e_{15}	e_{31}	e_{33}	χ_{11}	χ_{33}
PZT-5H	12.6	5.50	5.30	11.7	3.53	17.0	-6.50	23.3	151.0	130.0
PZT-5A	12.1	7.54	7.52	11.3	2.11	12.3	-5.20	15.8	81.1	73.5

The Eigen equation is formulated for determining the order of stress singularity as follows.

$$\left(p^2\,[\mathbf{A}] + p[\mathbf{B}] + [\mathbf{C}]\right)\{\mathbf{U}\} = \{\mathbf{0}\} \tag{15}$$

Where p represents the characteristic root, which is related to the order of singularity, λ, as $\lambda = 1-p$. [$\mathbf{A}$], [$\mathbf{B}$] and [$\mathbf{C}$] are matrices composed of material properties, and $\{\mathbf{U}\}$ represents the elastic displacement and electric potential vector.

The elastic displacement and electric potential equation is expressed by the following equitation.

$$u_j\left(r,\,\theta,\,\phi\right) = b_j\left(\theta,\,\phi\right) r^{1-\lambda} \tag{16}$$

$$\psi\left(r,\,\theta,\,\phi\right) = q\left(\theta,\,\phi\right) r^{1-\lambda} \tag{17}$$

By differentiating the above two equations, get the angular function of strain and electric field equation respectively. The stress and electric displacement distribution equations in the stress singularity region can be expressed as follows.

$$\sigma_{ij}\left(r,\,\theta,\,\phi\right) = K_{ij} r^{-\lambda} f_{ij}\left(\theta,\,\phi\right) \tag{18}$$

$$d_i\left(r,\,\theta,\,\phi\right) = F_i r^{-\lambda} l_i\left(\theta,\,\phi\right) \tag{19}$$

Where r represents the distance from the stress singular point, $b_j(\theta,\,\phi)$ the angular function of elastic displacement, $q(\theta,\,\phi)$ the angular function of electric potential, $f_{ij}(\theta,\,\phi)$ the angular function of stress distribution, $l_i(\theta,\,\phi)$ the angular function of electric displacement, K_{ij} the intensity of singularity, F_i the intensity of electric field, and λ the order of stress singularity. Angular functions of stress components obtained from Eigen analysis in Eq. (15) are examined.
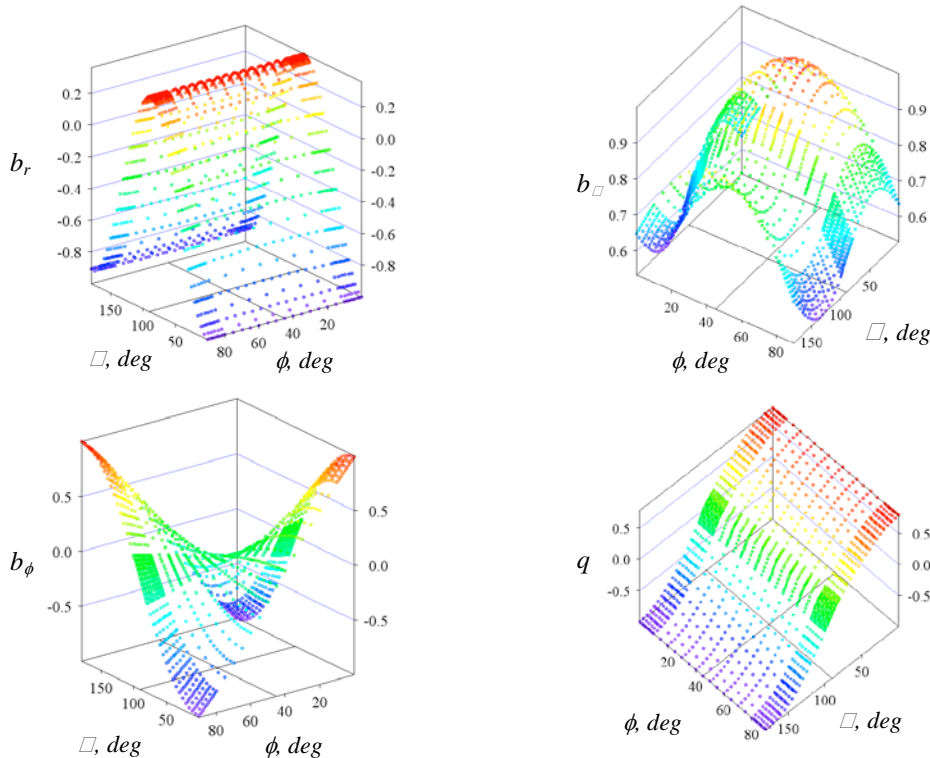
Fig. 3 Distribution of b_i & q against angle ϕ and θ

The distributions of elastic displacement and electric potential are shown in fig. 3. It is found that, the angular function of elastic displacement and electric potential is continuous at the interface of the joints and has larger value at the free edge than the inner portion. So there is a possibility to debond near the free edge of the joint. It is also found that the angular function of elastic displacement and electric potential at $\phi = 0°$ is agreed with that at $\phi = 90°$. The figure of b_θ and b_r is symmetry with respect to ϕ and the figure of b_ϕ and q is antisymmetry with respect to ϕ. The distributions of normalized angular function of strain and electric field with respect to the angle ϕ at $\theta = 90°$ in the singular field for the piezoelectric bonded structure are shown in fig. 4. It is shown from the figure that the strain and electric field have larger value near the free edge of the bonded joints.
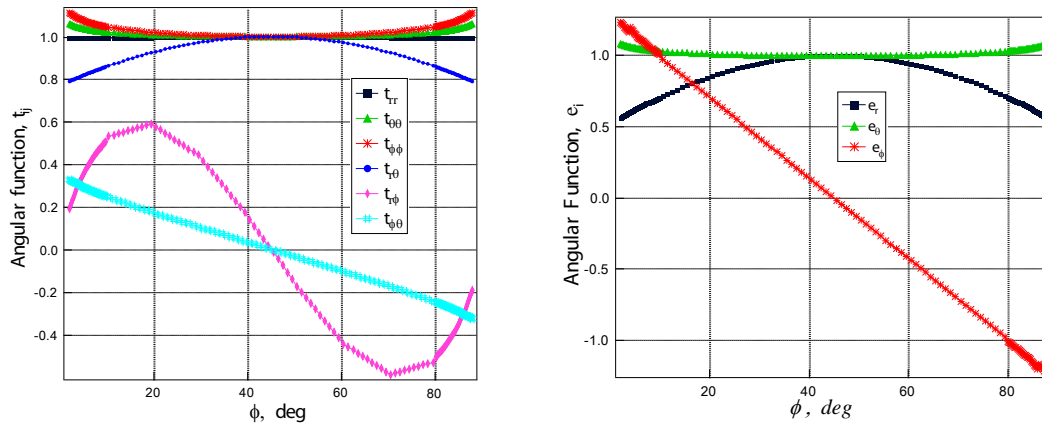
Fig. 4 Distribution of normalized angular function of strain and electric field against ϕ at $\theta = 90°$

The distributions of normalized angular function of stress and electric displacement with respect to the angle ϕ at $\theta = 90°$ for the piezoelectric bonded structure are shown in fig. 5. These distributions are nearly similar to the distribution of angular function strain and electric field. It is shown from the figure that the stress and electric displacement have larger value near the free edge of the bonded joints. So there is another possibility to debond and delamination occurs near the free edge of the bonded joints.
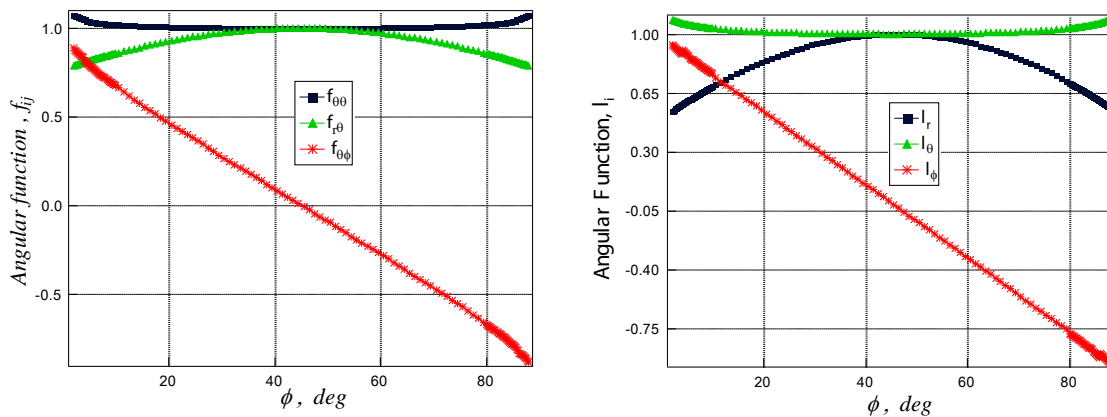
Fig. 5 Distribution of normalized angular function of stress and electric displacement against ϕ at $\theta = 90°$

4. Conclusion

In this paper, a finite element method formulation near the vertex of transversely isotropic piezoelectric dissimilar bonded joints was presented. Angular functions for singularity corner were derived from Eigen

analysis using a finite element method. From the numerical result, the following conclusions can be drawn for the piezoelectric bimaterial joints.

    a) The higher angular function occurs at the free edge of the material joint than the inner portion of the joint.

    b) The possibility to debond and delamination at the edge of the transversely isotropic piezoelectric dissimilar bonded joints was due to the higher stress and electric displacement concentration at the free edge.

5. References

[1] W. Attaporn, and H. Koguchi, "Intensity of stress singularity at a vertex and along the free edges of the interface in 3D-dissimilar material joints using 3D-enriched FEM", *CMES*, Vol. 39, No. 3, pp. 237-262, 2009.

[2] H. A. Sosa, "Plane problems in piezoelectric media with defects", *International Journal of Solids and Structure*, Vol. 28, pp.491-505, 1991.

[3] A. R. Zak, and M. L. Williams, "Crack point stress singularities at a bi-material interface", *Journal of Applied Mechanics*, Brielf Notes, pp.142-143, 1963.

[4] O. K. Aksentian, "Singularities of the stress-strain state of a plate in the neighborhood of an edge", *PMM*, Vol. 31, No. 1, pp.178-186, 1967.

[5] Y. Yamada, and H. Okumura, "Analysis of local stress in composite materials by 3-D finite element", *Proceeding of the Japan-U.S. Conference*, Tokyo, pp. 55-64, 1981.

[6] S. S. Pageau, and Jr. S. B. Biggers, "A finite element approach to three-dimensional singular stress states in anisotropic multi-material wedges and junctions", *International Journal of Solids and Structure*, Vol. 33, pp. 33-47, 1996.

[7] K. M. Liew, and J. Liang, "Modeling of 3D piezoelectric and elastic bimaterials using the boundary element method", *Computational Mechanics*, Vol. 29, pp. 151-162, 2002.

Selection of Constitutive Models for Concrete in simulating Reinforced Concrete Members

Sharmin Reza Chowdhury[1], Md. Shahid Mamun[2], Wahid Hassan[3]
[1,2]Ahsanullah University of Science and Technology (AUST)
[3]European University of Bangladesh (EUB)
E-mail: srchowy@yahoo.com

Abstract

Reliable, accurate and robust constitutive model for concrete is very much essential in simulating Reinforced Concrete Members such as Beam, Column and Shear wall properly. For an accurate and reliable prediction of Reinforced Concrete Members response an effective and robust hysteretic constitutive model for concrete is needed. A good concrete model addresses important issues such as the hysteretic behavior in both cyclic compression and tension, the progressive degradation of stiffness of the unloading and reloading curves for increasing values of strain, and the effects of confinement, tension stiffening and gradual crack closure. Refined and generalized model takes into account concrete damage and hysteresis, while retaining computational efficiency. In this paper a review of concrete constitutive models available in the literature has been made with their individual advantages and disadvantages in modeling Reinforced Concrete Members and at the end, which concrete constitutive model is appropriate for which type of member has also been discussed.

Keywords: *Constitutive Models, Concrete, Reinforced Concrete Members, Hysteretic behavior.*

1. Introduction

Characteristics of the constitutive relationships implemented in the model for concrete influence the analytical model response of Reinforced Concrete Members. Reliable, accurate and robust constitutive model for concrete is very much essential in simulating Reinforced Concrete Members such as Beam, Column and Shear wall properly. For an accurate and reliable prediction of RC member response, an effective and robust hysteretic constitutive model for concrete is needed. The tensile behavior of the model takes into account tension stiffening and the degradation of the unloading and reloading stiffness for increasing values of maximum tensile strain after initial cracking. Some concrete constitutive models have the inability of to simulate gradual gap closure due to progressive contact stresses within the cracks in concrete. This may impair significantly, the accuracy in predicting the pinching properties (i.e., characteristic variation in section stiffness from unloading to reloading in the opposite direction) of RC elements subjected to cyclic loading. Another limitation of some constitutive models is that it lacks the flexibility of a generalized model. Some model do not allow control on most of the parameters associated with the monotonic and hysteretic branches of the stress-strain relationship, thus restraining the calibration of the model or re-assessment of the parameters as new data become available**.** In this paper a review of concrete constitutive models available in the literature has been made with their individual advantages and disadvantages in modeling Reinforced Concrete Members.

2. Different Concrete Constitutive Models
Two different constitutive models with different capabilities are discussed in this study, the first being relatively simple and commonly used, and the latter more refined and generalized. Although two constitutive models are discussed below other concrete models are also discussed under these two main categories.

Hysteretic Constitutive Model by Yassin [7]

Studies on the stress-strain relations of concrete under cyclic loading have been much fewer than those under monotonic loading. Sinha et al. [2]) and Karsan and Jirsa [5] have studied the behavior of plain concrete

subjected to repetitions of compressive stress. It is found that the envelope for cyclic loading coincides with stress-strain curve for monotonic loading. The model by Yassin takes into account concrete damage and hysteresis, while retaining computational efficiency.

The monotonic envelope curve of the hysteretic model for concrete in compression follows the monotonic stress-strain relationship model of Kent and Park [3] as extended by Scott, Park and Priestley [1]. Even though more accurate and complete monotonic stress-strain models have been published since, the so-called modified Kent and Park model offers a good balance between simplicity and accuracy, and is widely used.

$$\varepsilon_c \le \varepsilon_0 \quad \sigma_c = Kf_c'\left[2\left(\frac{\varepsilon_c}{\varepsilon_0}\right)-\left(\frac{\varepsilon_c}{\varepsilon_0}\right)^2\right]$$

$$\varepsilon_0 < \varepsilon_c \le \varepsilon_{20} \quad \sigma_c = Kf_c'[1-Z(\varepsilon_c-\varepsilon_0)]$$

$$\varepsilon_c > \varepsilon_{20} \quad \sigma_c = 0.2Kf_c'$$
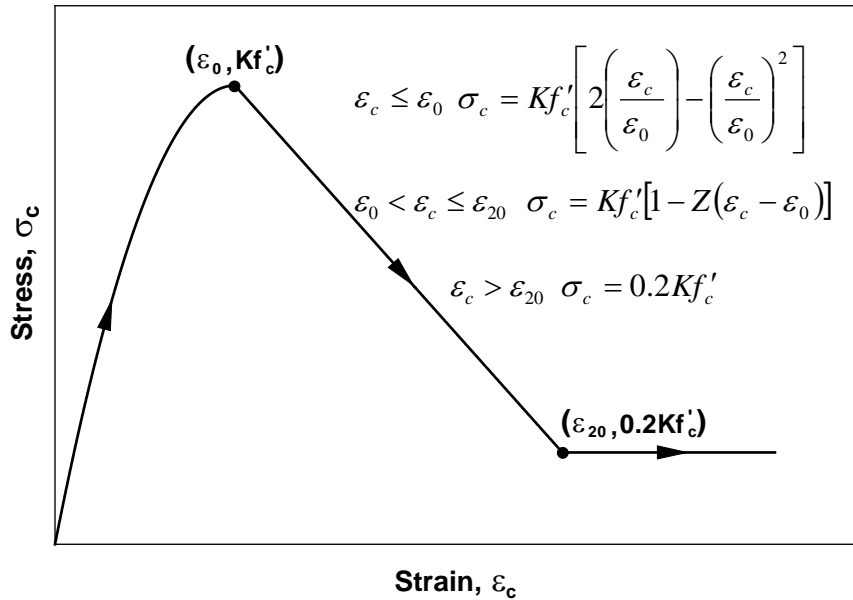
Fig. 1 The Modified Kent & Park Model [3] for Concrete in Compression

In the modified Kent and Park model (Figure 1), the monotonic concrete stress-strain $\left(\sigma_c - \varepsilon_c\right)$ relation in compression is described by three regions.
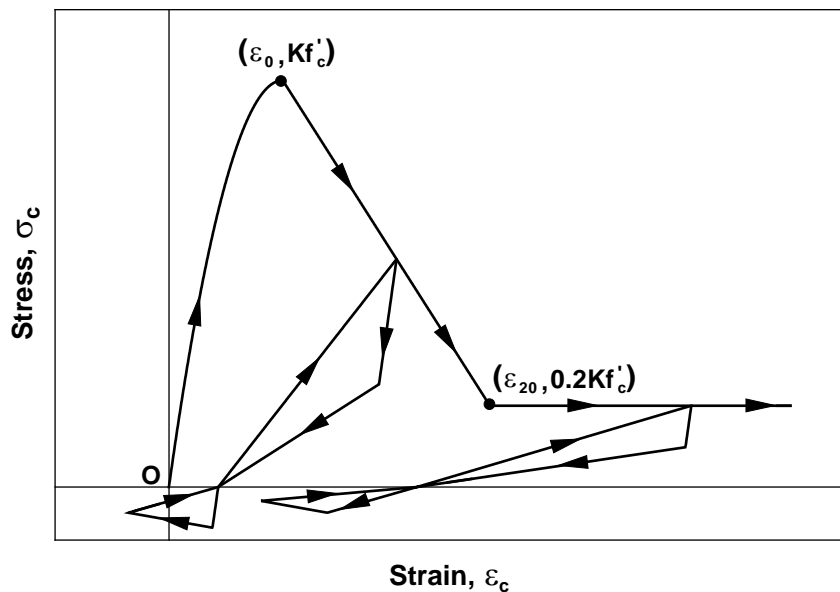
Fig. 2 Hysteretic Unloading and Reloading Rules (Yassin,[7])

The hysteretic unloading and reloading rules proposed by Yassin [7] are a set of linear stress-strain relationships, as shown in Figure 2. The figure illustrates that hysteretic behavior occurs in both compression and tension. Although the compressive and tensile hysteresis loops are continuous, they are discussed separately for the sake of clarity. Figure 2 shows two consecutive tensile hysteresis loops, which are part of a sample cyclic

history that also includes compressive stresses. The model assumes that tensile stress can occur anywhere along the strain axis, either as a result of initial tensile loading or as a result of unloading from a compressive state. In the latter case, a tensile stress occurs under a compressive strain. The tensile stress-strain relation is defined by three points with coordinates $(\varepsilon_t, 0)$, $(\varepsilon_n, 0)$ and $(\varepsilon_u, 0)$, as represented by points J, K and M, respectively in Figure 3.
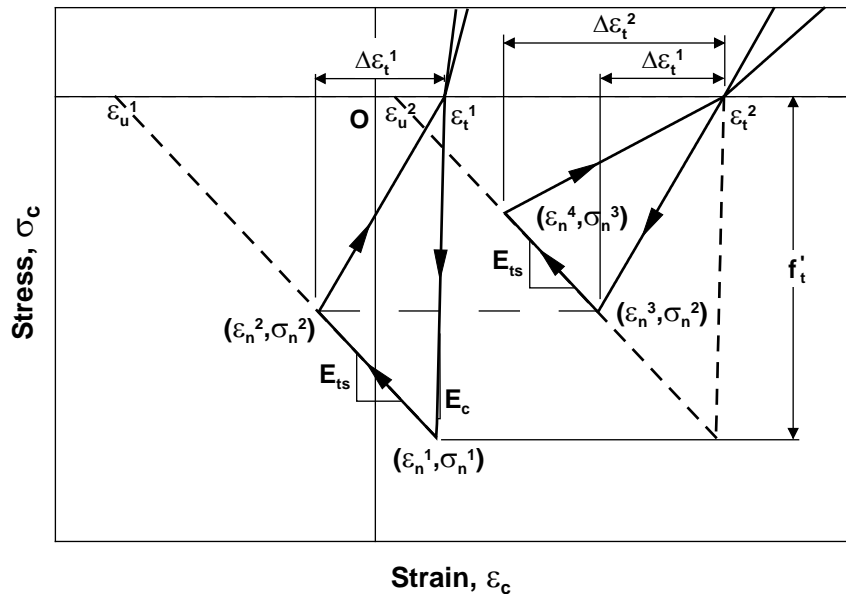
Fig. 3 Hysteresis Loops in Tension

Due to its computational efficiency and reasonable level of accuracy, the constitutive model is commonly used by researchers, and is implemented in the state-of-the-art computational platform OpenSees ("OpenSees[8]") developed by the Pacific Earthquake Engineering Research Center at the University of California, Berkeley. The model successfully generates continuous stress-strain behavior in hysteretic compression and tension, and considers damage in the form of cyclic stiffness degradation.

The primary shortcoming of this concrete constitutive model is the inability of the model to simulate gradual gap closure due to progressive contact stresses within the cracks in concrete. This may impair significantly, the accuracy in predicting the pinching properties (i.e., characteristic variation in section stiffness from unloading to reloading in the opposite direction) of RC elements subjected to cyclic loading. Another limitation of the constitutive model is that it lacks the flexibility of a generalized model. The model does not allow control on most of the parameters associated with the monotonic and hysteretic branches of the stress-strain relationship, thus restraining the calibration of the model or re-assessment of the parameters as new data become available. Furthermore, the monotonic stress-strain envelope associated with the constitutive model may be considered out-of-date, more accurate monotonic stress-strain models for both unconfined and confined concrete have been proposed since.

Hysteretic Constitutive Model by Chang and Mander [4]

The constitutive model by Chang and Mander [4] is an advanced, rule-based, generalized, and non-dimensional model that simulates the hysteretic behavior of confined and unconfined, ordinary and high-strength concrete in both cyclic compression and tension. Upon development of the model, the authors focused particular emphasis on the transition of the stress-strain relationship upon crack opening and closure, which had not been adequately addressed in previous models. Most existing models (including the model by Yassin [7] previously described) assume sudden crack closure with rapid change in section modulus (i.e., sudden pinching behavior). Similar to the model by Yassin [7], in the model by Chang and Mander, the monotonic curve forms the envelope for the hysteretic stress-strain relationship. This was shown to be a reasonable assumption based on experimental results presented by Sinha et al. [2] and Karsan and Jirsa [5], and modeled by Mander et al. [6] for unconfined concrete in cyclic compression. In the model by Chang and Mander, concrete in tension is modeled with a cyclic

behavior similar to that in compression. The model envelopes for compression and tension have control on the slope of the stress-strain behavior at the origin, and the shape of both the ascending and descending (i.e., pre-peak and post-peak) branches of the stress-strain behavior.

Compression Envelope Curve

The compression envelope curve of the model by Chang and Mander is defined by the initial slope E_c, the peak coordinate (ε_c', f_c'), a parameter r from Tsai's [9] equation defining the shape of the envelope curve, and a parameter $x_{cr}^- > 1$ to define the spalling strain (Figure 4).
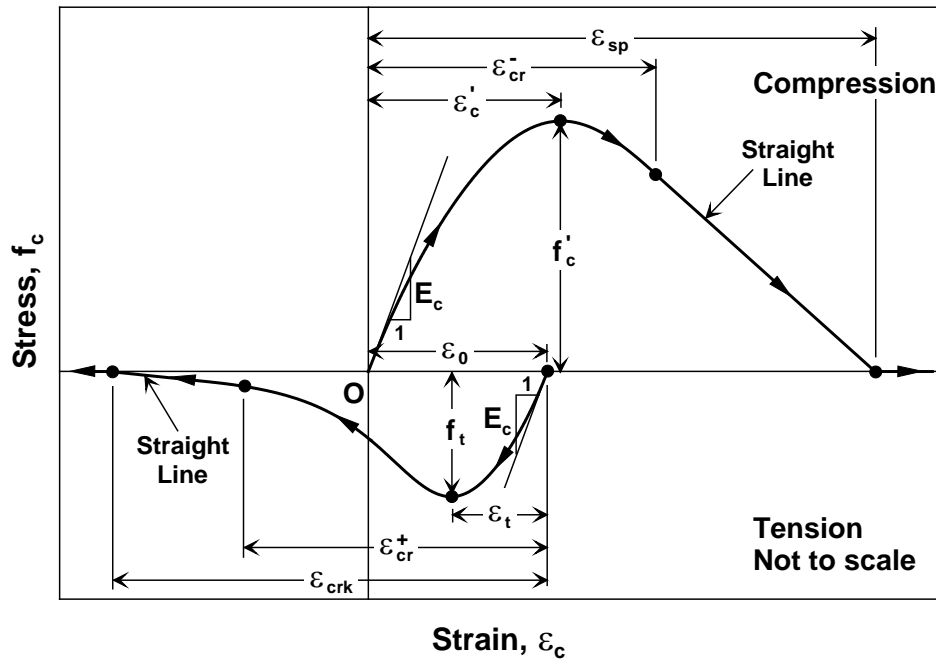
Fig. 4 Compression and Tension Envelope Curves of the Model by Chang and Mander [4]

Tension Envelope Curve
The shape of the tension envelope curve in the model by Chang and Mander is the same as that of the compression envelope curve (Figure 4). In terms of modeling generalized hysteretic behavior, the constitutive model uses smooth "connecting" curves for unloading and reloading between the compression and tension envelope curves, and smooth "transition" curves for partial unloading and reloading between the connecting curves (Fig. 5).
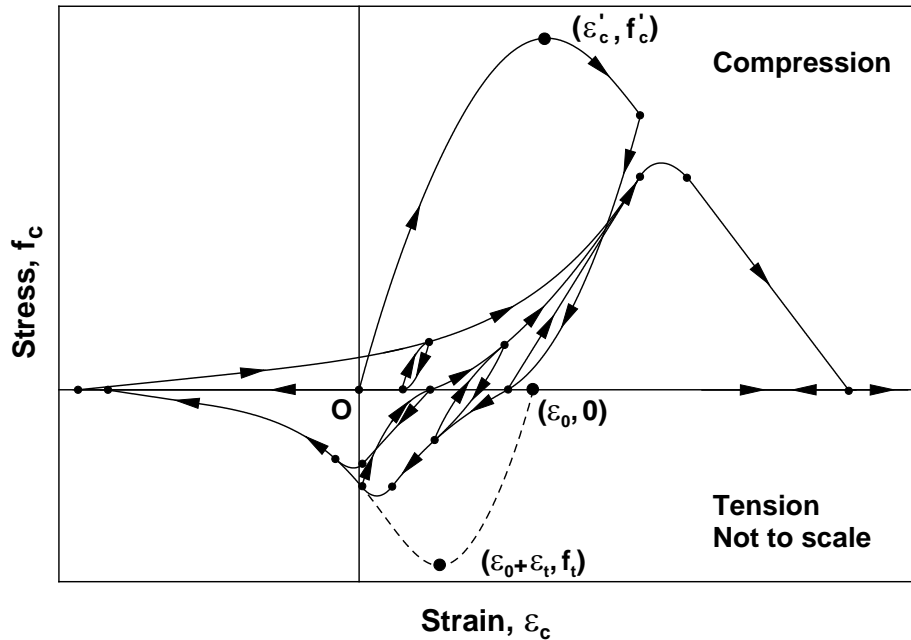
Fig. 5 Continuous Hysteresis in Compression and Tension

Overall, the model by Chang and Mander [4] is the current state-of-the-art uniaxial constitutive relationship for modeling the cyclic stress-strain behavior of concrete. It simulates gradual crack opening and closure under cyclic loading and incorporates a refined and well-established definition of the hysteretic properties. The model is in the form of a generalized stress-strain relationship, which can further be advanced, via re-assessment of model parameters, or upon availability of further experimental results (e.g., for cyclic tension). It allows control on the parameters associated with the monotonic envelopes as well as the hysteretic parameters for a refined calibration of the stress-strain relationship based on particular experimental results, or for conducting sensitivity studies on model parameters.

3. Conclusion

For an accurate and reliable prediction of Reinforced Concrete Members response an effective and robust hysteretic constitutive model for concrete is needed. Two different constitutive models for concrete (Yassin, [7]; Chang and Mander, [4]) have been discussed in this paper. Both models address important issues such as the hysteretic behavior in continuous cyclic compression and tension, the progressive degradation of stiffness of the unloading and reloading curves for increasing values of strain, and the effects of confinement and tension stiffening. However, the model by Chang and Mander [4], being the current state-of-the-art uniaxial constitutive relationship for modeling the cyclic stress-strain behavior of concrete, is clearly superior to the hysteretic model by Yassin [7]. The model by Chang and Mander is a generalized constitutive model that allows control on the parameters associated with the monotonic envelopes, as well as the hysteretic parameters, for a refined calibration of the stress-strain relationship based on particular experimental results. Furthermore, the model by Chang and Mander successfully simulates the gradual closure of cracks under cyclic loading, due to progressive contact stresses within the cracks. On the other hand, the model by Yassin assumes sudden crack closure, which may impair significantly, the accuracy in predicting the pinching properties of RC member. Due to these limitations, the model by Yassin is very seldom used in modeling RC members.

4. References

[1] B.D.Scott, R. Park, and M.J.N. Priestley, "Stress-Strain Behavior of Concrete Confined by Overlapping Hoops at Low and High Strain Rates", *Journal of the American Concrete Institute*, V. 79, No. 1, pp. 13-27,1982

[2] B.P. Sinha, K.H. Gerstle, and L.G. Tulin, "Stress-Strain Relations for Concrete under Cyclic Loading", Journal of the American Concrete Institute, V. 61, No. 2, pp. 195-211, 1964.

[3] D.C. Kent, and R.Park, "Flexural Members with Confined Concrete", *Journal of the Structural Division*, ASCE, V. 97, No. ST7, pp. 1969-1990,1971.

[4] G.A Chang, and J.B. Mander, "Seismic Energy Based Fatigue Damage Analysis of Bridge Columns: Part I – Evaluation of Seismic Capacity", *NCEER Technical Report* No. NCEER-94-0006, State University of New York, Buffalo,1994.

[5] I.D. Karsan, and J.O. Jirsa, "Behavior of Concrete Under Compressive Loadings", *Journal of the Structural Division*, ASCE, V. 95, No. ST12, pp. 2543-2563, 1969.

[6] J.B. Mander, M.J.N. Priestley, and R. Park, "Seismic Design of Bridge Piers", *Report* No: 84-2, Department of Civil Engineering, University of Cantebury,1984.

[7] M.H.M. Yassin, "Nonlinear Analysis of Prestressed Concrete Structures Under Monotonic and Cyclic Loads", *Dissertation*, University of California, Berkeley,1994

[8] "OpenSees – Open System for Earthquake Engineering Simulation", *Pacific Earthquake Engineering Research Center*, University of California, Berkeley. (http://opensees.berkeley.edu/OpenSees/developer.html)

[9] W.T. Tsai, "Uniaxial Compressional Stress-Strain Relation of Concrete", *Journal of Structural Engineering*, ASCE, V. 114, No. 9, pp. 2133-2136,1988.

Paper ID: MS-36

Analysis of Moisture Absorption Effect on The Longitudinal Three Point Bend Properties of Jute Epoxy Composite Processed Under Modified Compression Molding Process

Md. Rashnal Hossain[1, 2,] Md. Aminul Islam[1,] Ayasha Akter[1,] Aart Van Vuure[2] and Ignaas Verpoest[2]

[1] Department of Materials & Metallurgical Engineering, Bangladesh University of Engineering and Technology, Dhaka-1000, Bangladesh,

[2] Department of Metallurgy and Materials Engineering, Katholieke Universiteit Leuven, Kasteelpark Arenberg 44 bus 2450, 3001 Heverlee, Belgium

E-mail: hrashnal@gmail.com

Abstract

Commercialized use of natural fiber based polymer composite is of concern since the last two. Along with this the use of jute as reinforcement with polymeric materials has shown considerable interest globally. In this research two types of jute reinforcement namely Bangla White grade B and Bangla Tosha (BT) jute were used. The unidirectional jute preform was clamped while making jute epoxy composite. Longitudinal and transverse tensile and three point bend properties were studied according to ASTM D 3039 and ASTM D 790. Moisture sensitivity of the longitudinal three point bend property was also analyzed at 65%, 85% and 95% (RH) relative humidity. It was observed that the jute epoxy composite shows degradation of longitudinal three point bend strength and stiffness and this degrading affect increases with the increase in the RH value. The microbial growth was also observed. The fractographs of the composites were also analyzed under FEG SEM.

Keywords: Jute epoxy, BT, BWB, Relative humidity, Moisture gain

1. Introduction

Jute polymer composites have occupied the field of materials science due to the environmental awareness and to bring some modification of some existing everyday usable items. Continual research in this field has let scientist gather knowledge about this fiber and the matrix that can bring some social changes regarding materials science. But the basic problem to deal is its hygroscopicity for which cases modification of fiber is required [1, 2].

During composite fabrication if jute fiber inside matrix is inappropriately covered with the matrix, and if humidity is changed, then the equilibrium moisture content also changes. This change in moisture content either expands or shrinks the jute fiber thereby probing the fiber polymer interface and due to this reason jute polymer composite property degrades in presence of moist environment [3].

Jute as a natural fiber is hygroscopic in nature and while processing with polymer to make a composite involves pressure, temperature. At this condition although composite is formed, but the natural tendency of jute is to revert to its original shape like shape memory alloy via moisture gain. This implies in presence of moisture jute fiber within the composite body gains water and tries to get back to its early size and shape [4].

However, non-polar materials interact very poorly because of the hydrophilic nature of jute fiber. When a fiber composite fails by an interfacial or adhesive type failure it is presumed that part of failure arise from lack of sufficient chemical bonding between the fiber and matrix. But it is also likely that the part of failure arise from the inability to achieve ultimate molecular contact. Strength can be improved for the fiber reinforced polymer composite if the surface energies of both the fiber and the matrix are compatible. The adhesion between the plastic and polar lingo cellulosic fiber is critical in determining the properties of composite. Transcrystallinity around the fiber surface complicates the understanding of interfacial phenomenon since crystallite can act like cross links by many molecules together, although for jute thermoset composites this is quite different [5, 6].

Research on the moisture diffusion experiments of short jute reinforced PP composite showed dependence of fibre volume content, matrix molecular weight, and matrix modification which was validated according to the Fickian model [6, 7].

The water absorption behavior of pultruded jute polyester composite shows that the water absorption increases with increase in the immersion time. The water absorption process also showed geometry dependence. The decrease in mechanical properties with increasing in moisture content was attributed to the formation of hydrogen bonding between the water molecules and cellulose fibre thereby reducing the rigidity of the cellulose structure and interfering with interface properties [8].

The study of adhesive tensile and moisture absorption properties of randomly distributed areca fibre and maize powder reinforced urea formaldehyde composite showed decreased moisture absorption with decrease in the fibre to maize powder ratio and moisture content increases with the increase in the time duration and attains saturation [9].

The effect of fibrous reinforcement and solvent content on moisture uptake in composite laminate clearly show the contribution of the fiber reinforcement as well as solvent content on the water absorption rate and mechanical property changes [10].

The study of hemp fibre reinforced unsaturated polyester composites were subjected to water immersion. The study indicated that the percentage of moisture uptake increased as the fibre volume fraction increased due to the high cellulose content. Moisture induced degradation of composite samples was significant at elevated temperature [11].

The resistance of injection molded bamboo fiber reinforced polypropylene composite to hygrothermal aging and their fatigue behavior has shown moderate reduction of tensile property after aging. Moisture absorption and tensile strength degradation are suppressed by using maleic anhydride [12].

2. Experimental

BWB and BT Jute were procured from the Bangladesh Jute Research Institute (BJRI). Next to that the procured jute were washed and sun dried for further work. After that the jute fibers were cut up to 350mm length and washed with demonized distilled water and dried over night at 60°C temperature. Dry preforming technique (taking bunch of jute fiber of 350mm length from jute fiber stock and put under tension with adhesive tape on a 400/400 size 3mm aluminum plate) was followed for unidirectional preform preparation.

However jute polymer composite was prepared with modified compression molding technique. As resin material Epikot 828 LVEL (bisphenol A and epichlorehydrine type) epoxy resin was used and the curing agent was diaminocychlohexene. 35% and 60% volume containing BWB jute and 40% and 50% volume containing BT jute epoxy composites were fabricated with this technique.

The fabricated composites were tested for longitudinal and transverse tensile and three point bend properties according to ASTM D 3039 and ASTM D 790. Moisture sensitivity of the longitudinal three point bend property (ASTM D 790) was also analyzed at 65%, 85% and 95% (RH) relative humidity in a humidity chamber under 50°C temperature.

The percentage moisture gain was plotted against the square root of time (hour). Gradual moisture absorption behavior of the composites was also analyzed for all the composites. Only the longitudinal three point bending properties are discussed, due to the limited scope of the paper. At the final stage of moisture saturation the composite specimens were tested under three point bending according to ASTM D 790 and a plot of strength variation to that of % moisture gain was obtained. Microbial activity was also observed under SEM.

As additional work the BWB jute and BT jute single fiber tensile test was carried out in different set of experiment and the result is used here in this paper but discussion opted out due to paper limitation.

3. Results and discussion

The tensile property of BWB jute was found; strength 844.72MPa, stiffness 55.44 GPa and strain to failure is 1.64%. The tensile property of BT jute was found; strength 671.73 MPa, stiffness 34.63 GPa, and strain to failure 1.93%. The tensile strength of epoxy resin was found; strength 87.2 MPa, stiffness 3.89 GPa and strain to failure 2.14%.

3.1. Three point bending property of jute epoxy composites

Table 1 shows the three point bending behavior of BWB and BT jute epoxy composites in the longitudinal direction. The effect of volume fraction and the fiber wet ability with matrix is clearly observed in this table. And it can be said from the above table that the optimum jute fiber volume fraction for any kind of jute polymer composite must never exceed 50% volume to that of the whole composite.

If we consider Table 1 then we must notice that the experimentally obtained strength value rests within the theoretical strength value of jute epoxy composites. But the stiffness value is much higher than the theoretical value, which is attributed to the betterment of fiber matrix interaction inside composite due to modification in the composite processing technique. But due to wet ability problem this phenomenon does not go well with 60% volume containing BWB jute epoxy composite.

Table 1. Longitudinal three point bending property of BWB and BT jute reinforced composite

Name	Strength	SD	Stiffness	SD	Strain to Failure	SD
	Mpa		Gpa		%	
35%BWB	205.93	17.89	17.24	2.24	1.99%	0.10%
60%BWB	233.66	22.54	19.77	2.27	2.01%	0.21%
40%BT	245.22	15.86	22.03	1.43	1.67%	0.18%
50%BT	349.12	20.28	36.44	3.25	1.43%	0.09%

When jute composite is failed under longitudinal three point bend loading the fracture surface would look like the following as shown in Figure 1a to d.
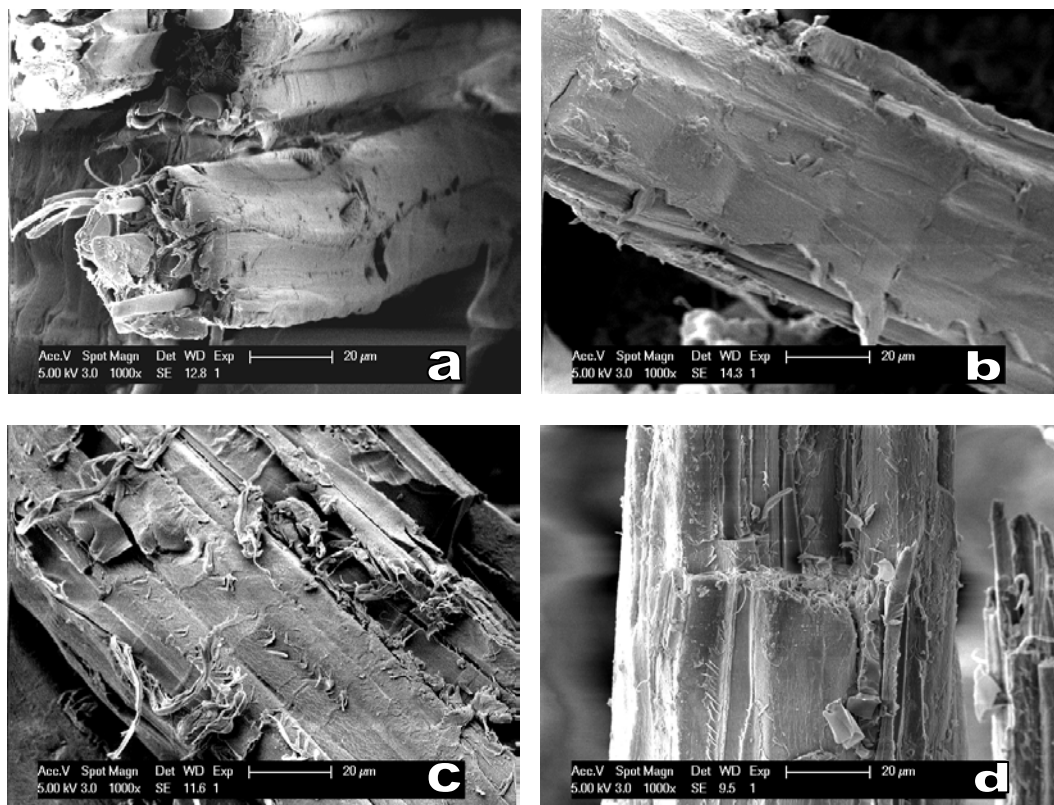
Fig 1: Fracture surface observation of unidirectional composite under longitudinal three point bend load; a) 35% BWB, b) 40% BT, c) 50% BT and d) 60% BWB

The messages from the figures are very clear that the BT jute contains the most resin debris (Fig 1b & c). But the wet ability is severely affected by higher volume of BWB jute as shown in Figure 1d, where as moderate amount of resin is adhered with BWB jute at 35% fiber volume fraction as shown in Figure 1a. Therefore BT jute showed better adhesion with epoxy compared to the BWB jute.

3.2. Effect of humidity on property of jute epoxy composite

There are two kinds of impact of moisture absorption on the properties of jute epoxy composites. First, as the relative humidity value increases the percentage moisture absorption increases and reaches a certain steady value at that condition we say that the moisture absorption of composites reaches saturation. There is also a time constraints that is under low RH value if longer time of moisture absorption is allowed then that also assists the jute fiber reinforced composite to reach a certain saturation value. This is since, with increasing RH there is particular percentage of moisture that remains in equilibrium with the jute fiber and the equilibrium moisture gain also varies with the variety of jute. Therefore it can be said that the jute

variety, relative humidity, time, temperature and equilibrium moisture content, all plays their role cumulatively during moisture absorption test.

Experiments have also revealed that as the jute volume fraction is increased the tendency of higher moisture absorption is also increased [6, 13]. For jute like natural fiber it is very hard to achieve proper wetting at the higher volume fraction composite, which means that this makes the composite more vulnerable to moisture attack.
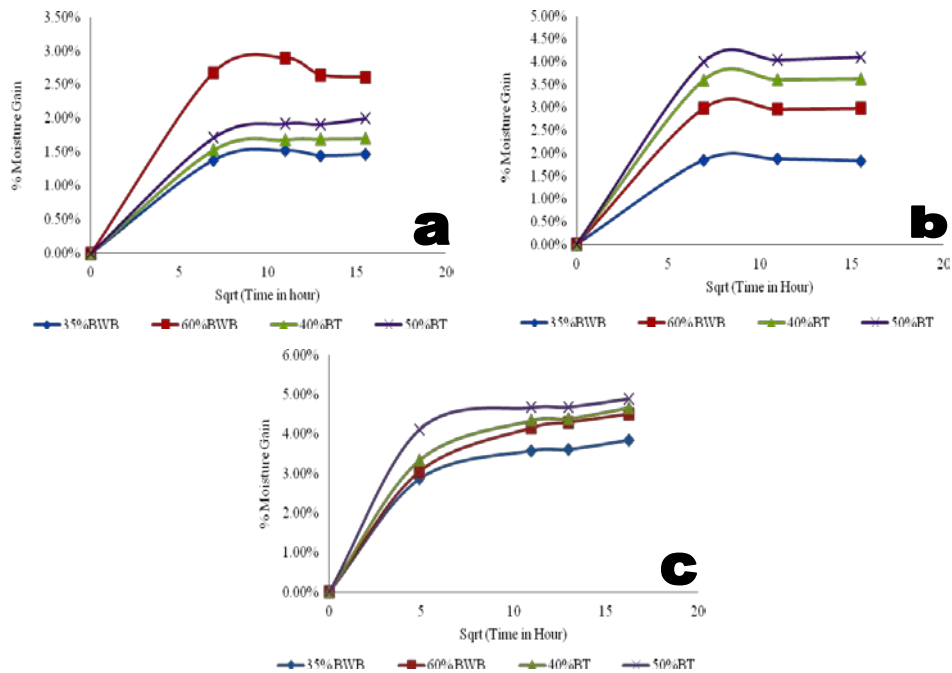
Fig 2: Moisture absorption behavior of jute epoxy composites at different relative humidity; a) 65%RH, b) 85%RH and c) 95%RH

Figure 2 a, b and c shows the moisture absorption characteristics of jute epoxy composites at two different fiber volume fractions. At 65% RH value the 40% and 50% BT jute reinforced composite showed intermediate moisture gain between the 35%BWB and 60% BWB jute reinforced epoxy composite (Fig 2a). Successively at 85% RH value both BWB and BT jute showed reinforcement volume fraction dependent moisture absorption behavior and BT jute showed higher moisture absorption compared to BWB jute (Fig 2b). But at 95%RH the initial moisture uptake rate is similar for both the 35% and 60% volume fraction BWB jute containing epoxy composites but BT jute reinforced composite clearly showed higher degree of moisture absorption (Fig 2c) . However, as the equilibrium moisture content is higher for the higher volume fraction jute containing epoxy composite so if we virtually combine the three charts we definitely notice that both the BWB and BT jute at different fiber volume fraction showed different moisture absorption at different RH value.
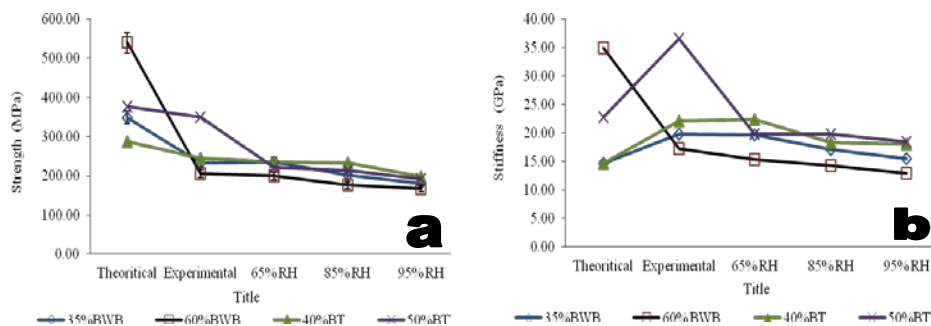
Fig 3: Effect of moisture absorption on the longitudinal three point bending property of jute epoxy composites; a) Strength and b) stiffness

Figure 3a shows the longitudinal three point bending strength degradation behavior of BWB jute epoxy composites at different relative humidity value. Before augmenting further a little reminder could be made,

that is both 35% and 60% volume fraction jute containing epoxy composite showed lower strength than the theoretical value. Additionally as moisture at different RH begins to penetrate the unidirectional jute epoxy composites, it showed strength degradation. Although not drastic but continual degradation of strength value is noticeable. Figure 3b shows the stiffness degradation trend of jute epoxy composites. Similar kind of behavior of BT jute reinforced composite was also observed. However, in this case the degradation is noticeable [6, 7, and 14].

Lignin is water repellent but susceptible to microbial action, but cellulose on the other hand is hygroscopic. However, during moisture gain the jute fiber bulges since the cellulose –OH group forms hydrogen bonding with the absorbed and adsorbed moisture. Consecutively as the fiber becomes dry it returns to its earlier shape. Therefore, in some sense jute fiber acts like shape memory alloy [14, 15].

Jute as a fiber contains 8% equilibrium moisture. The natural procedure is sun drying. But after oven drying if the jute fiber is taken in normal environment it again regains moisture [1 – 6, and16].
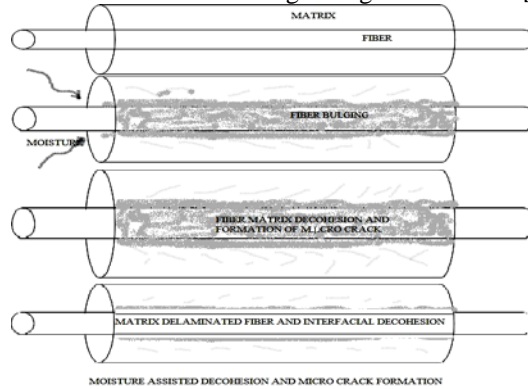
Fig 4: Schematic view of moisture absorption and effect at the interface of jute epoxy composite.

In the moist condition the jute fiber uptakes moisture and becomes bulged and it creates pressure at the jute polymer interface and as this moisture gain continues the jute fiber forces itself to regain its earlier shape. However, as the relative humidity of the environment differs so the moisture gain and discharge from the jute fiber also changes so as to ensure equilibrium. So this changing condition affects the cohesion and adhesion of jute fiber and polymer, which damages the fiber matrix interface and degrades the overall composite mechanical property and this is schematically shown in Figure 4.
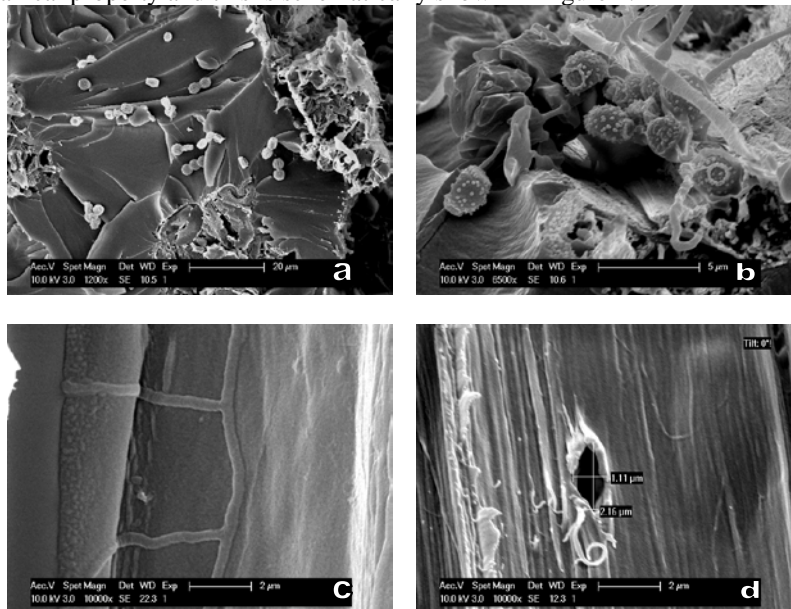
Fig 5: Bacterial growth on the a) epoxy matrix and b) jute fiber and bacterial action on ac epoxy matrix and d) jute fiber

The moisture absorption not only affects the fiber but also assists the microorganism to penetrate the composite body and synergize degrading affect, which is shown in Figure 5 a & b. So, during useful life the fiber should be effectively isolated from the environment to resist microbial action. From Figure 5 c & d it is observed that the bacterial action has perforated the fiber at some localized position and also created

channel like entity on epoxy resin. This action degrades the fiber property by decreasing the fiber strength, which intern influences the composite property.

4. Conclusion

Based on the above study the following conclusions could be made
1. Modified compression molding showed higher stiffness value of composites then theoretical and the actual reason is yet unknown.
2. The percentage moisture absorption is diffusion controlled and an equilibrium process and as the saturation level is attained the moisture absorption and desorption remains steady.
3. Moisture absorption assists in formation of microbial growth which degrades composite property. which is dependent on the time, temperature, relative humidity.

5. Acknowledgement

6. References

[1] . Bismarck, I. A. Askargorta, J. Springer, Cellulose Fibers; Surface Properties and the Water Uptake Behavior, Polymer Composites, Vol. 23, No. 5, 2002
[2] A. K. Bledzki, A. A. Mamun, O. Faruk, Abaca fibre reinforced PP composites and comparison with jute and flax fibre PP composites, eXPRESS Polymer Letters Vol.1, No.11, page 755–762, 2007
[3] B.A. Acha, F.A. Ramirez, L.A. Carlsson, A method to measure fracture toughness of the fiber/matrix interface using the single-fiber fragmentation test, Composites: Part A 40, page 679–686, 2009
[4] E. Mader, T.-T.-L. Doan, H. Brodowsky, Jute fibre/polypropylene composites II. Thermal, hydrothermal and dynamic mechanical behaviour, Composites Science and Technology, 67 page 2707–2714, 2007
[5] G. Marques, J. Rencoret, A. Gutiérrez and J. C. del Río, Evaluation of the chemical composition of different non-woody plant fibers used for pulp and paper manufacturing, The Open Agriculture Journal, 4, page 93-101, 2010
[6] H. Hamada, M. Sakaguchi, A. Nakai, N. Takeda, The mechanical properties of unidirectional thermoplastic composites manufactured by a micro-braiding technique, Composites Science and Technology, Volume 60, Issue 5, page 717–722, 2000
[7] J. Bras, N. Lavoine, I. Desloges, A. Dufresne, Microfibrillated cellulose – Its barrier properties and applications in cellulosic materials: A review, Carbohydrate Polymers Volume 90, Issue 2, 1, pages 735–764, 2012
[8] J.C. Seferis, F.U. Buehler, Effect of reinforcement and solvent content on moisture absorption in epoxy composite materials, Composites: Part A 31, page 741–748, 2000
[9] J.Y. Yu, Z.P. Xia, L.D. Cheng, L.F. Liu, W.M. Wang, Study on the breaking strength of jute fibres using modified Weibull distribution, Composites: Part A 40, page 54–59, 2009
[10] K.N. Bharath, R.P. Swamy, Adhesive Tensile And Moisture Absorption Characteristics Of Natural Fibres Reinforced Urea Formaldehyde Composites, International Journal of Recent Trends in Engineering, Vol. 1, No. 5, 2009.
[11] M. A. Hazizan, L. W. Cheng, Z.A. Mohd Ishak, A. Abu Bakar, M.A. Abd Rahman, Water absorption study on pultruded jute fibre reinforced unsaturated polyester composites, Composites Science and Technology 69, page 1942–1948, 2009
[12] M. M. Thwea, K. Liaob, Durability of bamboo-glass fiber reinforced polymer matrix hybrid composites Composites Science and Technology 63, page 375–387, 2003
[13] H.N. Dhakal, Z.Y. Zhang, M.O.W. Richardson, Effect of water absorption on the mechanical properties of hemp fibre reinforced unsaturated polyester composites, Composites Science and Technology 06, 019, 2006,
[14] M. Hasan, M. R. Rahman, M. M. Huque, M. N. Islam, Improvement of physico-mechanical properties of jute fiber reinforced polypropylene composites by post-treatment, Composites: Part A 39, page 1739–1747, 2008
[15] R. P. Singh, A. P. Kumar, B. D. Sarwade, Degradability of composites, prepared from ethylene–propylene copolymer and jute fiber under accelerated aging and biotic environments, Materials Chemistry and Physics 92, page 458–469, 2005
[16] S. J. Eichhorn, C. A. Baillie, N. Zafeiropoulos, L. Y. Mwaikambo, M. P. Ansell, A. Dufresne, K. M. Entwistle, P. J. Herrera-Franco, G. C. Escamilla, L. Groom, M. Hughes, C. Hill, T. G. Rials, P. M. Wild, Review current international research into cellulosic fibres and composites, Journal of Materials Science 36, page 2107 – 2131, 2001

Stress Analysis of an Internal Grooved Pressure Vessel

Abdul Mohaimen Safi

Department of Mechanical Engineering, BUET, Dhaka- 1000, Bangladesh
E-mail: mohaimensafi@gmail.com

Abstract

Pressure vessels are used in a variety of application in both industry and private sector. They appear in these sectors as industrial compressed air receiver and domestic hot water storage tank. Until recently primary analysis method for calculating stress had been hand calculation and empirical curves. New computer advances have made numerical computation a powerful tool in the study of pressure vessel especially in determining stresses in grooves which are difficult to analyze by hand calculation. This paper presents a numerical investigation for stress distribution in a cylindrical pressure vessel having internal groove under the application of internal pressure. Solutions especially at the groove region which are observed as the critical zone are determined by finite element numerical technique. The effect of groove radius and the thickness ratio of the of the pressure vessel have also been studied.
.

***Keywords:** Pressure vessels, internal groove, finite element technique.*

1. Introduction

Pressure vessels are closed containers designed to hold gases or liquids at a pressure different from the atmospheric pressure. They may be of any shape and size ranges from cold drink bottles to high pressure steam boilers used for engineering application. The word "Design" means not only to create, and calculate the detail dimensions of the pressure vessel but also to find out the mode of failure and selection of materials type and its environmental behavior [1]. The increasing industrial demand for pressure vessels which have application in chemical, nuclear, petrochemical, oil, power plant and military equipment have concentrated the attention of engineers on this particular area of engineering to find out most likely method of damage, method of stress analysis and reliability of results [2]. Though experimental methods give the most reliable results, it is very costly, as it requires special equipments, testing facilities etc. Analytical solution of every problem is almost impossible because of complex boundary conditions and shapes. For this reason the numerical methods had become the ultimate choice by the researchers in the last few decades. Invention and rapid improvement of the computing machines, i.e. sophisticated high performance computers, also played an important role for the increasing popularity of the numerical methods. Stress analysis of a pressure vessel having internal groove requires the solution of partial differential equations. There are various numerical methods available for the solution of partial differential equations. Among them most popular methods are: Finite Element Method (FEM) and Finite Difference Method (FDM). The finite element method is a numerical technique for obtaining approximate solution to a wide variety of engineering problems. Although originally developed to study stresses in complex airframe structures, it has since been extended and applied to the broad field of continuum mechanics because of its diversity and flexibility as an analysis tool. The finite difference model of a problem gives a point wise approximation to the governing equations. With finite difference techniques we can treat some fairly difficult problems; but for example, when we encounter irregular geometries or an unusual specification of boundary conditions, we find that finite difference techniques become hard to use. A finite element model of a problem gives a piece wise approximation to the governing equations. Since these elements can be put together in a variety of ways, they can be used to represent exceedingly complex shapes. In the present paper numerical simulation for a non-circular pressure vessel having internal groove under the application of internal pressure has been investigated using ANSYS one of the most popular finite element method software.

s
2. Equations for non-circular pressure vessel

For non-circular vessels, the hoop stress in an obround is comprised of a shape-dependent bending component superimposed on the pressure-induced membrane component. A representative obround shape is represented in figure 1 & the corresponding stress components at the noted critical points are as follows [3]

Membrane Stress (σ_m):

$$\text{Locations A, B:} \quad (\sigma_m)_{A,B} = \frac{PR}{t} \tag{1}$$

$$\text{Locations C, D:} \quad (\sigma_m)_{C,D} = \frac{P(R+L_2)}{t} \tag{2}$$

Bending Stress (σ_b):

$$\text{Locations A, B:} \quad (\sigma_b)_{A,B} = \pm\frac{PL_2RC_1c}{6AI} \tag{3}$$

$$\text{Locations C, D:} \quad (\sigma_b)_{C,D} = \pm\frac{PL_2c}{6I}\left[3(L_2 + 2R) - \frac{C_1}{A}\right] \tag{4}$$

Where,

$$I = \frac{t^3}{12}$$
$$C_1 = L_2^2(2 + 3\pi) + 12R^2$$
$$A = 2\left(\frac{L_2^2}{R}\right) + \pi R$$

$$C = \frac{t}{2} = \text{distance from neutral axis to outer surface}$$

Total Hoop Stress (σ_t):

$$\text{Locations A, B:} \quad (\sigma_t)_{A,B} = (\sigma_m)_{A,B} + (\sigma_b)_{A,B} \tag{5}$$

$$\text{Locations C, D:} \quad (\sigma_t)_{C,D} = (\sigma_m)_{C,D} + (\sigma_b)_{C,D} \tag{6}$$
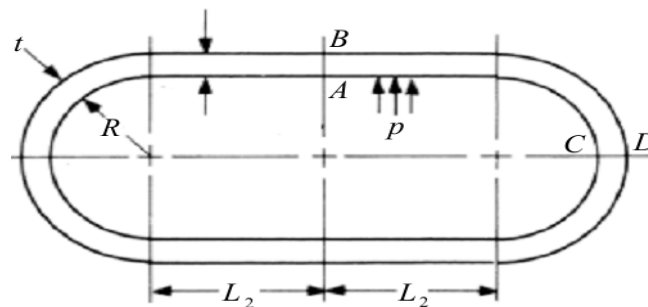
Fig. 1. Non-circular pressure vessel

3. Model development

The geometry of the problem is shown in Fig 2. As the vessel is axially symmetric about its central axis, an axisymmetric analysis was performed using two-dimensional, 8-node quadrilateral elements (Plane 82) with the axisymmetric option activated. In addition, the vessel is symmetric about a plane through the center of the cylinder. Thus, only a quarter portion of the vessel was modeled as indicated by the shaded area in Fig 2. Once the axisymmetric option was invoked, ANSYS automatically applied axisymmetric boundary conditions along the Y-axis. The material of the plate is high strength alloy steel; Poisson's ratio $v=0.33$, Young's modulus E=200 GPa. Uniform Pressure was applied on all lines that make up the inner surface of the vessel.
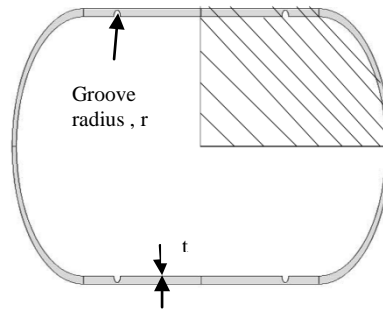
Fig. 2. Model Geometry

4. Meshing

Created geometrical model is discretized into nodes and elements. The process is called meshing. The Ansys program can automatically generate nodes and elements, provided that element size is specified. The element size controls the fineness of the mesh. The smaller the element size the finer the mesh. For the present problem 7200 elements have created, density of mesh at the groove is shown in Fig 3.
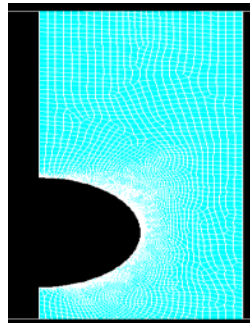
Fig. 3. Density of mesh at the internal groove

PLANE 82 (8-nod 2-D) elements shown in Fig 5 have been used in the analysis. PLANE 82 elements provide more accurate results for mixed (quadrilateral-triangular) automatic meshes and can tolerate irregular shapes without much loss of accuracy. The 8-node elements have compatible displacement shapes and are well suited to model curved boundaries. The element may be used as a plane element or as an axis symmetric element. The element has plasticity, creep, swelling, stress stiffening, large deflection, and large strain capabilities. [4]
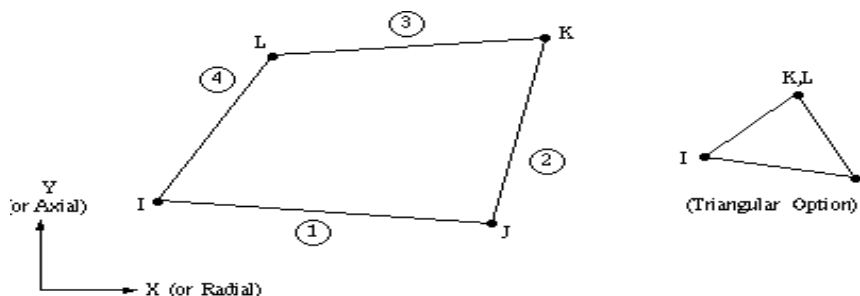
Fig. 4. PLANE 82 elements with 8 nodes

5. Results and discussions

The solution of stress components σ_r, σ_l and σ_t for each nodal point within the elastic limit has been obtained. The variations of values of σ_r, σ_l and σ_t with the change of non-dimensional ratio x/t were plotted for some selected sections. The selected sections are shown in Fig. 6.
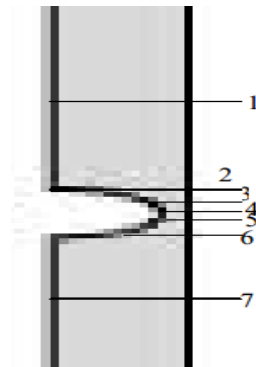
Fig. 5. Selected sections for studying the distribution of stresses

The distribution of stress component σ_r (radial stress) for some selected sections are shown in Fig. 7. For a constant value of x/t the maximum value of σ_r is obtained at the midpoint along the groove. The value of σ_r is zero outer most ends which satisfy the applied boundary condition.
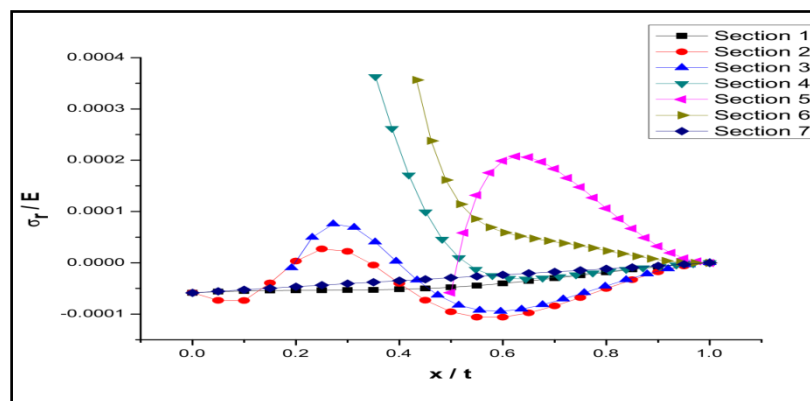
Fig. 6. Distribution of σ_r

The distribution of stress component σ_l (longitudinal stress) for some selected sections are shown in Fig. 8. For a constant value of x/t the maximum value of σ_l is obtained at the midpoint along the groove. It is found that for section 1 and 7 the value of σ_l is almost identical. So the distribution of stresses varies around the groove and becomes uniform large distance away from the groove.
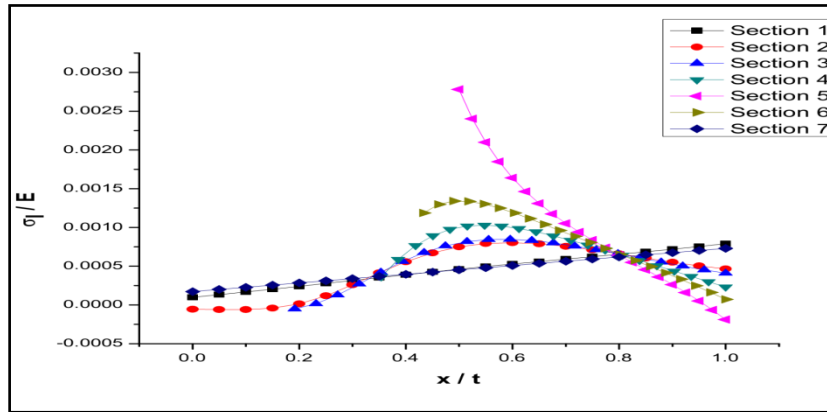
Fig. 7. Distribution of σ_l

The distribution of stress component σ_t (hoop stress) for some selected sections are shown in Fig. 9. For a constant value of x/t the maximum value of σ_t is obtained at the midpoint along the groove. It is observed that only section 1 and 7 the stress distribution is linear which indicate that distribution of stresses varies around the groove.
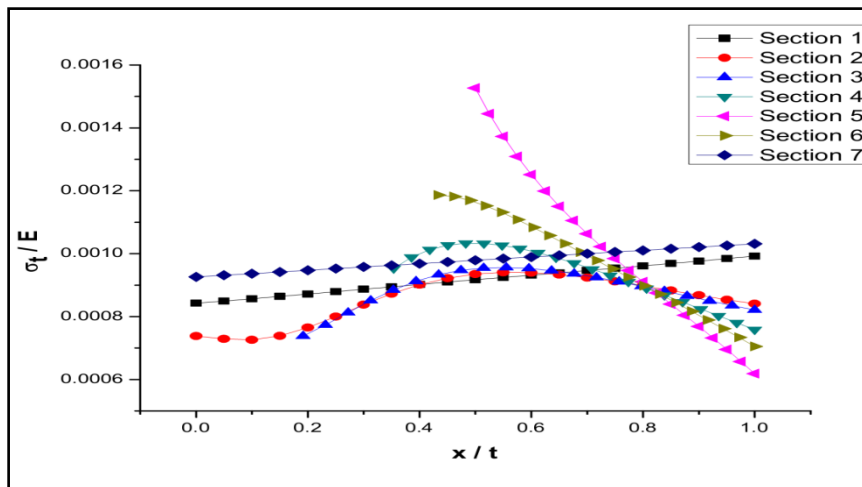
Fig. 8. Distribution of σ_t

The effect of degree of groove radius to thickness ratio on the pressure vessel

The effect of degree of groove radius to thickness ratio is studied by plotting the variations of values of σ_r, σ_l and σ_t with the change of non-dimensional ratio r/t for section 5. The distribution of stress component σ_r (radial stress) with the change of r/t is shown in Fig. 9. As appears for constant x/t the value of σ_r increases as the value of r/t increases for the same loading. So for the internal grooved pressure vessel r/t is an important factor.
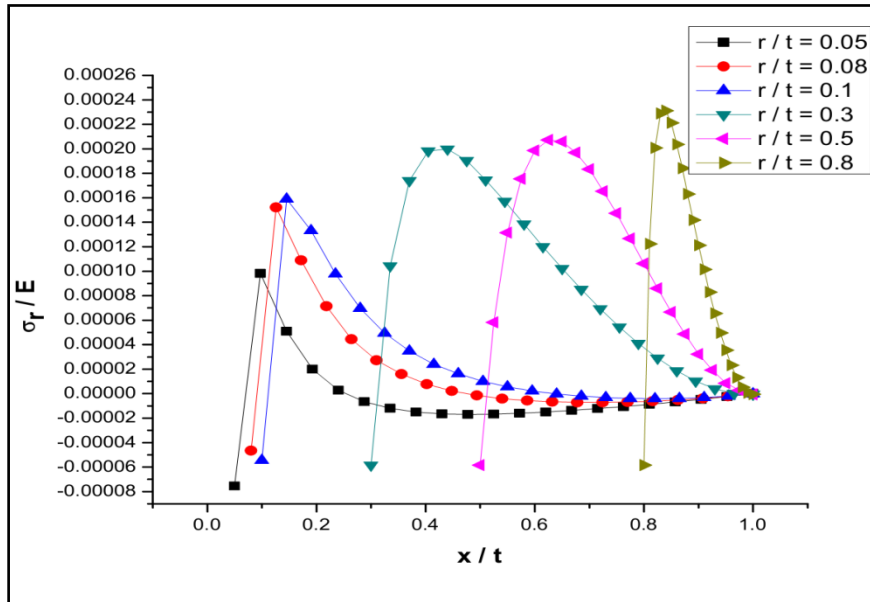
Fig. 9. Distribution of σ_r with the change of r/t

The distribution of stress component σ_l (longitudinal stress) with the change of r/t is shown in Fig. 10. It is observed that for constant value of x/t value of σ_l increases with the increase of r/t. It is found that with the decrease r/t for the same loading the stress distribution becomes identical as in case for r/t = 0.05, r/t = 0.08 and r/t =0.1. It is also appears that with increase of r/t curves becomes parallel to Y-Axis.
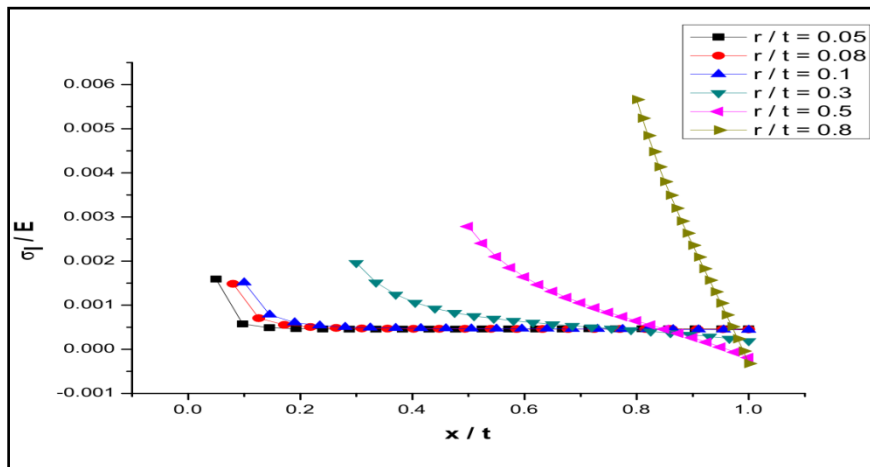
Fig. 10. Distribution of σ_l with the change of r/t

The distribution of stress component σ_t (longitudinal stress) with the change of r/t is shown in Fig. 11. It is observed that for constant value of x/t value of σ_t increases with the increase of r/t. This graph nature is similar to the graph plotted in Fig. 10. So from both graph it can be said that r/t ratio should be less than 0.3 for designing pressure vessel having internal groove.
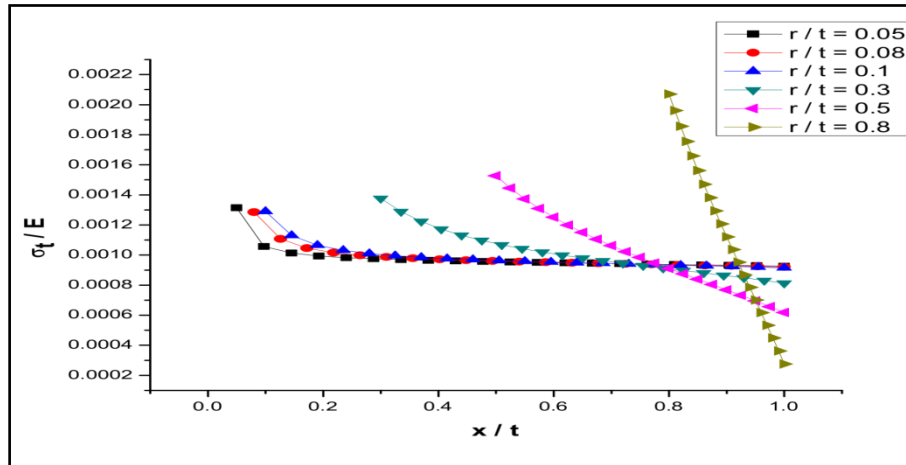
Fig. 11. Distribution of σ_t with the change of r/t

6. Conclusions

The present study provides the solution for stress components of a non-circular pressure vessel having internal groove subjected to an internal pressure using finite element approach. Both quantitative and qualitative results of pressure vessel obtained which establish the soundness and appropriateness of the present finite element approach.

7. References

[1] Vikram V. Mane, Vinayak H.Khatawate, Ashok Patole, "Finite Element Analysis of Ellipsoidal Head Pressure Vessel", Interntional Journal of Engineering and Research Applications (IJERA) ISSN: 2248-9622, 2012.

[2] Donatello Annaratone, Pressure Vessel Design, Springer, 3rd edition, pp. 2-5, 2007.

[3] Jonathan C. Wang, "Stress Analysis of an Elliptical Pressure Vessel Under Internal Pressure", Rensselaer Polytechnic Institute, 2005.

[4] "ANSYS" Theory Manual and Expanded ANSYS Workbook

An Iteration Method for Near-tip singular fields of a crack in a Power- law Hardening Material Using Asymptotic Analysis

Md. Arefin Kowser[1], Md. Mahiuddin[2]

[1]Department of Mechanical Engineering, Dhaka University of Engineering & Technology, Gazipur,
[2]Department of Mechanical Engineering, Dhaka University of Engineering & Technology, Gazipur
E-mail: nadimduet@yahoo.com

Abstract

In this paper an asymptotic analysis of the near-tip stress and displacement fields of a crack in a power-law hardening material has been presented. Singular exponent λ is investigated for the determination of singular stress and displacement fields for the crack. Symmetric loading condition is applied in this analysis. To determine the singular exponent, λ strain compatibility equation has been derived where 4th order differential equation has been solved using Range-Kutta method. The solution technique of non-linear compatibility equation, the calculation results are presented as well. All results are calculated with the assumption of plane strain condition. The solution obtained for λ is compared with the results of other researcher solved for crack problem.

Keywords: Asymptotic analysis, singular stress, singularity, compatibility equation, Range-Kutta method, Non-linear solution, crack.

1. Introduction

In recent years, a considerable amount of work has been done in studying crack growth behavior in power-law hardening materials [1-4]. The importance of these studies stems from the fact that the crack growth behavior in the material may significantly affect the integrity of the structure made of that material. The basic approach used in characterizing the particulate material is based on linear elastic or non linear fracture mechanics. According to the theories, crack growth behavior is controlled by the local stress/strain near the crack tip. Therefore, the values of local stress/strain near the crack tip must be determined. When crack occurs, the high stress at the crack tip will induce high damage near the crack tip region. The high damage zone at the crack tip is defined as the failure process zone, which is a key parameter in fracture mechanics [14-16]. Experimental data reveal that when the local strain reaches a critical value, small voids are generated in the failure process zone. The heterogeneity of the microstructure plays a key role for local damage and strain distributions near the crack tip. Experimental results indicate that the high strain field is localized within 1 mm of the crack tip. Also, the time - dependent damage initiation and evolution processes are contributing factors to the non-steady crack growth in this material [17-19]. Recently the interfacial crack mechanism expected much interest, largely due to the existence of interfacial fracture in lots of advanced materials such as polycrystalline alloys, structural ceramics, and composites. Early research work on this field can be found in Williams, England, Erdogan, Rice and Sih and so on [5-10]. As for the interface cracks of the elastic-plastic materials, a significant progress was made by Shih and Asaro in 1988 [11]. Through the detail full-field computational investigations by the finite element method, they found that the near tip fields of crack on biomaterial interfaces have the nearly separable form solutions of the HRR type in an annular region within the plastic zone. Wang presented an exact asymptotic analysis for a crack lying on the interface of an elastic-plastic material and linear elastic material. A separable singular stress field of the HRR type has been found in the plastic angular zone around crack tip [12].

A crack in a far field which is tensile in a direction perpendicular to it is considered. A solution to compatibility equation is sought in the immediate vicinity of the crack tip where the stresses are large, and, on the basis of the theory which has been laid down, are unbounded as the crack tip approached [13]. An asymptotic expansion of the solution is attempted in the form,

$$\phi = r^s \, \widetilde{\phi_1}(\theta) + r^t \, \widetilde{\phi_2}(\theta) + \ldots \ldots \tag{1}$$

Where, if the first term is to be singled out as the dominant one, s < t etc, our search will be restricted to only the dominant term in such an expansion,

$$\phi = Ar^{\lambda+1} \, \tilde{\phi} \, (\theta) \tag{2}$$

Where the amplitude A will permit us to adjust the amplitude of $\tilde{\phi}$ in some arbitrary, yet appropriate manner.
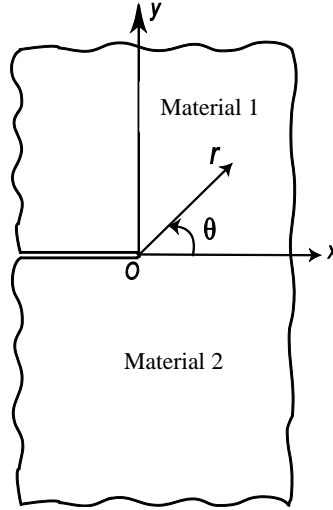
Fig.1: Conventions at crack tip

2. Mathematical Equations

Stress and strain relationships

The generalized dimensionless relationship between strain and stress governed by a power-law form and J_2- deformation theory is

$$\varepsilon_{ij} = \left(1+\nu\right) s_{ij} + \frac{\left(1-2\nu\right)}{3} \sigma_{kk} \delta_{ij} + \frac{3}{2} \alpha \sigma_e^{n-1} s_{ij} \tag{3}$$

$$\varepsilon_{ij} = \left(1+\nu\right) \sigma_{ij} - \nu \sigma_{kk} \delta_{ij} + \frac{3}{2} \alpha \sigma_e^{n-1} s_{ij} \tag{4}$$

$\sigma_{kk} = \sigma_{rr} + \sigma_{\theta\theta} + \sigma_{zz}$; For plane strain condition: $\varepsilon_{zz} = 0$; $\sigma_{zz} = \nu(\sigma_{rr} + \sigma_{\theta\theta})$

Where, $\varepsilon_{ij} = \dfrac{\overline{\varepsilon}_{ij}}{\varepsilon_y}$, $\varepsilon_y = \dfrac{\sigma_y}{E}$, $s_{ij} = \dfrac{\overline{s}_{ij}}{\sigma_y}$ and $\sigma_{ij} = \dfrac{\overline{\sigma}_{ij}}{\sigma_y}$ $\tag{5}$

$$\sigma_e = \sqrt{\frac{3}{2} s_{ij} s_{ij}} \tag{6}$$

And, $s_{ij} = \sigma_{ij} - \dfrac{1}{3} \sigma_{kk} \delta_{ij}$ $\tag{7}$

It is noted that the barred quantities in Eq. (5) are the non-normalized field variables, $(\sigma_y, \varepsilon_y)$ is a reference point for the uniaxial stress -strain curve, $\overline{\sigma}_{ij}, \overline{\varepsilon}_{ij}$ *and* $\overline{s}_{ij}$ are the stress, strain and deviatoric stress component along ij direction, where i, j are used for subscript indicates x, y or r, θ (ij denotes rr , $\theta\theta$ and $r\theta$). E is the initial slope of the stress-strain curve called Young's modulus, δ_{ij} is the two dimensional Kronecker delta symbol, ν is the Poisson ratio, α and n are hardening coefficient and hardening exponent, respectively. σ_e is

the effective stress and s_{ij} is the stress deviator. Stress quantities normalized by yield stress and strain quantities are normalized by corresponding yield strain.

Equilibrium

In problems, the equilibrium equations are automatically satisfied for all stresses derived from the Airy stress function ϕ when the stresses are defined in the following manner,

$$\sigma_{rr} = \frac{1}{r}\frac{\partial \phi}{\partial r} + \frac{1}{r^2}\frac{\partial^2 \phi}{\partial \theta^2} \tag{8}$$

$$\sigma_{\theta\theta} = \frac{\partial^2 \phi}{\partial r^2} \tag{9}$$

$$\sigma_{r\theta} = \frac{1}{r^2}\frac{\partial \phi}{\partial \theta} - \frac{1}{r}\frac{\partial^2 \phi}{\partial r \partial \theta} \tag{10}$$

Where ϕ is called the Airy stress function.

The dimensionless stress function ϕ and coordinate r are given in terms of dimensional quantities (barred) by

$$\phi = \frac{\overline{\phi}}{\sigma_y L^2} \quad \text{and} \quad r = \frac{\overline{r}}{L}, \text{where } L \text{ is the characteristic length (for example half length of the crack).}$$

Compatibility and strain-displacement equations

Using small deformation theory, the compatibility equation in terms of strain components is written,

$$-\frac{1}{r}\frac{\partial \varepsilon_{rr}}{\partial r} + \frac{2}{r}\frac{\partial \varepsilon_{\theta\theta}}{\partial r} + \frac{\partial^2 \varepsilon_{\theta\theta}}{\partial r^2} - \frac{2}{r^2}\frac{\partial \varepsilon_{r\theta}}{\partial \theta} + \frac{1}{r^2}\frac{\partial^2 \varepsilon_{rr}}{\partial \theta^2} - \frac{2}{r}\frac{\partial^2 \varepsilon_{r\theta}}{\partial r \partial \theta} = 0 \tag{11}$$

Plane strain condition

$$\varepsilon_{zz} = 0; \ or \ \sigma_{zz} = \nu\left(\sigma_{rr} + \sigma_{\theta\theta}\right)$$

$$\varepsilon_{rr} = (1+\nu)\left\{(1-\nu)\sigma_{rr} - \nu\sigma_{\theta\theta}\right\} + \frac{3}{2}\alpha\sigma_e^{n-1}s_{rr} \tag{12}$$

$$\varepsilon_{\theta\theta} = (1+\nu)\left\{(1-\nu)\sigma_{\theta\theta} - \nu\sigma_{rr}\right\} + \frac{3}{2}\alpha\sigma_e^{n-1}s_{\theta\theta} \tag{13}$$

$$\varepsilon_{r\theta} = (1+\nu)\sigma_{r\theta} + \frac{3}{2}\alpha\sigma_e^{n-1}s_{r\theta} \tag{14}$$

In this approximation, the elastic strains in compared with the plastic strains are small and can be neglected in the asymptotic analysis. Hence according to the plastic deformation theory the three dimensional stress-strain relations take the form,

$$\varepsilon_{ij} = \frac{3}{2}\alpha\sigma_e^{n-1}s_{ij} \tag{15}$$

The small deformation strain-displacement relations are as follows,

$$\varepsilon_{rr} = \frac{\partial u_r}{\partial r} \tag{16}$$

$$\varepsilon_{\theta\theta} = \frac{1}{r}u_r + \frac{1}{r}\frac{\partial u_\theta}{\partial \theta} \tag{17}$$

$$\varepsilon_{r\theta} = \frac{1}{2}\left(\frac{1}{r}\frac{\partial u_r}{\partial \theta} + \frac{\partial u_\theta}{\partial r} - \frac{u_\theta}{r}\right) \tag{18}$$

Boundary conditions

$$\left(\sigma_{\theta\theta}\right)_{\theta=0} = 0 \qquad \left(\sigma_{\theta\theta}\right)_{\theta=\pi} = 0$$

and

$$\left(\sigma_{r\theta}\right)_{\theta=0} = 0 \qquad \left(\sigma_{r\theta}\right)_{\theta=\pi} = 0 \tag{19}$$

Governing Differential Equation

Assumed, $\phi = Ar^{\lambda+1}\tilde{\phi}$

Compatibility equation becomes in the form of,

$$C \times \frac{\partial^4 \tilde{\phi}}{\partial \theta^4} = -B\left(\frac{\partial^3 \tilde{\phi}}{\partial \theta^3}, \frac{\partial^2 \tilde{\phi}}{\partial \theta^2}, \frac{\partial \tilde{\phi}}{\partial \theta}, \tilde{\phi}, n, \lambda\right) \tag{20}$$

Where B and *C* are derived using Mathematica software. Equation (20) is the fourth-order ordinary differential equation of $\tilde{\phi}_1^k$. The governing differential equation and boundary conditions define an Eigen value problem. A fourth-order Runge-Kutta method and the shooting method were used to solve the problem. The Mechanical properties of power-law hardening materials are given in Table 1. E is Young's modulus, V is the Poisson's ratio.

Table 1. Mechanical Properties of cracked materials

Properties	E[GPa]	v	σ_y [MPa]	n	α	p₀ [MPa]
Material I	108	0.33	30	3	10.1	130
Material II	108	0.33	30	3	10.1	130

Stress calculation

$$\sigma_{rr} = Ar^{\lambda-1}\left[\left(\lambda+1\right)\tilde{\phi} + \frac{\partial^2 \tilde{\phi}}{\partial \theta^2}\right] \tag{21}$$

$$\sigma_{\theta\theta} = Ar^{\lambda-1}\left(\lambda+1\right)\lambda\tilde{\phi}. \tag{22}$$

$$\sigma_{r\theta} = -Ar^{\lambda-1}\lambda\frac{\partial \tilde{\phi}}{\partial \theta} \tag{23}$$

$$\sigma_e = Ar^{\lambda-1} \times 2^{1-n} \times 3^{\frac{n-1}{2}}\left\{\left(\lambda^2-1\right)^2 \tilde{\phi}^2 - 2\left(\lambda^2-1\right)\tilde{\phi}\left(\frac{\partial^2 \tilde{\phi}}{\partial \theta^2}\right) + \left(\frac{\partial^2 \tilde{\phi}}{\partial \theta^2}\right)^2 + 4\lambda^2\left(\frac{\partial \tilde{\phi}}{\partial \theta}\right)^2\right\}^{\frac{1}{2}} \tag{24}$$

Displacement Calculation

$$u_{rp} = 2^{1-n}3^{\frac{n+1}{2}}\alpha A^n \frac{r^{n\lambda-n+1}}{\left(n\lambda-n+1\right)}\left(\left(1-\lambda^2\right)\tilde{\phi} + \frac{\partial^2 \tilde{\phi}}{\partial \theta^2}\right)$$

$$\times\left\{\left(\lambda^2-1\right)^2 \tilde{\phi}^2 - 2\left(\lambda^2-1\right)\tilde{\phi}\left(\frac{\partial^2 \tilde{\phi}}{\partial \theta^2}\right) + \left(\frac{\partial^2 \tilde{\phi}}{\partial \theta^2}\right)^2 + 4\lambda^2\left(\frac{\partial \tilde{\phi}}{\partial \theta}\right)^2\right\}^{\frac{n-1}{2}} \tag{25}$$

$$u_{\theta p} = \frac{-2^{-1-n}3^{\frac{n+1}{2}}\alpha A^n r^{n\lambda-n+1}}{\{n(\lambda-1)\}(n\lambda-n+1)}\left\{\left(\lambda^2-1\right)^2\tilde{\phi}^2 - 2\left(\lambda^2-1\right)\tilde{\phi}\left(\frac{\partial^2\tilde{\phi}}{\partial\theta^2}\right) + \left(\frac{\partial^2\tilde{\phi}}{\partial\theta^2}\right)^2 + 4\lambda^2\left(\frac{\partial\tilde{\phi}}{\partial\theta}\right)^2\right\}^{\frac{n-3}{2}}$$

$$\times\left[4\lambda^2\left\{\left(4n(\lambda-1)-\lambda+4\right)\lambda+1\right\}\frac{\partial^3\tilde{\phi}}{\partial\theta^3} + \left\{(7n-4)\lambda^2-4(n-1)\lambda+n\right\}\left(\frac{\partial^2\tilde{\phi}}{\partial\theta^2}\right)^2\frac{\partial\tilde{\phi}}{\partial\theta}\right. \tag{26}$$

$$+\left\{4\lambda^2\left(\frac{\partial\tilde{\phi}}{\partial\theta}\right)^2 + n\left(\frac{\partial^2\tilde{\phi}}{\partial\theta^2}\right)^2\right\}\frac{\partial^3\tilde{\phi}}{\partial\theta^3} + 2\left(\lambda^2-1\right)\tilde{\phi}\left(\frac{\partial^2\tilde{\phi}}{\partial\theta^2}\right)\left\{-\left\{(5n-2)\lambda^2-4(n-1)\lambda+n\right\}\frac{\partial\tilde{\phi}}{\partial\theta} - n\frac{\partial^3\tilde{\phi}}{\partial\theta^3}\right\}$$

$$\left.+\left(\lambda^2-1\right)^2\tilde{\phi}^2\left\{\left(3n\lambda^2-4n\lambda+4\lambda+n\right)\frac{\partial\tilde{\phi}}{\partial\theta} + n\frac{\partial^3\tilde{\phi}}{\partial\theta^3}\right\}\right]$$

To satisfy the boundary conditions for the crack case

$\frac{\partial\tilde{\phi}}{\partial\theta} = 0$ And $\frac{\partial^3\tilde{\phi}}{\partial\theta^3} = 0$, where other unknowns $\tilde{\phi}$, $\frac{\partial^2\tilde{\phi}}{\partial\theta^2}$, λ also calculated.

Assumed at $\theta=0$, $\tilde{\phi}=1.0$, $\frac{\partial^2\tilde{\phi}}{\partial\theta^2}$, λ and after integration $\tilde{\phi}=\tilde{\phi}^i$, $\frac{\partial\tilde{\phi}}{\partial\theta}=\left(\frac{\partial\tilde{\phi}}{\partial\theta}\right)^i$, $\frac{\partial^2\tilde{\phi}}{\partial\theta^2}=\left(\frac{\partial^2\tilde{\phi}}{\partial\theta^2}\right)^i$ and

$\frac{\partial^3\tilde{\phi}}{\partial\theta^3}=\left(\frac{\partial^3\tilde{\phi}}{\partial\theta^3}\right)^i$ where the error are calculated as,

$$error1 = (\lambda+1)\lambda\tilde{\phi}^i \tag{27}$$

$$error2 = -\lambda\left(\frac{\partial\tilde{\phi}}{\partial\theta}\right)^i \tag{28}$$

Finally the error value is calculated by, $error = \sqrt{(error1)^2 + (error2)^2}$ (29)

The final solution is obtained from the minimum error region and calculated numerically the solution where the minimum error occurs. The solution point finding techniques are shown in Fig. 2 and Fig. 3.
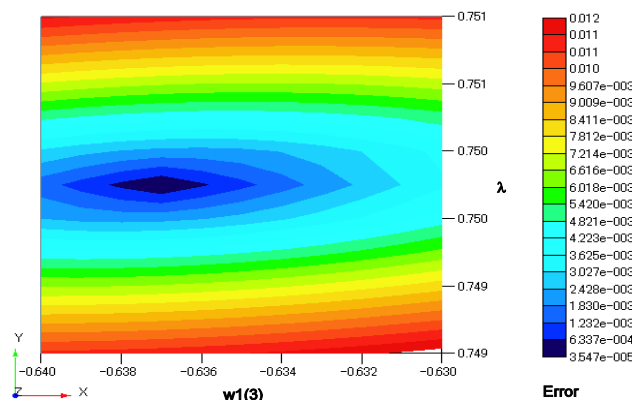
Fig. 2: Identify the minimum error region for $w1(3)$, λ
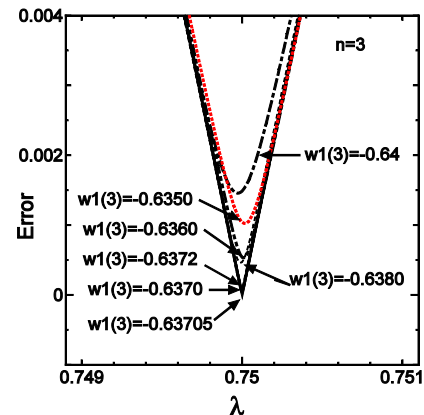
Fig. 3: Point which shows the minimum error

3. Results and Conclusion

Fig.3 finally shows the solution point (point which shows the minimum error is the solution point). The value of $w1(3) = -0.63705 \pm 5\times10^{-5}$ and $\lambda = 0.75 \pm 1\times10^{-5}$ obtained for the minimum error.

Characteristics of singular stress field near the crack-tip are investigated numerically from the solution of differential equation governing the stress function obtained from compatibility equation. Fig. 4 shows the

angular variation of normalized stresses near the tip of a crack for plane strain condition under the symmetric loading condition. The angular variation of normalized displacements for plane strain is shown in Fig. 5.
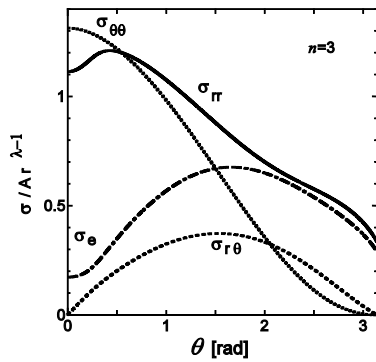
Fig. 4: θ - variations for normalized stresses at crack tip for plane strain condition
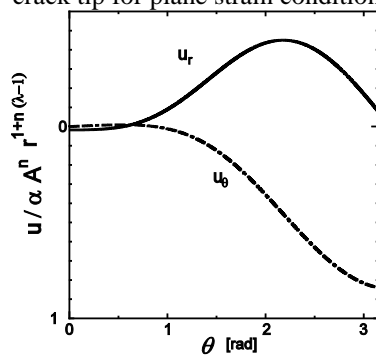
Fig.5: θ - variations for normalized displacement at n = 3

The stress fields can be expressed by $r^{\lambda-1}$ and displacement is proportional to $r^{1-n(\lambda-1)}$. Where r is the distance from the crack tip and λ is the Eigen value called singular exponent. For the continuity of displacements requires $\lambda > 0$ and from the stress fields' unbounded stress occur when $\lambda < 1$, a value of λ such that $0 < \lambda < 1$ will give unbounded stress near the tip of the crack.

For presenting the results, it is necessary to give an idea about the accuracy of the numerical technique and the reliability of the program used. Here, ten thousand segments are taken along the angular edges, and fourth-order Runge-Kutta method is used for the solution of differential equation. An agreement has also been obtained with the solutions investigated by Hutchinson is presented in Table 2 and the value of λ is 0.75 measured for the power-law hardening exponent n = 3 for the plane strain condition under symmetric loading for the crack. Stress and displacement fields for n = 5, 7 and n = 13 are also determined which are not presented here. Which means presented iteration method is suitable for the determination of near tip singular fields for crack of power-law materials of different co-efficient. In the future study, the solution will be presented the effect of the addition of another term with the dominating first term iteratively.

Table 2. Comparisons of results of nonlinear crack (plane strain condition)

Power-law hardening exponent, n	$\tilde{\phi}$	$\dfrac{\partial^2 \tilde{\phi}}{\partial \theta^2}$	Error	λ	Error	by J.W.Hutchinson
3	1.0	-0.63705	$\pm 5 \times 10^{-5}$	0.75	$\pm 1 \times 10^{-5}$	0.75

4. References

[1]   Liu, C.T. and Smith, C.W., "Near Tip Behavior in a Particulate Composite Material- An Experimental and Analytical Investigation," Proc. Of 2n International Conf. on Computational Engineering Science, Aug. 1991

[2]   Smith, C.W. and Liu, C.T.," Effects of Near-Tip Behavior of Particulate Composites on Classical Concepts," Journal of Composite Engineering, Vol.1, No 4, 1991

[3]   Liu, C.T. and Ravi-Chandar,K.," Local Fracture and Crack Growth Behavior in a Particulate Composite Material," Journal of reinforced Plastics and Composites, Vol.l5/No.2 1996.

[4]   Liu, CT.," The Effect of Micro Damage on Time-Dependent Crack Growth in a Composite Solid Propellant," Journal of Mechanics of Time Dependent Materials, Vol.1, 1997.

[5]   Williams ML. Bull Seismol,"The stress around a fault or crack in dissimilar media." Soc America, Vol. 49, pp. 199-204, 1959

[6]   England AH."A Crack Between Dissimilar Media." J Appl Mech, Vol. 32, pp. 400-402, 1965

[7]   Erdogan F., "Stress Distribution in a Xonhomogeneous Elastic Plane with Cracks." J. Appl Mech, Vol. 30, pp. 232-236, 1963

[8]   Rice JR and Sih GC. , "The Bending of Plates of Dissimilar Materials With Cracks," J Appl Mech, Vol. 32, pp. 418-443, 1965

[9]   Hutchinson JW, Mear M and Rice JR., "Crack Paralleling an Interface Between Dissimilar Materials.", J Appl Mech, Vol. 54, pp. 828-832, 1987

[10]   Rice JR., "Elastic fracture mechanics concepts for interfacial cracks." J A. M, Vol. 55, pp.98-103,1988

[11]   Shih CF and Asaro RJ., "Elastic-plastic analysis of cracks on bimaterial interfaces: Part I—small scale yielding." J Appl Mech, Vol. 55, pp. 299-316, 1988

[12]   Wang TC., "Higher-order analysis of near-tip fields around an interfacial crack between two dissimilar power-law hardening materials" Engng Fract Mech, Vol. 37, pp. 525-538, 1990

[13]   JW., "Plastic stress and strain fields at a crack tip", J Mech Phys Solids, Vol 16, pp. 13-31, 1968

[14]   Shih CF, Asaro RJ., "Elastic plastic analysis of cracks on bimaterial interfaces: Part II -Structure of small-scale yielding fields.", J Appl Mech, Vol. 56, pp. 763-779, 1989

[15]   Shih CF, Asaro RJ, O'Dowd NP., "Elastic-plastic analysis of cracks on bimaterial interfaces: Part llI—large-scale yielding." J Appl Mech, Vol. 58, pp. 450-463, 1991

[16]   Shih CF, Asaro RJ., "Elastic-plastic and asymptotic fields of interface cracks." Int J Fract, Vol. 42, pp. 101-116, 1990

[17]   Aravas N, Sharma SM., "An elastoplastic analysis of the interface crack with contact zone." J Mech Phys Solids, Vol. 39, pp. 311-344, 1991

[18]   Shih CF., "Cracks on bimaterial interfaces: elasticity and plasticity aspects." Mater. Sci Engng, Vol. A 143, pp. 77-90, 1991

[19]   Shih CF., "Small scale yielding analysis of mixed mode plane strain crack problems." Fracture analysis. ASTM STP, 560, pp. 187-210, 1974

Ceramics in Bangladesh: Its Recent Evolution and Future Prospect

M. A. A. Mahmood[1*], M. S. Rahman[1], Tasmia Zaman[1]

[1]Department of Glass and Ceramic Engineering, Rajshahi University of Engineering & Technology, Rajshahi-6204, Bangladesh

Corresponding author: abdullah2038@yahoo.com

Abstract

In recent years ceramic industries in Bangladesh has grown up in a large extent. It is playing a great role on Country's export earnings. This paper discusses the factors affecting this revolution and reflects on likely future developments. In the domestic market as well as in the comparative international market Bangladeshi suppliers are making a remarkable business. Especially in the international market, high quality ceramic and porcelain wares, such as dinner sets, tea and coffee sets, has created a great impression. This market is spreading rapidly throughout the world. There are some reasons to have this extraordinary achievement in the field of Glass and Ceramics in Bangladesh. Those factors have been described here in comparison with some other related areas. The current revolution of this sector and its impact on the country's economy together with future prospect has also been explicated in this research.

Keywords: Ceramics, glass, export earnings, constraints.

1. Introduction

The term Ceramics was originally used for pottery and earthenware collectively. Today, it comprises a much wider range of materials, including metallic oxides, nitrides and carbides. These materials are used in application areas ranging from household items (porcelain, sanitary wares, and art wares) to high-performance tools for industrial use (ball bearings, cutting tools, isolators, catalysts). In addition to their great hardness, ceramics are also resistant to thermal and chemical influences, making them highly suitable for applications where the product is subjected to high mechanical or thermal stress [1]. Ceramics, with their unique properties and diverse applications, hold the potential to revolutionize many industries, including automotive and semiconductors [2].

The Ceramic industries in Bangladesh have continued to expand since 1958 with the establishment of first ceramic industry, Tazma ceramic industries Ltd. The industry grew faster with the booming property business in tiles, tableware, sanitary ware and electrical sector. Growing market demand boosted development of new factories producing high quality ceramic products.

Demand of ceramic products over the world is increasing day by day. As a result new industries of different sizes have been establishing in different areas of Bangladesh to meet the present demand. Government of Bangladesh has taken initiative to establish new factories and educational institutions about Glass and ceramics. This sector is a potential sector for export earnings after garments sector in Bangladesh.

In recent years due to bad economic conditions over world export earnings of ceramic products during 2011-2012 fiscal years faced different difficulties. As a result it decreases a certain amount from the previous fiscal years. Economic specialists thought the Ceramic sector in Bangladesh can turn the country's economy to a way where the hope will be alive to build a developed Bangladesh.

2. Salient features of ceramic industries

Production of ceramics

Ceramic industries have come a long way from its humble beginnings. A total of roughly 50 ceramic manufacturers are operating in Bangladesh today [3] which produce over 40,000 tones of ceramic products a year [4]. Among them Ceramic tableware, sanitary ware, tiles and insulators are especially popular now-a-days. Especially tiles are using as a luxury construction material and its demand is increasing day by day for constructing modern buildings. This sector is increasing over Bangladesh much rapidly than other ceramic sectors.

Ceramic industry took a formal start in this country in 1958 with the establishment of Tajma Ceramic Industries Ltd. at Kabi Nazrul Islam Sarak, Bogra. It is the oldest modern ceramic manufacturing plant in Bangladesh and is also the only ceramic industry located in North Bengal [5]. Milestone development of ceramic industries in Bangladesh can be written as follows:

Table1: Milestones of Development of Ceramic Industries in Bangladesh

1958	Establishment of Tajma Ceramic Industries Ltd. Started with manufacturing porcelain tableware.
1960	The Pakistan Ceramic Industries Ltd established.
1966	The Pakistan Ceramic Industries Ltd started its production. It produced Ceramic products for the domestic market.
1972	The Pakistan Ceramic Industries Ltd was renamed as Peoples Ceramic Industries Ltd
2001	Bangladesh had ten ceramic industry units. Five of them are fairly large and these are Shinepukur Ceramic Industries, Monno Ceramic Industries, Bengal Fine Ceramic Industries, Peoples Ceramic Industries and Standard Ceramic Industries. These companies produce high quality ceramic and porcelain wares.
2013	At present, there are about 50 ceramic industries in Bangladesh producing different types of ceramic products.

Source: Banglapedia – National encyclopedia of Bangladesh [5]

Ceramic products

Different types of ceramic products have been producing over the country for using in different purposes in different areas. Those common types of products with some common examples are shown in the following table [6].

Table2: Ceramic products and its applications

Industry Segment	Common Examples
Structural clay products	Brick, sewer pipe, roofing tile, clay floor and wall tile (i.e., quarry tile), flue linings
Whitewares	Dinnerware, floor and wall tile, sanitary ware, electrical porcelain, decorative ceramics
Refractories	Brick and monolithic products are used in iron and steel, non-ferrous metals, glass, cements, ceramics, energy conversion, petroleum, and chemicals industries
Glasses	Flat glass (windows), container glass (bottles), pressed and blown glass (dinnerware), glass fibers (home insulation), and advanced/specialty glass (optical fibers)

Abrasives	Natural (garnet, diamond, etc.) and synthetic (silicon carbide, diamond, fused alumina, etc.) abrasives are used for grinding, cutting, polishing, lapping, or pressure blasting of materials
Cements	Used to produce concrete roads, bridges, buildings, dams, and the like
Advanced ceramics	
Structural	Wear parts, bioceramics, cutting tools, and engine components
Electrical	Capacitors, insulators, substrates, integrated circuit packages, piezoelectric, magnets and superconductors
Coatings	Engine components, cutting tools, and industrial wear parts

3. Prospect of ceramic industries

Growth of Ceramic Industries

The country's ceramic industry is now in a very good condition as the sector has grown up more than 200 per cent in last 5 years [7]. This sector has some positive advantages including low labor wages compared to other ceramic competitive countries. Traditionally, ceramic industry is a labor-intensive sector and companies in developed countries experience difficulties in remaining competitive due to rising labor cost and recent global financial crisis. Bangladesh, being a gas rich, low-labor cost economy and having advanced 'bone china' technology, is perfectly positioned to be a strategic partner in production and supply of ceramic goods (Board of Investment, Bangladesh).

At present, there are satisfactory number of ceramic industries in Bangladesh and further new industries is being set up. Out of them a few's performance is excellent and they export both porcelain and bone china products to many countries of Europe and America. According to Bangladesh Ceramic-ware Manufacturers' Association (BCMA), this sector is now a market of around four thousand crores taka (1crore=10 million and 1$=85Tk) with as many as 35 thousand people employed. Local industries meet around 80 percent of the country's demand and export around 330 crores of ceramic products per year [8].

At present, there are about 50 glass and ceramic industries in Bangladesh where specialized persons are needed to develop new products and maintain best quality of the products. Some of the major names in this sector are FARR Ceramics, People's Ceramic, Shinepukur, Monno Ceramic, Bengal Fine Ceramic Industries, Standard Ceramic Industries, RAK Ceramics (Bangladesh) Ltd, Fu-Wang Ceramic Industry Ltd, Akij Ceramics Ltd. Etc.

Raw materials

The prime raw materials of ceramic products are white clay and sand. About 95% of raw materials for making quality and exportable ceramic products in Bangladesh are imported from abroad. The materials are imported mainly from China, Japan, Indonesia, Rumania, Germany, New Zealand, South Korea and India. The largest deposit of white clay in Bangladesh was first discovered in 1957 at Bijoypur of Mymenshingh. The total reserve of white clay from this region is estimated to be 2.57 million tons. Clay was also found in jaflong of Sylhet. But there is no clay or sand treatment plant at these places [9].

To ensure proper quality and goodwill of all ceramic products high quality of raw materials is very essential. The machinery and equipment are to be modern and conform to the latest technology and standard. The quality of products also depends on laboratory facility, quality control and testing mechanism. The products that are available in market now are: dinner sets, tea sets, coffee sets, soup sets, fruit sets, plates, bowls, flower vases, mugs and various types of souvenir items. Good quality of raw materials can ensure products of ovenproof, chill-proof, dishwasher-proof and free from any chemical hazards. Thus physical, chemical, mechanical, Electrical, thermal and optical properties can be affected by the quality of raw materials.

Competitiveness

Bangladesh exports different types of products to different countries every year. Among them garment sector export about 75% product [10],[11]. Compare to others sectors ceramic sector earning quite rapidly and it is increasing each year. Due to low labor cost and better quality of products it is attracting by foreigners and thus impacting on countries economy.

Table3: Sector wise export earning of fiscal year 2011-2012

Items	Export (M$)	% of Total Export
Woven garments	9603.34	39.54
Knitwear	9486.39	39.0585
Frozen food	598.42	2.46388
Leather & leather products	330.16	1.35937
Jute & jute goods	1233.66	5.07937
Chemical fertilizer	17.68	0.07279
Ceramics	**33.75**	**0.13896**
Engineering products	515.41	2.12211
Chemical products	130.14	0.53583
Others	2338.71	9.62921
Total	24287.66	100

Source: Export Promotion Bureau (EPB), Bangladesh [12]

Export earning of ceramics in different fiscal years

Bangladesh exports ceramic products to about 50 countries including USA, UK, Italy, Germany, France, Spain, Norway, Sweden, Turkey, Poland, Australia, New Zealand, Canada, Mexico, Brazil and Chile. Industry people said, At least 75 per cent of the total exports of the products go to Europe, about 15 per cent to the US market and remaining 10 per cent to other markets [13].
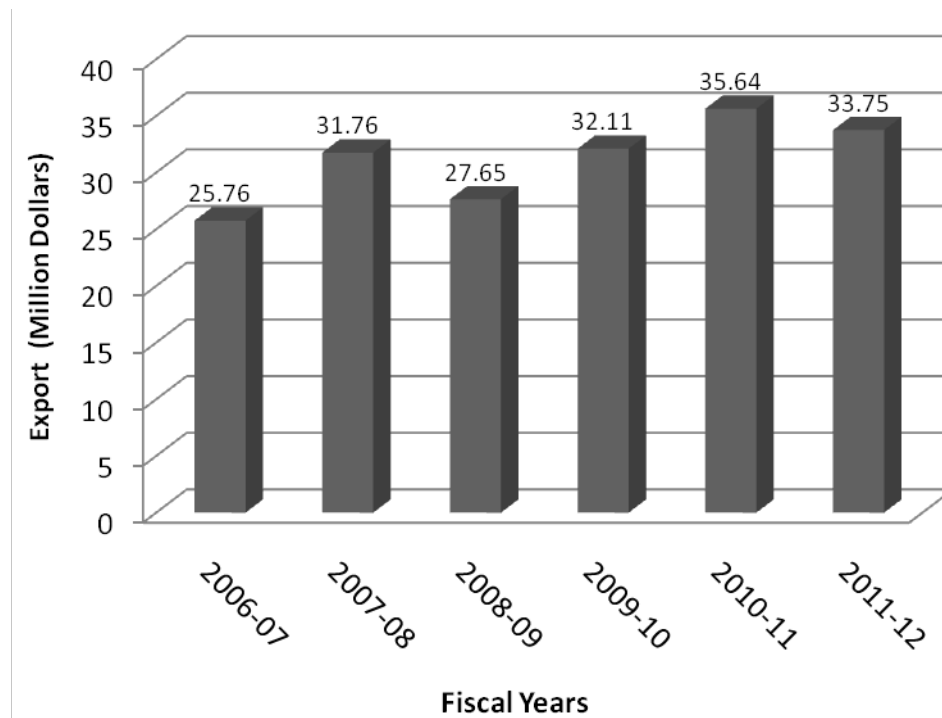
Fig. 1: Direct export of ceramic products in different fiscal years
Source: Export Promotion Bureau, Bangladesh [12].

Ceramics export of Bangladesh witnessed negative growth in the last financial year 2011-12 due to an economic crisis in Europe, the biggest export destination [14].Ceramic exports brought $33.75 million in the financial year

2011-12, down by more than 10 per cent from that of the previous year, according to Export Promotion Bureau (EPB). Earnings from ceramics export stood at $14.62 million during July-November period of this financial year, down by 2.66 per cent from that of the corresponding period of the last financial year. EPB data show ceramics export target was missed by 3.88 per cent in the first five months of the current financial year 2012-13 [15].

3. Constraints

Though ceramic industries in Bangladesh have been increasing rapidly, it has a lot of problems. Followings are the major constraints for developing the ceramic industries:
- Poor/inadequate power supply.
- Tight budget
- Lack of funding organization
- Inadequate motivation for commercialization.
- Instability of government policies
- Inadequate enforcement of intellectual property rights
- Testing facilities for quality control services
- Lack of relevance of the research activities to their needs and difficulty in accessing research funds
- Lack of awareness
- Skilled manpower development
- Technical consultancy services

The following paragraph describes the way forward for avoiding all the constraints to prosper in the ceramic sector.

4. The way forward

The ceramic industry of Bangladesh could become a basic building block for the country's construction and housing sector; however, this sector is already contributing to the country's economic progress through export earnings, foreign currency savings and generating employment. The industry people say this is possible provided the government supports this sector with due diligence. The government has promised to extend all sorts of cooperation to make Bangladesh the hub of ceramic goods production in the world. Bangladesh government has already drawn a policy to prevent the import of low quality ceramic products having health hazard ingredients. To discourage import of tiles and sanitary ware items, supplementary duty on imports has already increased to 45 percent in place of existing 20 percent [16]. Besides, the government has also promised uninterrupted power and gas supply for this sector. Moreover, the certain provisions of the Budget 2009-10, for instance, providing accommodation for all by 2021, would have positive impact on the ceramic industry as well [17],[18]. If the ceramic industry of Bangladesh can overcome the stated limitations, it has every potential to grow and become a big foreign exchange earner for the country with its dazzling products in the era of globalization.

5. Conclusions

Ceramic sector in Bangladesh has opened a new era of producing and exporting ceramic products. This sector has a great potential to earn export money from 50 different countries over the world. The quality of Bangladeshi ceramic products fascinated the international customers. Hence there is a great opportunities to invest in this sector. Government and private sectors are advised to improve the quality of research and development at different research institutions of Ceramic Engineering and Technology through increased funding. Clear policies and strategies to establish link between Research Institutes and Industry in Bangladesh are imperative for technical progress.

6. References

[1] Isiaka Olajide Odewale, Felix Ugah Idu and Victor Tyonenge Amaakaven, "Hindrances and prospects of ceramic technology development in Nigeria", *International Journal of Science Innovations and Discoveries*, Volume 3, Issue 1, January-February 2013.

[2] Retsch, Inc., Successful Analysis Newtown, Retrieved from: http://www.retsch-us.com/. December 15, 2012.

[3] Akhteruzzaman Yusuf, "Ceramics on the Upswing: Exporting Dinnerware", "http://www.bangladesh-business.net/PageDetails.php?Id=124".

[4] Ceramic Industry in Bangladesh, Retrieved from "http://www.studymode.com/join.php?join_type=upgrade"

[5] Zakir Hossain Bhuiyan, "Bangladesh Ceramic History", Banglapedia – National encyclopedia of Bangladesh, Retrieved from: http://www.bpedia.org/C_0071.php

[6] W.D. Kingery. *Ceramic fabrication processes*, (Technology Press of Massachusetts Institute of Technology, 1959).

[7] HT Syndication, "Ceramic Industry in Bangladesh", the Financial Express, Aug 28, 2012.

[8] AB Quddus, "Career in Glass and Ceramics Engineering", Retrieved from: http://www.eduinfo24.com/career-in-glass-and-ceramics-engineering/

[9] History of ceramics, Retrieved from: "http://ace-bd.com/wp-login.php?redirect_to=http%3A%2F%2Face-bd.com%2Fknowledge%2Fhistory-of-ceramic%2F".

[10] Musauid, "Investment Opportunity – Major Sectors in Bangladesh", June 14, 2007.

[11] M. Serajul Islam, "PROSPECTS AND CHALLENGES OF PLASTIC INDUSTRIES IN BANGLADESH", Journal of Chemical Engineering, IEB,Vol. ChE. 26, No. 1, December 2011

[12] Export Promotion Bureau. Retrieved from: http://www.epb.gov.bd/

[13] Shah Alam Nur, "Ceramic exports income falls 10pc", Trade and Market, The Financial Express, July 15, 2012.

[14] Sajjadur Rahman, "Ceramic exports on the wane", the daily star, September 25, 2011.

[15] Shah Alam Nur, "Ceramic goods exporters in search of new markets", Trade and Market, the Financial Express, 31 December 2012.

[16] Nusrat Jahan, "Ceramic Industry of Bangladesh: A Perspective from Porter's Five Forces Model", *Journal of Business and Technology,* Volume– V, Issue– 02, July-December, 2010.

[17] Hossain, S. 2009, August 3. "Ceramic Ware Exporters Aim Sturdy Business". Daily New Age, Dhaka.

[18] Islam, M. S.2010, April 16. "Ceramic Importers Turn Manufacturers", the Independent.

Effects of Internal Resistance on the photovoltaic parameters of Solar Cells

Robin Khan, and M.F.Hossain[*]

Department of Electrical and Electronic Engineering, Rajshahi University of Engineering & Technology,
Rajshahi-6204, Bangladesh.
E-mail: [*]faruk94_ruet@yahoo.com

Abstract

Solar cells are promising devices for clean electric generation and have attracted intensive research. Like all other electrical power generators, solar cells possess internal series resistance(Rs) which affects significantly their power conversion efficiency(PCE). Moreover the simulation and design of solar cell systems also require an accurate knowledge of the series resistance and extracting the series resistance(Rs) , shunt resistance(Rsh) for solar cells is therefore of vital importance. Rs effects on the efficiency, I_{SC}, fill factor(FF).The internal series resistance(Rs) in the equivalent circuit model of the solar cell causes output voltage to reduce as the output current to increase and the shunt resistance(Rsh) causes internal power losses by diverting some of the created current away from the output path. With the aim of increasing conversion efficiencies the series internal resistance (Rs) is 0 ohm(short circuit) and shunt resistance(Rsh) of infinity(open circuit).This paper describes the optimized series& shunt resistance by matlab simulation.

Keywords: *Photovoltaic cell, Solar cell model, Matlab simulation, Fill factor, Maximum power point.*

1. Introduction

The research for the renewable energy has become an important topic in the 21st century with the problem of energy crisis becoming more and more aggravated, resulting in increased exploitation and search for new energy resources such as wind, water, geothermal, and solar energy around the world [1]. Due to its inexhaustible and environmentally friendly energy, the research in solar energy has become an increasingly important topic in recent years [2]. Photovoltaic (PV) Solar Cells have been used for many decades. Today, with the focus on greener sources of power, Solar cell has become an important source of power for a wide range of applications. Besides assisting in the reduction of the emission of greenhouse gases, they add the much- needed flexibility to the energy resource mix by decreasing the dependence on fossil fuels. Photovoltaic (PV) generation has many advantages such as cleanness maintenance-free, inexhaustible and noiselessness [3].

An accurate knowledge of solar cell parameters from experimental data is of vital importance for the design of solar cells and for the estimates of their performance. Thus, different solar cell models have been developing to describe their electrical behavior, but the electrical equivalent circuit is a convenient and common way in most simulation studies. The five parameters of interest in the equivalent circuit are the photo-current (I_{PV}), series resistance (R_S), diode saturation current (I_0), parallel resistance (R_{SH}) and the ideality factor (A). The current-voltage relationship of a solar cell is described by a mathematical equation that is both implicit and nonlinear, therefore; the evaluation of these parameters has been the subject of investigation of several authors. While some authors use numerical analysis methods to solve the implicit nonlinear equation of I-V relation [4-6], others use analytical methods with a series of simplifications and approximations [7-9].

In this work, we elaborate a MATLAB script file program, which uses to compute the five parameters of the single diode model of illuminated solar cells. The results obtained by simulation show the effect of internal resistances on the photovoltaic performances has been investigated and discussed. The consistency between the data and obtained the parameters given by the manufacturer, namely: short circuit current (I_{SC}), open circuit voltage (V_{OC}) and maximum power point (P_{mpp}).
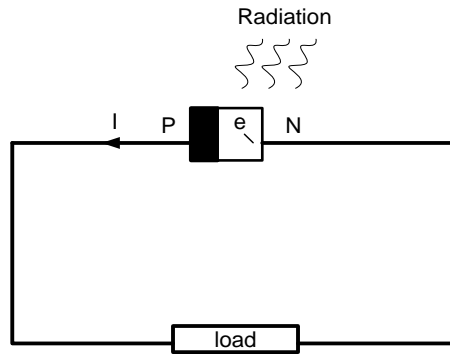
Fig. 1: Photocurrent generation principle.

2. Solar Cell Model

Figure 1 shows the p-n junction solar cells with photocurrent generation. Solar cells consist of a p-n junction fabricated in a thin wafer or layer of semiconductor (usually silicon) [2].

A solar cell is the building block of a solar panel. A photovoltaic module is formed by connecting many solar cells in series and parallel [2, 10]. Considering only a single solar cell; it can be modeled by utilizing a current source, a diode and two resistors. This model is known as a single diode model of solar cell [2,3,10]. Two diode models are also available but only single diode model is considered here in Fig. 2. It includes a current source, diode, a series resistance and a shunt resistance [5, 6].
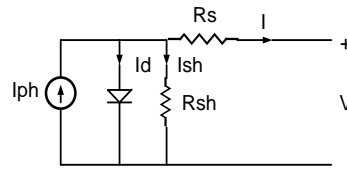
Fig. 2: solar cell equivalent circuit.

In view of that current to the load can be given as:

$$I = I_{ph} - I_o\left(\exp\left(\frac{q(V + IR_s)}{kT}\right) - 1\right) - \frac{V + IR_s}{R_{sh}} \qquad (1)$$

In this equation, Iph is the Photo current, Io is the reverse saturation current of the diode, k is the Boltzmann constant, T is junction temperature, N is the ideality factor of the diode, q is the electron charge, v is the voltage across the diode, R_s & R_{sh} series and shunt resistance of the cell respectively. Based on the eq. (1) the I-V & P-V curves of the solar cell are obtained by matlab simulation.

3. Shunt Resistance Effect

The shunt resistance of any PV cell should be large enough for higher output power and fill factor. In fact, for a low shunt resistor, the PV cell current collapses more, higher power loss and lower fill factor, from eq. (2) it is shown by matlab simulation as varying shunt resistance [11, 12].

$$I = I_{ph} - I_o\left(\exp\left(\frac{q(V)}{nkT}\right) - 1\right) - \frac{V}{R_{sh}} \qquad (2)$$
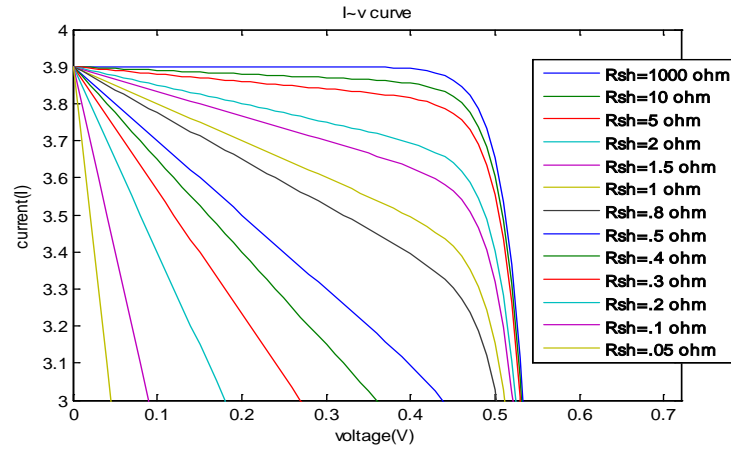
Fig. 3: I-V curves of at varying R_{sh}.
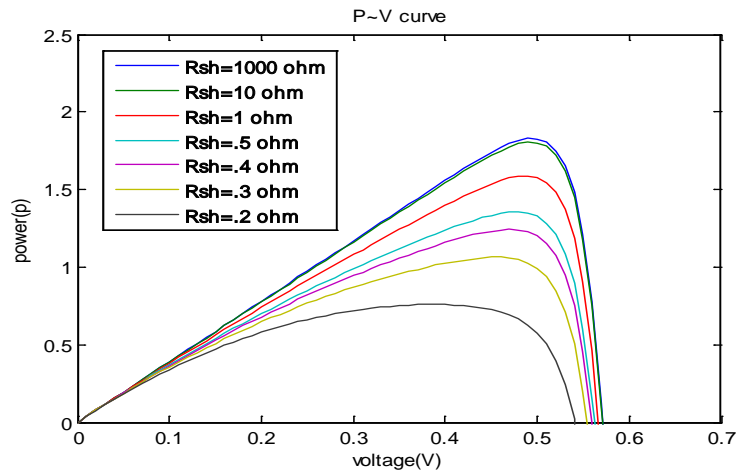
Fig. 4: P-V curves of at varying R_{sh}.

From Fig. 3 & Fig. 4 it is decided that the optimized shunt resistance is 1000 ohm for the solar cells.

4. Series Resistance Effect

With the increasing of the series resistance collapses the PV cell voltage, causes the higher power loss, lower fill factor and the cell efficiency. From the eq. (1) it is shown [10] that with the increasing the series resistance the above parameters are decreasing which is obtained in Fig. 5.

$$V = IR_s + \frac{kT}{q} log \frac{I+I_0+I_L}{I_0} \tag{3}$$
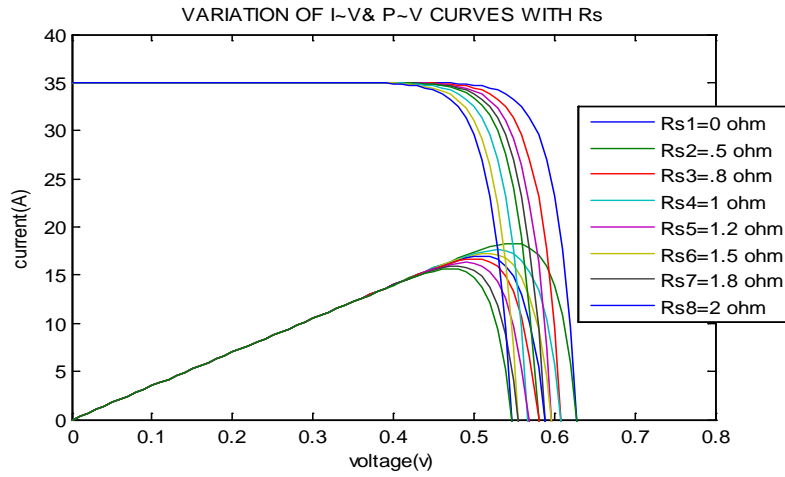
Fig. 5: I-V&P-V curves at varying Rs.

From the eq. (3) by varying load current I we can be obtained the I-V&P-V curves of solar cells at varying series resistance.
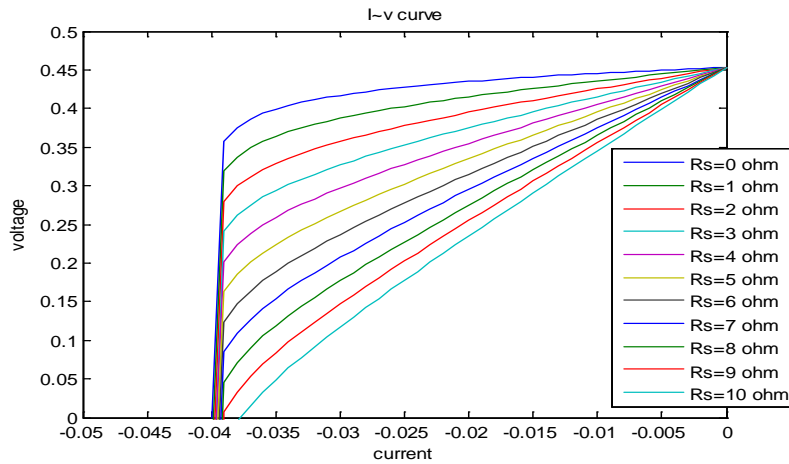
Fig. 6: V-I curves of at varying Rs.
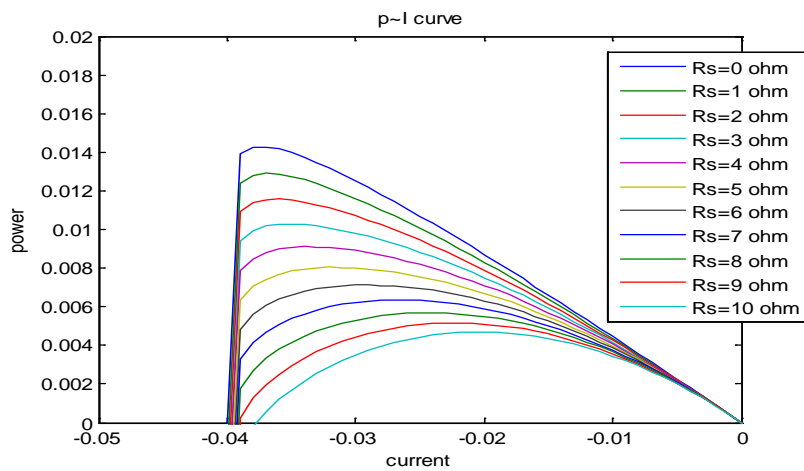
Fig. 7: V-P curves of at varying Rs.

From the Fig. 6, 7, and 8 the optimized series resistance is 1milli ohm by matlab simulation.

5. Coincide Optimized R_s & R_{sh}
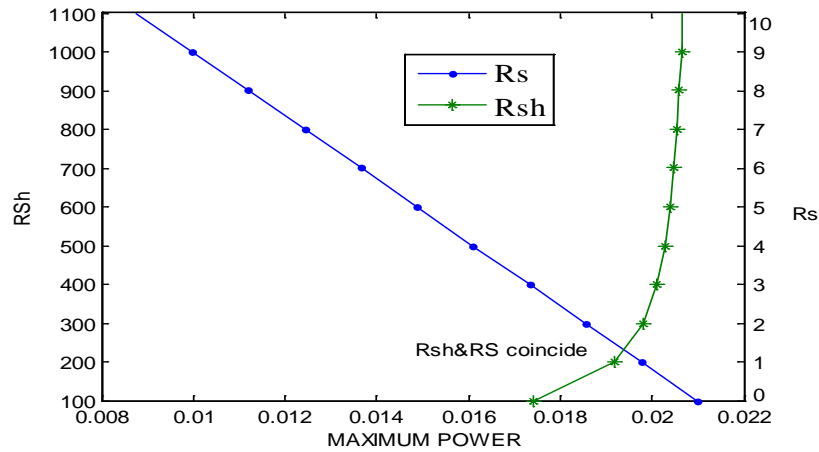
Fig. 8: optimized resistance at varied Pmax.
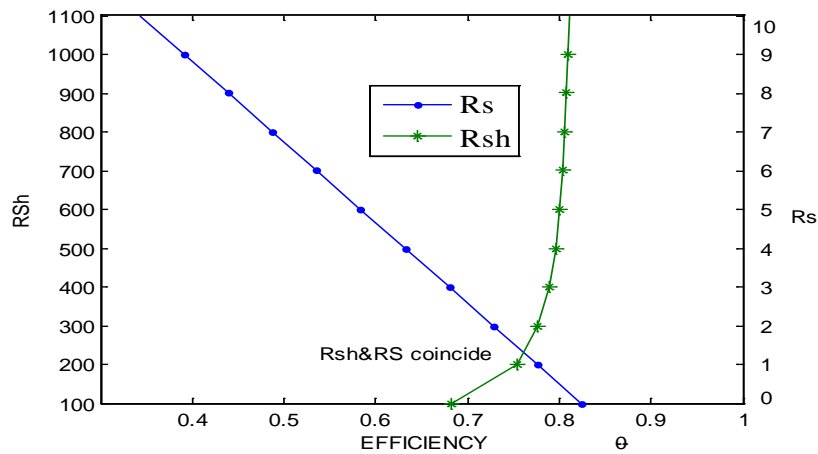
Fig. 9: optimized resistance at varied efficiency.
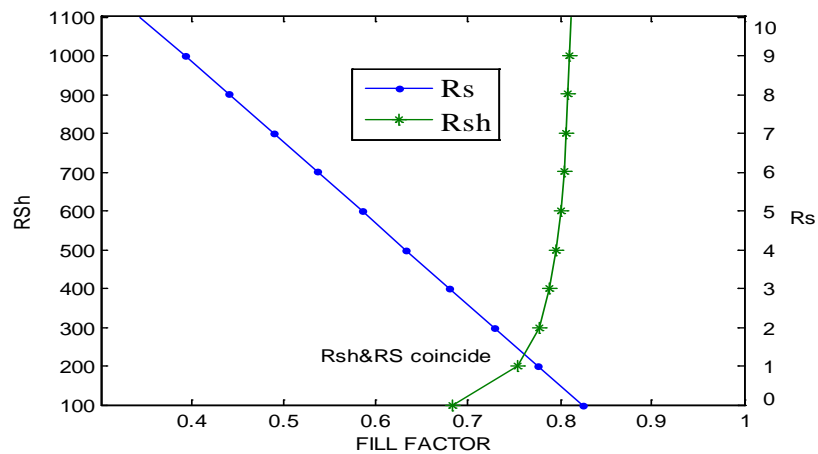
Fig. 10: Optimized resistance at varied fill factor.

From the Fig. 8,9,10 it is shown that with the increasing of series resistance fill factor, maximum power, efficiency decreases and with the increasing of shunt resistance those parameters increases and the optimized

coincide series and shunt resistance is R_S=1.2 ohm& R_{sh}=240 ohm. Then optimized curves for the solar cell is obtained by matlab simulation.
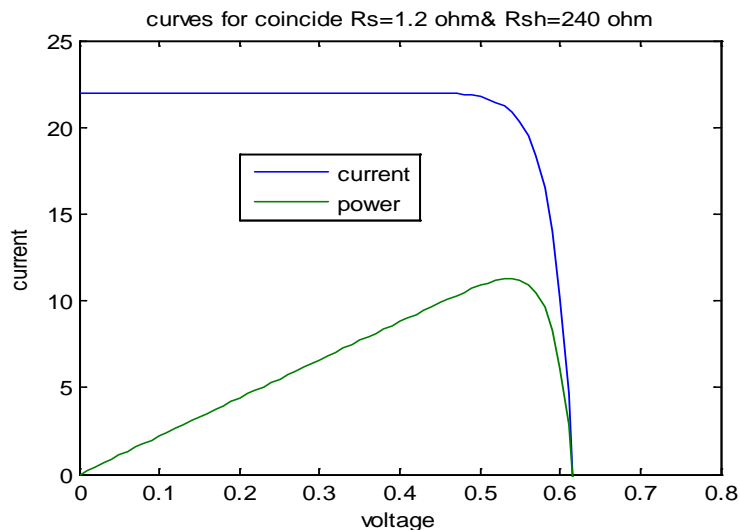
Fig11: I-V&P-V curves for optimized solar cell.

6. Conclusion

The effects of internal resistance of PV cells were investigated by using Matlab simulation program. The simulation of ideal photovoltaic solar cell shows how it is possible to increase the efficiency of solar cell in theory and electrical load will affect the performance of solar cell. It also shows how internal design of solar cell can affect the efficiency of solar cell, such as the internal series resistance& shunt resistance. To experimental characterization of the PV cells is a time consuming and costly task, so to overcome this problem Matlab simulation techniques are used to simulate the behavior of PV cells under different conditions. The fill factor mainly decreases with the value of series and shunt resistances, which in turns reduces the efficiency of PV cells. So the performance of PV cells is maximized by optimizing the value of series and shunt resistances. The optimized value of series and shunt resistances are 1.2 and 240 ohm, respectively.

7. References

[1] Vandana Khanna, Bijoy Kishore Das, Dinesh Bisht ,''MATLAB/SIMELECTRONICS Models Based Study of Solar Cells'', *Journal,* Vol.3, No.1, 2013.
[2] Vijay Garg, Sandeep Saini, "Simulation of Photovoltaic Cell Using Matlab*", The International Journal Of Engineering And Science (IJES)*, Vol. 2, No. 7, pp. 39-42, 2013.
[3] N. Belhaouas, M.S. Ait Cheikh, A. Malek, and C. Larbes, "Matlab-Simulink of photovoltaic system based on a two-diode model simulator with shaded solar cells" *Revue des Energies Renouvelables,*Vol. 16, No. 1, pp. 65-73, 2013.
[4] B.BA and M.KANE, "Determination of polysilicon solar cell parameters using electrical short-circuit current Decay method", *Solid-State Electronics*, Vol. 42, N0. 4, pp. 541-545, 1998.
[5] L.Sandrolini, M.Artioli,U.Reggiani, "Numerical method for the extraction of photovoltaic module double-diode model parameters through cluster analysis", *Applied Energy*, Vol. 87, pp. 442-451, 2010,
[6] Kashif Ishaque, Zainal Salam, Saad Mkhilef, Amir Shamsudin "Parameter extraction of solar photovoltaic modules using penalty-based differential evolution", *Applied Energy*, Vol. 99, pp. 297-308, 2012.
[7] Amit Jain, Avinashi Kapoor "Exact analytical solution of the parameters of real solar cells‖ using Lambert W-fonction" *Solar Energy Materials & Solar cells,* Vol. 81, pp. 269-277, 2004.
[8] T. Easwarakhanthan, J. Bottin, I. Bouhouch, C.Boutrit, "Nonlinear minimization algorithm for determining the solar cell parameters with microcomputers", *Int. J. Solar Eng*, Vol. 4, pp. 1–12, 1986.
[9] Z. Ouennoughi, M. Chegaar, "A simple method for extracting solar cell parameters using the conductance method", *Solid State Electron*, Vol. 43, No. 11, pp. 1985–8, 1999.

[10] Dominique Bonkoungou, Zacharie Koalaga, Donatien Njomo, "Modelling and Simulation of photovoltaic module considering single diode equivalent circuit model in MATLAB", *International Journal of Emerging Technology and Advanced Engineering*, Vol. 3, No. 3, pp. 494-502, 2013.

[11] Jeyraj Selvaraj, Nasrudin A. Rahim,, "Multilevel Inverter For Grid-Connected PV System Employing Digital PI Controller", *Industrial Electronics, IEEE,* vol. 56, No. 1, pp. 149-158 , 2009.

[12] Tarak Salmi, Mounir Bouzguenda, Adel Gastli, Ahmed Masmoudi, "MATLAB/Simulink Based Modelling of Solar Photovoltaic Cell", *International Journal of Renewable Energy Research, Vol.* 2, No. 2, pp. 213-218, 2012.

APPENDIX

Table 1. Solar cells parameters

NAME	SYMBOL	VALUE	UNIT
Reverse saturation	I_o	1×10^{-9}	A
Electronic charge	q	1.6×10^{-19}	C
Series resistance	R_s	.001	Ω
Boltzmann constant	K	1.3×10^{-23}	J/K
Photo current	I_{ph}	4	A
Shunt resistance	R_{sh}	1000	Ω
Temperature	T	300	K
Voltage	v	0:0.01:0.6	volt

Table 2. Variation of FF & P_{max} with Rs

SERIS RESISTANCE	MAXIMUM POWER	FILL FACTOR
0 ohm	0.021	0.8274
1 ohm	0.0198	0.775
2 ohm	0.0186	0.7237
3 ohm	0.01733	0.6738
4 ohm	0.0161	0.6251
5 ohm	0.0149	0.5777
6 ohm	0.0137	0.5315
7 ohm	0.0124	0.4867
8 ohm	0.0112	0.443
9 ohm	0.00998	0.4006
10ohm	0.00875	0.3595

Table 3. Variation of FF & P_{max} with Rs

SHUNT RESISTANCE	MAXIMUM POWER	FILL FACTOR
100 ohm	0.0174	0.7065
200 ohm	0.0192	0.7669
300 ohm	0.0198	0.7871
400 ohm	0.020	0.7972
500 ohm	0.0203	0.8032
600 ohm	0.0204	0.8072
700 ohm	0.0205	0.8101
800 ohm	0.02055	0.8123
900 ohm	0.0206	0.814
1000 ohm	0.02064	0.8153
1100 ohm	0.02069	0.824

Paper ID: MS-44

Implimentation of Computer-controlled Electrodeposition methodology for Depositing Metal Oxide Thin Films

Md. Hasibul Islam, Md. Faruk Hossain*, Shuva Paul, Mohua Fardousi
Department of Electrical and Electronic Engineering, Rajshahi University of Engineering & Technology,
Rajshahi-6204, Bangladesh.
*E-mail: faruk94_ruet@yahoo.com

Abstract

Metal-oxide thin films (ZnO, TiO_2 and other so on) have received considerable interest from scientists due to their remarkable performance in electronics, optics and photonics. In this study we have reported a way of fabricating films applying different conditions in a computerized way where PC has been interfaced with Keithley 2400 Source Measure Unit (SMU) with Lab-view software and controls the electrodeposition mechanism either in a voltage or current controlled way. The potential difference between the electrodes, current flow and resistivity of the electrolyte, duration of deposition of molecule on the substrate and their corresponding features as well as curves (I-V, R-V and I-T) become visible in the computer monitor using 'LabVIEW' software. Additionally, we fabricated ZnO films on Fluorine Doped Tin Oxide (FTO, SnO_2:F) substrate from an electrolyte of metallic-salt [$Zn(NO_3)_2$]. Almost precise potential difference of 0.718V (DC) was provided by Keithley 2400 Source Measure Unit between the working electrode and counter electrode of a zinc nitrate electrolyte [0.5M of $Zn(NO_3)_2$ solution; 0.0125:1.375 = zinc nitrate : water (molar weight)] resulting in a smooth deposition of metallic oxide on FTO substrate. I-V, R-V and I-T curves have been analyzed to prove the already built ZnO formation mechanism. Both the as-deposited and annealed films stance with semi-conductive behavior where a marginal differences in resistivity exist between this two.

Keywords: *Electrodeposition, KEITHELY source measure unit, LabVIEW, FTO, ITO, Coating.*

1. Introduction

At present century huge population, advanced industrialization, rising number of hunger demands immense power to meet those challenges around the world. In the 20th century, people developed so many techniques and methods for producing and distributing power from solar system, but most of these methods were costly as well as inefficient and beyond the reach of common people. To make those things better and cost effective people developed so many ideas, application of thin films on solar cell is one of them, it not only increase efficiency of solar cell but make it cost effective and versatile for applying different purposes [1].

Today electrodeposition method has been received a great attention due to its fidelity for fabricating high standard nano-structured thin-films of different metal oxides such as ZnO [2-5], Cu_2O [6-8], TiO2 [9] and other so on. Electrodeposition technique [10] has the following advantages (I) thickness and morphology of films can be precisely controlled by adjusting electrochemical parameters such as current or potential, (II) uniform and compact thin-films can be synthesized either on substrates of complex shapes or in column shaped material, (III) higher deposition rates can be easily obtained over conventional processing. Since deposition on substrate takes place at the rate of current flowing through the circuit and potential applied to the electrodes, this method facilitates both the current controlled and voltage controlled deposition on the substrate, which is accomplished by "2400 KEITHLEY Source Measure unit" without resulting any heat.

ZnO is an n-type semiconductor with a band gap of 3.37 eV and transparent metal oxide. It can be applied in ultraviolet-emitting diodes, piezoelectric devices, electron-field emitters, heterogeneous catalyst for methanol synthesis and short wavelength electro-optical devices [11].

ZnO thin-films was successfully fabricated on different conducting substrates [10, 12-14], in this work, we will explain the computerized electrodeposition methodology in detail and the formation mechanism of zinc oxide [10, 15-17] on FTO substrate utilizing the V-T, R-V, I-T and I-V characteristics.

2. Electrodeposition Set-up

It namely comprises of three parts (fig. 1.): (A) Computerized Controlling Unit, (B) "2400 KEITHLEY source measure unit" and (C) Direct deposition unit.

A. Computerized controlling unit

The following are the supported operating system for PC to drive the basic operation of required software:
  i.   Windows XP Professional service pack 1 or later
  ii. Windows 2000 Service pack 3 or later
  iii. Windows NT Service pack 6a or later
  iv. Windows 98 Second edition only
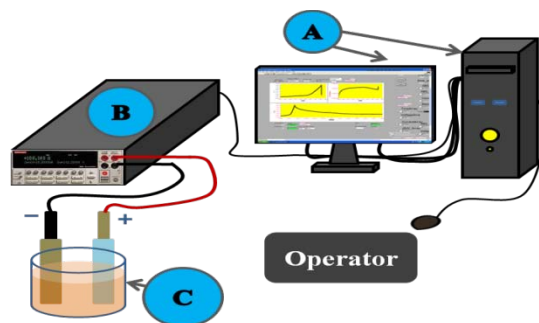
Fig. 1. Visualization of Electrodeposition set-up, (A) Computerized controlling unit, (B) "2400 KEITHLEY source measure unit", (C) Direct Deposition Unit

This unit requires some software and instrument drivers to install for driving the instrument (KEITHLEY) through a automatic controlling process in a computerized way. The required softwares are:
a. GPIB Controller Installation:
  To communicate with instrument using GPIB, it needs to install compatible GPIB controller card and associated software drivers in the computer before installing Instrument Drivers. The driver is compatible with the following GPIB controller cards: Keithley Instruments GPIB cards (ISA, PCI, PCMCIA), CEC GPIB cards (ISA, PCI), National Instruments GPIB cards (ISA, PCI, PCMCIA) and INES GPIB cards (PCMCIA)
b. KEITHLEY and INES PCMCIA Controller Installation:
  In the case of installing 'INES' driver software we did not install the HP I/O libraries but we selected NI compatibility mode. When installing the INES driver software, if the hardware test fails, it is recommended to change the Interrupt selection to none.
c. Instrument Driver Installation:
  There are some other essential drivers in KEITHLEY those were installed correctly.

Use of LabVIEW:

After installing all the drivers LabVIEW was installed. We used LabVIEW to provide input function to the instrument and to illustrate the output mechanism graphically in the computer monitor. The LabVIEW is well suited to "2400 KEITHLEY source measure unit" device. Moreover, to explain the mechanistic origin of deposited material it facilitates I-V, R-V, I-T curves of the direct deposition unit, additionally LabVIEW accommodates Offset voltage, Voltage step, Timer action and current offset for precise and accurate application of current and voltage to the working stage. The step wise data of different parameters (voltage, current and resistance) are stored in the specified directory as text when operator presses the end switch.

B. 2400 KEITHLEY source measure unit:

Keithley's Series 2400 Source Measure Unit (SMU) Instruments are designed specifically for test applications that demand tightly coupled sourcing and measurement. All Source Meter models provide precision voltage and current sourcing as well as measurement capabilities. Each Source Meter SMU instrument is both a highly stable DC power source and a true instrument-grade 6½-digit multimeter. The power source characteristics include low noise, precision, and readback. The multimeter capabilities include high repeatability and low noise. The result is a compact, single-channel, DC parametric tester. In operation, these instruments can act as a voltage source, a current source, a voltage meter, a current meter, and an ohmmeter.

C. Direct Deposition Unit:
It is mainly demanded by two basic parts the first one is electrolyte, second one is Electrodes. Electrolyte depends on what material is going to be deposited on substrate. Electrodes are of three types (i) working electrode, (ii) counter electrode and (iii) reference electrode. Normally deposition takes place on working electrode. Conventionally reference electrode is used in the purpose of fixing the voltage and current precisely, as we have employed "2400 KEITHLEY source measure unit" so it is optional in our study. There are two types of deposition one is cathodic deposition and another is anodic deposition, depending on the deposition process the substrates are specified to the electrodes. In our study we maintained a cathodic deposition.

3. Experimental Detail

ZnO was electrochemically deposited on FTO substrate. Prior to experiments, firstly the FTO quartz crystal has ultrasonically been cleaned with 99% ethanol solution for 15 minutes in order to remove organic residue and then ultrasonically cleaned with distilled water for 5 minutes, finally it has been rinsed thoroughly with distilled water and dried using air compressor for three minutes. Beakers have been cleaned with 75% nitric acid (HNO_3), then with 95% ethanol and then thoroughly cleaned with distilled water.

To maintain the same concentration of solution zinc sheet has been used as counter electrode to provide Zn^{++} ion in the solution. FTO has been arranged as working electrode on which deposition takes place and both the electrodes are placed 1.5cm apart in the solution. 0.5M solution of $Zn(NO_3)_2$ has been prepared with ultra-pure water and stirred for 15 minutes, the whole experiment has done in room temperature.

Electrodeposition has been executed at constant potential of 0.72V using 2400 KEITHLEY source measure unit for 10 minutes, the current-voltage characteristic of the solution has been measured in a computerized way using LabVIEW and all the data have been stored as text for further analysis of the experiment. I-V, R-V, V-T and I-T curves founded in the experiment have been analyzed for understanding the formation mechanism of ZnO on FTO substrate.

4. Result and Discussion

Current vs Voltage(I-V), Current vs Time(I-T) and Resistance vs Voltage(R-V) curves commence to be visible on the computer monitor when completing whole circuit a direct commend via labVIEW is provided to start. It works in two ways (i) Sourcing Unit and (ii) Measuring Unit.

In Sourcing Unit the decimal input of voltage/current is suitably converted into binary format so that this signal becomes compatible to GPIB driver. GPIB driver compatible for both instrument as well as PC works to communicate between them. GPIB driver conveys those signals to KEITHLEY 2400 to develop a voltage/current source of prescribed amplitude. The block diagram is shown below (fig. 2.):
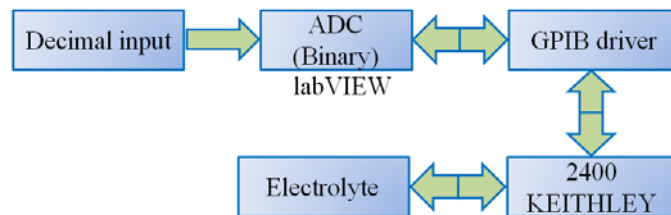
Fig. 2. Block diagram of Sourcing Unit.

In sourcing unit labVIEW stores the fixed magnitude of input value by letting it expands comparing with instrument output from zero, when instrument output acquires the prescribed value as input it continues running towards definite time keeping all the magnitude of compared inputs stored.

In measuring unit KEITHLEY 2400 measures the time varying impedance between output ports as well as current through loads along with supplying as a sourcing unit (voltage), when it works as a current source, it measures impedance and potential difference.
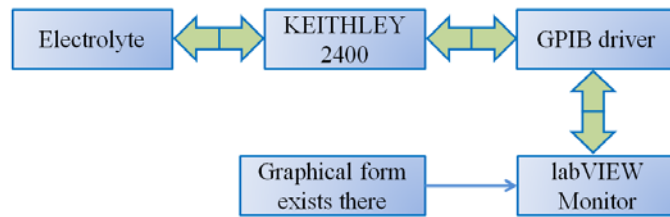
Fig. 3. Block diagram of Measuring Unit.

Current through two electrodes (two output ports of instru-ment) and impedance between two electrodes are measured and measuring data are sent to the labVIEW monitor via GPIB driver by KEITHLEY 2400 (fig. 3.). Subsequently data storing and portraying functions take place in LabVIEW section.

$$NO_3^- + H_2O + 2e^- \rightarrow NO_2^- + 2OH^-, \text{---------------------} (1)$$
$$O_2 + 2H_2O + 4e^- \rightarrow 4OH^-, \text{-----------------------------} (2)$$
$$Zn^{2+} + OH^- \rightarrow Zn(OH)^+ /FTO, \text{--------------------------}(3)$$
$$Zn(OH)^+/ITO + OH^- \rightarrow ZnO/FTO + H_2O, \text{--------------}(4)$$
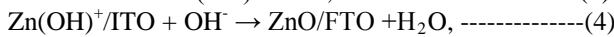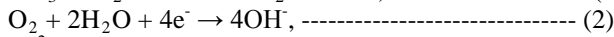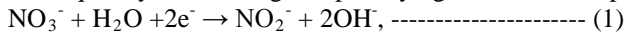
These conventional equations reveal how ZnO gets deposited on a substrate. At the beginning the nitrate ions, water travelling around cathode and electron from cathode come close together to form nitrous ion and hydroxyl ion (eq-1), if the solution is oxygen saturated then travelling oxygen, water and electron from cathode form additional hydroxyl ions (eq-2) relentlessly in the solution and increase pH of the solution as well as cathode (FTO). Proportion to the number of electrons get released for producing hydroxyl ions, Zn^{2+} ions get rid of Zn sheet located at anode and affiliate to the existing hydroxyl ions in the solution to form zinc hydroxide ion $[Zn(OH)^+]$ (eq-3). Finally, positively charged zinc hydroxide [Zn(OH)+] ions attract to the negatively charged cathode where hydroxyl ions exist due to higher pH of substrate, then according to eq-4, ZnO is formed with different structure on the substrate (FTO) and H_2O release in the solution, this process repeats cyclically. When ZnO grows on the substrate it increases the resistance of the substrate that limits the flow of current in the solution so after a certain period the growth of zinc oxide as well as flow of current reduces by a margin. So we can conclude that the in spite of constant potential due to semiconducting properties of ZnO, current as well as growth of ZnO get hampered by a margin with the passage of time. Now we will elaborate and explain the formation procedure utilizing the data that we had found during electrodeposition using our proposed set-up.
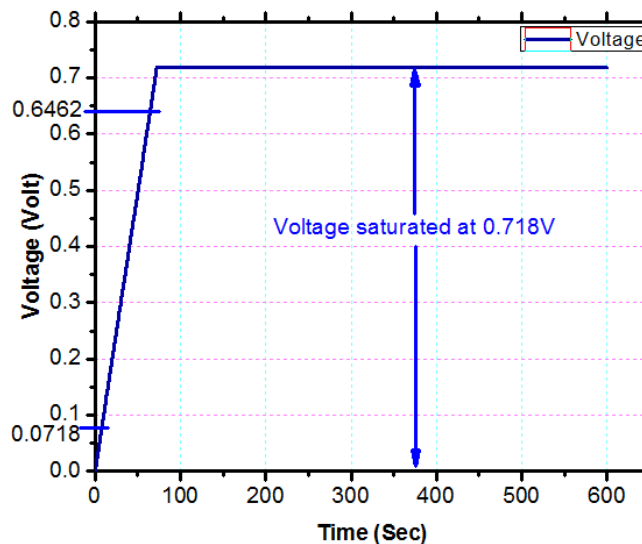
Fig. 4. Voltage versus Time curves.
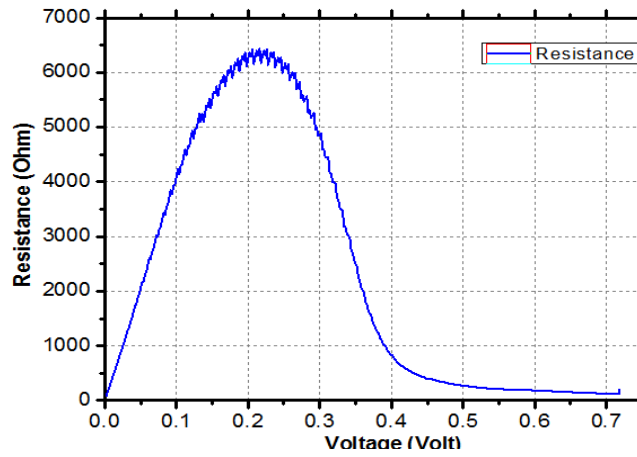
Fig. 5. Resistance versus Voltage curve
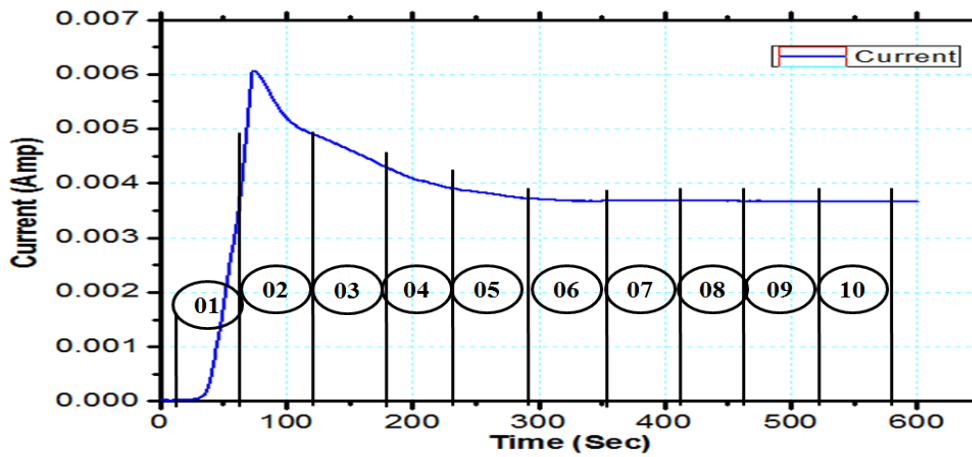
Fig. 6. Current versus Time curve
(the ten separate regions indicates ten speculated steps of deposition).

Fig. 7. Current vs Voltage curves

During the starting of rising time (fig. 4.), there exists lower affinity between the ions due to low potential (0.0712 V) between the electrodes that results higher resistance ultimately very lower current through the

circuit, in this period some Zn^{++} ions directly deposits on FTO as Zn and some $Zn(OH)^+$ on FTO to form ZnO adhesively, this happened because at initial state electrolyte lacks of OH^- to form $Zn(OH)^+$, so deposition rate on the electrode (cathode:-FTO) is very low (fig. 6: 0 to 50 seconds). Here one thing needs to be remember if all the deposited materials were purely conductive that is metal (Zn, conductivity of metal and FTO are very same), conductivity would be increased with the increase in the number of ions in the electrolyte, but thorough observation of fig. 5, fig. 6 and fig. 7. does not satisfy that possibility could be happened. In that case, current was crucially bounded by a straight line falling down slowly after achieving the rated voltage (CD portion in fig. 7.).

So with the increase in potential difference between electrodes more ions (NO_2^- & OH-) form in the electrolyte (according to equation 01), so current increases along with deposition rate. Increasing hydroxyl ions (OH^-) in the electrolyte affiliate the revealed Zn^{2+} to form $Zn(OH)^+$ consequently ZnO on FTO.

The rising time of voltage is 57.8 seconds (fig. 4, from 7.212 seconds to 65.012 seconds), we consider this interval as resolution and analyze the whole experiment depending upon the number of electrons flowed in between these one resolution each times. The whole time period of experiment divides into 10 separate steps, during first step (rising) (from 7.212 seconds to 65.012 seconds), second step (65.212 seconds to 122.411 sec), third step (122.612 sec to 180.012 seconds), fourth step (180.21 sec to 237.612 seconds), fifth step (237.812 sec to 295.212 sec), sixth step (295.212 sec to 352.411 sec), seventh step (352.611 sec to 410.012 sec), eighth step (410.212 sec to 467.411 sec), ninth step (467.612 sec to 524.812 sec), and tenth step (525.012 sec to 582.212 sec) consecutively the number of electrons that flew through the circuit are 5507, 29585, 25463, 22424, 21035, 20445, 20426, 20413, 20360 and 20338 (all data are calculated according fig. 6, utilizing MATLAB). In the first two steps number of electrons has been increased, but at rated voltage after achieving its apex the number of electrons in each step decreases exponentially (fig. 6.).

The above figures evolve a clear concept, that on to the FTO surface something deposits (ZnO-semiconductor) that hinders the flow of current through the circuit. Within 72.212 seconds indicated by the maximum current (fig. 6.), deposited composites (ZnO) cover the maximum surface of FTO causing the further flow of electrons limited through the circuit.

Fig. 8. Visualization of deposition in between middle of the second steps to the end

In between middle of second step and the last step current is exponentially reduced and saturated after a certain period, this phenomenon is depicted by the above figure (fig. 8.), after a thin deposition of ZnO and Zn(very little in amount) on FTO, it loses it metal like conductivity but tunnel like access made due to accumulation of zinc (Zn) on FTO causes further electron to flow resulting equation 1 to conduct, consequently more OH^- produces around cathode, meanwhile some more Zn ions (Zn^{++}) enhance the tunnel as before and repeat the system cyclically. OH^- in turn affiliate the dissolved Zn^{++} to form $Zn(OH)^+$ that stay in a queue to form more ZnO on FTO (fig. 8.).

We use a 25ml, 0.5M $Zn(NO_3)_2$ electrolyte in order to provide sufficient amount of NO_3^- to produce enough OH^- and NO_2^- by reduction of nitrogen. By conventional mathematics of chemistry, the electrolyte contains

some 1.50575×10^{22} nitrate ions (NO_3^-), which in turn easily enable to meet some 212387 (calculated from I-T data of LabVIEW; fig. 4.) electron that flows during 10 minutes of experiment in the purpose of producing OH^- causing reduction of Nitrogen.

Fig. 9. Image of deposited material on FTO, (a) Top view, (b) 3D view

The above figure (fig. 9.) depicts the post condition of deposition. After drying in normal air we found a resistivity of 1.52MΩ along 1cm distance on the surface of deposited material. Similarly on the surface of FTO it was 0.00Ω in one centimeter distance.

As we use an electrolyte of dehydrated zinc nitrate and distilled water, so deposited material having current limiting as well as highly resistive property can only be an oxide type semiconductor composition (Zinc oxide).

5. Conclusion

We were successfully arranged the two electrodes electrodeposition set-up in a computerized controlled way, where all electrical quantities were visible as graphics and data were stored five times in a second as text at the target directory inside the computer without using any data logger as extra manual device. Finally using the mentioned set-up, we fabricated a film of ZnO on FTO successfully and explained its deposition mechanism that resembles with the inbuilt ZnO formation mechanism.

6. References

[1] Grätzel, M., "Photoelectrochemical Cells." Nature 414, 338-344, 2001.

[2] M. Izaki and T. Omi, "Characterization of Transparent Zinc Oxide Films Prepared by Electrochemical Reaction", *J. Electrochem. Soc.,* 144, 1949 (1997).

[3] M. Izaki, "Morphology evolution and photoluminescence properties of ZnO films electrochemically deposited on conductive glass substrates", *J. Electrochem. Soc.,* 146, 4517 (1999).

[4] M. Izaki and J. Katayama, "Chemical Solution Deposition of Semiconductor Films", *J. Electrochem. Soc.,* 147, 210 (2000).

[5] T. Yoshino, S. Takanezawa, T. Ohmori, and H. Hasuda, "The Electrochemical Society (ECS) publications are no longer hosted on Scitation", *Jpn. J. Appl. Phys., Part 2,* 35, L1512 (1996).

[6] T. D. Golden, M. G. Shumsky, Y. Zhou, R. A. VanderWerf, R. A. Van Leeuwen, and J. A. Switzer, "Fabrication and Characterization of ZnO/Cu$_2$O Solar Cells Prepared by Electrodeposition", *Chem. Mater.,* 8, 2499 (1996).

[7] E. W. Bohannan, L. Y. Huang, F. S. Miller, M. G. Shumsky, and J. A. Switzer, *Langmuir,* 15, 813 (1999).

[8] J. Lee and Y. Tak, "Epitaxial growth to thin films formation of Cu2O by electrodeposition", *Electrochem. Solid-State Lett.,* 2, 559 (1999).

[9] Seok-In Na, Seok-Soon Kim, Woong-Ki Hong, Jeong-Woo Park, Jang Jo, Yoon-Chae Nah, Takhee Lee, Dong-Yu Kim,"Fabrication of TiO2 nanotubes by using electrodeposited ZnO nanorod template and their application to hybrid solar cells", Electrochimica Acta, vol 53 (2008), pp. 2560–2566,, 25 October 2007.

[10] Jaeyoung Lee and Yongsug Tak, "Electrodeposition of ZnO on ITO Electrode by Potential Modulation Method", Electrochemical and Solid-State Letters, 4(9) C63-C65 (2001), July 18, 2001.

[11] Zheng et al., 2002; Wang et al., 2003; Suh et al., 2002; Kim et al., 2004

[12] Lifen Xu, Yi Guo, Qing Liao, Jianping Zhang and Dongsheng Xu, "Morphological Control of ZnO Nanostructures by Electrodeposition", *J. Phys. Chem. B* 2005, *109,* 13519-13522, may 19, 2005.

[13] Bingqiang Cao, Fengqiang Sun and Weiping Caia, "Electrodeposition-Induced Highly Oriented Zinc Oxide Ordered Pore Arrays and Their Ultraviolet Emissions", *Electrochemical and Solid-State Letters,* 8 (9) G237-G240 (2005), July 18, 2005.

[14] B. POSTELS, A. BAKIN, H.-H.WEHMANN, M. SULEIMAN, T. WEIMANN, P. HINZE and A.WAAG, "Electrodeposition of ZnO nanorods for device application" Appl. Phys. A 91, 595–599 (2008), April 4, 2008.

[15] Jaeyoung Lee, Sang Cheol Nam and Yongsug Tak, "On the Origin of Electrodeposition Mechanism of ZnO on ITO Substrate" Korean J. Chem. Eng., 22(1), 161-164 (2005), 28 October 2004.

[16] Yang Yang, Xiaohui Wang, Changku Sun and Longtu Li, "Photoluminescence of ZnO nanorod-TiO_2 nanotube hybrid arrays produced by electrodeposition" JOUR

[17] NAL OF APPLIED PHYSICS 105, 094304 (2009), 1 May 2009.

[18] Tsutomu Shinagawa, Kuniaki Murase And Masanobu Izaki, "Sustainable Electrodeposition of ZnO by a Galvanic Contact Method" *Electrochemical and Solid-State Letters,* 12 (9) D72-D75 (2009), July 9 2009.

Investigation of Optical Properties of ZnO Thin Films Prepared by Sol-gel Method

Shuva Paul, and Md. Faruk Hossain*
Department of Electrical and Electronic Engineering, Rajshahi University of Engineering and Technology
Rajshahi-6204, Bangladesh
*E-mail: faruk94_ruet@yahoo.com

Abstract

Through this study, ZnO thin films have been deposited on a clear glass substrate by sol-gel method with and without polyethylene glycol (PEG) content and also optical properties of the deposited films have been investigated. Using PEG, with zinc acetate precursor, has enhanced the chance to obtain the porous structure of ZnO films. After annealing the films at 550^0C for 2h, optical transmittance measurements have been carried out with UV/Visible spectrometer at 200-900 wavelengths. The film are highly transparent in the visible range and the average transparency with and without PEG contented ZnO films, beyond 400nm wavelength, has been found to be of 93% and 90% respectively. A blue shift in both direct and indirect allowed band gap has been found with the addition of PEG. The direct and indirect allowed band gap of ZnO films with PEG content has been found to be of 3.24 eV and 3.14 eV respectively.

Keywords: sol-gel, PEG content, optical properties, band gap.

1. Introduction

Owing to the drastic developments in the fields of nanoscale science from the last few decades, study of one-dimensional (1D) materials has become one of the most interesting fields of scientific research, leading to the worldwide popularity of semiconductor nanocrystals because of their special properties in comparison with those of bulk materials [1]. In particular, Zinc oxide (ZnO) is an inexpensive n-type semiconductor which crystallizes in hexagonal Wurtzite structure (c=5.025 and a=3.249) [2]. ZnO is also a member of transparent conductive oxides (TCO) and has become one of the best options as transparent conductive electrodes for dye-sensitized solar cells due to high chemical stability, a textured surface, high conductivity and high transparency in the visible range. It is widely used for manufacturing of LEDs, OLEDs, liquid crystal displays, flat panel displays, piezoelectric transducers, surface acoustic devices, varistors, spin functional devices and UV-light emitters [3]. For photonic applications in the UV or blue spectral range [4], ZnO is the most promising material due to its wide band gap energy (3.37 eV) [5] and high exciton-binding energy (60 meV) [6] allows efficient excitonic emission even at room temperature. Moreover, ZnO technologically exhibits outstanding antimicrobial properties and exceptional UV attenuation characteristics: blocking 95% of all UV radiation that can be utilized in cosmetics, paints, varnishes, plastics and so on [7]. Last but not least, ZnO has tunable morphologies such as nanocrystals, nanowires, nanorods and nanolipsticks, nanotubes that causes to increase surface-to-volume ratio and has potential application in UV lasers, detectors, gas sensors and dye-sensitized solar cell [5][8].

ZnO thin films have been prepared by various deposition techniques, such as RF magnetron sputtering [9], spray pyrolysis [10], pulsed laser deposition [11], chemical vapor deposition [12], molecular beam epitaxy [13] and sol-gel process [14-15]. Sol-gel method is widely used for ZnO thin films fabrication over other methods for some advantages, e.g. its ability to prepare high quality of films of difficult shapes in large scale, simplicity, safety, low cost of the apparatus and raw materials [16-17]. The optical and structural properties of sol-gel derived ZnO thin films depend critically on several parameters such as annealing temperature, deposition technique, withdrawing rate, drying process, presence of polyethylene glycol (PEG) content and so on[5-6].

It has been reported that, in order to obtain high photon-to-current conversion efficiency of dye-sensitized solar cells, surface of ZnO photoanode should be porous in nature that has been accomplished by using PEG as

surface modifier [5]. The present paper reports on preparation of ZnO thin films on glass substrate through conventional sol-gel method with different PEG content. The optical properties of the resulting films have been investigated and band gap energy has been determined.
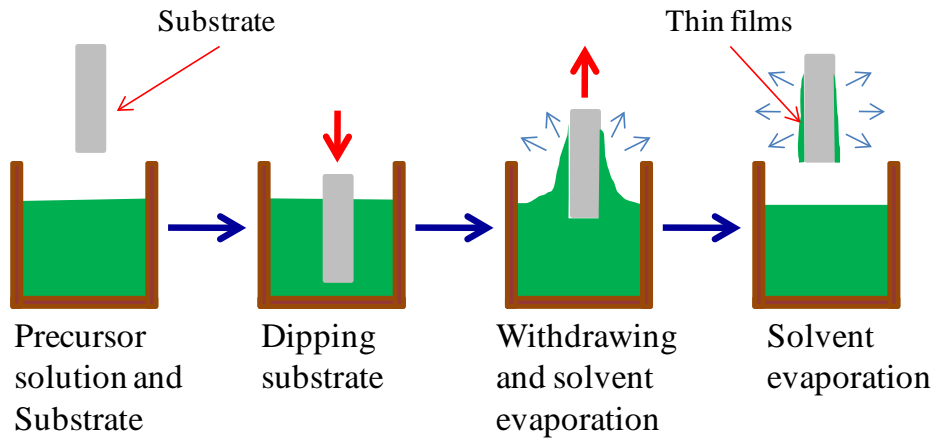
Fig.1. Different stages of sol-gel dip coating process

2. Fundamentals of Sol-gel dip coating

Sol-gel is a very well known wet chemical process, from which dense film, xerogel, areogel and ceramic fibers can be derived by using dip coating, gelling, precipitating and spinning method respectively. A sol is generally known as the molecular suspension of solid particles of ions in a solvent. When the solvent from sol begins to evaporate, ions left behind begin to join in a continuous network which is known as gel.

Fig. 1 shows the various stages of sol-gel dip coating method. At first a metal alkoxide solution, known as precursor solution, is prepared to yield sol and a substrate is cleaned on which films have to be deposited. At the second stage substrate is made to go through the solution at a suitable rate and after complete dipping is left in the solution for a while. Substrate withdrawing from the solution is the most critical point of dip coating process. In order to get uniform thickness of the films, substrate must be withdrawn vertically at a constant rate. While withdrawing, solvent from the surface of the film is evaporated and as well as draining occurs. Withdrawing rate affects the quantity of solid particles or ions left on the substrate that in turn affects the thickness. Generally, higher withdrawing rate produces milky films with increased thickness than lower rate.

2. Experimental Section

Chemical Reagents

ZnO precursor solution was prepared using absolute ethanol (M=46.07, CH_3CH_2OH, EtOH) as solvent, zinc acetate di-hydrate (M=219.50, $Zn(CH_3COO)_2.2H_2O$, ZAD) as precursor, diethanolamine (M=105.14, $[CH_2(OH)CH_2]_2.NH$, DEA) as chelating agent, polyethylene glycol (M_{av}=2000, $H(OCH_2CH_2)_nOH$, PEG) as organic template and de-ionized water.

Preparation of ZnO thin films

ZnO thin films were prepared by using conventional sol-gel dip coating method according to reference [6]. At first, in 20ml of absolute ethanol 4.39g of zinc acetate was dissolved to yield a concentration of 1.0 mol/L. The solution was then stirred thoroughly on a magnetic stirrer for 30 min and a milky solution was obtained. Then 1.93ml of DEA and 0.72ml of de-ionized water was added into the emulsion, adjusting the molar ratio of DEA/ZAD as 1:1 and that of de-ionized water/ZAD as 2:1, followed by further stirring for 20 min. Meanwhile, the emulsion became clear. Finally, PEG of 1.0g and 0.75g was separately added into above prepared sol and was continuously stirred for 2h until a transparent sol was obtained. Glass micro-slides were used as substrate for deposition of ZnO films. The substrates were cleaned ultrasonically, first in ethanol and subsequently in ion exchanged distilled water for 15 min each at 50^0C. Then using conventional dip-coating method prepared transparent sol was coated on clear glass substrate. The dipping and withdrawing rate was about 1cm/min. The coated films were kept at room temperature and after that were dried at 350^0C for 30 min each. The process above was repeated for three times and after giving the final coating, the films were kept at room temperature for 24h. Finally, the obtained as-deposited films were annealed at 550^0C at a heating rate of 20^0C/min and left at

550^0C for 2h.The optical properties of the deposited films were measured by UV/Visible spectrometer at 200-900 nm wavelengths using reference substrate. From transmittance spectra absorbance was determined using Beer-Lambert Law and optical band gap was found using Tauc relationship.

ZnO Films   Bare glass
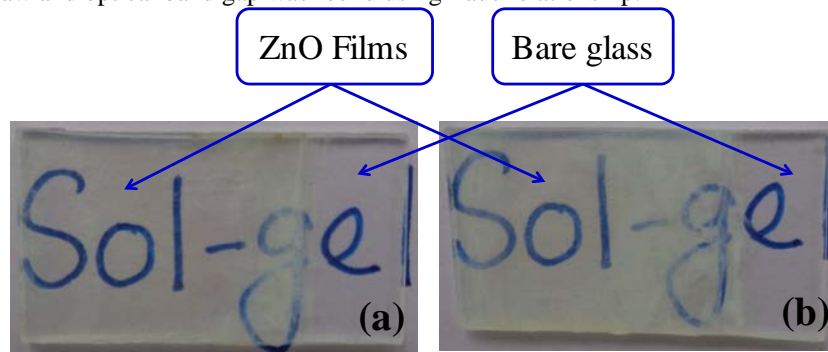
Fig. 2. Images of ZnO thin films on glass substrate with (a) with PEG, and (b) without PEG.

3. Results and discussion

Fig.2(a) and **Fig.2(b)** shows the images of ZnO thin films on glass substrate with and without PEG content respectively. It is clearly seen that, the prepared films are visually transparent. It is also to be noted that PEG-aided ZnO films are more transparent than without PEG, this may due to the fact that the generated colloidal dispersion was very stable as PEG has been added with the metal oxide solution. Measured optical properties of the films also agree with this.

Fig.3 shows the optical transmittance of ZnO thin films with and without PEG content in the wavelength (λ) range 300-900 nm. It can be observed that the films are highly transparent in the visible range of the electromagnetic spectrum with an average transmittance values up to 93% beyond the wavelength of 400 nm for PEG-aided ZnO films and presents sharp ultraviolet cutoff at approximately 370 nm. On the other hand, ZnO films without PEG content shows UV cutoff at about 360 nm with average transmittance of 90% beyond 400 nm. Transmittance for both with and without PEG ZnO films reaches to maximum value at higher wavelength. Below the wavelength of 550 nm transmittance of PEG contented ZnO films is lower than that of ZnO films without PEG. This may due to increase of interface scattering. It has been reported that use of PEG produces ZnO films porous and microring like structure and with smaller grain size [5]. Interface scattering is increased due to porous structure [18].

Fig. 4 shows the absorption spectrum of sol-gel derived ZnO films with and without PEG content. It is clearly observed that both films have a very low absorption at transparent region and high absorption at ultraviolet region. It is to be noted that, absorption at UV-region for PEG contented ZnO films is higher to that of ZnO films without PEG content. The reason is that PEG inclusion results ZnO films with smaller grain size and hence surface to volume ratio has been increased. Again ZnO films without PEG may have a smaller thickness. Due to high transparency at visible range and high absorption at UV-region, ZnO films with PEG content have the potentiality to be applicable for optical window application and UV detectors.
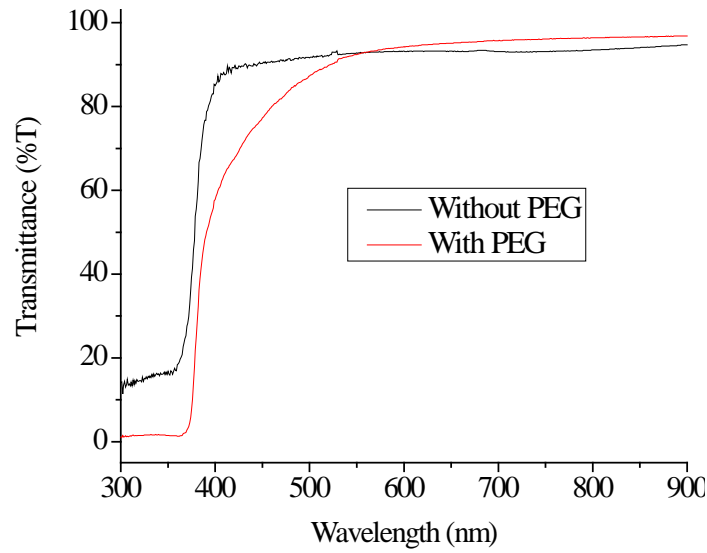
Fig. 3. Optical transmittance ZnO thin films
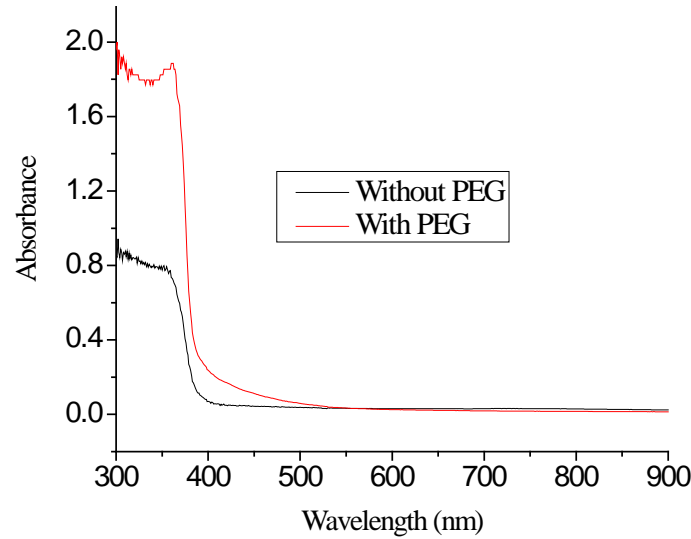
Fig. 4. Optical absorbance of ZnO thin films

The direct and indirect allowed optical transitions between valance and conduction bands can be evaluated by fitting a straight line in strong absorption spectral region using the Tauc relationship. According to Tauc law dependence of absorption co-efficient (α) on photon energy (hν) can be given by [19]

$$(\alpha h \nu) = A(h\nu - Eg)^r \tag{1}$$

Where α is the absorption co-efficient, A is the edge width parameter, and hν is the photon energy, and r is a constant, for direct allowed transition r equals ½ and for indirect allowed transition equals 2.

Fig. 5 shows the plot of $(\alpha h\nu)^2$ vs. hν of prepared ZnO films grown with and without PEG content. The optical band gap for direct allowed transition of the films have been determined from the extrapolation of the linear portion of $(\alpha h\nu)^2$ vs. hν at α= 0. Direct transition band gap is found to be of 3.03eV for without PEG that has been shifted to UV-region with a value of 3.24 eV when PEG has been added. Although this value is smaller than the bulk value of 3.37 eV but still it is in good agreement with previously reported data of ZnO thin films [20].
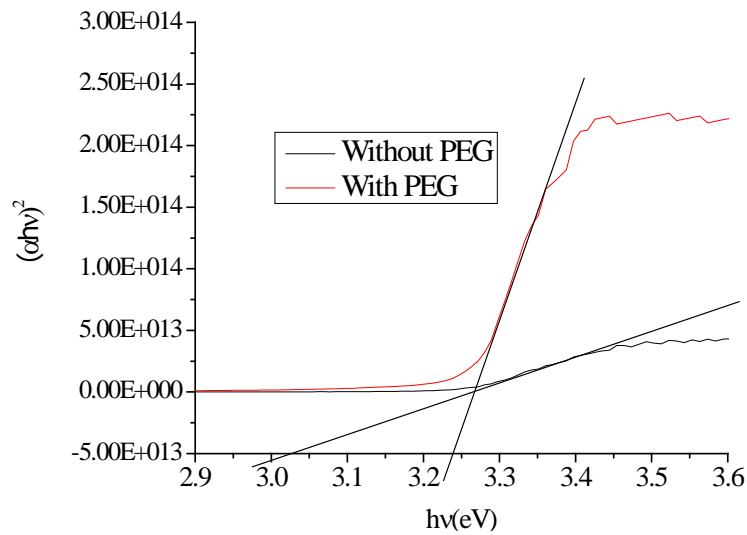
Fig. 5. Plot of $(\alpha h\nu)^2$ vs. $h\nu$ of ZnO thin films.
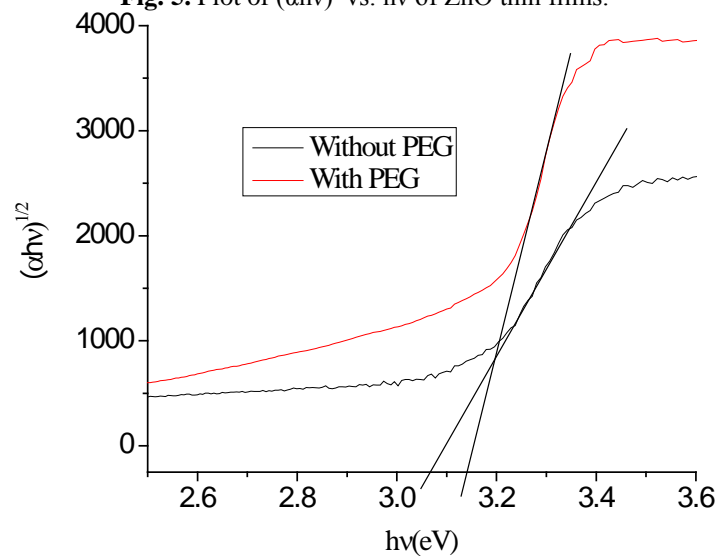
Fig. 6. Plot of $(\alpha h\nu)^{1/2}$ vs. $h\nu$ of ZnO thin films.

Fig. 6 shows the plot of $(\alpha h\nu)^{1/2}$ vs. $h\nu$ and band gap for indirect allowed transition has been determined by extrapolating the straight line portion of the spectrum at $\alpha= 0$. Here blue shift in the band gap has also been seen but smaller with compared to direct transition. Indirect band gap for ZnO films without and witho PEG has been found to be of 3.07 eV and 3.14 eV respectively that are greater than the previously reported indirect band gap of ZnO [21].

4. Conclusion

ZnO thin films were successfully prepared on glass substrate, with PEG as organic template, by simple and effective sol-gel dip coating technique using zinc acetate as precursor. In order to obtain crystal structure of ZnO, as-deposited films were calcined at 550^0C for 2h. The results have revealed that, ZnO thin films with PEG content show better optical performance than ZnO thin films without PEG content. It was found that, both direct and indirect band gap for ZnO films with PEG content was higher and was of 3.25 eV and 3.16 eV respectively. Higher transmittance in the visible region and higher absorption in the UV-region has made the films potentially able for the application as transparent conductive oxide (TCO).

5. Acknowledgement

11. References

[1] Z.L. Wang, "Zinc oxide nanostructures: growth, properties and applications", *J. Phys.: Condens. Matte.,* vol.16, pp. 829-858, 2004.

[2] C.Y. Tsay1, M.C. Wang, and S.C. Chiang, "Effects of Mg Additions on Microstructure and Optical Properties of Sol-Gel Derived ZnO Thin Films", *Materials Transactions*, Vol.49, No.5, pp. 1186-1191, 2008.

[3] F.K. Shan, B.I. Kim, G.X. Liu, Z.F. Liu, J.Y. Sohn, W.J. Lee, B.C. Shin and Y.S. Yu, "Blueshift of Near Band Edge Emission in Mg Doped ZnO Thin Films and Aging," *Journal of Applied Physics*, Vol.95, No.9, pp. 4772-4776**,** 2004.

[4] A.B. Djurisˇic´ and Y.H. Leung, " Optical Properties of ZnO Nanostructures", *small,* vol.2, No. 8-9, 944 – 961, 2006.

[5] M.F. Hossain, S. Biswas, M. Shahjahan, and T. Takahashi, "Study of sol-gel derived porous ZnO photoelectrode for the application of dye –sensitized solar cells," *J. Vac. Sci. Technol. A*, vol.27, No.4, pp.1047-1051, 2009.

[6] M.F. Hossain, Z.H. Zhang and T. Takahashi, "Novel micro-ring structured ZnO photoelectrode for dye-sensitized solar cell," *Nano-Micro Lett*., vol.2, pp. 53-55, 2010.

[7] D.S. Carr, B. Baum, "Zinc Oxide/Synegist systems provide improved UV control", *Modern Plastics,* pp. 64-68, 1981.

[8] M.F. Hossain, T. Takahashi, S. Biswas, "Nanorods and nanolipsticks structured ZnO photoelectrode for dye-sensitized solar cells", *Electrochemistry Communications*, vol. 11, pp. 1756-1759, 2009

[9] Y.R. Park, D. Jung, K.C. Kim, S.J. Suh, T.S. Park and Y.S. Kim, "Physical Properties of Transparent Conducting Indium Doped Zinc Oxide Thin Films Deposited by Pulsed DC Magnetron Sputtering," *Journal of Electroce- ramics*, Vol.23, No.2-4, pp. 536-541, 2009.

[10] S. Ilican, Y. Caglar, M. Caglar and B. Demerci, "Poly- Crystalline Indium-Doped ZnO Thin Films: Preparation and Characterization," *Journal of Optoelectronics and Advanced Materials*, Vol.10, No.10, pp. 2592- 2598, 2008.

[11] N. Naghavi, A. Rougier, C. Marcel, C. Gueary, J.B. Leriche and J.M. Tarascon, "Characterization of Indium Zinc Oxide Thin Films Prepared by Pulsed Laser Deposition Using a $Zn_3In_2O_6$ Target," *Thin Solid Films*, Vol.360, No.1-2, pp. 233-240, 2000.

[12] J.H. Lee and B.O. Park, "Transparent Conducting ZnO:Al, In and Sn Thin Films Deposited by the Sol-Gel Method," *Thin Solid Films*, Vol.426, No.1-2, pp. 94-99, 2003.

[13] A. Ohtomo, M. Kawasaki, T. Koida, K. Masubuchi, H. Koinuma, Y. Sakurai, Y. Yoshida, T. Yasuda and Y. Segawa, "Mg_xZn_{1-x} O as a II-VI Widegap Semiconductor Alloy," *Applied Physics Letters*, Vol.72, No.19, pp. 2466-2468, 1998.

[14] M. Rezaee, R. Abadi, M. Behdani, H. Arabshahi and N. Hosseini, "Indium-Doped Zinc Oxide Thin Films by Sol- Gel Method," *International Review of Physics*, Vol.3, No.4, pp. 219-223, 2009.

[15] E. J. L. Arredondo, A. Maldonado, R. Asomoza, D.R. Acosta, M.A.M. Lira and M. de la L. Olvera, "In- dium-Doped ZnO Thin Films Deposited by the Sol-Gel Technique," *Thin Solid Films*, Vol.490, No.2, pp. 132-136, 2005.

[16] F.E. Ghodsi and H. Absalan, "Comparative Study of ZnO Thin Films Prepared", *Acta Physica Polonica A,* Vol.118, No.4, pp. 659-664, 2010.

[17] A.J. Hurd and C.J. Brinker, "Optical sol-gel coatings : ellipsometry of film formation", *J. Phys. France*, Vol.49, pp. 1017-1025, 1988.

[18] C.X. Xu, G.P. Zhu, X. Li, Y. Yang, S.T. Tan, X.W. Sun, C. Lincoln and T.A. Smith, "Growth and Spectral Analysis of ZnO Nanotubes," *Journal of Applied Physics*, Vol.103, No.9, 2008.

[19] Z. Liu, J. Li, J. Ya, Y. Xin, and Z. Jin, "Mechanism and characteristics of porous ZnO films by sol-gel method with PEG template". *Materials Letters*, Vol.62, pp. 1190-1193, 2008.

[20] N. Shakti, P.S. Gupta, "Structural and Optical Properties of Sol-gel Prepared ZnO Thin Film", *Applied Physics Research*, Vol.2, No.1, pp. 19-28, 2010.

[21] W.R. Saleh, N.M. Saeed, W.A. Twej, M. Alwan, " Synthesis sol-gel derived highly transparent ZnO thin films for optoelectronic applications", *Advances in Materials Physics and Chemistry*, vol.2, pp. 11-16, 2012.

Investigation of the Photovoltaic performance of Si-based solar cells under different Light Illuminations

Mst. Rebeka Sultana, Md Faruk Hossain*, and Mst Hasnara Khatun

Department of Electrical & Electronic Engineering, Rajshahi University of Engineering & Technology

Rajshahi-6204, Bangladesh

Email: faruk94_ruet@yahoo.com

Abstract

Today's solar cells are simply not efficient enough and currently too expensive to manufacture for Large scale electricity generation. However, Nanotechnology may open to the production cheaper and slightly more efficient solar cells. . So I would examine the current solar cell Technologies available. Device performance under extended duration illumination is an essential characterization step for any PV technology, because light exposure can produce a variety of effect which influence the determination of both initial and long term stabilized device performance. For a silicon photovoltaic, light exposure leads to degradation of module power output, while light temperature leads to improvement. So I would like to investigate the performance of photo voltaic cell under different light condition .I also investigate the Photovoltaic performances for a Cell, for a Module, for a Panel, and for two panels with different illuminations. It will be helpful to calculate the efficiency of solar cell. The component which required for my task is very simple and cheap

1. Introduction:

At present century huge population, advanced industrialization, rising number of hunger demands immense power to meet those challenges around the world. Today people developed so many techniques and methods for producing and distributing power from solar system, but most of these methods were costly as well as inefficient and beyond the reach of common people. To make those things better and cost effective people developed so many ideas, application of thin films on solar cell is one of them, it not only increase efficiency of solar cell but make it cost effective and versatile for applying different purposes [1].

The word photovoltaic comes from "photo" meaning light, and "voltaic which refers to producing electricity. Therefore, the photovoltaic process is "producing electricity directly from sunlight."When application require larger amounts of electricity [3].
Photovoltaic's are best known as a method for generating electric power by using solar cells to convert energy from the sun into a flow of electrons. The photovoltaic effect refers to photons of light exciting electrons into a higher state of energy, allowing them to act as charge carriers for an electric current. The photovoltaic effect was first observed by Alexandre-Edmond Becquerel in 1839. [5]
Solar energy is a clean and carbon-free energy resource with tremendous potential for electricity generation. Light emitted by the sun and falling on the earth is one of the most abundant energy resources. Over 15,000 EJ (1.5x1022 J) of solar energy reaches earth every day, compared to daily energy consumption of approximately 1.3 EJ by human activity [8]Solar cell provides electricity for rural areas or third world countries. Since electricity demand in these areas is not high, and the areas are distantly spaced out, it is not practical to connect them to an electrical grid. However this is an ideal situation for solar energy. [2]

The solar cell which are available in the market are given with rated power ,open circuit voltage, short circuit current, but it is not given how much the solar panel is efficient according to sunlight. The efficiency is the most commonly used parameter to compare the performance of one solar cell to another. To determine the efficiency we have to find I-V characteristics of the cell and fill factor.

2. **Experimental setup**

For my thesis work I have used ET 250 photovoltaic Trainer. The ET 250 trainer contains two such solar modules. The tilt of the module can be adjusted. Cables can be used to connect the two modules in series or parallel. A slide resistor simulates varying loads. Thus the slide resistor makes it possible to record current-voltage curves. The separate measuring unit provides display all relevant variables. Sensors on the solar module detect illuminance and temperature. In order to ensure there is sufficient illuminance, the trainer should be operated with sunlight or the optional light source. In figure we can see the ET 250 Photovoltaic Trainer and in figure 2 its different parts are indicated.
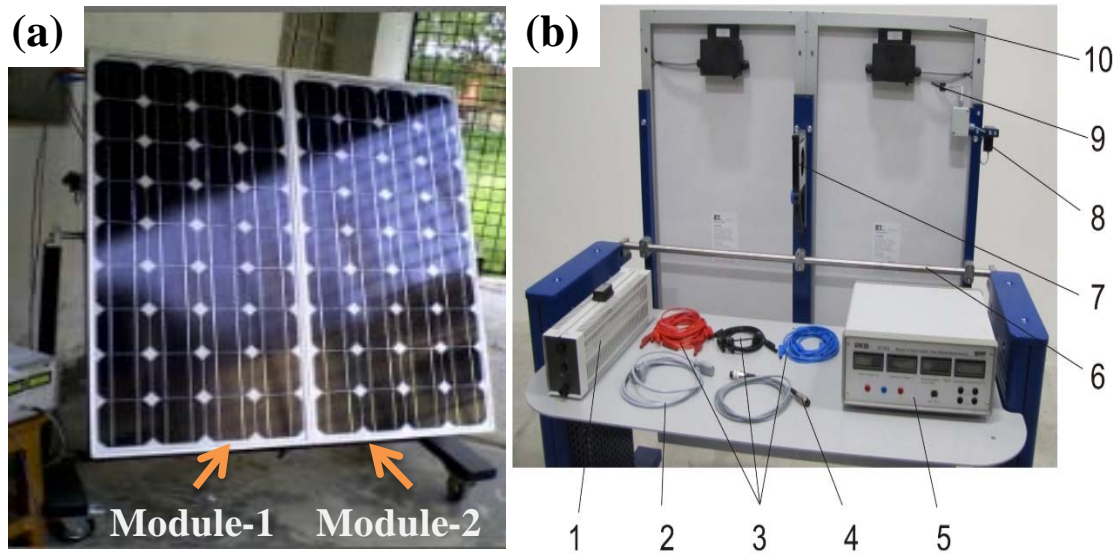
Fig. 1. (A) Front view of two modules of 85Wp (Model ET 250); (b) Back view of solar modules and Unit Layout of ET 250 Photovoltaic Trainers with all accessories.

Fig. 2. Photovoltaic parameters measuring unit.

Figure 1(a) shows front view of two modules of 85Wp (Model ET 250). Each module has 36 cells in series. Figure 1(b) exhibits the Back of PV modules and overall unit layout of ET 250 photovoltaic trainers with all accessories. The numbers 1-10 displays the listed accessories: 1-Variable resistor with slider, 2-Power cable, 3-Set of cables for series and parallel connection, 4-Measuring cable, 5-Measuring Unit, 6-Tilt axis, 7-inclinometer, 8-Illuminance sensor, 9-Temperature sensor, 10-Solar modules. The most important part of the trainer is the combined measuring unit, as shown in Fig. 3. Here the photocurrent (A), photo voltage (V), irradiation intensity (kW/m^2), and environmental temperature have been measured by this measuring unit and digitally displays these data.

The technical Data for solar module is given in Table 1. The short circuit and open circuit voltage of each module is 5.29A and 21.94V, respectively. The overall area of 36 cells is 0.63 m^2. The maximum power of each module is 85W at peak light irradiation.

Table 1. Standard Photovoltaic's parameters of each of the Module of ET 250 Photovoltaic trainer

Number of cells	36(monocrystalline)
Module area	0.63m²
Max. Power	85Wp
Short-circuit current	5.29A
Open-circuit voltage	21.94V
Slide resistor	0...10 Ohm
Measuring ranges Temperature	0…100°C
Voltage	0...20V
Current	0...20A
Illuminance	0...2000W/m²
LCD digital Displays	0…199.9mv DC

3. Characteristics parameters

The solar cells are characterized by the following parameters:

Fill Factor: The fill factor is defined as the ratio of the actual maximum obtainable power to the product of the open circuit voltage and short circuit current. [4] FF describes how closely the current voltage characteristics curve approximates the ideal rectangle form. This is a key parameter in evaluating the performance of solar cell.

$$Fill\ Factor = \frac{Vmp*Imp}{Voc*Isc} \qquad (1)$$

Where, Vmp is voltage at maximum power point,

Imp is current at maximum power point

Efficiency: The efficiency is the most commonly used parameter to compare the performance of one solar cell to another. Efficiency is defined as the ratio of energy output from the solar cell to input energy from the sun. [8][6]

$$Effiency, \eta = \frac{Voc*Isc*FF}{Pin} \qquad (2)$$

Here, Voc= open circuit voltage

Isc=short circuit current,

FF=fill factor

Pmax=maximum power obtained from the curve

Pin=Input power /intensity

Efficiency depends on the type of cell. For the module efficiency value, the output power is divided by the total radiation incident on the module. Because the entire area of the module is not covered by with the solar cells (for example, frames and space between the single solar cells are not active area), the module efficiency value is lower than the efficiency value of the single cell. [9]

4. Result and Discussion:

The result of investigation of solar cell under different light condition is given here

Condition 1: Parallel Connection of two modules
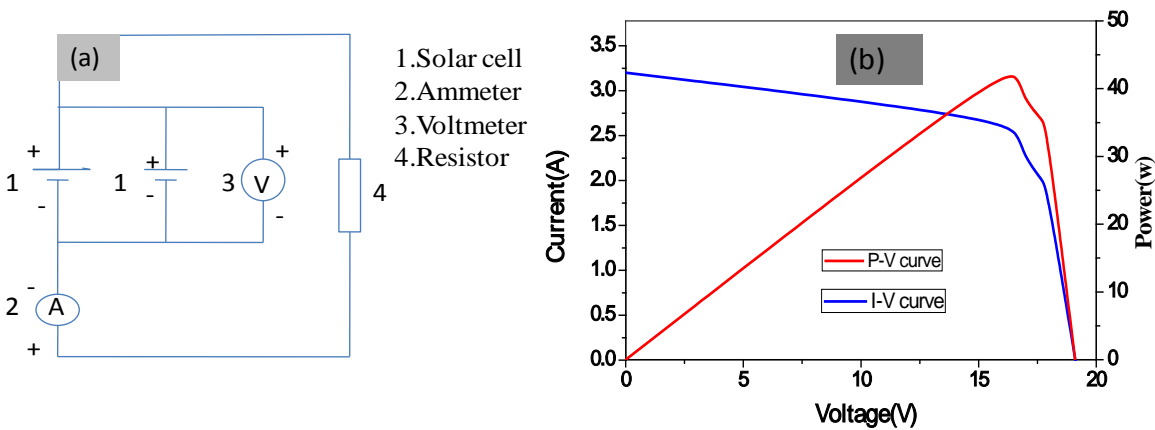
Fig.4 (a) Circuit diagram of the parallel connection of two module (b) I-V and P-V characteristics curves of fig (a)

Figure 4 shows the parallel connection of two modules and the I-V and P-V characteristics curves of parallel connection of two modules at noon when lights was sufficient. In this condition open circuit voltage was19.1V, Short Circuit Current=3.2A, automatically obtained intensity=0.58KW/m^2.Calculated Intensity=0.69kw/m^2. In a 10 x 10 cm^2 cell the input power is 100 mW/cm^2 x 100 cm^2 = 10 W. So the fill factor was 0.7023which is calculated from equation (1) , which is good for any solar cell. Finally efficiency was obtained as 4.9% from equation (2)

Condition .2: Series Connection of two modules
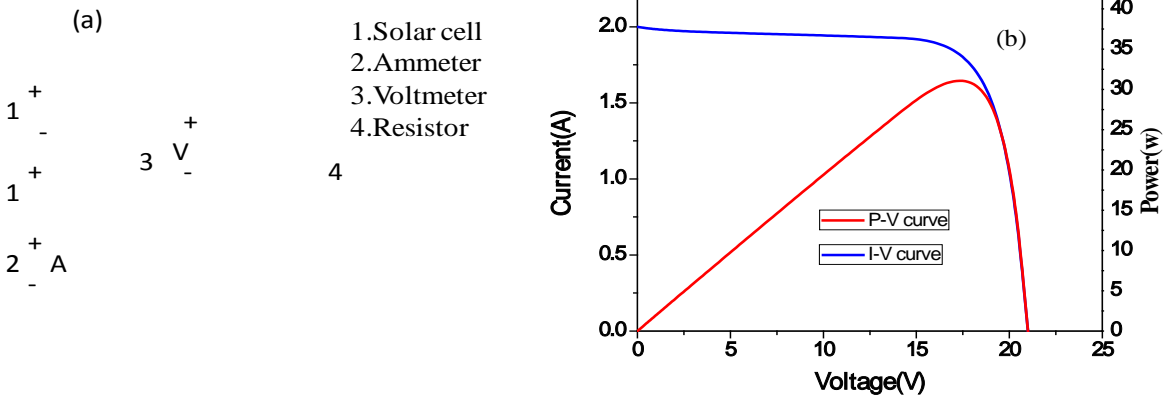
Fig.5 (a) Series connection of the two module (b) I-V and P-V characteristics curve of the connection of fig (a)

Figure 5 shows the series connection diagram of two modules. Figure 6 shows the I-V and P-V characteristics of two modules connected in series .This data was taken during time period 10.30 in morning. In this condition fill factor was 0.882 and efficiency was 3.75%.Here   Open Circuit Voltage=21V, Short Circuit Current=2A, automatically obtained intensity=0.78KW/m² .Average intensity: 54388lx .Calculated Intensity=0.776kw/m².

Condition 3: One module with at 11.30A.M
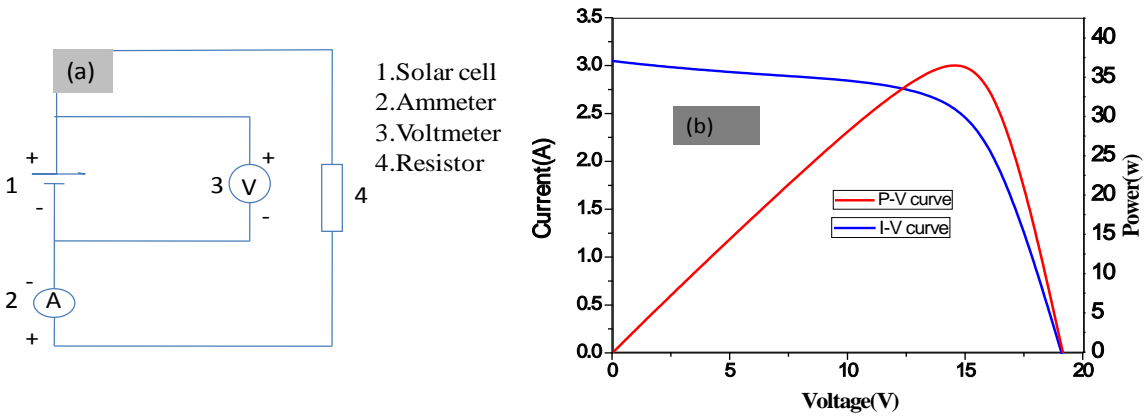
Fig.6 (a) Circuit diagram of one module (b) I-V and P-V characteristics curves of the connection of fig. (a).

The I-V and P-V curves of one module of a solar cell are shown in fig.6.The experiment was performed at 11.30A.M.The light was sufficient. Open Circuit Voltage=19.1V, Short Circuit Current=3.05, automatically obtained intensity=0.58KW/m².Calculated Intensity=0.69kw/m².,fill factor was 0.663 and efficiency was 8.8%.

Condition: 4: Characteristics of one module with column 1 and 4 closed
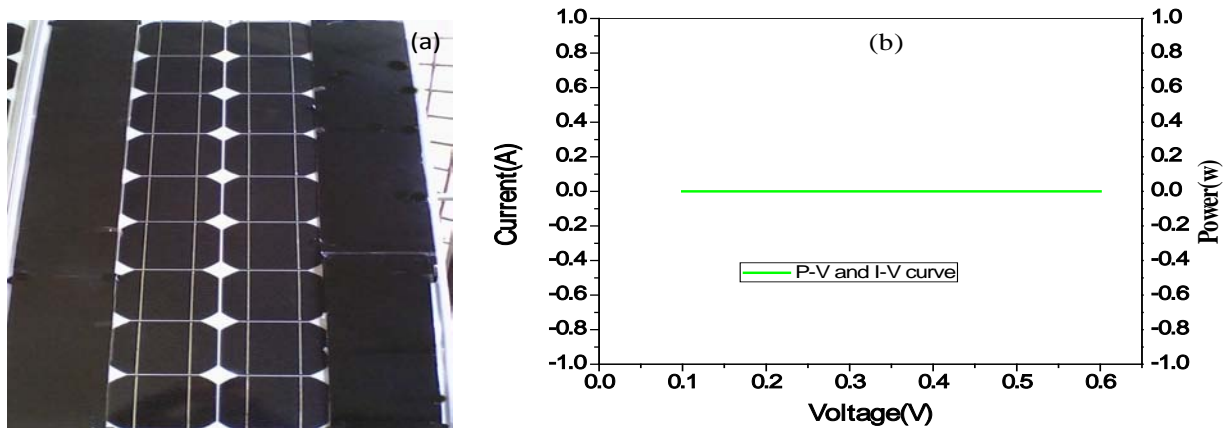
Fig.7 (a) One module with column 1 and 4 closed (b) I-V and P-V characteristics curves of the connection of fig. (a)

The I-V and P-V characteristics curves are shown in the figure (7).There is no variation of current when resistance was varied. So the fill factor and efficiency in this case is zero. This is because, PV cells are connected in series and two columns are closed there existing an open circuit .So the current becomes zero. In this period light was enough.

Table 2. Comparison between all conditions:

Conditions	Open circuit voltage, Voc(V)	Short circuit current, Isc(A)	Obtained Intensity KW/m^2	Calculated Intensity KW/m^2	Fill Factor, FF	Efficiency, η
Parallel Connection of two module at 12.30 A.M with sufficient light	19.1	3.2	0.58	0.69	0.7023	4.9%
Series connection of two module at 10.30A.M	21	2	0.78	0.776	0.882	3.75%
One module at 11.30AM	19.1	3.05	0.58	0.69	0.663	8.8%
One module with column 1 and 4 closed	15	0.1	0.40	64.8	0	0%

5. Conclusion:

From the I-V curves at different condition we can see that there is a significant effect of intensity of light. In addition to reflecting the performance of the solar cell itself, the efficiency depends on the spectrum and intensity of the incident sunlight and the temperature of the solar cell. Therefore, conditions under which efficiency is measured must be carefully controlled in order to compare the performance of one device to another. Changing the light

intensity incident on a solar cell changes all solar cell parameters, including the short-circuit current, the open-circuit voltage, the FF, the efficiency etc.The solar cell available at the market are given with their open circuit voltage, short circuit current, maximum power etc. But efficiencies are not given. So the efficiency calculated in this way will be helpful for us to compare the performance of one device to others. Fill factor is the key parameter in evaluating the performance of solar cell, Typical commercial solar cells have a fill factor >0.7.Grade B solar cell have a fill factor usually between 0.4 to0.7. [7]

References

[1] Grätzel, M., "Photoelectrochemical Cells." Nature 414, 338-344, 2001.

[2] Choi, Charles. "Nanotech Improving Energy Options." Space Daily. New York: May

27, 2004. <http://www.spacedaily.com/news/nanotech-04zj.html>.

[3] Alfred Smee (1849). *Elements of electro-biology,: or the voltaic mechanism of man; of electro-pathology, especially of the nervous system; and of electro-therapeutics*. London: Longman, Brown.

[4] Shockley W., J. Bardeen and W. Brattain, "The Theory of P-N Junctions in Semiconductors and P-N Junction Transistors," *Bell System Technical Journal,* Vol 28: 1949, pp. 435 Semi conductive Materials Transistor. ISSN : 0005-8580.

[5] The photovoltaic effect. Encyclobeamia.solarbotics.net. Retrieved on 12 December 2010.

[6] Cheng-Hsiao Wu and Richard Williams (1983). "Limiting efficiencies for multiple energy-gap quantum devices". *J. Appl. Phys.* **54**: 6721. Bibcode:1983JAP....54.6721W. doi:10.1063/1.331859.

[7] T.Bazouni: What is the Fill Factor of a Solar Panel". http://www.solarfreaks.com/what-is-the-fill-factor-of-a-solar-panel-t138.html. Retrieved 2009-02-17.

[8] R. R. King, et al., "40% efficient metamorphic GaInP/GaInAs/Ge multifunction solar cells," *Appl. Phys. Lett.*, vol. 90, 2007 pp. 183516-1.[9] Nikhil Jain, "Design of III-V multifunction solar cells on silicon substrate" May 6, 2013 ,Blacksburg, VA

[9] A.Gotezberger,V.U.Hoffmann,"Ptotovoltaic Solar Energy Generation"2005,ISSN 0342-4111

Paper ID: MS-47

Design and Fabrication of handmade screen printing for thin film applications

Hasnara Hasi, Md. Faruk Hossain, Mst. Rebeka Sultana, Robin Khan, Hasibul Islam
Department of Electrical and Electronic Engineering
Rajshahi University of Engineering & Technology
Rjashahi-6204, Bangladesh
Email: faruk94_ruet@yahoo.com

Abstract—The aim of this work is design and fabricate a screen printer for depositing TiO_2 thin films from TiO2 paste. Screen printer system has been prepared by wood frame and silk screen. TiO2 paste is prepared with the help of TiO2 powder. The size and shapes of each thin film has been exactly same as the mask of screen printer. The mask and prepared thin film have been compared and investigated in this work.

1.Introduction

With ever-increasing political and economic oil conflicts as well as climate change, a growing need for renewable energy that comes from natural resources, such as sunlight, wind, rain, tides and geothermal heat, is warranted. Wars have been caused in part to protect oil supplies, and millions of tons of pollutants and greenhouse gases are emitted into the atmosphere every year due to the burning of fossil fuels to create energy. There is no other area of technology than renewable energy technologies that can both "meet the challenges of climate change and secure an energy supply in an intelligent manner" [1].A number of options for new technologies of renewable energy exist, that is, from geothermal to wind to hydrogen fuel cells to hydropower; however, one of the most accessible and widely used technologies is solar energy. Solar power does not create any noise when it is working, "is non-polluting, does not generate greenhouse gases, and creates no waste products,"[2].which is also why it is an increasingly preferred renewable energy. Additionally, the potential for solar power is immense [3].

This is why, a project has been gone to implement to develop solar cell by using screen printing process. By screen printing process thin film can be produced. A thin film is a layer of material ranging from fractions of a nanometer to several micrometers in thickness [4]. Electronic semiconductor devices and optical coatings are the main applications benefiting from thin-film construction. A familiar application of thin films is the household mirror, Work is being done with ferromagnetic and ferroelectric [1] thin films for use as computer memory. It is also being applied to pharmaceuticals, via thin-film drug delivery. Thin-films are used to produce thin-film batteries. Thin films are also used in dye-sensitized solar cells[5]. In recent years, the manufacturers of thin-film solar modules have brought costs down and gained competitive strength through advanced thin film technology.

Screen printing method is far better than other method such as sol-gel method, sputtering method .By using screen printing process, sixteen cells of dimension 2x2cm,42 cells of dimension 1x1cm and 133 cells of dimension 0.5x0.5cm are made on glass plate of dimension 10x10cm.This is because, a quite large number of cell can be produced economically at a time by using screen printing method. But by sol-gel method and sputtering method cannot produce more cells at a time .Sol-gel can produce one cell at a time.

When it comes to creating many copies - When it has to make copies in a wholesale quantity, screen printing is the right option. The solar panels are going to used   again and again if we are going to make many copies. It is an economical way and works out cheaper [6]. Cost recovery becomes easier and we would end up making good profits.   Screen printing is a quick process as compared to other methods of advertising. When our advertisement is viewed by millions of prospective customers, it would definitely convert some of these prospects into your clients. The process of screen printing is simple and hassle free[7]. The only requisites are

the screen panels and the requisite materials. With these, we can kick start our business. The colors dry quickly and you could start showing the ads to the targeted audience [8].

 When it comes to larger designs, screen printing is the ideal choice. We can choose to be more creative and resourceful when it comes to selecting the screen panel's size. It is possible to make larger counterparts of the design, without any distortion to the texts and images. When it comes to digital printing, it is not very easy to make adjustments. Wide range of utility - Screen printing can be used effectively for a variety of things. Screen printing is used for printing designs on clothes, fabrics and garments. It also caters to printing on product labels, printing of circuit boards, adding different designs to balloons etc[9].In this work Screen printing system has been degined and fabricated with the help of   wood frame and silk screen.TiO2 films has been deposited on glass substrate by this screen printer with different size and shape. Overall screen printing process has been discussed in this work.

2. EXPERIMENTAL SECTION

First step: Wood frame
Involves a screen of woven material such as synthetic fiber that has been glued to a wood frame under tension.
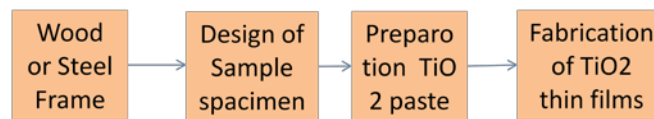
Figure1: Schematic block diagram of different for whole   screen printing process

Second step: Design of sample specimen:
Silk is filled with a coating solution by squeegee. Then it is made dehydrated by dryer machine .After that the desired output which we want is printed in tracing paper by using computer .The tracing paper is placed for 5 to 10 minutes on the silk screen and placed it in a sunny place for few minutes . After this time the tracing paper is withdrawn. Then we get the desired design.

Third step: Preparation of TiO_2 paste
TiO2 nanostructure films were deposited on glass by using a screen printer.TiO2 paste were prepared as follows: 0.5 g of TiO2 powder was mixed with 0.1 ml of acetylacetone, and was grounded mechanically. During vigorous stirring, 4 ml mixture of water and ethanol (1:1, in vol. %), and 0.4 ml of Triton X-114 were added.

Fourth Steps: Fabrication of TiO_2 thin films
At first the wood frame is placed on a glass substrate and after that the solution(TiO_2) is placed on screen and a squeegee is forced on the screen and then drawn linearly across the screen thus forcing coating solution through the open areas onto the substrate and at the end desired output on a glass substrate.This diluted paste was used for the TiO_2 coating on the glass by the use of a screen printer. Then by this process cell pattern can be reproduce 2x2cm and 1x1cm onto a glass .

3. RESULTS AND DISCUSSIONS

Figure 2 (a) shows the mask pattern of 2x2 cm for 16 pieces of samples. The vertical and horizontal Space between two nearest thin films is 0.4cm and 0.5cm, respectively. Figure 2(b) exhibits the picture of prepared TiO_2 films on glass substrate. The dimension of glass substrate is 10x10cm² and thin films is covered space is 8.5x8.8cm² on the same glass substrate. TiO2 films also recovered space is 8.5x8.8cm².
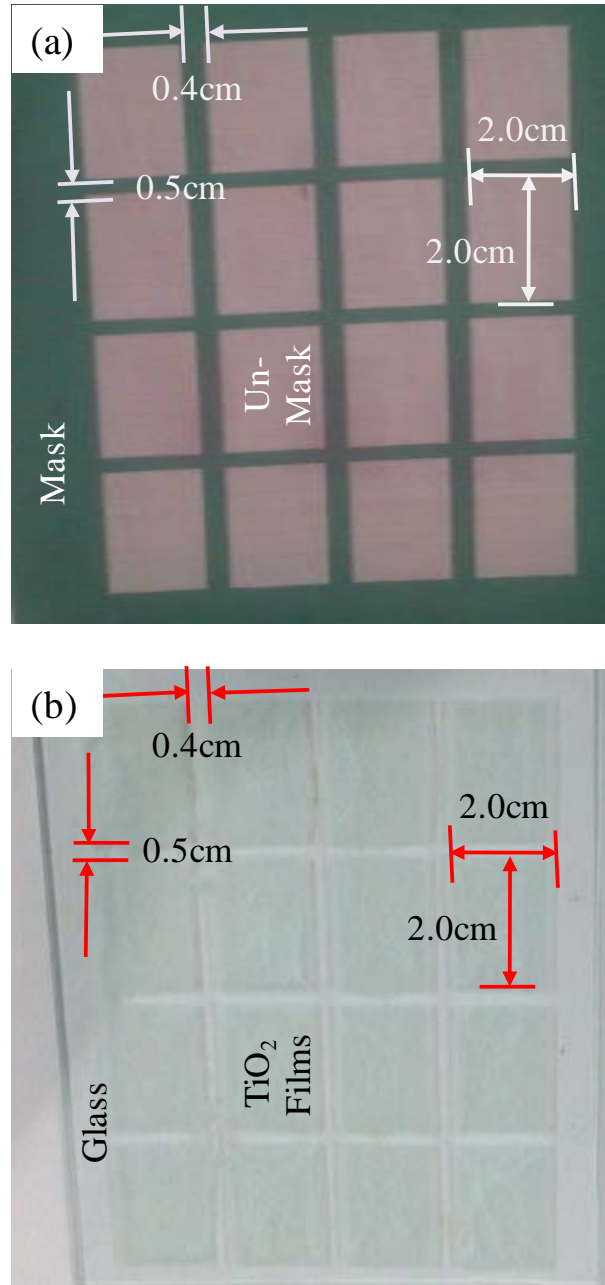
Figure 2: It is a design for screen printing process

Figure 3(a) shows the mask pattern of 1x1 cm for 42 pieces of samples. Vertical and horizontal Space between two nearest thin film is 0.2cm and 0.4cm . Figure 3(b) shows picture of TiO2 films on glass substrate. The made TiO2 thin films is transparent because the line "EEE RUET" bellow the thin film glass substrate is shown. So the TiO2 thin film is transparent from figure 5 .The dimension of glass substrate is 10x10cm² and cell recovered space is 8x8.8cm².TiO2 films also recovered space is 8x8.8cm².

(a)

0.5cm

0.5cm

1.0cm

1.0cm

Mask

Un Mask

(b)

0.5cm

0.5cm

1.0cm

1.0cm

Glass

TiO$_2$ Films
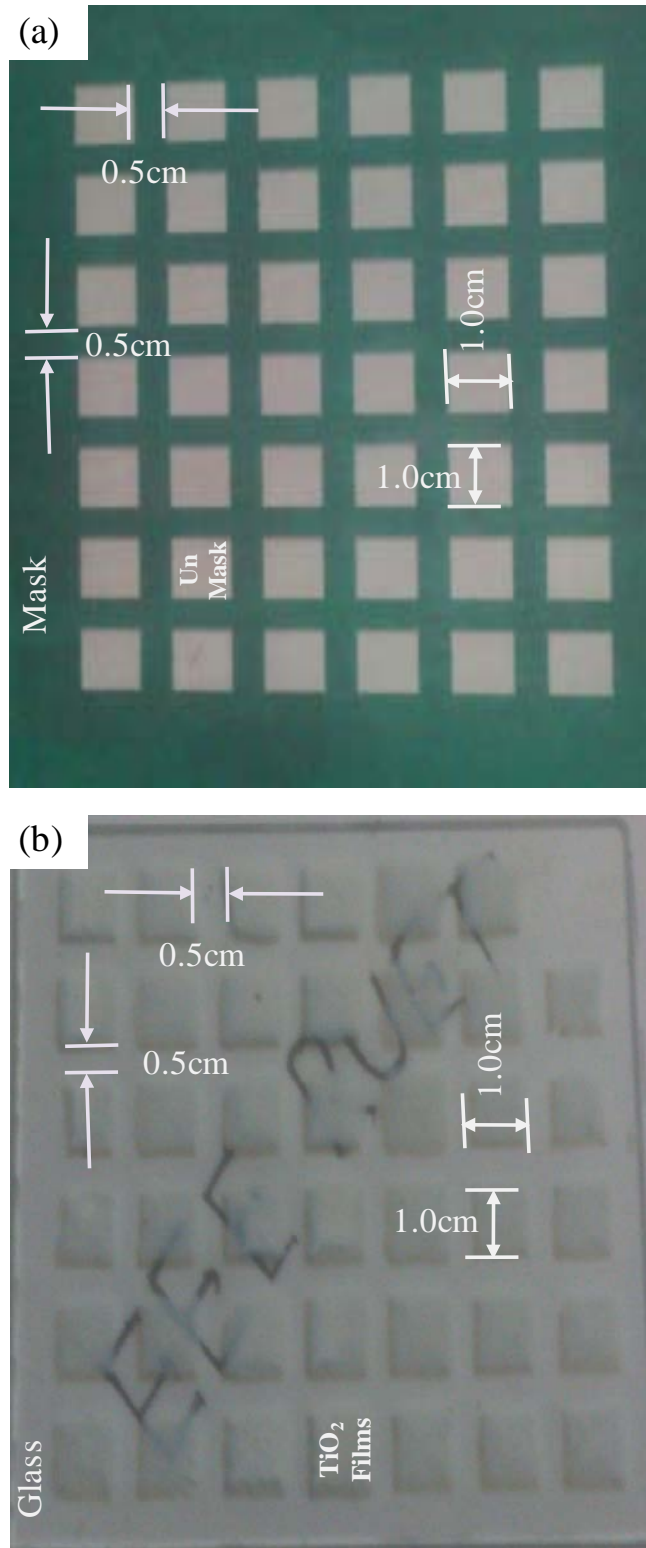
Figure 3: It is a design and fabrication of thin film of screen printing process[14]   .

4.Conclusion

For the above process, screen printer was made successfully by silk screen and wood frame.TiO_2 thin films have been deposited on glass substrate by using screen printer with various dimensions of 1x1cm and 2x2cm specimen. Sixteen TiO_2 thin films with dimension 2x2cm here is in the single glass substrate. Also forty two cell with dimension 1x1cm has been prepared by the same procedure. The space between two thin film has exactly same as the mask. This manual process can be modified in future by using computerized or microcontroller based automatic system. This screen printer may be used for large scale application by increasing the size and shape of the specimen. More over this screen printing is very cheap, quick process and very easy to use. It is an economic process and by this process solar cell can be made easily.

Figure 4:Design of screen printing process [10]

REFERENCES

[1].R.,Wengenmayr &.T.(Eds) Bührke. Renewable energy: Sustainable energy concepts for the future. Weinheim: Wiley-VCH,(2008).

[2].K.,Zweibel,J., Mason & F.,Vasilis. Solar grand plan. Scientific American.pp. 64-73. (2008, January).

[3].AmorphousSemiconductorsResearchGroup.Amorphoussilicon.Retrievedfrom
http://www.ayil.hacettepe.edu.tr/pages/Amorphous/Amorphous%20silicon.html,2010.

[4].Further mention of cost competitiveness: Solar Power Lightens Up with Thin-Film Technology, Scientific American, (April 2008).

[5].Thin films and InkTec awarded IDTechEx' Technical Development Manufacturing Award IDTechEx, April 15th 2009.

[6].P, Brenner , Printing photovoltaics. Industrial + Specialty Printing, 1(01),PP .26-33(,2010).

[7].Fraunhofer-Gesellschaft Screen-printed solar cells in many colors and designs ,evenuse din windows. Science Daily, *2008http://www.technologyreview.com/energy/21574/page1/.*

[8]. Zweibel, K., Mason, J., & Vasilis, F. Solar grand plan. Scientific American .pp. 64-73(2008, January).

[9].P.Brenner, Printing photovoltaics. Industrial + Specialty Printing,1(01),pp.26-33.http://www.ayil.hacettepe.edu.tr /pages/Amorphous /Amorphous%20silicon.htm(2010)

[10].Lenardic, Denis. Large-scale photovoltaic power plants ranking.pp. 1 – 50 *PVresources.com.*

[11].K,Bullis,Mass production of plastic solar cells. Technology Review. Retrieved from 2008, January 31 *http://www.sciencedaily.com/releases/2008/01/080130194130.html*

[12].U.S. Department of Energy . Photovoltaics. Retrieved from *www.eere.energy.gov/solar/pdfs/43684.pdf(2010).*

[13].F.M.,Vanek & Albright, L.D.Energy systems engineering: Evaluation & implementation. New York: McGraw Hil,(2008).

[14]. Various estimates of world module production are about 4 gigawatts (e.g., http://worldwatch.org/node/5449#notes)in *2007.*

[15]. S. Biswas, M.F. Hossain, T. Takahashi, T. Nakashima, Y. Kubota, A. Fujishima, Thin Solid Films .pp.516 (2008) 7313.

[16] .Y.C. Shen, H.H. Deng, J.H. Fang, Z.H. Lu, Colloids Surf., A Physicochem. Eng. Asp. 175, pp 135 (2000).

[17] .H. Hoppe, N.S. Sariciftci, Organic solar cells: an overview, J. Mater. Res. 19 ,pp.1924-1945–(2004) .

[18] C. Winder, N.S. Sariciftci, Low band gap polymers for photon harvesting in bulk heterojunctions solar cells, J. Mater. Chem. 14 ,pp.1077–1086(2004).

[19] S.E. Shaheen, D.S. Ginley, G.E. Jabbour, Organic-based photovoltaics: toward low-cost power generation, MRS Bull. 30,pp. 10–19(2005).

[20] R.A.J. Janssen, J.C. Hummelen, N.S. Sariciftci, Polymer–fullerene bulk heterojunction solar cells, MRS Bull. 30 ,pp.33–36. (2005)

[21] K.M. Coakley, Y. Liu, C. Goh, M.D. McGehee, Ordered organic–inorganic bulk heterojunction photovoltaic cells, MRS Bull. 30,pp.37–40 (2005).

[22] C.J. Brabec, J.A. Hauch, P. Schilinsky, C. Waldauf, Production aspects of organic photovoltaics and their impact on the commercialization of devices, MRS Bull. 30 ,pp.50–52 (2005).

[23] F.C. Krebs, Alternative PV: large scale organic photovoltaics, Refocus 6 (3),pp. 38–39(2005).

[28]. A. Kay, M. Grätzel, Sol. Energy Mater. Sol. Cells 99 pp 44(1996).

[24].T. Suntola,Thin film solar cells, Proceedings of the 11th European Photovoltaic Solar Energy Conference (Montreux, Schweiz, oct. 1992), Harwood, CH, pp. 977-980, 1993.

[25].Applied Materials . The world's most efficient solar cells. Retrieved from *http://www.appliedmaterials.com/technologies/solar/crystalline-silicon(2010)*.

Optimization of Process Parameters of Shielded Metal Arc Welding (SMAW) For Stainless Steel Welding

Dr. Naseem Ahmed[1], Soumen Halder[2], Md. Asadul Islam[2,] Niamat Ullah Ibne Hossain[2]

[1]Professor, Department of Mechanical Engineering, Khulna University of Engineering & Technology
[2]Students ,Department of Mechanical Engineering, Khulna University of Engineering & Technology
E-mail: Soumen.abhi@gmail.com

Abstract

Among the welding processes for stainless steel, shielded metal arc welding (SMAW) or stick welding is the most common. This process is used for stainless steel welding all over the country. The aim of this project was to find out the optimum current for stick welding. For this reason, a survey has been conducted in the welding workshops of Dhaka, Khulna and Chittagong to gather information about the most common electrode size and current they use to weld 12mm stainless steel rod. From the collected data welding has been performed on 12mm diameter stainless steel rod by using electrode size of 10 and 12 under different current levels. After performing the welding, tensile and bending test has been done for the welded joints. By analyzing the results from these two tests the optimum current for electrode size 10 and 12 has been determined for better welding performance.

***Keywords:** stick welding, Shielded Metal Arc Welding, Stainless Steel welding, current for stick welding.*

1. Introduction

Welding is a fabrication or sculpture process that joins materials, usually metals or thermoplastics, by causing coalescence. Coalescence is produced by heating to suitable temperatures with or without the use of either pressure or filler metal. Heat is generally produced by supplying alternating or direct current. Stainless steel is a form of steel which does not stain, corrode or rust by atmosphere like ordinary steel. In metallurgy, stainless steel, also known as inox steel or inox from French "Inoxydable", is defined as a steel alloy with a minimum of 10.5 or 11% chromium content by mass. In Khulna region stainless steels are welded by Shielded Metal Arc Welding process in most of the welding shops. Shielded metal arc welding (SMAW) is also known as manual metal arc (MMA) welding, flux shielded arc welding or informally as stick welding. This is a manual arc welding process that uses a consumable electrode, coated in flux to lay the weld. An electric current, in the form of either alternating current or direct current from a welding power supply, is used to form an electric arc between the electrode and the metals to be joined. This is the cheapest process to weld stainless steel. There are some other standard processes to weld stainless steel like MIG and TIG. But these processes are expensive and need expertise to perform welding operation. So, it is essential to study the effects of various process parameters of Shielded metal arc welding (SMAW) on weld quality and to optimize the process parameters to obtain good quality weld of stainless steel by using Shielded metal arc welding (SMAW) process.

2. Objectives

The objectives of this project work were given below:
i) To study about Shielded metal arc welding (SMAW) process.
ii) To gather information about the local Shielded metal arc welding (SMAW) techniques used in Khulna region to weld stainless steel.
iii) To gather information about various types of welding process and electrodes used in other region of Bangladesh for stainless steel welding.
iv) To optimize the Shielded metal arc welding (SMAW) parameters for proper stainless steel welding.

3. Plan of Work

The objectives of this project work has been fulfilled by the following steps:
i) Studying about Shielded metal arc welding (SMAW) process.
ii) Studying about various types of electrodes that can be used in Shielded metal arc welding (SMAW) to weld stainless steel.
iii) Visiting the local welding shops to gather information about their welding processes and equipments used in stainless steel welding. Also to collect similar information from other regions of Bangladesh
iv) Welding of stainless steel at various welding conditions by Shielded metal arc welding (SMAW) process and determination of the weld characteristics and mechanical properties.
v) Optimization of the Shielded metal arc welding (SMAW) process for stainless steel welding.

4. SMAW-Shielded Metal Arc Welding

SMAW is an electric arc welding process in which heat for welding is generated by an electric arc between a covered metal electrode and the base metal. The electrode coating provides shielding. The welding equipments for this process are currently the most inexpensive compared to the other welding methods. However, electrodes do create some inefficiency, such as stub loss and a slag coating, which must be removed.

To strike the electric arc, the electrode is brought into the contact with the work piece by a very light touch with the electrode to the base metal then is pulled back slightly. This initiates the arc and thus the melting of the work piece and the consumable electrode and causes droplets of the electrode to be passed from the electrode to the weld pool. As the electrode melts, the flux covering disintegrates, giving off shielding gases that protect the weld area from oxygen and other atmospheric gases. In addition, the flux provides molten slag which covers the filler metal as it travels from the electrode to the weld pool. One part of the weld pool, the slag floats to the surface and protect the weld from contamination as it solidifies. Once hardened, it must be chipped away to reveal the finished weld. As welding progress and the electrode melts, the welder must periodically stop welding to remove the remaining electrode stub and insert a new electrode into the electrode holder. This activity, combined with chipping away the slag, reduced the amount of time that the welder can spend laying the weld, making SMAW one of the list efficient welding processes. In general, the operator factor, or the percentage of the operators time spent laying weld, is approximately 25%. The actual welding technique utilized depends on the electrodes, the composition of the work piece and the position of the joint being welded. The choice of electrode and welding position also determine the welding speed. Flat welds required the least operator skill and can be done with the electrode that melt quickly but solidifies slowly. This permits higher welding speed. A slope, vertical or upside down welding requires more operator skill and often necessitates the use of an electrode that solidifies quickly to prevent the molten from flowing out of the weld pool. However, this generally means that the electrode melts less quickly, thus increasing the time required to lay the weld.

5. Experimental Procedure

The project work has been completed by several activities in a sequential way. First of all information about stainless steel, electrodes, welding parameters and details about shielded metal arc welding process has been gathered. This information has been gathered from several books, previous year thesis paper and also from various sites in internet. For this project work data have been collected from various shops in three different cities (Dhaka, Chittagong and Khulna) of Bangladesh. From these shops data for required current and electrode size for lap joining of two 12mm stainless steel rod have been collected. The amount of current and electrode size varies from shop to shop depending on worker's skill. Some collected data are given in a tabular form below:

Table-1: Data collected from various shops in three different cities:

Number of observations	Khulna		Dhaka		Chittagong	
	Electrode size	Current (amp)	Electrode size	Current (amp)	Electrode size	Current (amp)
01.	10	200	10	150	12	160
02.	12	80	12	80	12	140
03.	12	80	10	200	10	80
04.	12	100	10	140	10	140
05.	12	80	10	100	10	180
06.	10	150	12	70	12	120
07.	14	120	12	170	12	70
08.	10	140	10	130	12	100
09.	10	100	10	150	10	120
10.	12	160	12	100	10	180

After gathering the information about shielded metal arc welding process for stainless steel, the welding has been performed by using the data for particular electrode with particular current level that has been collected from various cities. The welding was performed on stainless steel rod of 12mm diameter. The electrodes used in this welding were from a company named Gemini. During the welding the gap between the rods was equal to the diameter of the electrode. The welding have been performed by using electrode of size 10(3.20mm) and 12(2.6mm) and current range was 70amp-190amp at an interval of 30amp. Total 20 specimens have been welded with10 specimens for each size of electrode. For different tests the lengths of the rods were 1 meter for 10 specimens and 0.5 meter for 10 more specimens. To achieve the optimum result welding time has been kept constant. Welding has been performed by professional person with good quality machines.

After the completing the welding the welded rods were brought to the laboratory for different tests. In this project tensile strength and bending strength have been measured. These two test have been performed by using Universal Testing Machine. The 1 meter long specimens were used to perform tensile test and 0.5 meter long specimens were used to perform bending test. The data collected from this two experiments are presented and compared in the given graphs below:
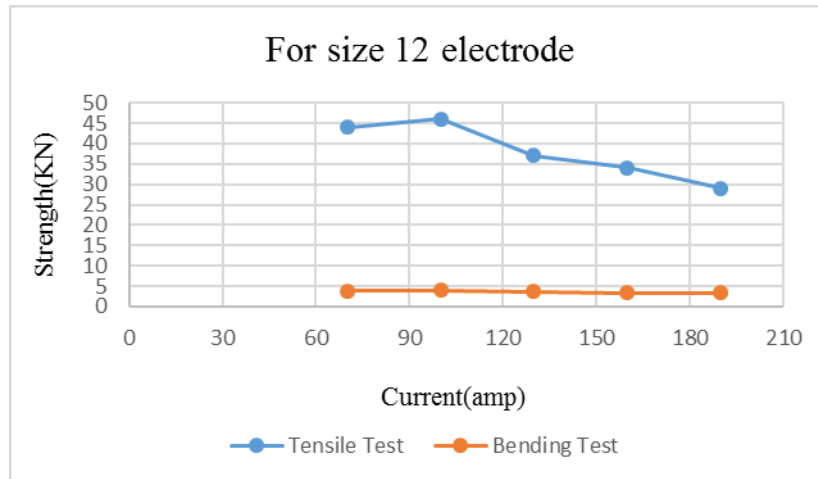
Figure-1: Change of strength with current for electrode size 12
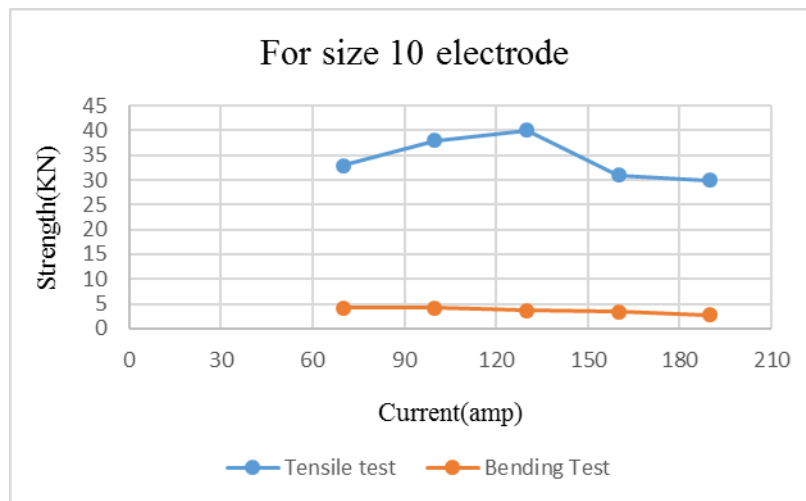
Figure-2: Change of strength with current for electrode size 10

6. Result

By analyzing the graphs it is observed that to get high quality welding for 12mm diameter of stainless steel rod by using size-10 electrode about 100amp current would be optimum current. To get high quality welding for 12mm diameter of stainless steel rod by using size-12 electrode around 100amp current would be optimum current. From the experimental data it is noticed that at low current such as at 70A current the strength of joints are relatively low. By the increase of current the strength of joints improves but again it starts to fall if the current is further increased. This is because, at low current supply the fusion doesn't occur properly. Incomplete fusion fails to produce sufficient heat to melt the filler metal properly thus the join remains weak. During high current supply excessive heat is produced. This excessive heat causes void, crack formation and partially spurt out molten metal. Thus the strength of joint decreases.

7. Conclusion

The data for this project has been collected from local road side welding shops. These shops use different current and electrode size for same purpose. They change the current and electrode size depending on their experience and skill without knowing which is appropriate. This type of attempt may cause some damage to the welded material. Improper welding can cause various problems in future. The aim of this project was to improve the welding quality in the road side shops by optimizing the welding parameters without increasing their cost. This project mainly deals with the welding current. By this project work, it has been observed that without changing the machineries, only optimizing the welding current it is possible to get good quality of welding.

References

[1] Jain, R.K, Production Process, Khanna Publishers, Delhi, 3rdEdition.

[2] Narang, G.B.S, Materials and Metallurgy, Khanna Publishers, 6th Edition.

[3] Avner, Y Sidney, Introduction to Physical Metallurgy, Tata McGraw-Hill Publishing Company Limited, 2nd Edition.

[4] Smith, Dave, Welding Skills and Technology, McGraw-Hill Inc, International Edition.

[5] Khanna, O.P, A Text Book of Welding Technology, Khanna Publishers, 2-B Nath Market, NaiSarak, Delhi.

[6] Zul Azri Bin Ismail, Effect of current on welding length based on electrode size, Technical University ofMalaysia Melaka.

[7] Mohd Zaim Bin Din, Experimental study on strength of spot welding, University Malaysia Pahang.